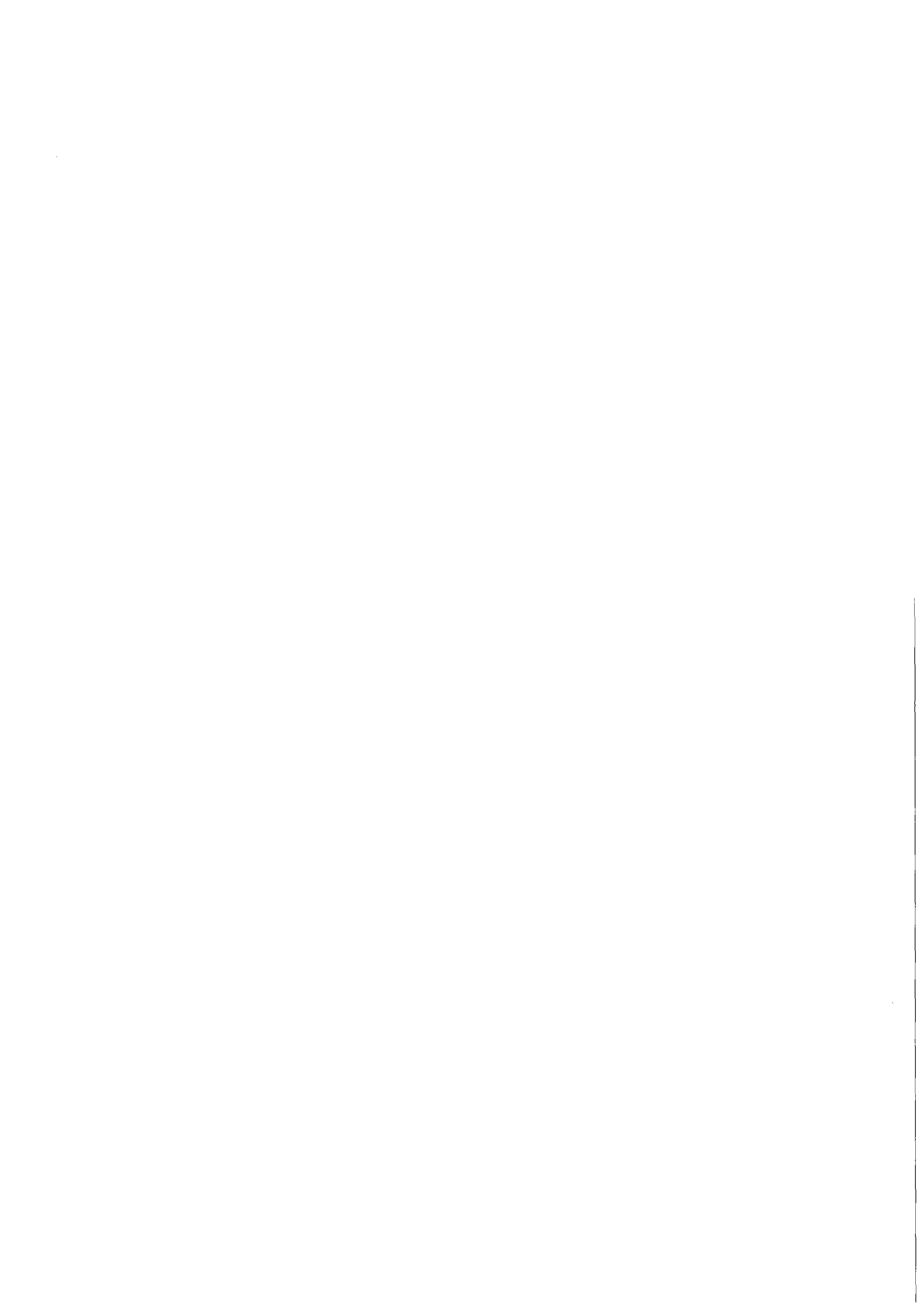# TASKA -

Tandem Spiegelmaschine Karlsruhe
A Tandem Mirror Fusion Engineering Test Facility

Volume 2

TASKA-Team
Institut für Technische Physik

KERNFORSCHUNGSZENTRUM KARLSRUHE

T A S K A - Tandem Spiegelmaschine Karlsruhe

A Tandem Mirror Fusion Engineering Test Facility

Volume 2

B. Badger[a]

F. Arendt[b]

H.M. Attaya[a]

K. Audenaerde[a]

H. Avci[a]

J.B. Beyer[a]

E. Bogusch[c]

G. Böhme[d]

D. Bruggink[a]

L. Buth[e]

L. Dietz[f]

H. Dittrich[b]

L. El-Guebaly[a]

G.A. Emmert[a]

J. Erb[b]

H. Frey[b]

B. Glaser[d]

G. Grant[g]

W. Heinz[b]

W. Hennhöfer[d]

W. Köhler[d]

P. Komarek[b]

G.L. Kulcinski[a]

M. Kuntze[h]

E.M. Larsen[a]

T. Lechtenberg[i]

H.G. Leiste[d]

X.Z. Li[a]

W. Link[d]

B.M. Manes[b]

W. Maurer[b]

C.W. Maynard[a]

F. Mehren[c]

E. Montalvo[a]

D. Mundt[c]

Z. Musicki[a]

E. Opperman[j]

J.E. Osher[k]

L.J. Perkins[a]

R.R. Peterson[a]

K.E. Plute[a]

U. Quade[c]

G. Ries[l]

H. Runge[c]

J.F. Santarius[a]

M.E. Sawan[d]

J.E. Scharer[a]

D.C. Schluderberg[g]

H. Schütz[c]

A. Suppan[d]

I.N. Sviatoslavsky[a]

D.K. Sze[a]

W. Tischler[c]

M.A. Vogel[j]

W.F. Vogelsang[a]

A.M. White[a]

W.G. Wolfer[a]

K.Y. Yuan[a]

D.B. Young[g]

(a)	UW/FPA	(e)	KfK-INR
(b)	KfK-ITP	(f)	Grumman Aerospace
(c)	Interatom	(g)	Babcock and Wilcox
(d)	KfK-IT	(h)	KfK-IK

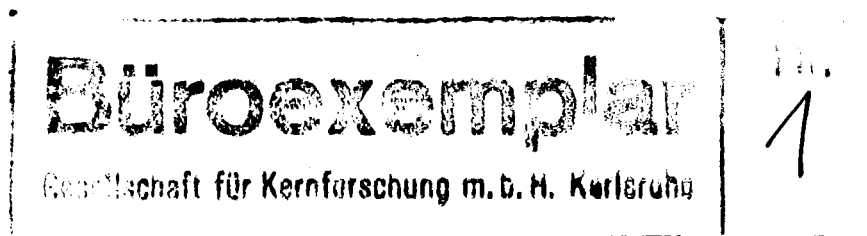|			
(i)	General Atomic
(j)	HEDL
(k)	LLNL
(l)	Siemens

Abstract:

TASKA (<u>Ta</u>ndem <u>Sp</u>iegelmaschine <u>Kar</u>lsruhe) is a near term engineering test facility based on a tandem mirror concept with thermal barriers. The main objectives of this study were to develop a preconceptual design of a facility that could provide engineering design information for a Demonstration Fusion Power Reactor. Thus TASKA has to serve as testbed for technologies of plasma engineering, superconducting magnets, materials, plasma heating, breeding and test blankets, tritium technology, and remote handling.

Zusammenfassung:

TASKA - Eine Tandem-Spiegel-Fusions-Testanlage

TASKA (<u>Ta</u>ndem <u>Sp</u>iegelmaschine <u>Kar</u>lsruhe) ist eine Testanlage für Technologien, die sich auf das plasmaphysikalische Konzept eines Tandem Spiegels mit thermischer Barriere stützt. Hauptziel der Studie war, eine Anlage zu entwerfen, die Auslegungsinformationen für einen Demonstrationsfusionsreaktor liefern soll. Daher muß TASKA als Testbett für Technologien dienen, wie etwa Plasmaengineering, supraleitende Magnete, Materialien, Plasmaheizung, Brut- und Testblankets, Tritiumtechnologie und Fernbedienung.

Table of Contents for TASKA

VII Testing Program

VII.1 Overview

An important function of TASKA is to provide a reactor relevant testing environment for both materials and blanket modules. To that end, the central cell region of TASKA has been designed to maximize the access to the test modules while at the same time provide sufficient tritium breeding to make TASKA self-sufficient. We have also separated the materials testing modules from those testing integrated blanket concepts because, in general, we wanted to maximize the damage rate in the materials modules.

It is also important to realize the time frame for which TASKA is designed. If it were to operate in the early 1990's, then TASKA could be providing useful information by the mid 1990's. Such information would be of great value to confirm the choice of materials and blanket concepts chosen for Demonstration reactors which themselves might be operating at the turn of the century. It is probable that the DEMO's would be under design in the mid 1990's. This distinction between confirmation and determination is quite important here. If we wanted to use TASKA to determine what materials and blankets should be used in the DEMO, then we would have to wait until high fluence data from TASKA is thoroughly analyzed and integrated in the DEMO design. This could not happen before the late 1990's which means that the DEMO would probably not be operating until the year 2010 or so. On the other hand, if we make the choices for the DEMO based on other test devices, such as light water and fast fission reactors, RTNS-II, or FMIT, then TASKA could be used to confirm that those choices were indeed reasonable. This would allow a DEMO to be designed in the early 1990's, built in the late 1990's and operating near the turn of the century. If the materials or blankets chosen for the

DEMO do not withstand the full fusion environment of TASKA, then the construction of the DEMO could be delayed until a suitable solution could be found.

Another aspect of the testing capabilities of TASKA which needs to be discussed is the ability of such a device to provide information for many other fusion concepts such as tokamaks, stellarators, etc. The real question is, can the pulsed environment (on the time scale of one burn cycle, ~100 seconds) of a tokamak or the plasma wall interaction of any toroidal device be simulated by a steady state, open-ended machine? Certainly one could surround samples with electrical heaters which could be periodically varied to produce temperature cycles. It is also possible to mechanically or pneumatically impose loads on structural members to simulate periodic stresses. However, such simulation procedures will require more complex testing modules and may seriously reduce the "high flux" test volume available for samples. Nevertheless, it could be done and in future designs such test capsules will be designed.

There are two areas where TASKA cannot reasonably simulate the environment of a tokamak, i.e., disruptions and first wall erosion. Disruptions are so violent that both the electromagnetic and thermal loads far exceed what could be programmed into a tandem mirror machine. The rapidly changing magnetic fields will impose loads on blankets and first walls which may cause them to fail prematurely. If we are to learn about such phenomena, they probably will have to be tested in a tokamak.

The high flux of charge exchange particles characteristic of divertor slots, limiters, or neutral beam ports can cause erosion by sputtering and/or blistering. While such effects may be present in the end plug region of TASKA, the lack of such an environment in the central cell where the neutrons

are produced means that the first wall environment in a TMR will be far less severe than for tokamaks. If a blanket concept or particular first wall material is susceptible to such particle fluxes, it will be very difficult to properly simulate it in TASKA.

In summary, TASKA is designed to test both materials and blanket concepts in a high temperature, high neutron fluence environment. The main task of TASKA is to confirm DEMO, material and blanket choices already made by previous tests at low fluence, or on the basis of a few specimens tested to high fluence in neutron spectra similiar to, but not exactly the same as in a fusion device. After confirmation is completed, TASKA can be used to develop the materials and blankets for the first generation of commercial reactors. The useful life of TASKA is expected to be ~15 years but with some modifications, 20 years may be possible. This would allow materials and blankets to be tested well into the 21st century.

VII.2 Materials Testing

VII.2.1 Introduction

The testing of materials for a Demonstration Reactor at the turn of the· century has placed some severe requirements on TASKA. For example, we need to obtain high integrated fluences (in the neighborhood of 5 MW-years/m^2) under reactor relevant conditions in the shortest possible time. These requirements prompted the REGAT (Reduced Damage Gradient) concept to be examined and a large amount of this chapter is devoted to its analysis. At this time the neutronic characteristics of the design have been investigated in the most detail, but some thought has also been devoted to the question of temperature control and ease of replacement.

The whole question as to how many, and what kind of materials samples need to be tested has been addressed in a manner similar to that in the INTOR, ETF, and to a limited degree, the FED projects. We have tried to benefit from these previous analyses and also tried to tailor the materials testing program to the tandem mirror program. Certainly much more work needs to be done in the future as feedback from the materials community is obtained.

The organization of this subchapter is as follows. First a generalized description of the neutronics of fusion test blankets is given and the particular geometrical advantages of the REGAT module are highlighted. Next, the specific test matrix considered for the magnetic fusion program is given along with the design of the TASKA-REGAT module. Finally, the neutronics analysis of the TASKA-REGAT module is given.

VII.2.2 Neutronics Survey Analysis

VII.2.2.1 Introduction

One problem with past materials test modules[1-4] has been the large

spatial variation in displacement damage (dpa), gaseous transmutation rates,

and nuclear heating from the first wall to the back of the module. In an

effort to minimize those gradients, we have designed a Reduced Gradient Test

Module (REGAT) for TASKA. In the REGAT design, the blanket region is cut back

from the first wall to leave the test module protruding into the vacuum cham-

ber (see Fig. VII.2-1). This results in direct exposure of the module sides

to source neutrons. Therefore, the damage gradients in the module are reduced

as compared to the traditional design which is surrounded on all sides by the

normal blanket and shield. A survey neutronics analysis of the REGAT module

is presented here to assess its effectiveness in reducing damage gradients and

enhancing the materials testing capability. The results for the REGAT module

used in TASKA are given and compared to the results for the current INTOR[2]

materials testing module in Section VII.2.4.

VII.2.2.2 Calculational Model

The materials testing module is placed at the center of the cylindrical

central cell section of the tandem mirror reactor. Fig. VII.2-1-a shows a

schematic of the traditional test module. The module is immediately behind

the first wall and surrounded on all sides by the normal blanket and shield.

In Fig. VII.2-1-b, the original REGAT design is shown with the test module

protruding into the vacuum chamber and directly exposed to neutrons on the

sides. An improved REGAT design is shown in Fig. VII.2-1-c. In this design,

the blanket region surrounding the module is tapered to increase the contri-

bution to the damage in the module from neutrons reflected from the blanket.

a) TRADITIONAL
MODULE

b) ORIGINAL REGAT
MODULE

c) IMPROVED REGAT
MODULE

PLASMA CENTER-LINE
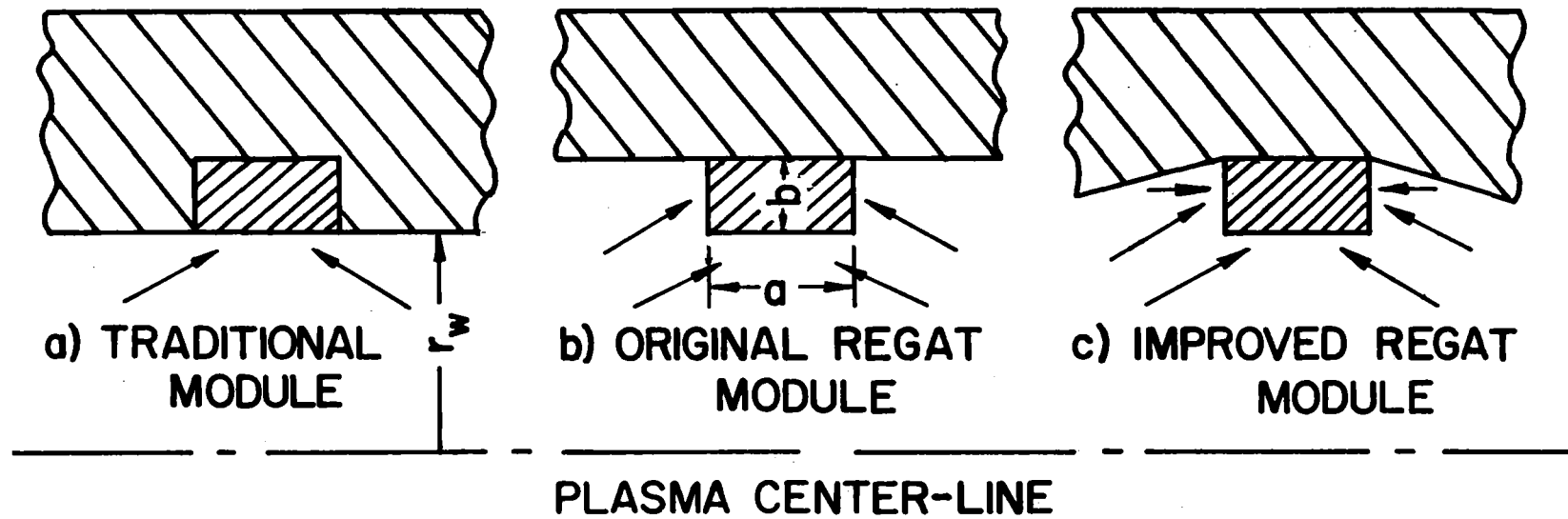
Fig. VII.2-1   Schematic of REGAT and traditional test modules.

Further enhancement of damage can be obtained when a neutron multiplier is used in the region of the blanket surrounding the module. In TASKA, neutron multiplication results from using $Pb_{83}Li_{17}$ liquid metal eutectic as a coolant/breeder. The REGAT module, with width a and thickness b, has an inner radius r_w. A blanket consisting of 81 v/o $Pb_{83}Li_{17}$ and 10 v/o structure made of the ferritic steel alloy HT-9 was considered in this work. Although the TASKA design was used in the calculations, the results are more general and apply to any linear fusion device.

Detailed neutronics calculations have been performed, using the three-dimensional Monte Carlo code MORSE,[5] to determine the spatial variation in the damage of different module designs. A coupled 25 neutron-21 gamma cross section library, consisting of the RSIC DLC-41B/VITAMIN-C data library[6] and the DLC-60/MACKLIB-IV response data library,[7] was used.

The combinatorial geometry capability of the MORSE code was used to model the geometry of the problem. The test module was divided into 60 zones with volume detectors used to estimate the quantities of interest in the different zones. An isotropic 14.1 MeV neutron source was sampled uniformly from a cylindrical plasma zone which is 20 m long and 32 cm in radius. Because of symmetry, only half the central cell was modelled with a reflecting albedo boundary used at the center of the module.

The geometry for the computational model used is given in Fig. VII.2-2. L is the central cell length and L_0 is the length over which the blanket is tapered. L and L_0 were taken to be 20 m and 4 m, respectively. The zones 1 to 30 were used to get the spatial variation of damage in the REGAT module. A 30 cm thick blanket was used in the calculations and is represented by zone 31.
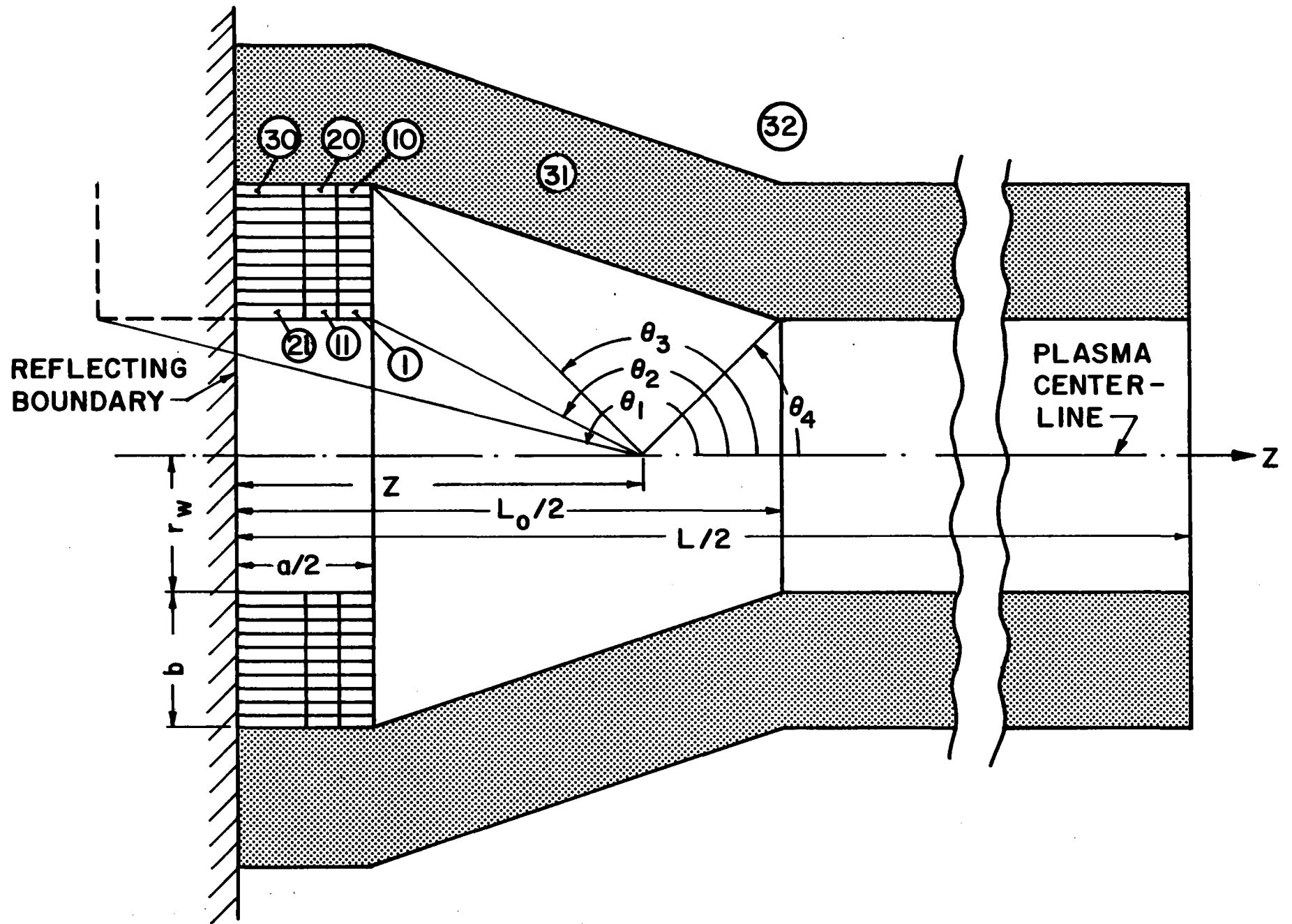
Fig. VII.2-2   Geometrical model used in Monte Carlo calculations.

Since the width of the test module is much smaller than the central cell length, a position dependent angular source biasing technique was used to get statistically adequate estimates for the neutron flux in the test module. This technique is similar to that used previously for the analysis of the end plug of a tandem mirror fusion reactor.[8]

First an axial position z is sampled uniformly along half the central cell from the distribution function

$$P(z)dz = 2dz/L .$$ (VII.2.1)

The polar angle θ is then picked from a biased distribution with 95% of the neutrons forced to have polar angles between θ_{min} and θ_{max}. This biased distribution is given by

$$P(\cos\theta)d\cos\theta = \begin{cases} \dfrac{0.95 \; d\cos\theta}{\cos\theta_{min} - \cos\theta_{max}} , & \theta_{min} < \theta < \theta_{max} \\[4mm] \dfrac{0.05 \, d\cos\theta}{2 + \cos\theta_{max} - \cos\theta_{min}} , & \theta_{min} > \theta > \theta_{max} . \end{cases}$$ (VII.2-2)

The value of θ_{min} is determined depending on the axial position of the source. The smallest of θ_2 and θ_3 is compared to θ_4 and the larger angle is considered as θ_{min}. For all axial positions, θ_{max} takes the value of θ_1. This leads to particles reaching the REGAT module without collision 95% of the time and particles suffering at least one collision before reaching the module 5% of the time. For the final estimates to be unbiased the statistical weight of the source is modified by the ratio of the unbiased to the biased distribution functions at the polar angle picked. An azimuthal angle ϕ is then sampled

VII.2-6

uniformly from the distribution function

$$P(\phi)d\phi = d\phi/2\pi \ . \qquad\qquad\qquad (VII.2-3)$$

Finally, a radius is sampled for the source particle from the distribution function

$$P(r)dr = 2rdr/r_p^2 \ , \qquad\qquad\qquad (VII.2-4)$$

where r_p is the plasma radius.

50,000 histories were used in the Monte Carlo calculations yielding less than 10% statistical uncertainties in the estimates for the damage rates in the different module zones. The results in this work are normalized to a wall loading of 1 MW/m^2 at the front surface of the module.

VII.2.2.3 Analysis of REGAT Module Performance

A series of survey calculations was performed for the REGAT module with different values for the width and thickness to investigate the effect of dimensions on the testing capability of the module. Calculations have also been performed for the traditional module design to assess the effectiveness of the REGAT module in reducing the damage gradients. In these survey calculations, a first wall radius of 40 cm was used. The test module was considered to consist of 50 v/o 316 SS and 50 v/o void. All the results presented here are normalized to a 1 MW-yr/m^2 fluence.

Figure VII.2-3 shows the spatial variation of atomic displacement and helium production rates in a 5 cm wide and 100 cm long REGAT module as compared to the equivalent traditional module. The peak damage rate occurring
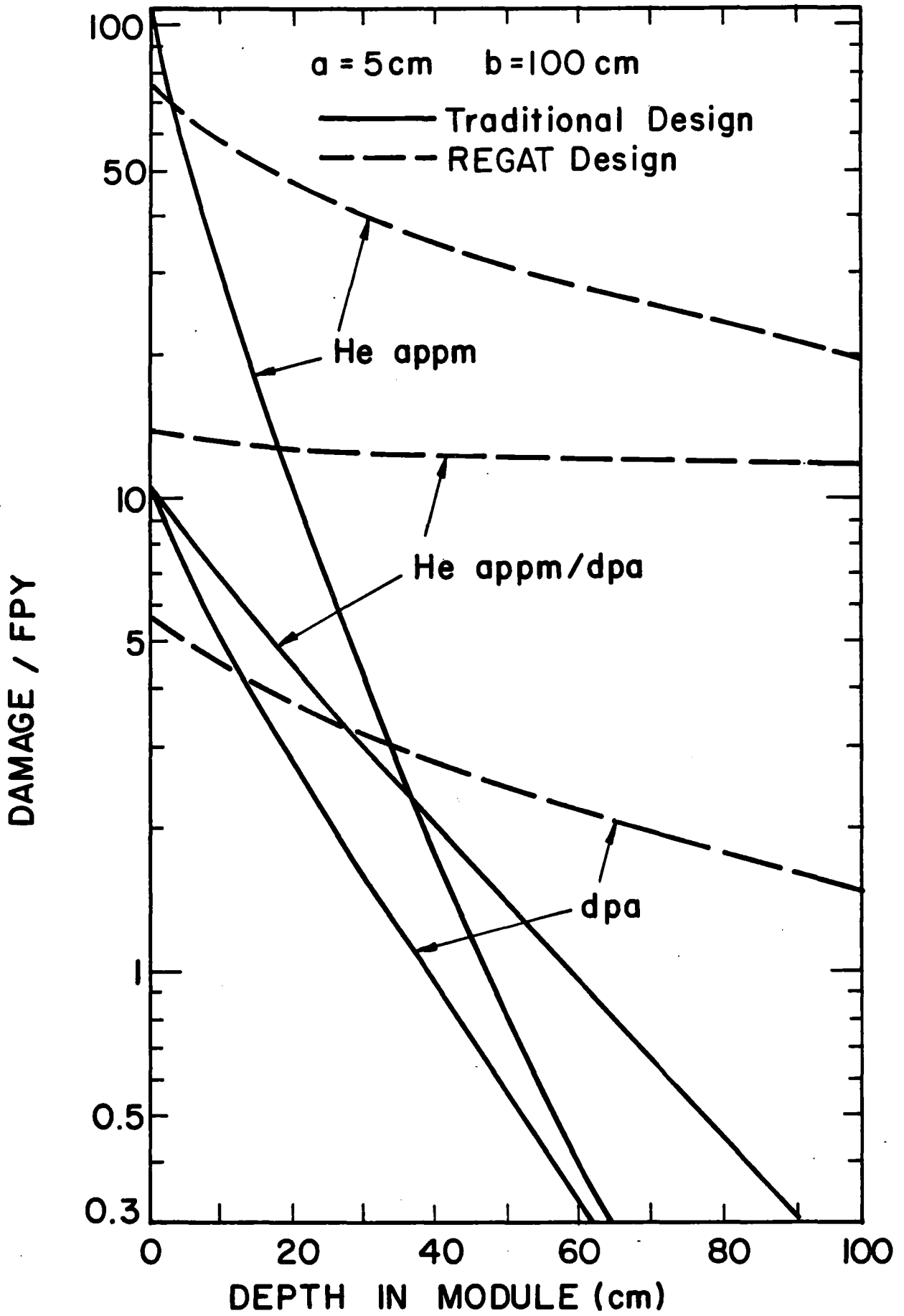
Fig. VII.2-3 Spatial variation of damage in traditional and REGAT modules.

at the front of the module is decreased in the REGAT module. The reason is that source neutrons missing the module will impinge on the adjacent first wall and after being slowed down can contribute to the damage of the front of the traditional module. This effect is more pronounced on the dpa which can be produced by neutrons with energies as low as ~ 1 keV. However, the gradients for both dpa and helium production rates are reduced considerably when the REGAT module is used. The net effect is that the average damage rates in the REGAT module are greater than those in a traditional module with the same dimensions. The spatial variation of helium to dpa ratio, which is an important parameter affecting microstructure evolution,[9] is also shown. A nearly uniform He/dpa ratio is obtained in the REGAT module. This results from the fact that less neutron spectrum softening occurs in the REGAT module when compared to the traditional module.

Table VII.2-1 gives the average and peak/average ratios for dpa and helium production rates for different REGAT module dimensions. Fixing the module width and decreasing the thickness results in increasing the average damage rates and reducing the gradients. This results from the reduced attenuation in the radial direction. Decreasing the width for a fixed length results also in increasing the average damage rates and reducing the gradients because of reduced attenuation in the axial direction.

It is clear from the results of Table VII.2-1 that decreasing the thickness b has more pronounced effect on increasing the average damage rates than does decreasing the width a. This results primarily from decreasing the peak damage rate occurring at the center of the front surface of the module as the width, a, decreases. Hence, for a fixed test module volume, it is expected that the average damage rate increases if one uses a wider module. In Fig.

VII.2-9

Table VII.2-1. Effect of Module Dimensions

on Damage Rates in the REGAT Module

		dpa/FPY		He appm/FPY	
a(cm)	b(cm)	Avg.	Peak/Avg.	Avg.	Peak/Avg.
5	100	2.37	2.271	30.62	2.535
5	50	3.25	2.131	41.63	2.254
7.5	50	3.19	2.302	39.20	2.564

VII.2-4, the volume integrated damage rate, used as a measure of the testing

capability of the module, is plotted versus module length for a fixed module

volume of 0.153 m^3. For the purpose of comparison, the results for the

traditional module are also included. Notice that the two modules give the

same results in the limiting case when the testing zone covers the whole

central cell length. The REGAT module has a higher performance factor than

that of the traditional module with the improvement being more prounounced

when a thick module is used. Hence, one gains significantly by using the

REGAT module when the area devoted for materials testing is limited by other

considerations such as tritium breeding.

Figure VII.2-5 shows the variation of dpa rate with depth in a 7.5 cm

wide and 50 cm thick module for the traditional design and three REGAT module

cases. In the first case, no neutron reflection from the surrounding blanket

is considered. The second case represents the original REGAT design with a
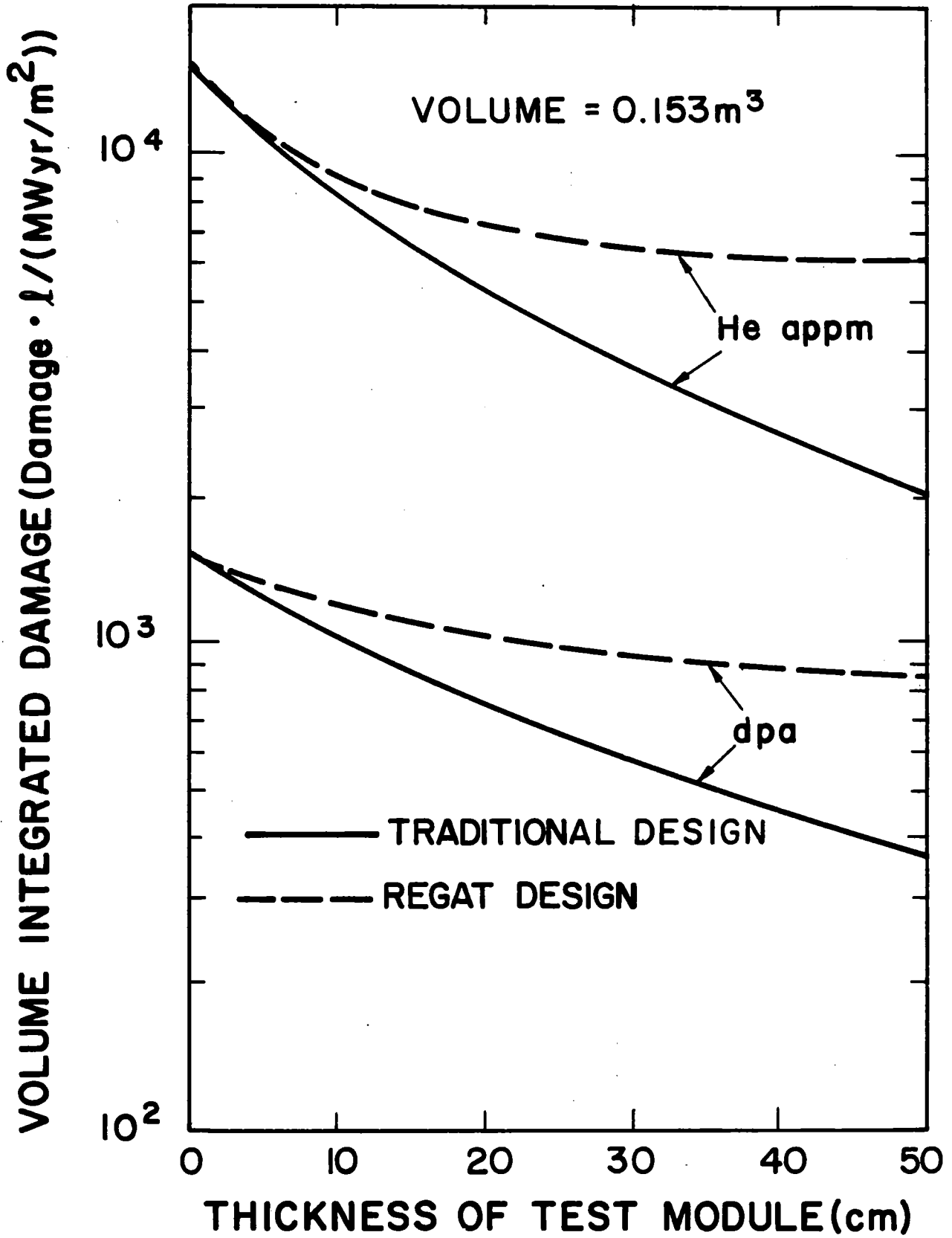
Fig. VII.2-4   Volume integrated damage as a function of module thickness
for a fixed volume.
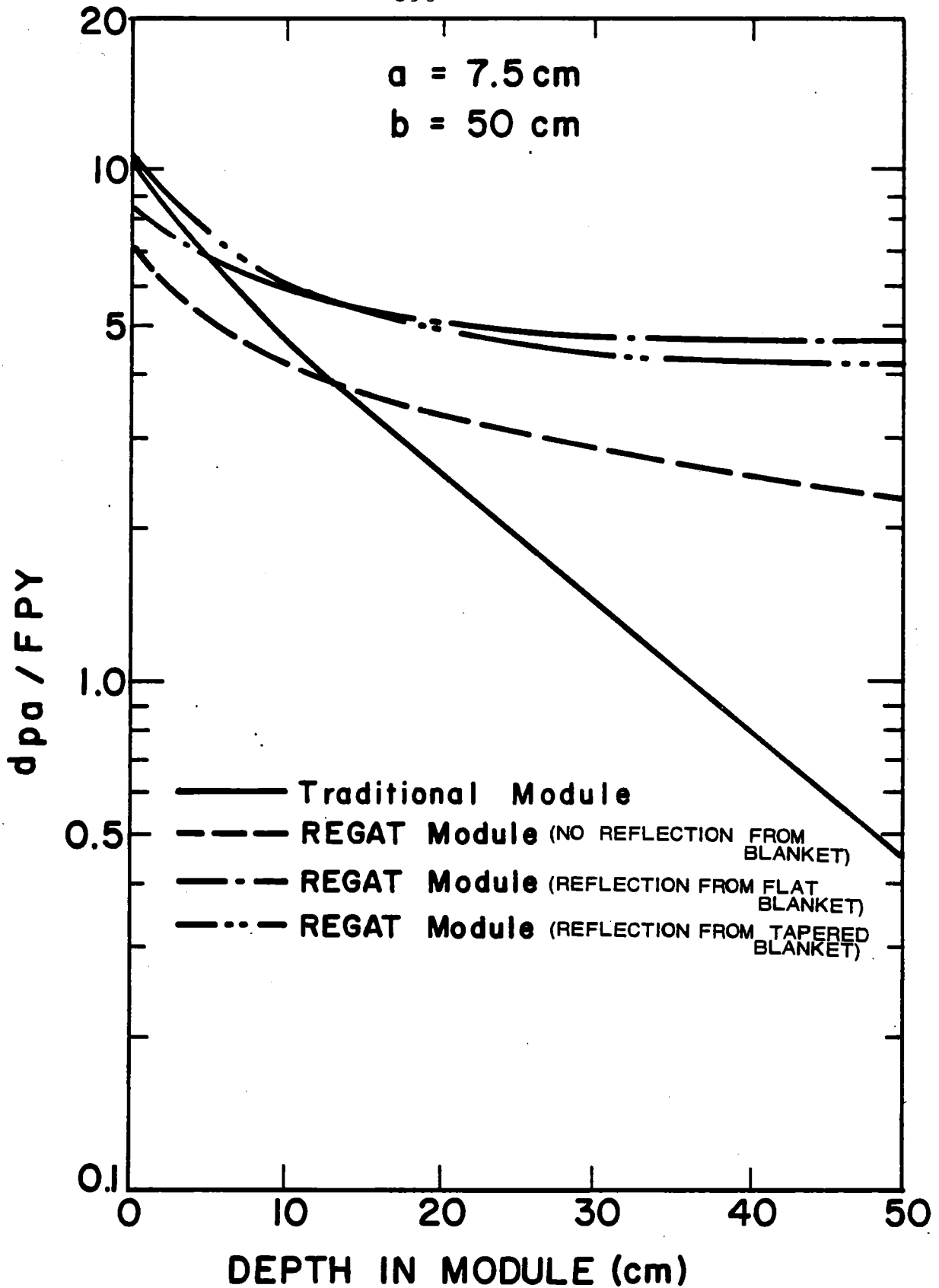
Fig. VII.2-5 Spatial variation of dpa rate for different module designs.

VII.2-12

flat blanket adjacent to the module and the third case represents the improved REGAT design with the adjacent blanket tapered as shown in Fig. VII.2-1. Table VII.2-2 shows the average and peak/average ratios for dpa and helium production in these cases. It is clear that, even in the case when no reflection from the blanket is considered, the REGAT module has higher average damage rates and less gradients than the traditional module. However, the peak damage in this case is much lower than that in the traditional module because of the lost contribution from source neutrons missing the module.

When neutron reflection and multiplication in the flat adjacent blanket are considered, the damage rate increases at all points of the module with the effect being more pronounced at the back of the module (which is closest to the blanket where the reflected neutrons originate). This results in higher average damage rates and less damage gradients. The effect on helium production is not as pronounced as that on dpa because most of the neutrons produced in (n,2n) reactions with lead in the blanket do not contribute to helium production.

The peak damage rate is increased further by tapering the inner surface of the blanket surrounding the module. On the other hand, the damage rate at the back of the module decreases because less source neutrons impinge directly on the back of the module side. This results in a slightly higher damage gradient. The effect is more pronounced for helium production, most of which is caused by direct source neutrons. The net result is that the average dpa rate increases while the average helium production rate decreases with tapering. Even though the damage gradients are slightly increased, using the improved REGAT design is recommended because it results in a higher average dpa rate and allows some test specimens to be exposed to high damage levels.

VII.2-13

Table VII.2-2. Effect of Neutron Reflection From the Blanket

on Damage Rates in a Test Module 7.5 cm Wide and 50 cm Thick

	dpa/FPY		He appm/FPY	
	Avg.	Peak/Avg.	Avg.	Peak/Avg.
Traditional module	2.342	4.27	13.045	7.69
REGAT module (no reflection)	3.188	2.30	39.202	2.56
REGAT module (reflection from flat blanket)	5.140	1.59	43.535	2.30
REGAT module (reflection from tapered blanket)	5.347	1.95	39.591	2.53

VII.2.2.4 Conclusions

An improved materials testing module for engineerng test facilities is presented. Detailed neutronics analysis shows that the REGAT design reduces the damage gradients and increases the average damage levels in the module significantly. The results of the survey calculations show that the improvement over the traditional design is more pronounced when a thick module is used. Hence, one gains significantly by using the REGAT module when the area devoted for materials testing is limited by other considerations such as tritium breeding. Tapering the inner surface of the blanket surrounding the REGAT module increases the contribution to the damage from reflected neutrons and hence increases the average dpa rate and allows more test specimens to be exposed to high damage levels.

VII.2.3 Test Matrix and Test Module Design Considerations

The test matrix for materials irradiations in TASKA is very similar to the matrix developed by the INTOR Test Program group[2] during its 1980 Phase-1 study. The TASKA test matrix is a list of materials test specimens and their required environmental and irradiation conditions. Test matrices in general provide a starting point for both experiment and facility designers by defining, in exact terms, what is to be irradiated and under what conditions. Given this information, along with the physical and neutronics features of the reactor, the experiment designer can then, in principle, design a specific test module or modules to physically contain and environmentally control the necessary number of materials test specimens. The test matrix specifications combined with the resultant test module designs are then used as a basis for many of TASKA's mechanical and operational requirements. Hence, the test matrix provides a basis for experiment design, which in turn provides a design basis for that portion of the TASKA facility that interfaces with and is required to support the testing program.

VII.2.3.1 Test Matrix

The TASKA test matrix specifies the type of materials with detail on specimen numbers, irradiation temperatures, fluences, stress, changeout frequencies and postirradiation testing conditions. The test matrix provides a basis for estimating the volume needed for materials testing in TASKA plus other information such as range of test temperatures, etc. Also, the frequency of specimen changeout must be accommodated by the test module design with minimal impact on reactor availability.

The test matrix is shown in Table VII.2-3. The presumed scope of the testing specified in the test matrix is that one or two candidate materials

TABLE VII.2-3

Proposed Materials Test Matrix -TASKA

Materials Surveillance	Mat. Var.[a]	Dup.[b]	Temp.[c]	Fluence[d]	Conditions	Total Specimens Mirror[e]	Total Specimens Tokamak[f]	Total Capsule[g] Mirror[e]	Total Capsule[g] Tokamak[f]
Tensile	3	2	2	2	2 rate/temp.	48	48	3	3
Fatigue	0(3)	0(2)	0(2)	0(2)	0(4) stress	0	96	0	4
Crack growth	1(2)	2	2	3	3 stress levels	36	72	1	2
Fracture	2	2	2	2	2 temp.	32	32	4	4
					Subtotal	116	248	8	13
Structural Materials									
Tensile	5	3	6	5	6 rate/temp.	2700	2700	10	10
Fatigue (High Cycle)	0(8)	0(3)	0(2)	0(4)	0(4) stress	0	768	0	29
Crack growth	3(6)	2	4	4	3 stress levels	288	576	3	6
Fracture	4	3	4	2	2 temp.	192	192	5	5
Swelling	10	5	10	5	4 post irr. tests	10,000	10,000	5	5
Stress relax.	6	4	6	-	5 stresses	720	720	3	3
Creep-rupture	6	2	6	-	5 stresses	360	360	2	2
In situ-cyclic	0(4)	0(2)	0(2)	-	0(4) stress levels	0	64	0	64
					Subtotal	14,260	15,380	28	124
Other Materials[h]									
Fatigue	.5	3	4	4	2 strain range	480	960	11	22
Tensile	15	3	6	4	4 rate/temp.	4,320	4,320	15	15
Dimensional stab.	15	5	6	4	4 post tests	7,200	7,200	4	4
Creep	10	2	6	-	4 stresses	480	480	2	2
In situ-cyclic	0(6)	0(2)	0(2)	-	0(4) stresses	0	96	0	96
Fracture	3	2	2	2	6 temp.	144	144	7	7
Elect. prop.	6	3	2	4	3 tests	432	432	18	18
Therm. Cond.	6	3	4	4	---	288	288	12	12
					Subtotal	13,344	13,920	69	176
					Total	27,720	29,548	105	313

[a] Materials x variations
[b] Duplication
[c] Number of irradiation temperatures
[d] Fluence levels
[e] Specifically for the Mirror Program
[f] Required for both Mirror and Tokamak Programs
[g] Capsule volume-390 cm³
[h] Ceramics, electrical, and heat dump materials
( ) Addition for tokamak program

have been identified (through extensive fission reactor and accelerator source screening programs) for the various applications (first wall, structure, insulators, etc.) and the extent of testing is determined by the number of specimens needed to determine quantitatively the critical properties of the irradiated materials.

The first portion of the test matrix (surveillance and structural materials) was developed for candidate first wall materials and other structural components receiving high exposure and the second portion of the test matrix was developed for other high exposure applications such as high heat flux components, armor, and RF. The test matrices reveal why large numbers of specimens are needed to provide design data.

In the test matrix, the types of tests are listed in the left hand column, and important test parameters are summarized as column headings across the top. The first parameter is "materials x variations" and refers to the number of base (candidate) materials and the number of variations in heat treatment or different conditions such as weldments to be tested. The second column refers to duplication of specimens, primarily to verify the reproducibility of data. In some cases such as specimens for swelling and phase stability, the duplication also allows for attrition in the postirradiation preparation of samples.

The next two columns refer to the two basic parameters of irradiation temperature and fluence. The numbers of separate irradiation temperatures and goal fluences are given in these columns.

Typically, parallel tests are performed at several irradiation temperatures in order to map expected temperature-dependent behavior over the range of interest. Usually, linear dependence of materials properties on tempera-

ture is not expected, especially near ceiling temperatures (above which useful service is not expected).

The microstructure of materials is often studied at more temperature conditions than are mechanical properties because swelling and phase stability are quite sensitive to temperature, and the more complete characterization of microstructures with temperature (and fluence) provides a qualitative guide for interpolating a coarser matrix of observations on materials properties. For example, microstructural observations were performed at intervals of about 50°C in irradiation tests supporting alloy development for the U.S. breeder program. In the test matrices for TASKA, the number of irradiation temperatures varies from four temperatures for several mechanical properties tests to ten temperatures for observations of swelling and phase stability.

Irradiation experiments typically include tests to a goal fluence, representing end-of-life conditions if possible, and several interim fluences. Irradiation experiments are expensive and take a long time. Consequently, preliminary predictions of material behavior are used for redirecting experimental objectives and for preliminary design data, pending corroboration with data at high fluences. However, the extrapolation of low fluence data to predict properties at high fluences can be grossly misleading. A rule of thumb is extrapolation by less than a factor of two in fluence (for moderate fluence levels, i.e. exceeding incubation doses for property changes) is acceptable. Data at several values of moderate to high fluences is desirable to define trends, especially where the properties after irradiation are only marginally acceptable. Five goal fluences are appropriate for some tests in TASKA on structural materials (components using "other" materials were assumed to be more easily replaceable than the first wall and have lower lifetime fluences).

VII.2-18

The column heading "Conditions" refers to test conditions other than temperatures and fluence. Most of the conditions, for example the strain ranges in fatigue tests, are conditions in postirradiation tests performed after the specimens are removed from TASKA. Another example of postirradiation test conditions is for tensile tests where both the strain rate and the postirradiation test temperature are variables. Typically, postirradiation tensile tests are performed at the irradiation temperatures, at a temperature slightly above the irradiation temperature, and at the temperature expected in the material during refueling or during repair. Designers use these data to predict behavior during operation and for fault conditions such as overheating and seismic response.

In the case of creep tests, the other "condition" is stress. The current techniques for in-reactor creep tests utilize sealed tubes pressurized to different stress levels. The diameters of the tubes are measured at several intervals of fluence after which the specimens are again placed in the reactor for further exposure.

The last two columns give the total number of specimens and the number of irradiation capsules (see Section VII.2.3.2.2 for capsule description) for two cases: (1) mirror relevant testing, and (2) mirror and tokamak relevant testing. The key difference between the two cases is that in (2), fatigue and crack growth specimens are not included. The total specimen numbers are the product of the previous columns. The number of capsules is simply the number of capsules required to hold the specified number of specimens.

The mirror, and mirror and tokamak cases require similar numbers of test specimens: 27,720 vs. 29,548, respectively. However, the irradiation volume required for the mirror and tokamak testing is nearly three times that of the

mirror-only test program. This is due to the relatively large number of specimens required to carry out the stress cycling tests. The configuration and size of material test specimens selected for the TASKA matrix are shown in Appendix VII.2-A.

Test Matrix Related Operations. The fluence requirements specified in the TASKA test matrix necessitate test module removal from the reactor at periodic intervals. The number and time between removals is a function of (1) the test matrix goal fluences, and (2) the rate at which damage is accumulated over the necessary specimen volumes.

The TASKA goal fluences are assumed to be 2, 5, 15, 25, and 50% of some goal fluence - assumed to be 200 dpa for structural materials. Hence, specimens will be discharged from the reactor at 4, 10, 30, 50, and 100 dpa levels.

Figure VII.2-6 is used to determine the time required to achieve the goal dpa levels. The figure illustrates the dpa level throughout a specimen capsule. The average dpa value is used to determine the discharge frequency.

Based on the above fluence level requirements and the dpa rate available in TASKA, the resultant capsule discharge sequence will be as illustrated in Fig. VII.2-7. The capsule discharge sequence is based on an initial test module loading of 252 capsules. At each interim examination, approximately 63 capsules are removed from the test module for specimen analysis. Sixty-three fresh capsules are then loaded into the test module for further irradiation along with the ~ 189 previously irradiated capsules which remained in the test module. This operational sequence minimizes the total time required to achieve the specified goal fluences. Table VII.2-4 summarizes some salient test matrix results and operational frequencies.

FIGURE VII.2-6

ASSUMPTIONS
- 1.5 MW/m^2
- CENTER PLANE OF MODULE
  (DOES NOT SHOW REGAT ADVANTAGE)
- 50% HT9, 50% VOID

A = STRUCTURAL MATERIALS
$\overline{\text{dpa}}$ = 13±3

B = SPECIAL PURPOSE MATERIALS
$\overline{\text{dpa}}$ = 7±4

MODULE WALL

SPECIMEN CAPSULE

A   B

DISTANCE INTO TEST MODULE

dpa PER FPY

HEDL 8112-077.3

FIGURE VII.2-7

HEDL 8112-077.1
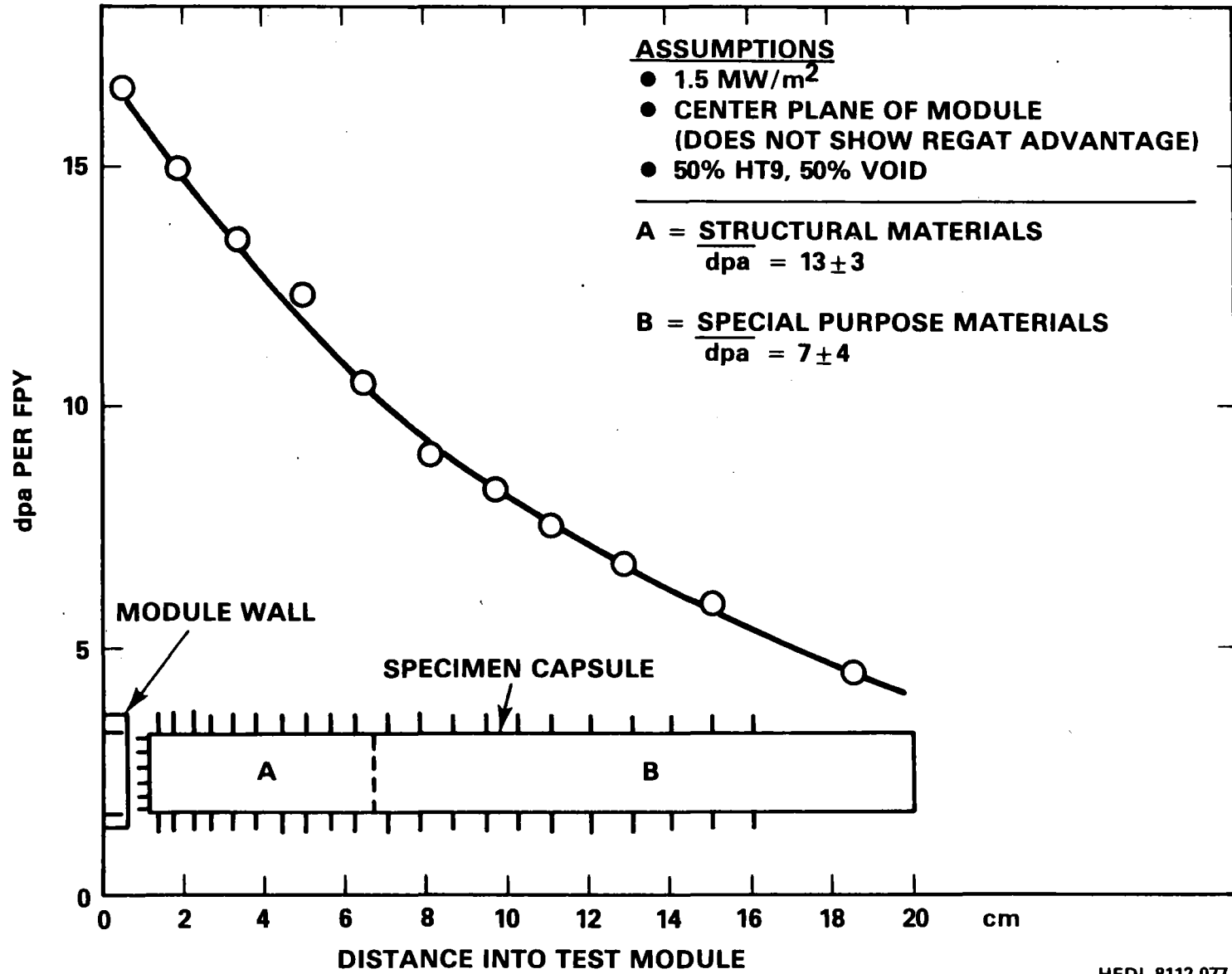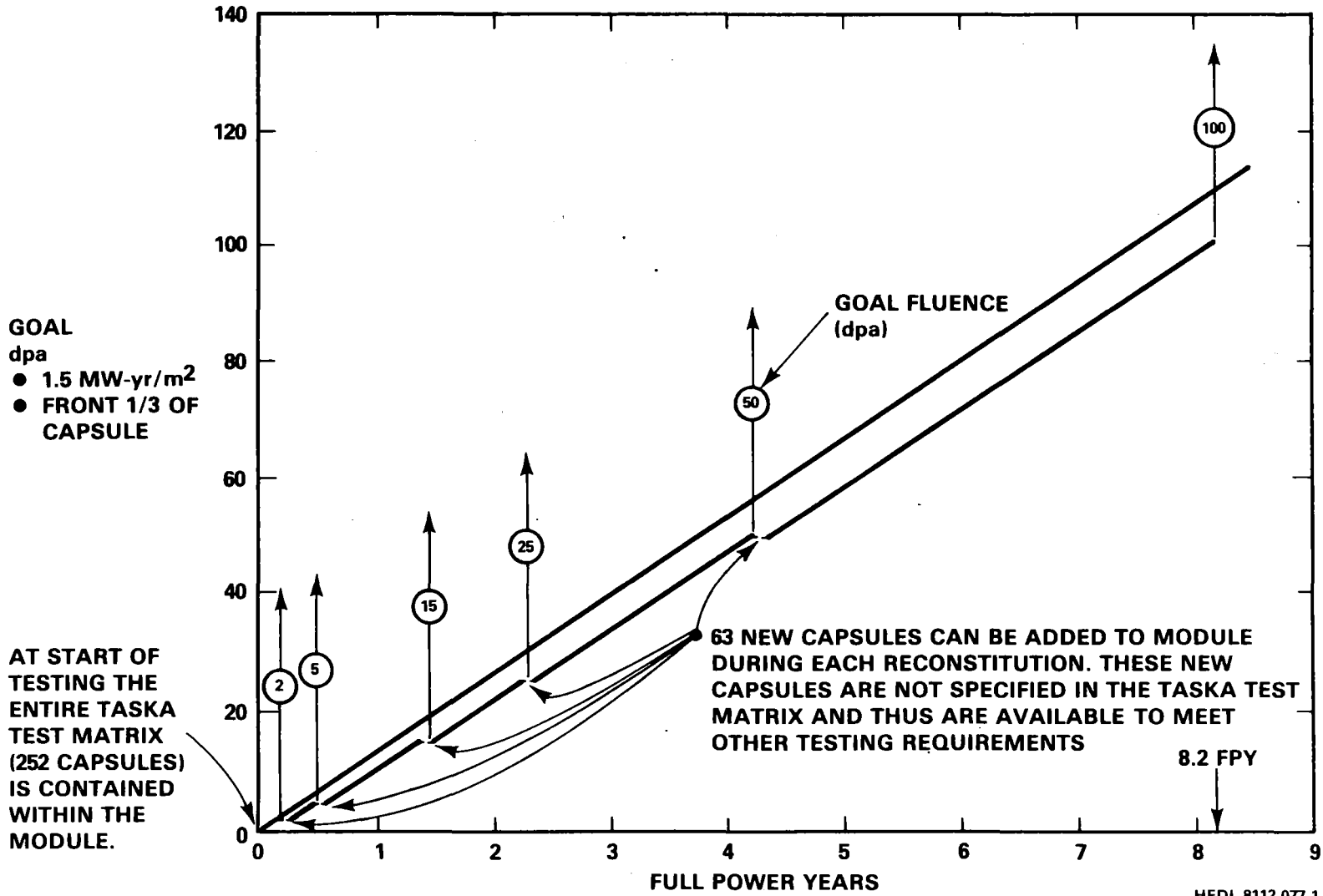
Table VII.2-4. Parameters Derived from TASKA Test Matrix

	Item	Value
1.	Number test modules (TM) in TASKA	1
2.	Number specimen capsules in TM	252[*]
3.	Time to achieve maximum fluence (FPY)	8.2
4.	Ave. time between TM changeouts from reactor (da)[+]	497
5.	Minimum time between TM changeouts (da)[+]	86
6.	Maximum time between TM changeouts (da)[+]	1432

[*]Mirror and tokamak specimens considered.

[+]Full power days.

VII.2.3.2 Test Module Design Considerations

The test module is the hardware that contains the materials test specimens and provides environmental containment as specimens are irradiated in TASKA. Figure VII.2-8 illustrates the key features of the test module concept design for TASKA. The key components of the test module, that will be referred to often in this chapter, are the (1) <u>specimen capsule</u> which contains the groups of individual material specimens, and (2) the <u>annular test module</u> which acts as the heat sink and holding fixture for specimen capsules.

The test module concept must be consistent with the requirements of the test matrix (Section VII.2.3.1) and with the mechanical and neutronics characteristics of the TASKA reactor. The reactor configuration therefore strongly affects the test module design and conversely the test module will have an impact on the availability, floor space, services, access, remote handling, and operations required by TASKA.

VII.2.3.2.1 Test Module Design Criteria and Concepts

The test module is based on the following general design requirements:

1. Reliability.

2. Minimum specimen temperature variation.

3. Quick turn-around (reconstitution).

Based on the above general test module requirements and features of the conceptual TASKA reactor design, the following more detailed critiera (Table VII.2-5) were established to guide the TM design. These requirements and criteria are consistent with the TASKA test matrix and were established as a result of materials testing experience gained through involvement in (1) the fast breeder reactor program, and (2) design studies supporting the Fusion Materials Irradiation Test Facility and the INTOR Phase-1 Study.

FIGURE VII.2-8

TANDEM MIRROR SINGLE UNIT TEST MODULE

SINGLE UNIT
TEST MODULE

TANDEM MIRROR
VACUUM BOUNDARY

MAGNET

VACUUM
SHROUD

REMOVABLE
SHIELD

ANNULAR
TEST MODULE

TEST SPECIMEN
CAPSULE

HEDL 8106-158.1A
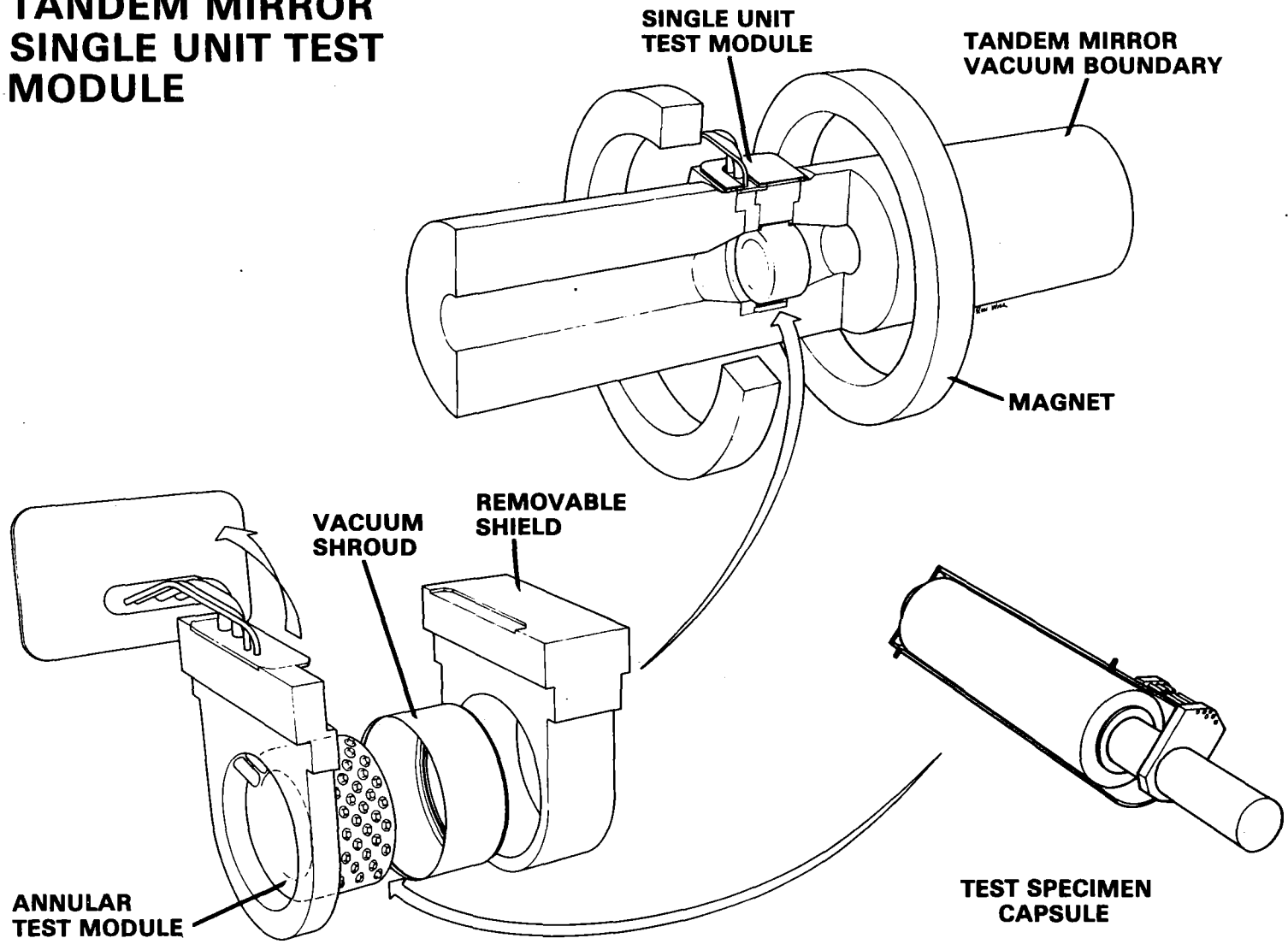
Table VII.2-5. Design Criteria

1. Test module shall pemit simultaneous irradiation of an array of specimen capsules within the first 20 cm of blanket region. Maximum axial reactor opening is 95 cm.

2. Test module components shall have a design lifetime of at least four full power years.

3. Temperature range available in designing specimen capsule shall be 300-650°C with a calculated variation in specimen temperature of less than 10°C.

4. Each specimen capsule shall have independent temperature control and monitoring capability.

5. Test modules shall be capable of accepting previously irradiated specimens and undergo reconstitution.

6. A portion of the test module shall interface directly with the plasma chamber. There will be no first wall between test module and plasma.

7. The test module shall interface with the adjoining blanket and shield consistent with the REGAT concept, and consistent with biological shielding requirements.

8. Test module design shall maximize utilization of the available flux-volume.
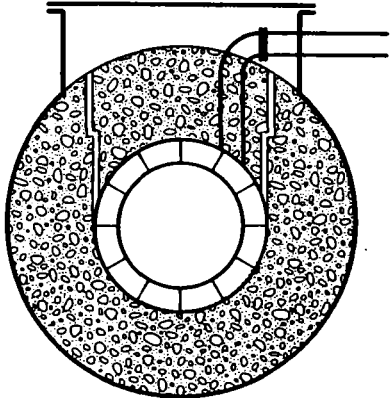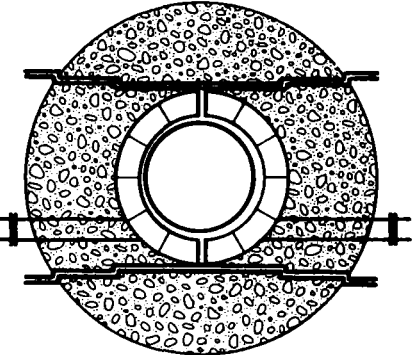
Test Module Design Concepts. Since the above criteria do not uniquely define a single test module, a number of concepts were considered. Table VII.2-6 graphically illustrates four TM concepts that were considered. The concepts were evaluated according to the considerations listed horizontally along the top of the table. Questions posed by designers in evaluating the considerations are as follows. Reliability: Will the design last and is the design solid and simple? Versatility: Can the design accommodate a range of specimen types and sizes and can the overall test module configuration be changed as programmatic considerations mature and evolve? Fabricability: Can standard welding, machining and forming techniques be employed? Remote Handling: Can the test module be inserted and removed from the reactor utilizing standard remote systems? Can service leads be connected and disconnected; is there sufficient space and access for remote operations? Specimen Access: Can specimen capsules be easily removed from the test module; can the specimens be removed from the capsules routinely? Volume Utilization: Is the volume occupied by the TM being used to irradiate an optimum number of material specimens? Sealing: Can the TM systems and components be hermetically sealed?

Based on a qualitative assessment of the above considerations the "single unit test module" (Table VII.2-6) was selected as the reference design concept. The reference test module is the simplest design structurally and is inserted into the reactor vertically requiring only an overhead crane. Access for service connection and atmospheric sealing is from the top, thus avoiding the congested areas typically found along the sides of a reactor. The TM is removed from TASKA as a single unit - and it is recommended that the TM be directly transported into a hot cell for disassembly.
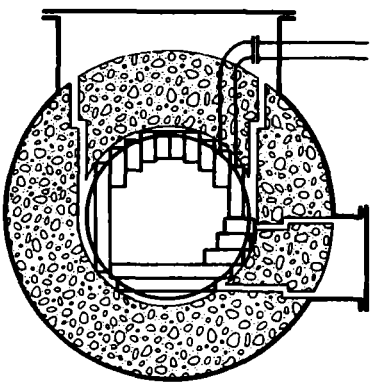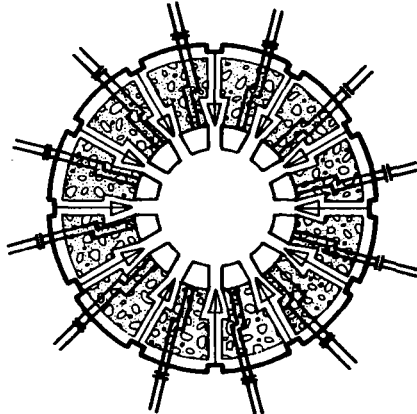
VII.2-27

TABLE VII.2-6

TEST MODULE CONCEPTS

CONCEPT	RELIABILITY	VERSATILITY	FABRICABILITY	REMOTE HANDLING	SPECIMEN ACCESS	VOLUME UTILIZATION	SEALING	COMMENTS
1. SINGLE UNIT MODULE	+	+	+	+	−	+	+	DUAL HORIZONTAL ACCESS REQUIRED
2. CLAMSHELL MODULE	+	+	O	O	−	+	+	TO REMOVE SPECIMENS ENTIRE MODULE IS WITHDRAWN

——— VACUUM BOUNDARY   + = GOOD

——— MATERIALS TEST   O = FAIR
MODULE AND SERVICES   − = POOR

HEDL 8106-158.16

TABLE VII.2-6 (cont.)

TEST MODULE CONCEPTS

CONCEPT	RELIABILITY	VERSATILITY	FABRICABILITY	REMOTE HANDLING	SPECIMEN ACCESS	VOLUME UTILIZATION	SEALING	COMMENTS
3. MULTIUNIT MODULE	O	+	–	O	O	O	–	SPECIMENS CAN BE REMOVED WITHOUT REMOVING ENTIRE MODULE
4. DIRECT ACCESS MODULES.	O	O	O	–	+	O	O	REQUIRES 360° ACCESS

——— VACUUM BOUNDARY   + = GOOD

——— MATERIALS TEST   O = FAIR
MODULE AND SERVICES   – = POOR

HEDL 8106-158.18

The three other TM concepts are considered to be viable; however, they are progressively more complex and have more "parts", require more access space and in general are considered less reliable and harder to handle remotely. A more detailed description of the TM design will now be given.

VII.2.3.2.2 Test Module Design Details

The major components of the TASKA materials test module, shown in Fig. VII.2-8, are the helium cooled heat sink (annular test module), the biological shield and the specimen capsules. The temperature within each of the 351 specimen capsules is pre-determined by engineering the thermal barrier between the specimen capsule and the heat sink. Individual capsules can be independently accessed and are designed to operate at a predetermined temperature within the range of 300 to 650°C. The total irradiation volume within a single TASKA test module is 138 liters. Table VII.2-7 lists the detailed test module design values determined during the initial concept design.

Test Module. TASKA allocates one reactor opening for materials testing - located between two of the central cell magnets. The test module is inserted into TASKA vertically through a rectangular 140 x 200 cm opening in the vacuum vessel. Appendix VII.2-B illustrates test module design details and location within the reactor. The annular test module consists of a titanium, helium filled pressure vessel structure which is penetrated by 351 capsule holes. The capsule holes are arranged with their long axes along radial lines with the open end of the capsule hole facing away from the plasma. The capsule holes are arranged in staggered rows on a triangular pitch. Helium flows circumventially inside the module perpendicular to, and outside of, the capsule holes. Instrumented specimen capsules shown in Fig. VII.2-9 can be inserted in any of the 351 capsule holes. The specimen capsule outside diameter is

Table VII.2-7. Design Values

Reactor Opening

• Maximum axial opening of 95 cm

Test Module

• Material of construction: 0.635 cm thick titanium alloy (Ti-6Al-4V)

• Size: Inside radius - 50 cm

    Outside radius - 70 cm

    Length - 69.2 cm (end to end) 44.2 cm straight section

• No. of capsule tubes: 351

• Total heat generation: 1145 kW

• Coolant: helium at 3448 kPa and 125°C

• Flow rate: 72.9 x 10^3 ℓ/min

• Coolant pipe size: 20 cm diameter

• Instrumentation per capsule tube: 2 pair thermocouple leads - chromel-

    alumel

    2 gas leads - 0.158 cm diameter for gas

    gap control

Specimen Capsule

• Material of construction: 316 stainless steel

• Size: 5 cm diameter by 20 cm long

• Specimens: various shapes packed to 50% of capsule volume in NaK (22/78)

• Instrumentation: (2) 0.158 cm diameter stainless steel sheathed MgO

    insulated thermocouples

• Sealing: all welded construction with bellows for NaK expansion

• Gas gap: variable annulus 0.018-0.076 cm filled with helium or neon or

    mixtures of the two gases

FIGURE VII.2-9

CAPSULE
CHANNEL

GAP
TUBES

ELECTRICAL
CONTACT

THERMOCOUPLES

TEST
CAPSULE

ADJUSTABLE
INSULATING
GAP

CAPSULE
CHANNEL
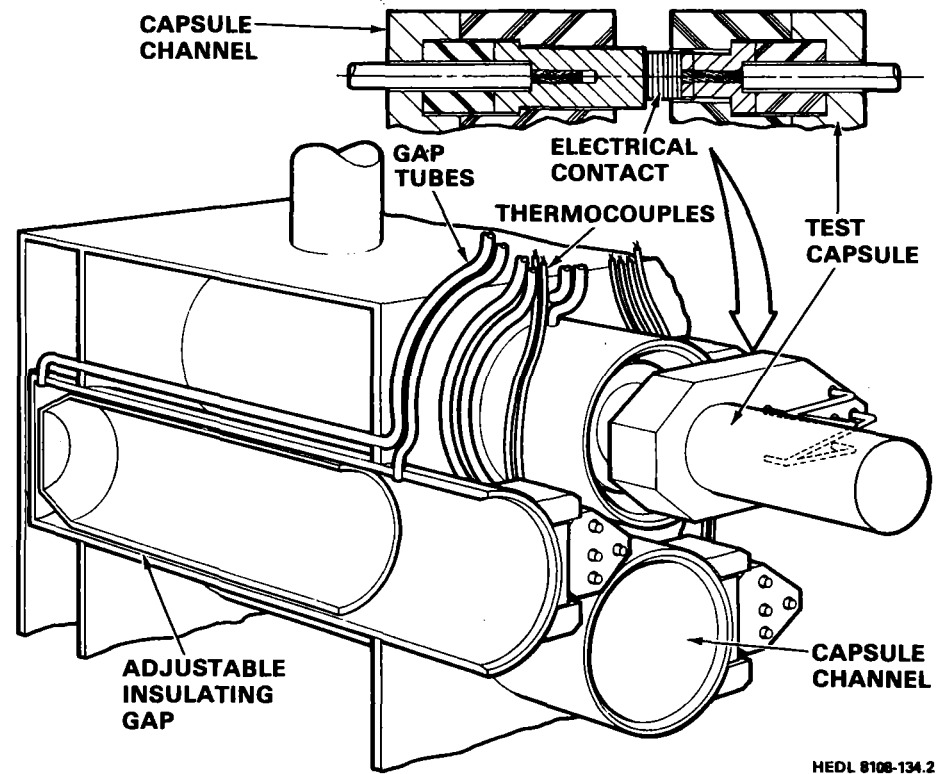
HEDL 8108-134.2

spaced from the inside wall of the capsule hole by a gas gap. This gap be-
comes "sealed" when the specimen capsule is inserted into the capsule hole.

Neutron and gamma heat deposited in the test specimens is transferred by
conduction via the NaK liquid metal to the capsule wall, across the insulating
gap, through the outer wall, which is cooled on the outside by the circulating
helium system. Two 1.6 mm O.D. tubes are provided to access the insulating
gap near the top and bottom of each of the 351 capsule holes. These tubes can
provide inert gas to the insulating gap space. Two (2) lines are provided to
the gap to permit either a static or dynamic supply of gas. In addition, they
allow for on-line change-out of gas.

Two pair of thermocouple leads are connected to each of the 351 capsule
holes and are routed between capsules along the top front surface of the
module. The electrical leads terminate in an electrical connector which is
positioned near the entry of each capsule hole. This connector becomes mated
with the specimen capsule thermocouple leads when the capsule is inserted in
the capsule hole. The electrical leads (702 pair of thermocouples) and tubes
(702) are routed from the module, along the helium coolant lines through
stepped openings in the shield plug. From there they are run to instrument
cabinets located in the experiment support area.

Coolant System. The coolant system is designed to remove heat from the
test module structure and the specimen capsules contained within it. The
various coolant media considered are listed in Table VII.2-8; they are:
water, sodium and helium. From a heat transfer and remote handling stand-
point, water is the most effective coolant. However, as discussed in Section
VII.2.1, the presence of water in the test module moderates the high energy
neutrons to such a degree that their damage energy is reduced by a factor of

Table VII.2-8. Comparison of Coolants for TASKA Test Module

	Water	Sodium*	Helium
DPA reduction to test specimen	Large	Medium	None
MHD effects	Medium	Large	None
Compatibility with structural materials	Good	Medium	Best
Pressure required, psig	100	30	500
(kPa)	(690)	(207)	(3448)
Pipe size to module, inches	1-1/2	2	8
(cm)	(3.8)	(5.0)	(20)
Coolant circulation component	Centrifugal pump	E.M. Pump	Compressor blower
Activation of coolant	Some	Severe Na^{22}	Slight to none
Structural materials	Thin wall stainless steel	Thin wall stainless steel	Thick wall stainless steel
Stress levels	Low	Very low	High
Heat transfer coefficient (H)	Medium	High	Low

*Sodium requires trace heating and cannot be operated below 125°C.

~ 2. Sodium is difficult to handle, becomes highly activated, requires a trace heat system and has an adverse effect on neutron damage energy (though not as great as water). Helium, while not as good as water or sodium from a heat removal standpoint, is inert, relatively easy to handle and has minimal impact on the dpa-volume as discussed in Section VII.2.1. Therefore, helium was selected as the reference coolant for the initial TM conceptual design.

To evaluate the performance of the helium cooled TM the temperature profile from the bulk helium coolant to the center of the specimen capsule was calculated. Figure VII.2-10 illustrates the results of one such calculation for the case in which the total heat removed from the specimen capsule was uniformly averaged over the capsule wall area (i.e., heating gradients were not considered). The average neutron induced heating rate was assumed to be approximately 5 W/cm^3 over the capsule volume. For the materials within the capsule, 5 W/cm^3 corresponds to 1.26 W/g. Table VII.2-9 summarizes the temperature profile data for the average case (Fig. VII.2-10) and for the region of the specimen capsule receiving the maximum power input (region closest to plasma).

As heat flows from the inside of the specimen capsule to the helium coolant it encounters its greatest resistance at (1) the engineered gas gap, and (2) at the boundary layer between the helium coolant and the outside of the capsule hole. The thermal conductivity of the engineering gas gap can be controlled by varying the composition of gas (helium and neon) within the gap. By varying the mixture of the two gases, it is possible to vary the thermal conductivity (K), and hence the temperature drop across the gap (ΔT), by approximately +100%, -50%. This allows the temperature of the capsule to be controlled to a certain degree. The range of control is, however, strongly

**TEMPERATURE PROFILE FROM HELIUM COOLANT INTO
SPECIMEN CAPSULE (q = 1.26 W/gm)**

$$\Delta T_{GAP} \; \alpha \; \frac{q}{K_{GAP} \left(\begin{smallmatrix} +100\% \\ -50\% \end{smallmatrix} \right)}$$

650°C (MAX GAS GAP)

328°C (MINIMUM GAS GAP)

GAS GAP
CONTROL

HEDL 8112-077.2

VII.2-36
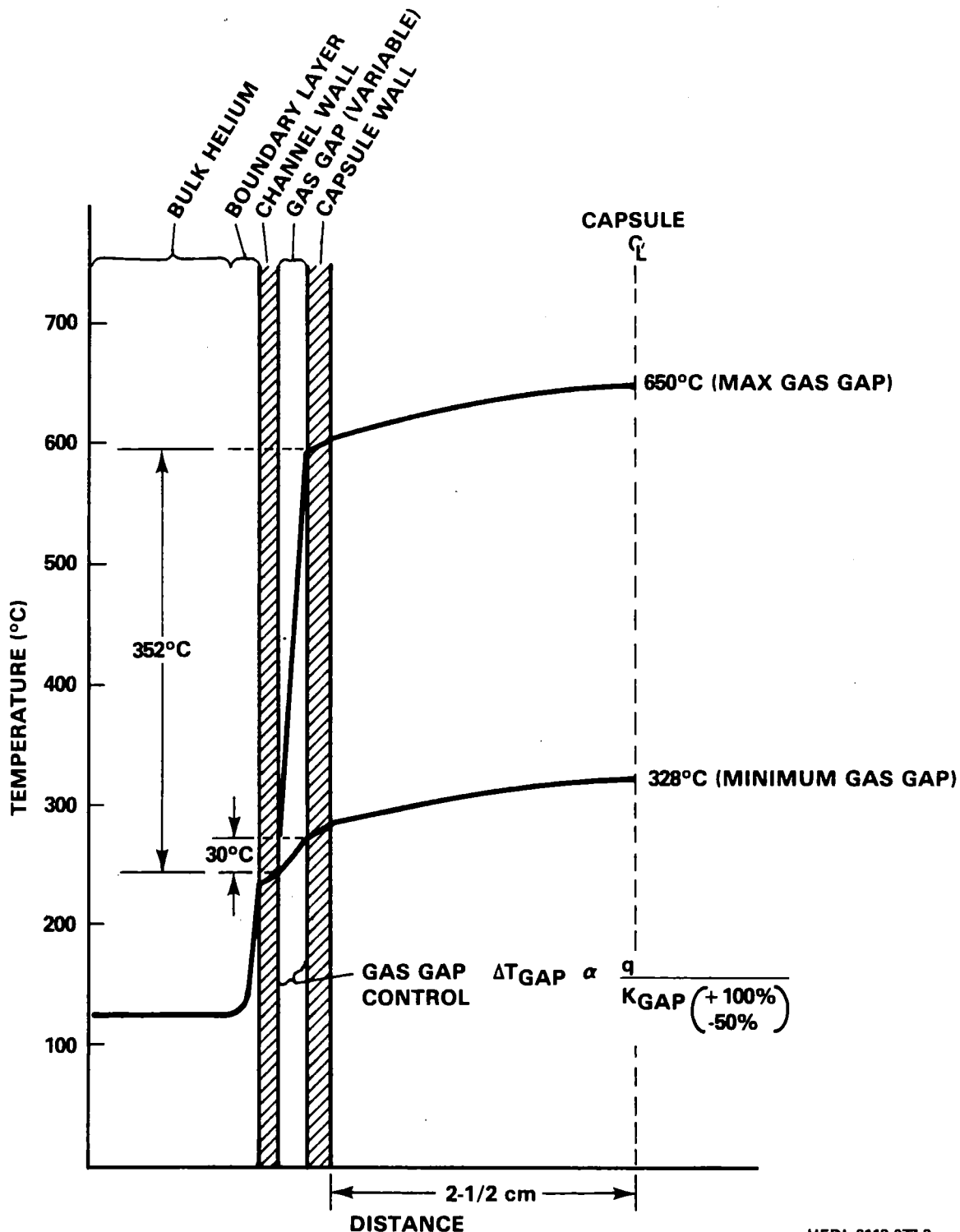
Table VII.2-9. Test Module Temperature Profile

Basis: Avg. Heating Rate + 1.26 W/g (Max. = 2.57 W/g)

Bulk Helium ΔT = 50°C

Helium Convective Heat Transfer Coefficient = 794 W/m^2°C*	Temp. °C Average	Temp. °C Maximum
Helium Inlet	100**	100**
Bulk Helium ΔT	50	50
Helium Outlet	150	150
Helium Film ΔT	86	174
Capsule Tube Outside	246	234
Capsule Tube ΔT	10	20
Capsule Tube Inside	256	344
Gas Gap ΔT (Variable)	30-352	30-222
Specimen Capsule ΔT	42	84
Capsule Center	328-650	458-650

*140 BTU/hr·ft^2°F for capsule tube with extended surface.

**Provides ΔT of 75°C to cool with water at 25°C.

+Based on 1.8 MW/m^2.

dependent upon the magnitude of the ΔT across the gap. As illustrated in Fig. VII.2-10 for the case in which the capsule centerline temperature is 650°C, the ΔT_{gap} (352°C) represents a significant fraction of the total temperature drop between the capsule and bulk helium coolant. For the low temperature capsule, the ΔT_{gap} (30°C) is only a small fraction of the total ΔT, hence, temperature control is virtually lost.

The difficulty in achieving temperature control (as well as the minimum required temperature of 300°C) is due to the large helium boundary layer temperature drop. The boundary layer dominates the ΔT between the bulk helium coolant and specimen capsule centerline temperature (at temperatures approaching T_{helium}). The obvious solutions to this problem are to (1) increase the velocity of the helium, which reduces the boundary layer ΔT, and/or (2) to reduce the inlet helium temperature which allows the ΔT_{gap} to become a larger fraction of the total ΔT. Both solutions were considered to be impractical due to the already significant helium mass flow rates (73 x 10^3 ℓ/min) and power (1145 kW) contained in the helium. Other means of attaining a lower and more controllable minimum temperature include reduction of specimen capsule diameter and optimization of overall test module mass. Further design is required to access these options.

<u>Specimen Capsule (Fig. VII.2-9)</u>. Each specimen capsule is a circular stainless steel cylinder 5 cm diameter by 20 cm long. Material test specimens are positioned inside each capsule. A NaK liquid metal heat transfer bond is provided between test specimens and capsule wall. Each capsule is provided with two or more chromel-alumel thermocouples for measuring test specimen temperature. The capsule wall thickness is adjusted during fabrication to provide a gap between it and the capsule hole. This gap is sized so that when

it is filled with a particular insulating gas it will provide the desired test specimen temperature. This gap can be of uniform width or it can be stepped along the capsule axis to compensate for different heating rates between the front and the back end of the capsule. The top of each capsule includes a cylindrical canopy which seals the gap when the capsule is inserted in the tube. A metal bellows with a compressible space is provided for thermal expansion of the NaK bond.

To cover the entire temperature range (300-650°C) requires relatively high and low thermal conductivity media in the gap. Helium and neon were selected - helium because of its good thermal conductivity and neon because of its lower thermal conductivity and reduced activation (when compared to argon). The practical range of gas gaps is approximately 0.0175 to 0.10 cm. A 0.0175 cm gap is believed to be the minimum controllable gap width from a fabrication standpoint and for gap widths above approximately 0.10 cm convection starts adding to conduction which makes temperature prediction less reliable.

In summary, for gas gap widths ranging from 0.0175 to < 0.10 cm filled with an atmosphere of helium or neon, the range of average specimen capsule temperatures is 328 to 650°C. For that portion of the specimen capsule receiving the maximum neutron heating rate ($\sim$ 10 W/cm^3) the attainable specimen capsule temperatures are 458-650°C. (This assumes no axial heat transfer - only radial.) Hence, the initial design concept does not meet the specified low temperature criteria of 300°C. Design optimization and further thermal analysis will be required to meet the specified temperature criteria.

VII.2.3.3 Test Module Operations and Handling

The frequency of test module removal is a function of the test matrix fluence requirements discussed in Section VII.2.3.1 and the reliability of the test module. If one looks only at the fluence requirements the materials test module will be removed from the reactor and transported to a disassembly hot cell every ~ 500 full power days (Table VII.2-4). There will be additional removals from the reactor as random failures occur within the test module and test module control and data acquisition equipment.

When problems and failures occur within the test module the entire test module will have to be removed from the reactor for repair. The design does not accommodate maintenance internal to the vacuum flange while in the reactor. Therefore, in order to maximize TASKA availability a second test module should always be available for insertion when the primary module requires repair. The transfer of the module from reactor to the disassembly hot cell should be a simple, efficient operation with minimal impact on other reactor systems. Simplicity in module removal is the principal reason vertical access was chosen for the materials test module. It is believed that vertical access has minimal impact on surrounding reactor support systems, requires minimal floor space and involves straight line, vertical lifts using only an overhead crane.

The operations required to remove a test module from TASKA are given in Table VII.2-10.

VII.2.3.4 Summary and Conclusions

A materials testing scenario for TASKA was presented in the form of a test matrix. The test matrix lists the type of materials test, the irradiation temperatures, goal fluences and details relating to stresses and

Table VII.2-10. Operations Required for Test Module Removal from Reactor

Operation	Comment	Approximate Time to Complete Operations (hrs)
1. Following reactor shutdown and cooldown period, disconnect helium piping and instrument leads.	Hands-on operation.	16
2. Unbolt flange from vacuum boundary of machine.	Hands-on.	4
3. Unbolt large module cover-plate from pipe penetration flange.	Hands-on.	4
4. Swing cover-plate over helium piping and remove. Protect sealing surfaces.	Hands-on.	8
5. Secure OH crane to test module. Lift entire test module from reactor.	As soon as lift begins operations become remote.	4
6. Transfer test module to hot cell for disassembly (or load TM into a large cask for transfer).	Totally remote viewing and handling.	3
7. Place test module in rotating, indexing figure in hot cell.	Hot cell operation utilizing crane, electromechanical and master slave manipulators.	8

Table VII.2-10 (Cont'd.)

8. Remove shield plug and shear vacuum cover seal which covers specimen capsule tubes.	Remote operation.	16-32
9. Withdraw specimen capsules from capsule holes and replace with new capsules.	Utilize rotating removal machine which indexes on each row of capsule holes.	24-48
10. Verify integrity of test module and all specimen capsules. Leak test system, service lead continuity check.	All systems and components must be verified operable.	48-120
11. Replace vacuum cover and weld, reassemble shield plug to module. Prepare for transfer back to reactor.	---	48-72

Total Time: 182-319 hrs.

The times estimated in Table VII.2-10 are actual working hours (assumes 50 minutes are worked each hour) assuming success-oriented operations.

postirradiation test conditions. It was shown that the entire TASKA test matrix consisting of nearly 30,000 test specimens could be completed in approximately eight full power years utilizing on the average less than half of the volume in a single test module. The maximum fluence achieved by any group of specimens is over 100 dpa.

The test module was designed to contain and thermally control the test specimens within the vacuum boundary of the reactor. Helium was chosen as the bulk heat removal fluid because it has the least moderating effect upon the neutrons and therefore results in the greatest dpa-volume for a given test module space envelope. Helium is acceptable from a heat removal standpoint; however, further design optimization will be required to verify the limits of test module operation.

The operational impacts of materials testing upon TASKA should be minimal as long as reliable test modules can be designed and fabricated. The test module concept presented in this section requires minimal handling in the vicinity of the reactor - the majority of test module remote operations occur during test module disassembly which occurs in hot cell facilities removed from the reactor operating gallery.

VII.2.4 Neutronics Analysis for the REGAT Module of TASKA

VII.2.4.1 Introduction

One major requirement of TASKA is to provide a capability to test materials for the mirror program and preferably for the tokamak program as well. Testing materials for the tokamak program requires including fatigue and crack growth specimens. While the number of such specimens is not great, the volume per specimen is large. The TASKA materials testing module is designed to accommodate specimens to test materials for both programs. Results of the neutronics analysis for the REGAT module of TASKA are given here and compared to the results for the current INTOR materials test module.

VII.2.4.2 Neutronics Results

The improved REGAT design shown in Fig. VII.2-1-c is used in TASKA. The module has an inner radius of 46 cm and a thickness of 20 cm. The neutronics results presented here are given for two designs. In the first design, the REGAT module is cooled by helium and has a width of 70 cm, yielding a total module volume of 493 liters. In the second design, water is used as a coolant and a width of 50 cm is used, yielding a total module volume of 352 liters. Water was considered as a coolant because of the difficulty of maintaining low irradiation temperatures with helium cooling. A smaller module width is used in the water cooled case in order to compensate for the increased damage gradients resulting from higher neutron attenuation in water. In this case, the module is still large enough to accommodate specimens to test materials for both the mirror and tokamak programs. The current INTOR materials testing module has a volume of 135 liters.

In TASKA, the test capsules represent 40 v/o of the module. The capsules consist of 50 v/o NaK, which is used as a thermal contact material, and 50 v/o

316 SS, which represents the specimens and the capsule structural material. The module structure represents 20% of the module volume and is made of Ti-6Al-4V and 316 SS in the gas and water cooled cases, respectively, Water occupies 15 v/o of the water cooled volume. Because of severe neutron attenuation in water, an effort was made to reduce the water content in the REGAT module of TASKA. The INTOR materials test module has a 36 v/o of water. Table VII.2-11 gives the test module composition for INTOR and the two designs used in TASKA.

The neutronics results presented in this section are based on the initial assumption that the test capsules represent 40% of the module volume. However, later in the study when the modules were designed in detail, it was found that the cylindrical capsules represent only 28% of the module volume because of the annular geometry of the module. The later number corresponds to a 30% reduction in the capsule volume. However, the lower steel content will result in ~ 10% increase in the average dpa, or a 20% decrease in the dpa·ℓ value. The 40% capsule volume fraction can be easily maintained by designing conically shaped test capsules with diameters of 5 and 5.37 cm at the front and back of the module, respectively. Therefore, we will address the 40% volume fraction case in the rest of this chapter.

For the purpose of comparison, one-dimensional neutronics calculations have been performed for the current INTOR materials test module which is 15 cm thick and 135 liters in volume. Figure VII.2-11 shows the variation of dpa rate with depth in the test module as obtained from the one-dimensional cylindrical calculations. The results are given for the test module of INTOR and the two designs used in TASKA. Note that the results for TASKA give the conditions at the center of the module with effects of using the REGAT design

Table VII.2-11. Test Module Composition

	INTOR	H_2O Cooled TASKA	He Cooled TASKA
Module structure	316 SS 24 v/o	316 SS 20 v/o	Ti-6Al-4V 20 v/o
Specimen and capsule structure	316 SS 17 v/o	316 SS 20 v/o	316 SS 20 v/o
Coolant	H_2O 36 v/o	H_2O 15 v/o	He 40 v/o
Thermal contact material	NaK 17 v/o	NaK 20 v/o	NaK 20 v/o
Void	6 v/o	25 v/o	0 v/o
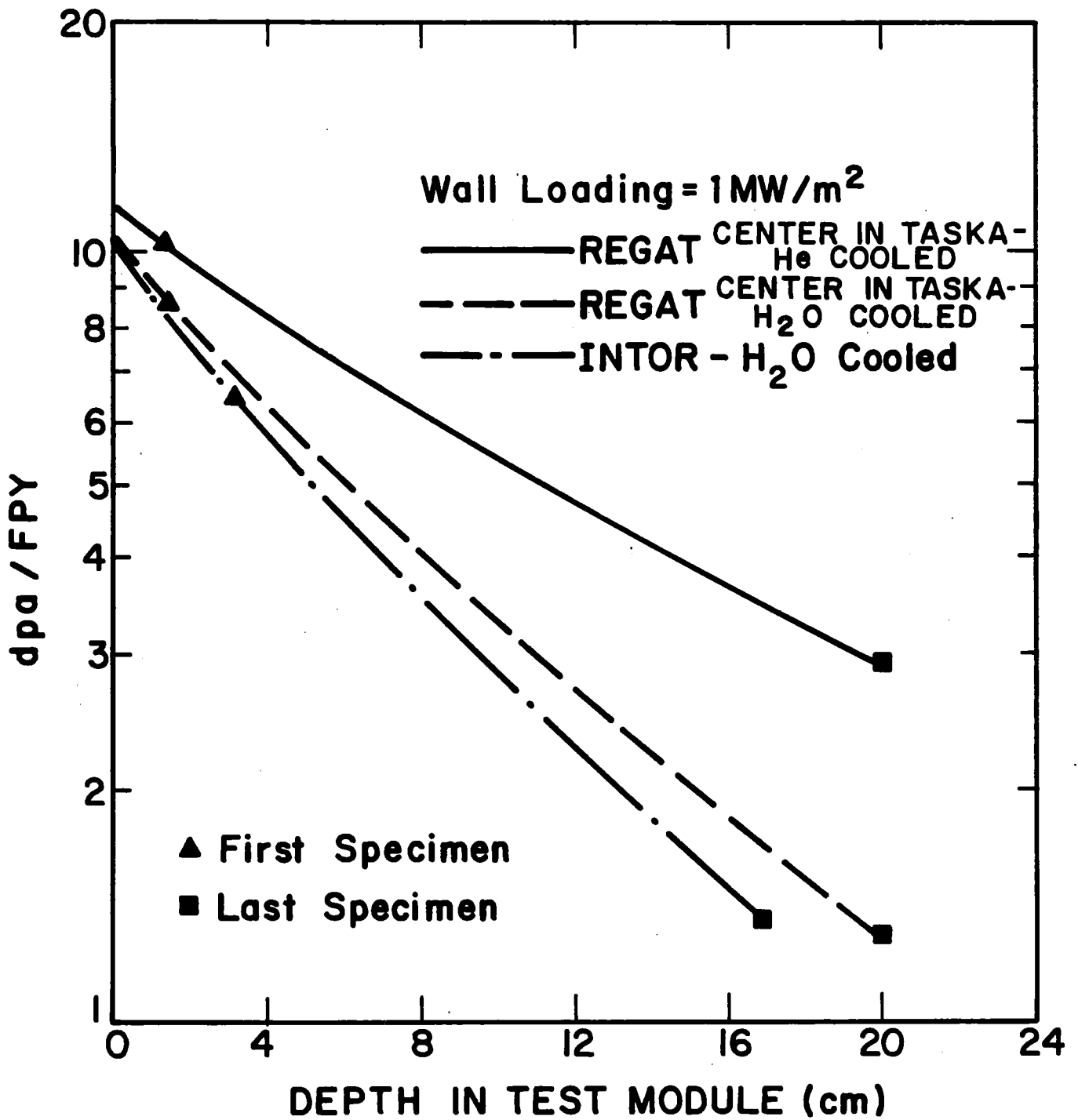
Fig. VII.2-11   One-dimensional results for dpa in TASKA and INTOR modules.

not shown. The results are normalized to unit wall loading. Because of the high heat flux in INTOR, a 19.6 mm thick separate water cooled first wall is required. The module and capsule walls have a total thickness of 13 mm. This implies that the specimen exposed to the highest irradiation level is placed at a depth of 32.6 mm from the first surface in INTOR and 13 mm in TASKA. This results in a smaller peak damage rate in INTOR.

Detailed three-dimensional neutronics calculations were performed to calculate the damage profiles in the REGAT materials testing module designs of TASKA. Figures VII.2-12 and VII.2-13 show the equal dpa contours for the gas and water cooled cases, respectively. The results are given for a fluence of 1 MW - yr/m^2. Note that if the traditional design is used, these contours will reduce to a set of parallel horizontal lines. The effect of using the REGAT design on reducing the damage gradient is clear. These results suggest also that small test specimens might be irradiated at the center of the module while larger specimens, such as those required for the tokamak program, can be irradiated at the sides of the module. It is clear that the water cooled design results in higher damage gradients because of the increased neutron attenuation in water.

Figures VII.2-14 and VII.2-15 give the equal helium appm contours for the gas and water cooled cases, respectively. Again, it is clear that the gas production gradient is reduced as a result of using the REGAT design. Since the threshold energy for the helium production reaction is much higher than that for atomic displacement, the helium production decreases sharply as one moves from the side of the module towards the center. Hence, using the REGAT design results in a more pronounced effect on reducing dpa gradients than on reduced helium production gradients. Higher helium production gradients are
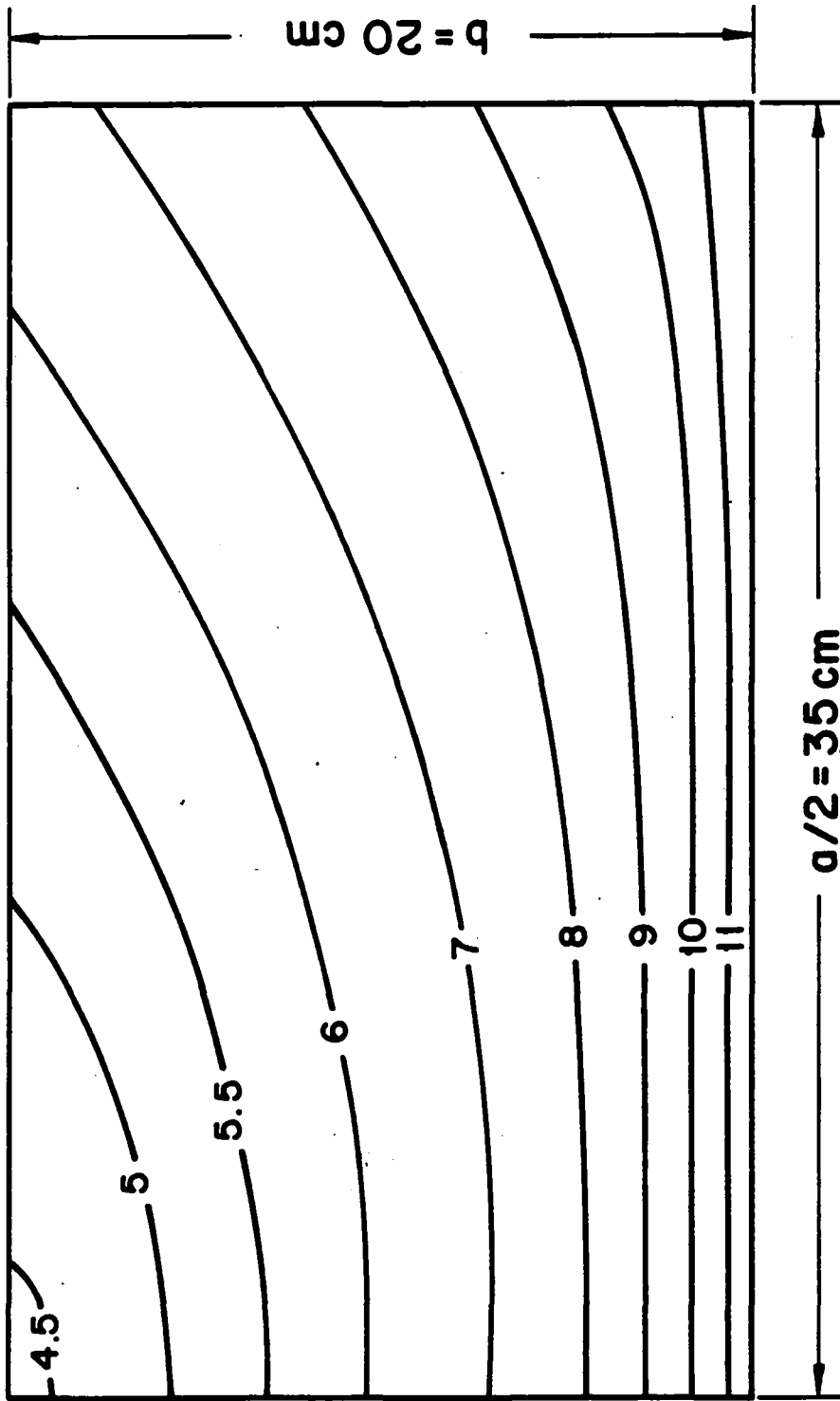
Fig. VII.2-12 Equal dpa contours in the gas cooled REGAT module.
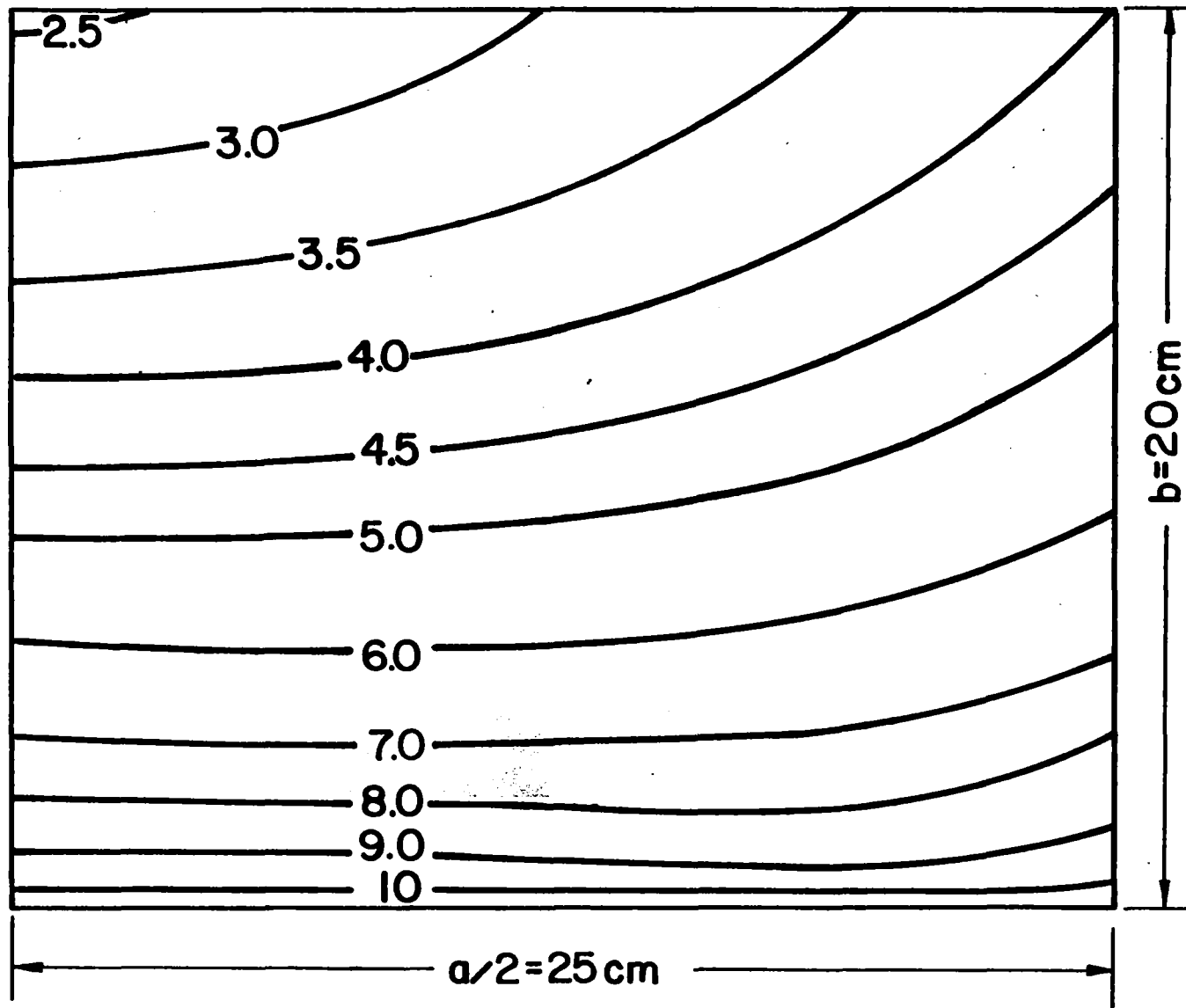
Fig. VII.2-13 Equal dpa contours in the water cooled REGAT module.
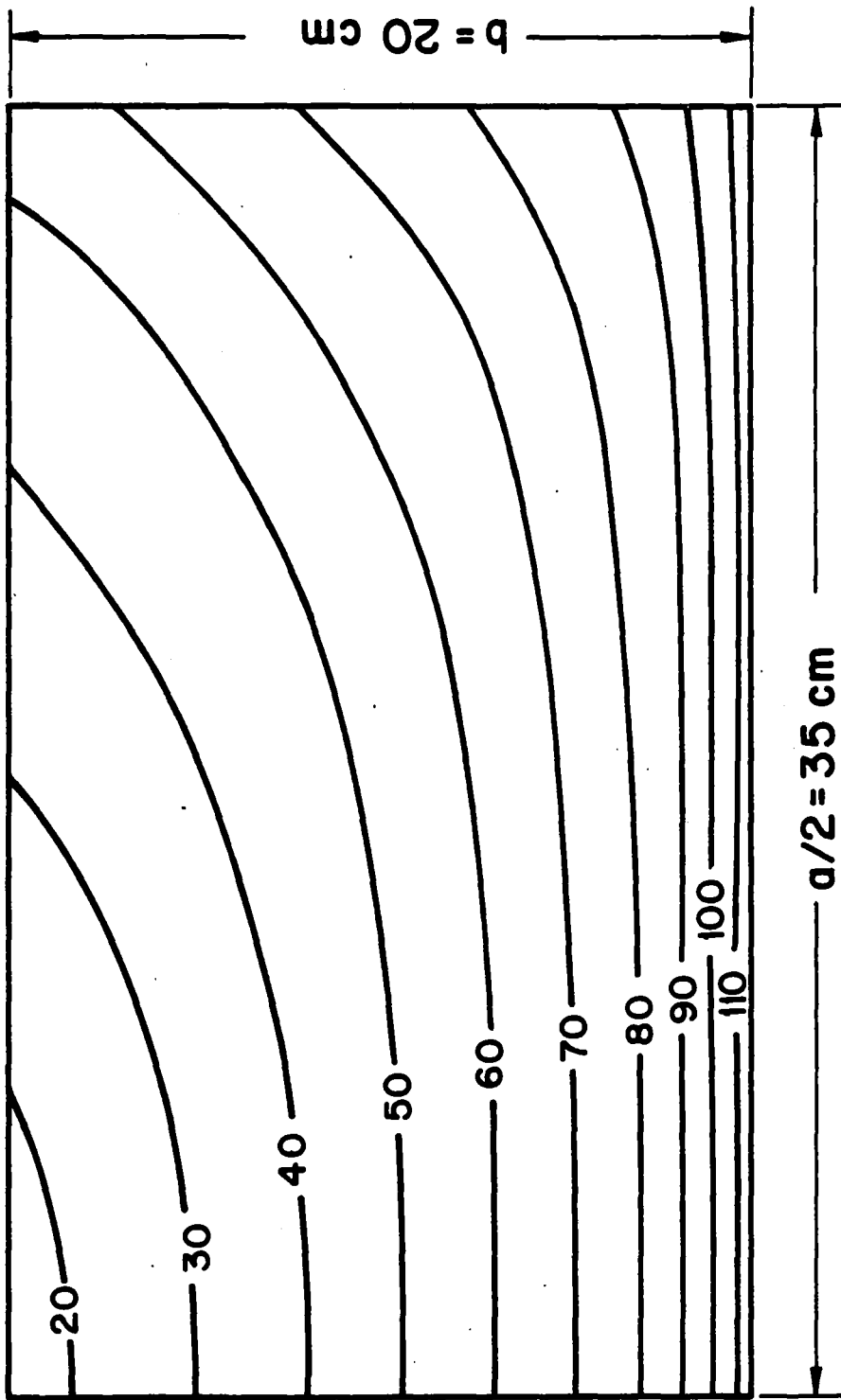
Fig. VII.2-14 Equal helium appm contours in the gas cooled REGAT module.
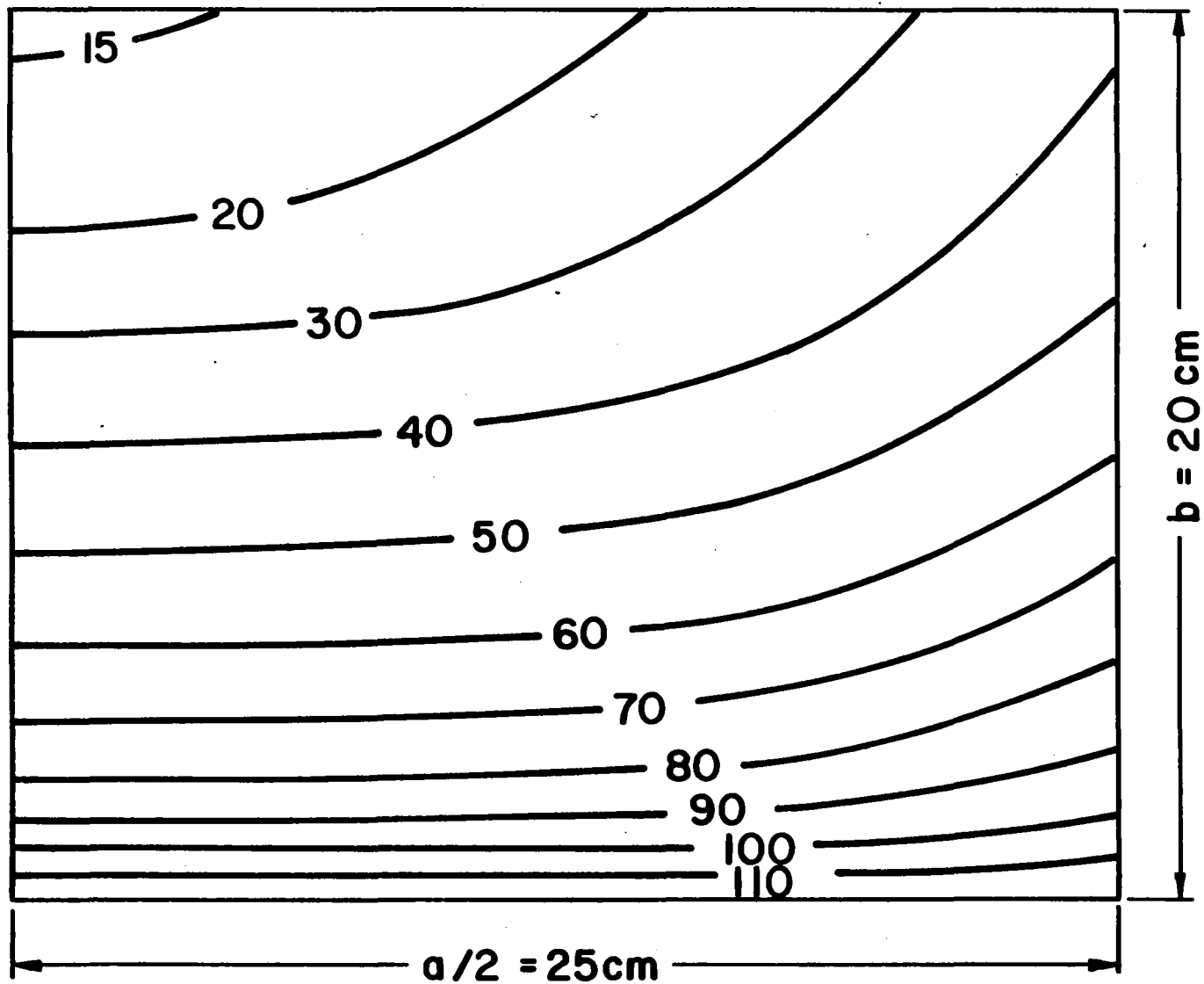
Fig. VII.2-15 Equal helium appm contours in the water cooled REGAT module.

obtained when water is used as compared to the gas cooled case. However, the effect on helium production, which is produced by neutrons with energies $\gtrsim 1$ MeV, is not as pronounced as that on dpa which can be produced by neutrons with energies as low as ~ 1 keV.

Figures VII.2-16 and VII.2-17 show the dpa levels that can be obtained in different volumes of the gas and water cooled modules, respectively. Figures VII.2-18 and VII.2-19 give the results for helium production. For the purpose of comparison, the results for the traditional design are also included. The results are normalized to a wall loading of 1 MW/m^2. It is clear that in using the REGAT design, one can achieve higher damage levels using the same test volumes. The results show that using the REGAT design has a more pronounced effect on increasing dpa levels than on increasing gas production levels. It is clear also that the improvement over the traditional design is more pronounced in the water cooled case than in the gas cooled case.

Table VII.2-12 gives the average and peak/average dpa and helium production rates in the gas and water cooled REGAT modules of TASKA and the INTOR materials testing module. The results are normalized to a unit wall loading. Coupled neutronics and photonics calculations were performed to calculate the power density profiles in the different modules. The results are summarized in Table VII.2-13. The results are normalized to a unit wall loading.

Another way of expressing the damage in the test specimen is to sum the product of the damage level times the volume of the test zone that can produce that damage level. This parameter accounts for the number of specimens that can be irradiated to high levels. It can be calculated by multiplying the average damage level by the total test capsule volume in the module. For a unit fluence of neutron irradiation, the dpa times capsule volume values are
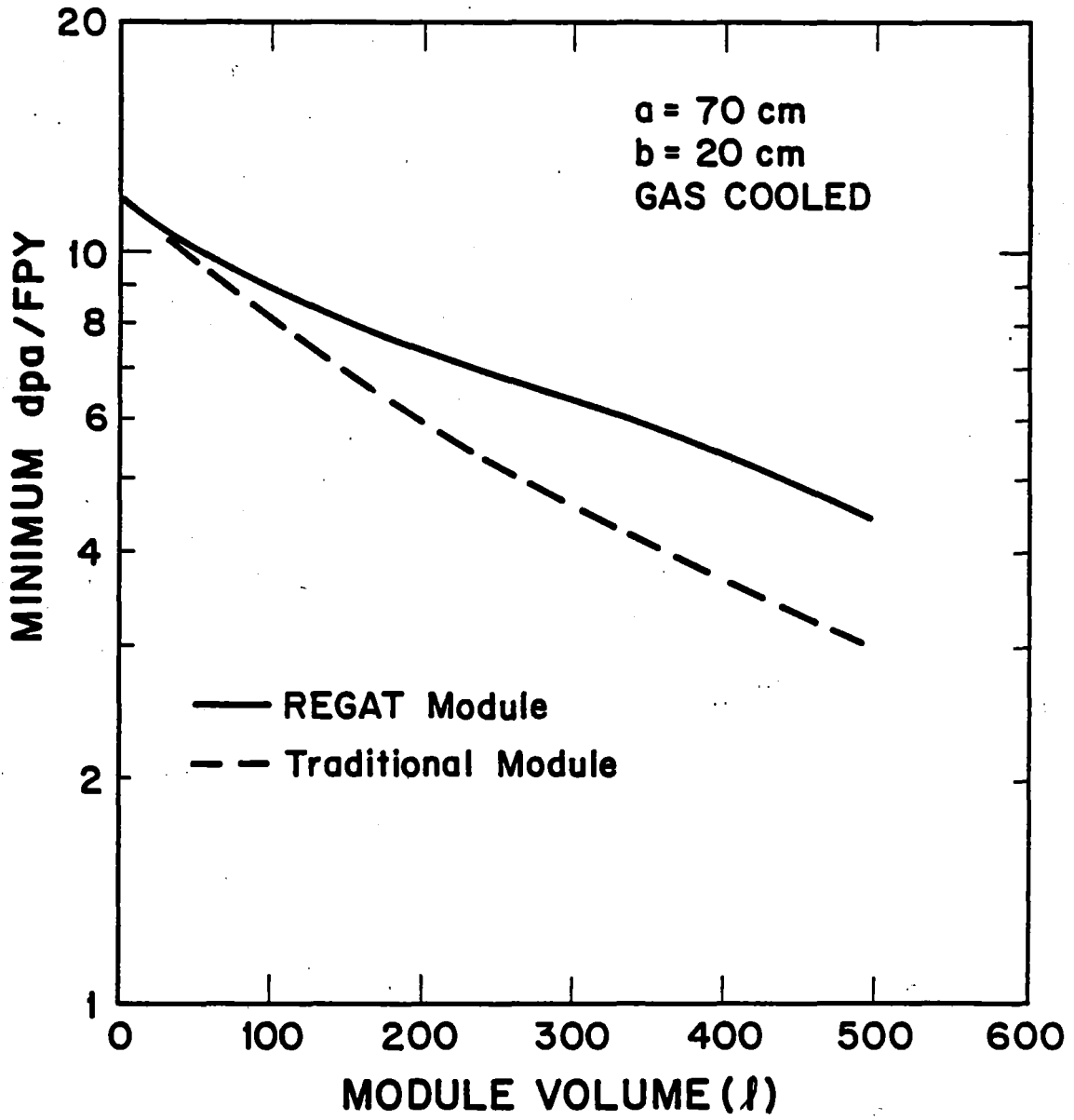
Fig. VII.2-16 Dpa rate vs. volume in the gas cooled REGAT module.

VII.2-54
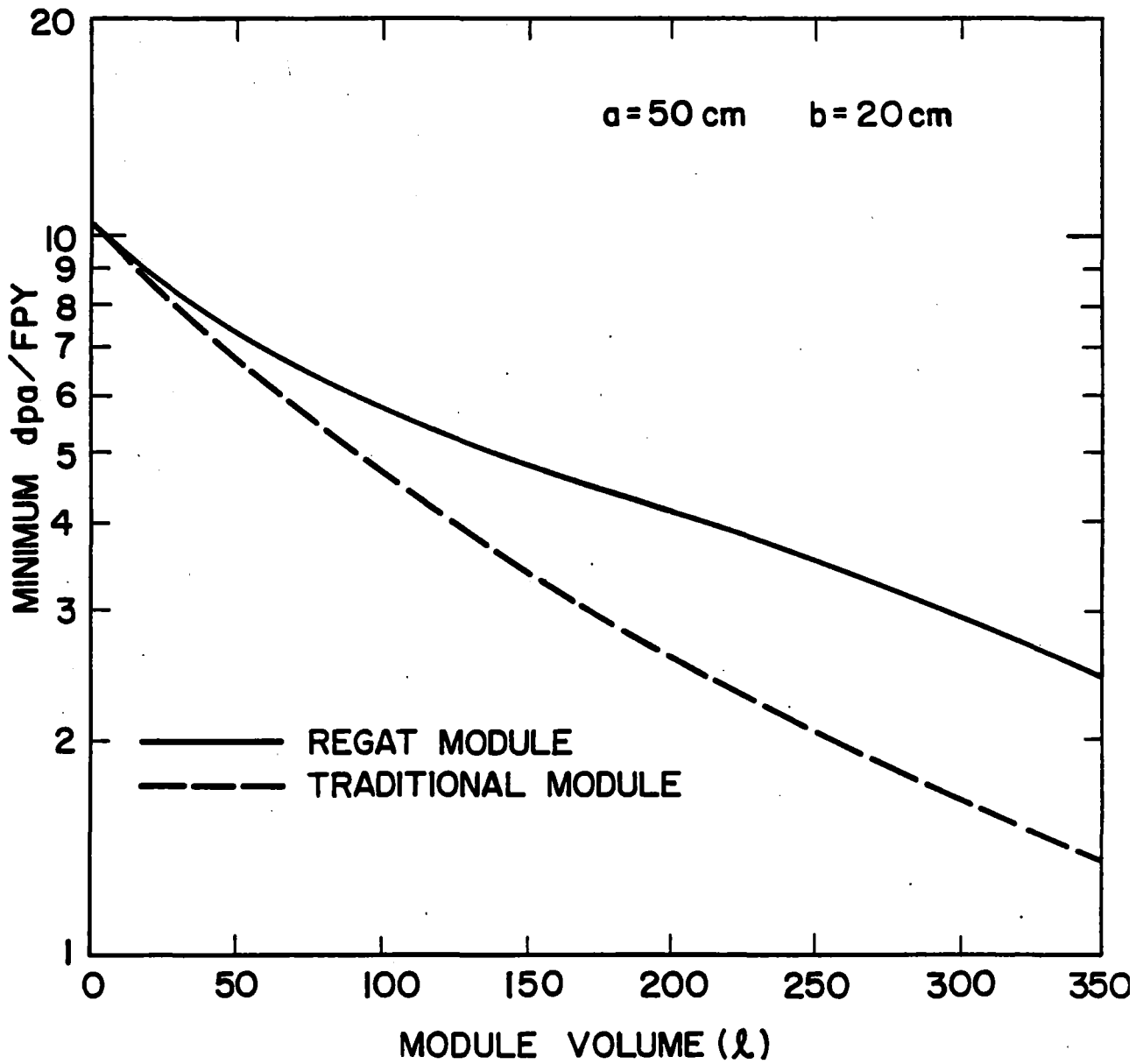
Fig. VII.2-17 Dpa rate vs. volume in the water cooled REGAT module.
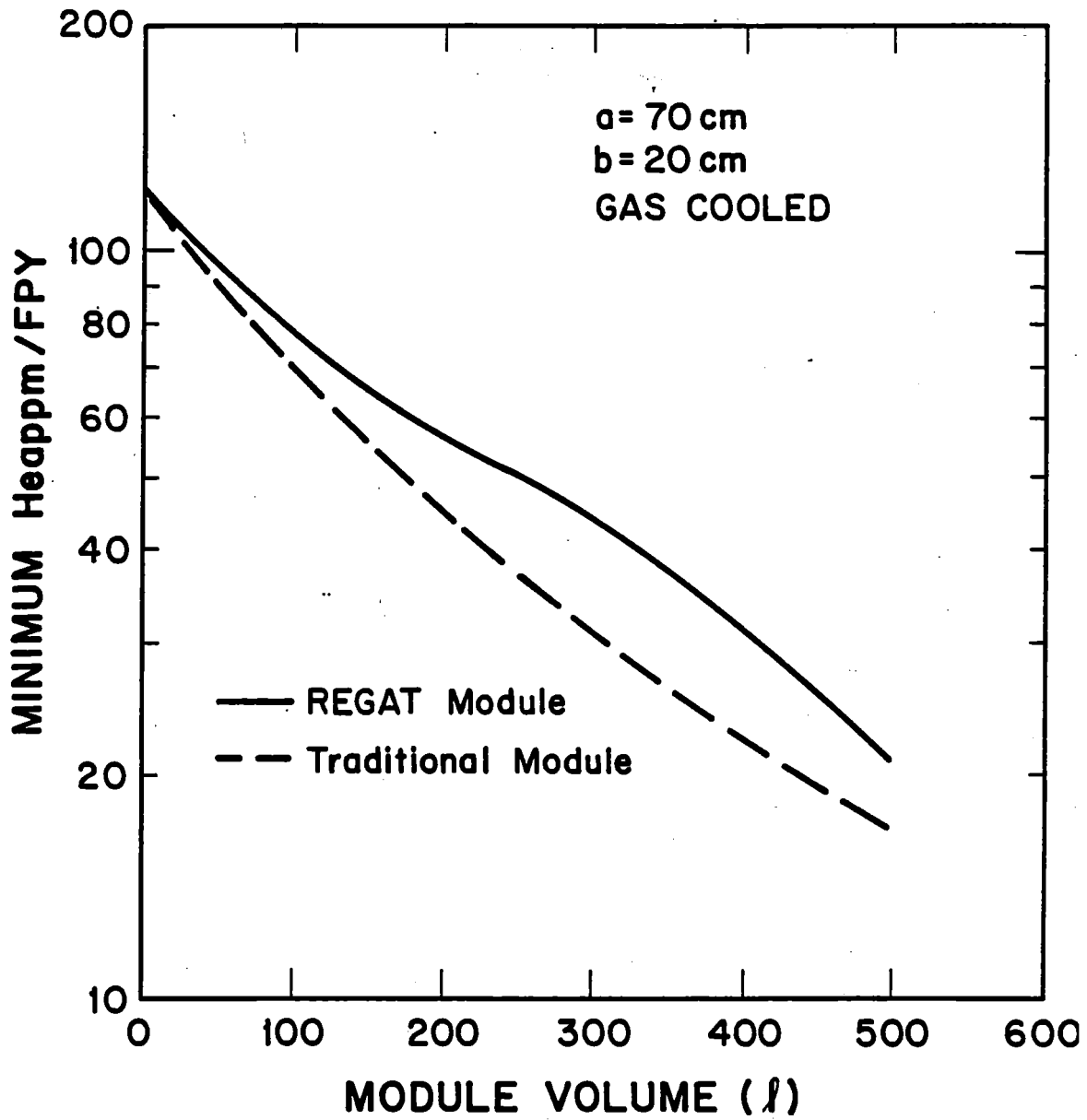
Fig. VII.2-18 Helium appm rate vs. volume in the gas cooled REGAT module
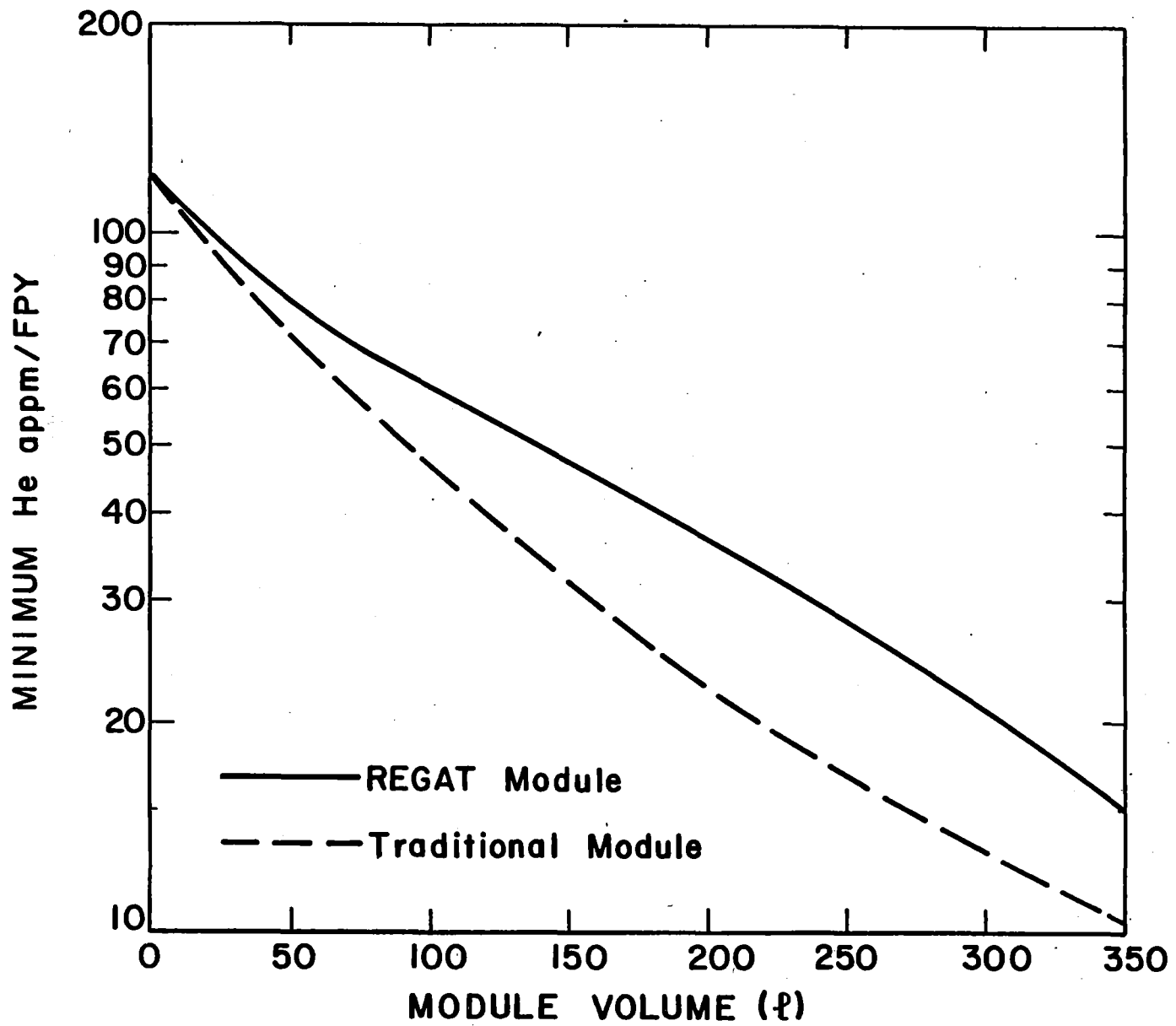
Fig. VII.2-19 Helium appm rate vs. volume in the water cooled REGAT module.

Table VII.2-12.   DPA and Helium Production Rates in the

Different Test Modules for Unit Wall Loading

	dpa/FPY		He appm/FPY	
	Ave.	Peak/ Ave.	Ave.	Peak/ Ave.
Gas cooled REGAT	7.30	1.56	49.03	2.12
Water cooled REGAT	5.14	1.96	44.00	2.31
Water cooled INTOR	3.90	2.24	40.00	2.59

Table VII.2-13.   Power Densities in the Different Test

Modules for Unit Wall Loading

	Power Density (W/cm^3)		
	Peak	Average	Minimum
Gas cooled REGAT	3.87	2.15	1.78
Water cooled REGAT	7.74	4.84	2.46
Water cooled INTOR	10.69	6.28	3.37

1438, 725, and 176 dpa ℓ for gas cooled REGAT, water cooled REGAT, and INTOR, respectively. The values for helium appm times capsule volume are 9659, 6204, and 1800 He appm ℓ, respectively.

We have assumed that TASKA will operate on the following schedule which is identical to that of INTOR.[2]

Year	% Availability
1	10% (hydrogen operation)
2-3	15%
4-7	25%
8-15	50%

Therefore, the device is expected to operate for 5.3 full power years (FPY). Combining this with the neutron wall loading of 1.5 MW/m^2 in TASKA yields a total fluence of 7.95 MW-yr/m^2. Hence, the accumulated dpa times volume in the helium cooled REGAT module is 11,416 dpa ℓ and 5764 dpa ℓ in the water cooled module of TASKA. If the traditional water cooled design is used, the corresponding value is 4149 dpa ℓ. This implies that a gain of ~ 40% in the materials testing capability of TASKA can be achieved with the REGAT design.

Combining the availability values with a startup date of 1990 and a wall loading of 1.5 MW/m^2 yields the average dpa and cumulative dpa ℓ values given in Figs. VII.2-20 and VII.2-21, respectively. The values for the cumulative He appm ℓ are given in Fig. VII.2-22. For the purpose of comparison, the results of the materials testing modules of FMIT, RTNS-II, and INTOR are included. The results are summarized in Table VII.2-14.

The first observation one can make from Fig. VII.2-20 is that current devices like RTNS-II cannot provide either the damage level or the volume in a

CUMULATIVE DAMAGE IN FUSION MATERIALS TEST FACILITIES
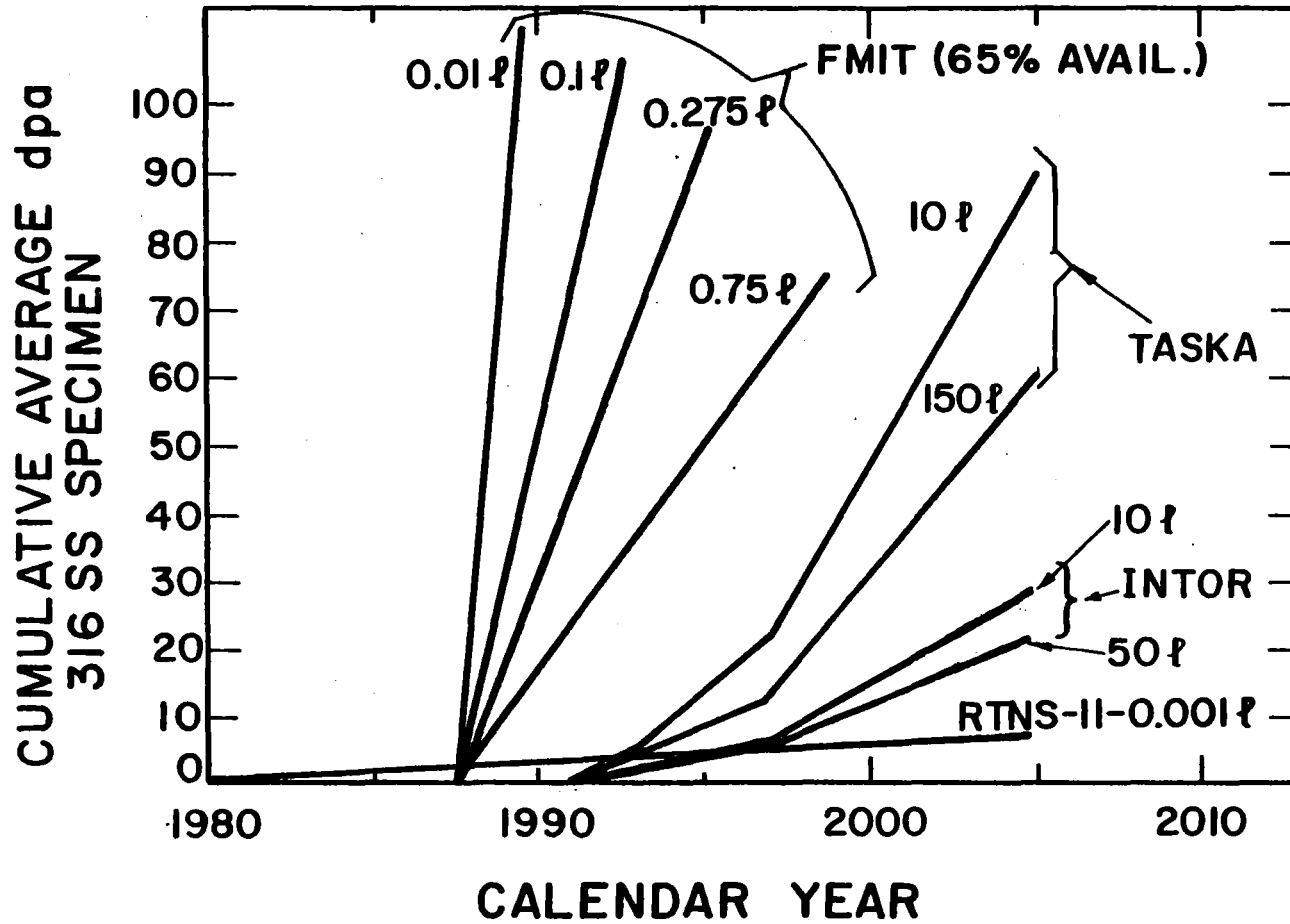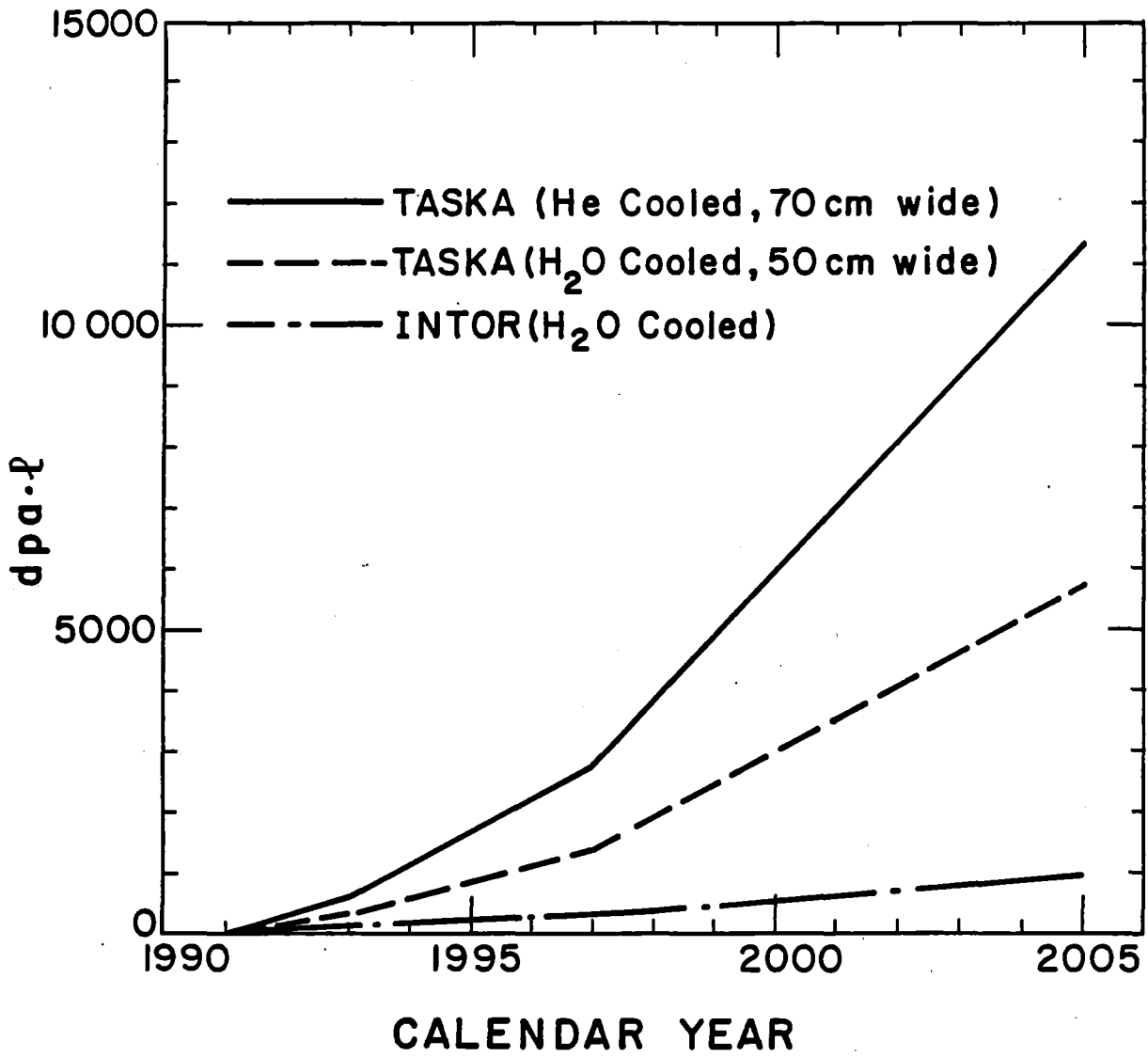
Fig. VII.2-20

Fig. VII.2-21 Cumulative dpa x test module volume for TASKA and INTOR.
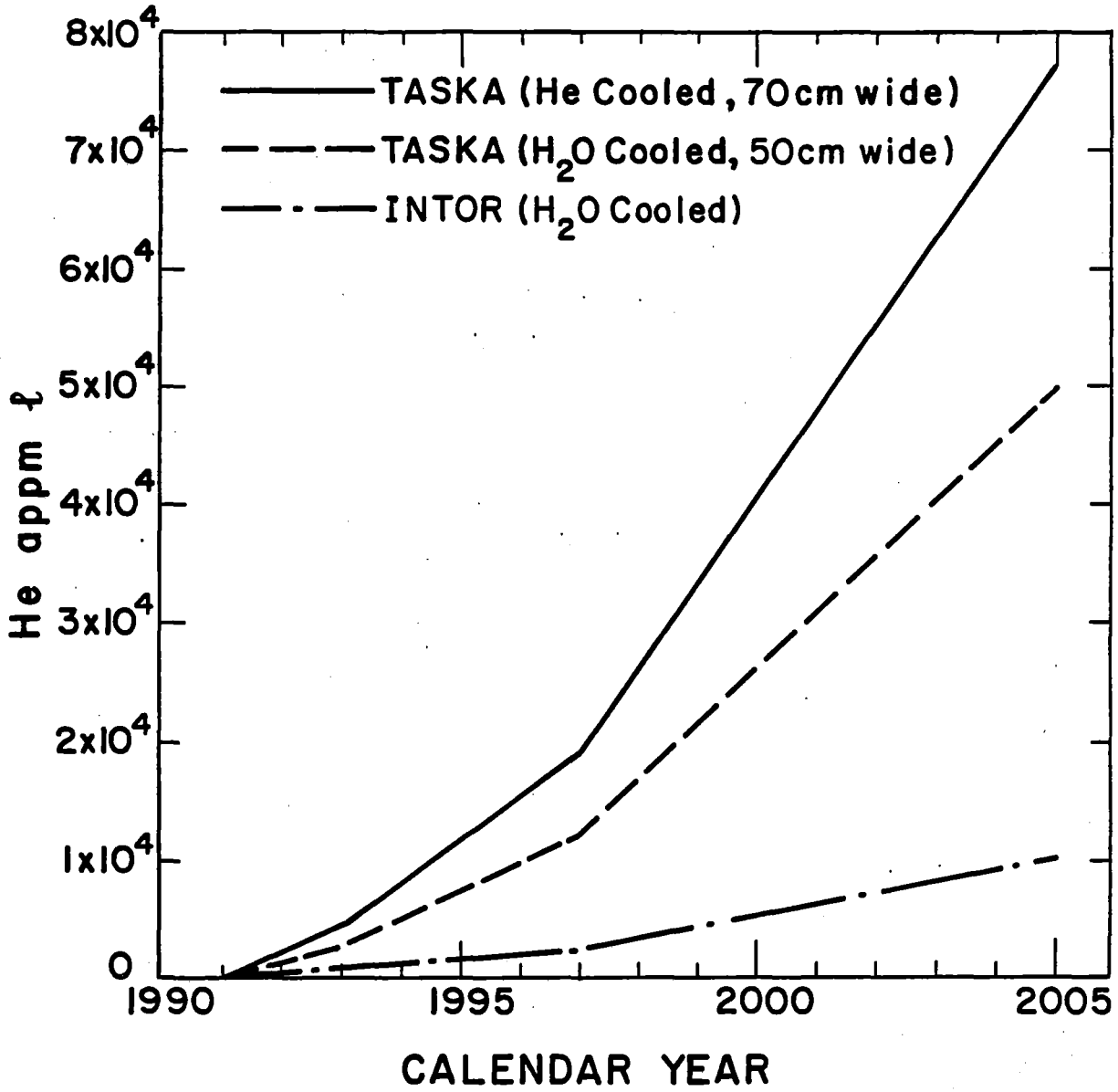
Fig. VII.2-22 Cumulative helium appm x test module volume for TASKA and INTOR.

Table VII.2-14.   Comparison Between Different Test Module Designs

	He Cooled TASKA	H$_2$O Cooled TASKA	H$_2$O Cooled INTOR
Area (m^2)	2.02	1.45	0.90
Ave. dpa per MW-yr/m^2 (10 ℓ)	11	7	5
Module volume (ℓ)	493	352	135
Capsule volume (ℓ)	197	141	45
Ave. dpa per MW-yr/m^2 (capsule)	7.3	5.14	3.9
Cumulative dpa·ℓ	11416	5764	965
Relative figure of merit	12	6	1
Average He appm per MW-yr/m^2	49	44	40
Cumulative He appm·ℓ	76861	49322	9922
Relative figure of merit	8	5	1

reasonable time. If FMIT is operating in 1986, very high values of damage can be achieved by 1990. It is seen that dpa levels of more than 100 could be obtained in a testing volume of ~ 10 cm^3. Lower damage rates are obtained in larger testing volumes of FMIT and values of 100 dpa could be achieved by the mid-1990's in ~ 500 cm^3 of test volume. As valuable as this information is, the qualification of an engineering alloy requires 10's of liters of test volume.

The large test volume requirements are most likely to be filled by devices like INTOR or TASKA. Figure VII.2-20 shows that one could achieve ~ 90

dpa in specimens by 2005 in 10 liters of TASKA test volume or ~ 30 dpa by the same time period in INTOR. Obviously, either of these devices could be used for a major alloy qualification program but TASKA seems to have a higher performance factor.

The above conclusions can be restated by comparing the dpa·ℓ values for TASKA and INTOR. This is done in Fig. VII.2-21. The water cooled REGAT module of TASKA has a dpa times volume figure of merit that is a factor of ~ 6 higher than that for the current INTOR materials testing module. A relative figure of merit of ~ 12 is obtained when the REGAT module is cooled by helium. There are several reasons for the low values obtained in INTOR as compared to TASKA. The wall loading in TASKA is 1.5 vs. 1.3 MW/m^2 in INTOR. While TASKA is a steady state machine, INTOR has a duty cycle of ~ 0.8. A thick, separate water cooled first wall is required in INTOR because of the high heat flux. This results in further attenuation of the neutron flux to the samples. While an effort was made to decrease the water volume in the test module for TASKA, the INTOR module has a 36 v/o of water. Finally, using the REGAT design in TASKA allows using large test volumes without the penalty of reduced damage level.

VII.2.4.3 Conclusions

We conclude from this analysis that a gain of ~ 40% in the materials test-ing capability of TASKA can be achieved with the REGAT design. The damage pro-files in the REGAT module suggest that large test specimens, such as those re-quired for the tokamak program, can be irradiated at the sides of the module where the lowest damage gradients occur. The water cooled REGAT module of TASKA has a dpa times volume figure of merit that is a factor of ~ 6 higher

VII.2-64

than that for the current INTOR materials testing module. A relative figure

of merit of ~ 12 is obtained when the gas cooled REGAT module is used in TASKA.

References for Section VII.2

1. B. Badger, et al., "TETR - A Tokamak Reactor to Qualify Materials and Blanket Components for Early DT Fusion Power Reactors", University of Wisconsin Fusion Engineering Program Report UWFDM-191 (1977).

2. W.M. Stacey, Jr., et al., "USA Conceptual Design Contribution to the INTOR Phase-I Workshop", INTOR/81-1 (June 1981).

3. D. Steiner, W.R. Becraft, and P.H. Sager, J. Fusion Energy 1, (1981) 5.

4. C.A. Flanagan, D. Steiner, and G.E. Smith, ORNL/TM-7777 (June 1981).

5. RSIC Code Package CCC-203, "MORSE-CG", Radiation Shielding Information Center, ORNL.

6. RSIC Data Library Collection, "VITAMIN-C, 171 Neutron, 36 Gamma-Ray Group Cross Sections Library in AMPX Interface Format for Fusion Neutronics Studies", DLC-41, ORNL.

7. RSIC Data Library Collection, "MACKLIB-IV, 171 Neutron, 36 Gamma-Ray Group Kerma Factor Library", DLC-60, ORNL.

8. M. Ragheb and C. Maynard, "Neutronics Shielding Analysis for the End Plug of a Tandem Mirror Fusion Reactor", University of Wisconsin Fusion Engineering Program Report UWFDM-398 (1981).

9. N. Ghoniem and M. Takata, "Modelling Helium Behavior in Fusion Reactor Structural Materials", Proc. of SMIRT-6 Conf. on Structural Mechanics in Reactor Technology, Paris, France, August 1981.

Appendix VII.2-A

Materials Test Specimens Specified

in the TASKA Test Matrix

Figure VII.2-A-1

BULK MATERIALS TESTING
MATERIALS TEST SPECIMENS

TENSILE SPECIMEN
SURVEILLANCE TENSILE (ST)

48 mm
12.5 mm diam
6.4 mm diam
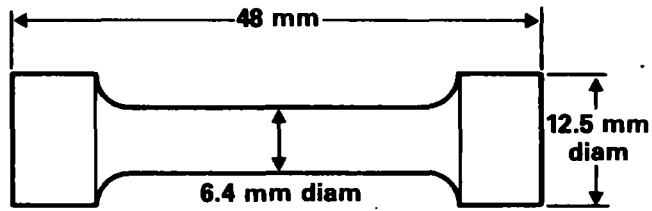
TENSILE SPECIMEN
FLAT TENSILE (FT)

45 mm
.75 mm
5 mm
1.5 mm
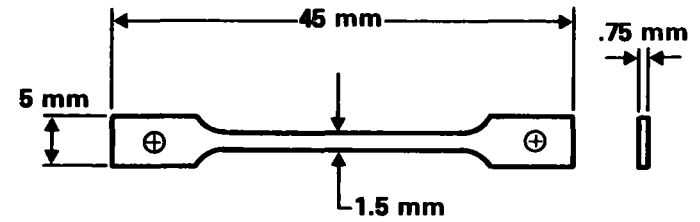
TENSILE SPECIMEN
ROUND TENSILE (RT)

48 mm
6.4 mm diam
3 mm diam
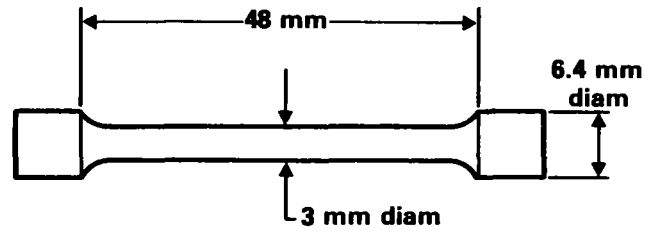
Fig. VII.2-A-2

BULK MATERIALS TESTING
MATERIALS TEST SPECIMENS

FRACTURE TOUGHNESS
COMPACT TENSION LARGE (CTL)
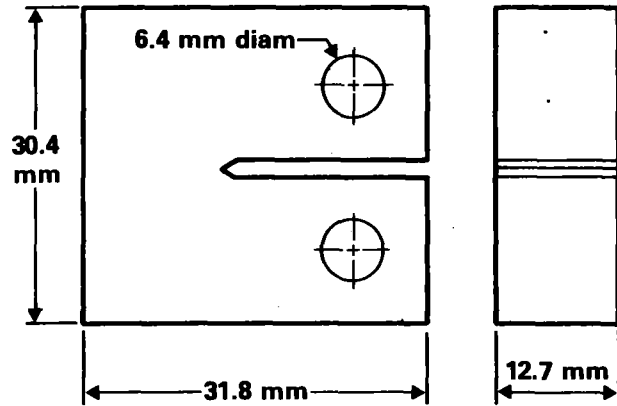
FRACTURE TOUGHNESS
COMPACT TENSION (CT)
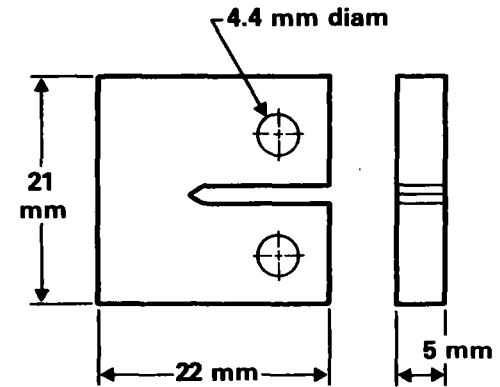
FRACTURE TOUGHNESS
CHARPY SPECIMEN (CH)
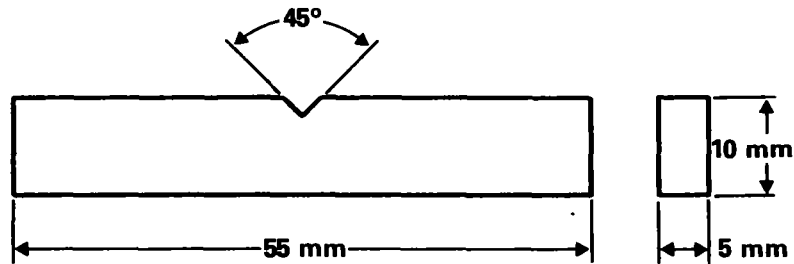
HEDL 8106-158.9

VII.2-68

– 652 –

Fig. VII.2-A-3

BULK MATERIALS TESTING

MATERIALS TEST SPECIMENS

FATIGUE-CRACK GROWTH RATE SPECIMEN

25 mm

18.8 mm

90 mm

6 mm

IRRADIATED SECTION

2.5 mm
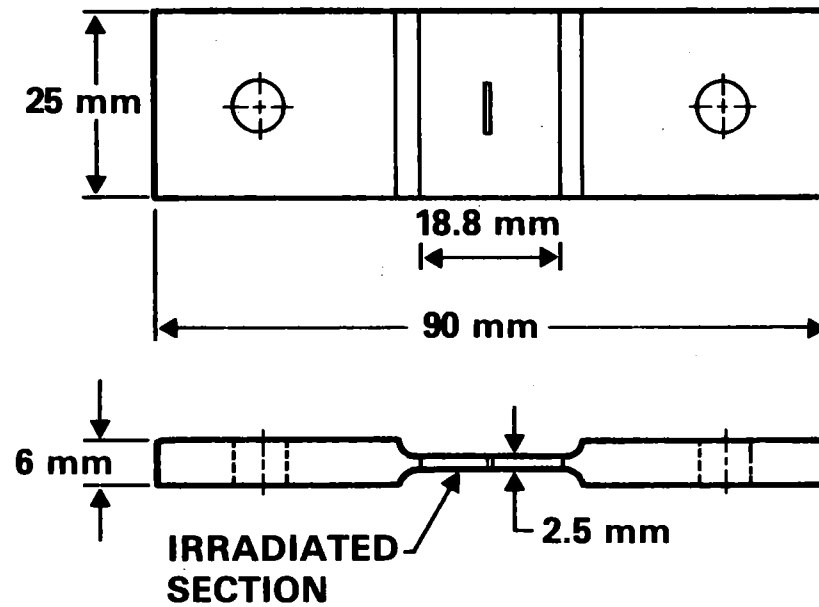
FULL SCALE

HEDL 8106-158.4

Fig. VII.2-A-4

BULK MATERIALS TESTING
MATERIALS TEST SPECIMENS

CONSTANT-AMPLITUDE LOAD-CONTROLLED HIGH-CYCLE FATIGUE SPECIMEN (HC)

6 mm THREAD   3 mm diam

6 mm diam

9 mm

38 mm
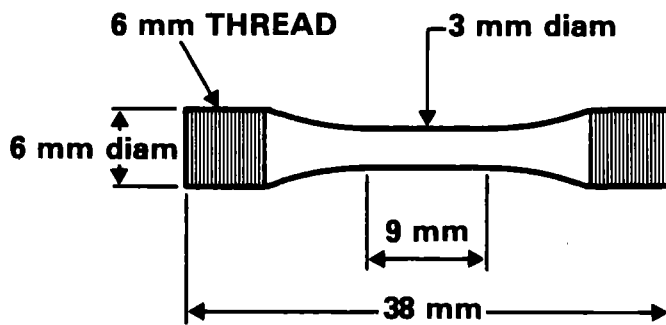
CONSTANT-AMPLITUDE STRAIN-CONTROLLED LOW-CYCLE FATIGUE SPECIMEN (LC)

6 mm THREAD

6 mm diam

3 mm diam

27 mm
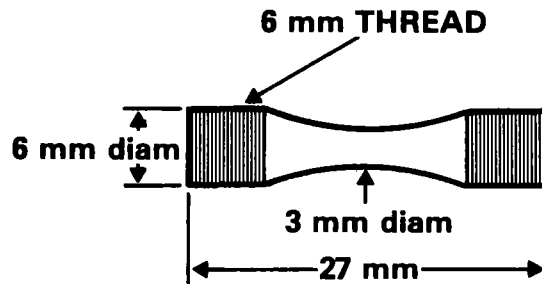
HEDL 8106-158.7

VII.2-70

Appendix VII.2-B

Test Module and Specimen Capsule

Design Details

Fig. VII.2-B-1
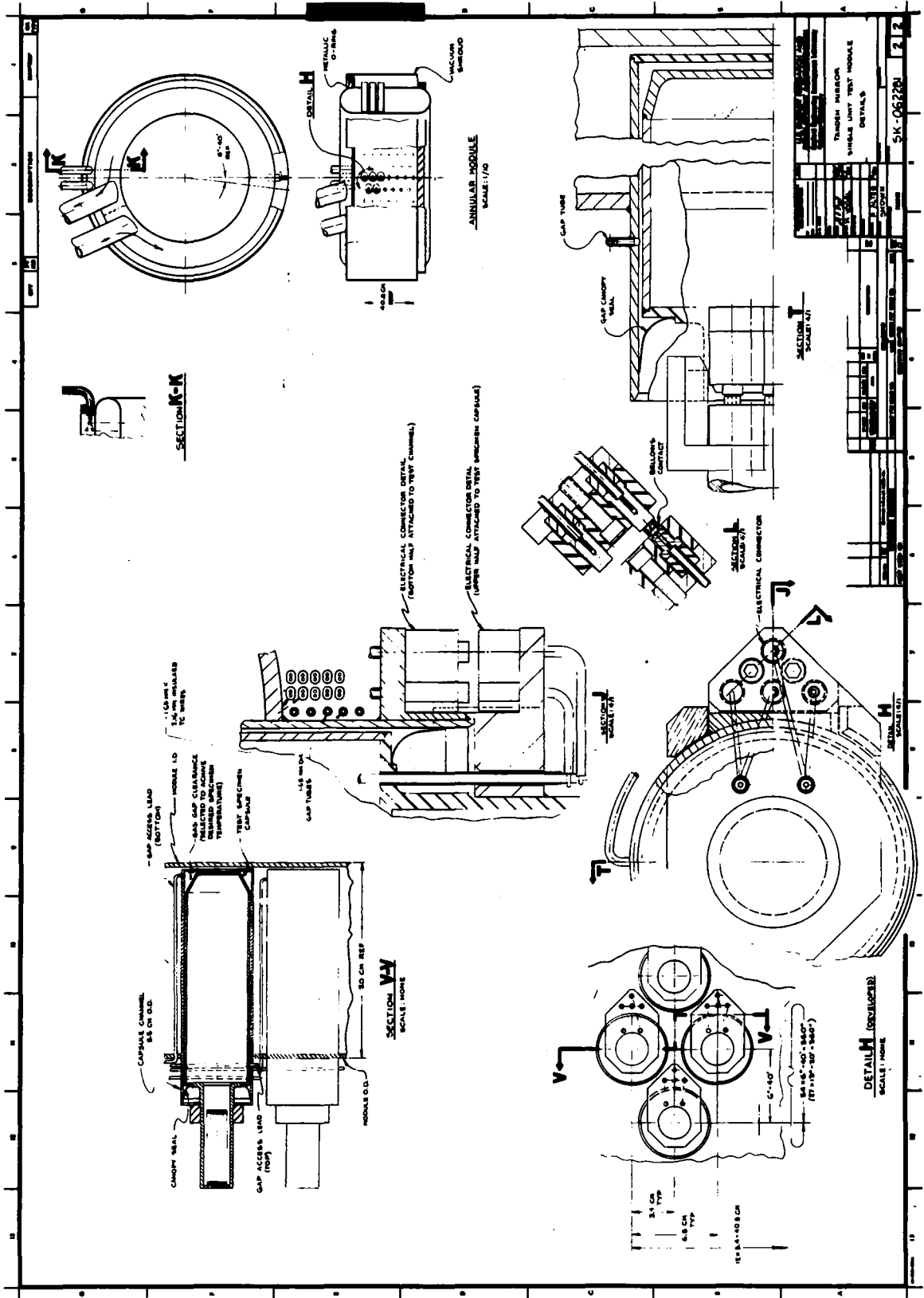
Fig. VII.2-B-2
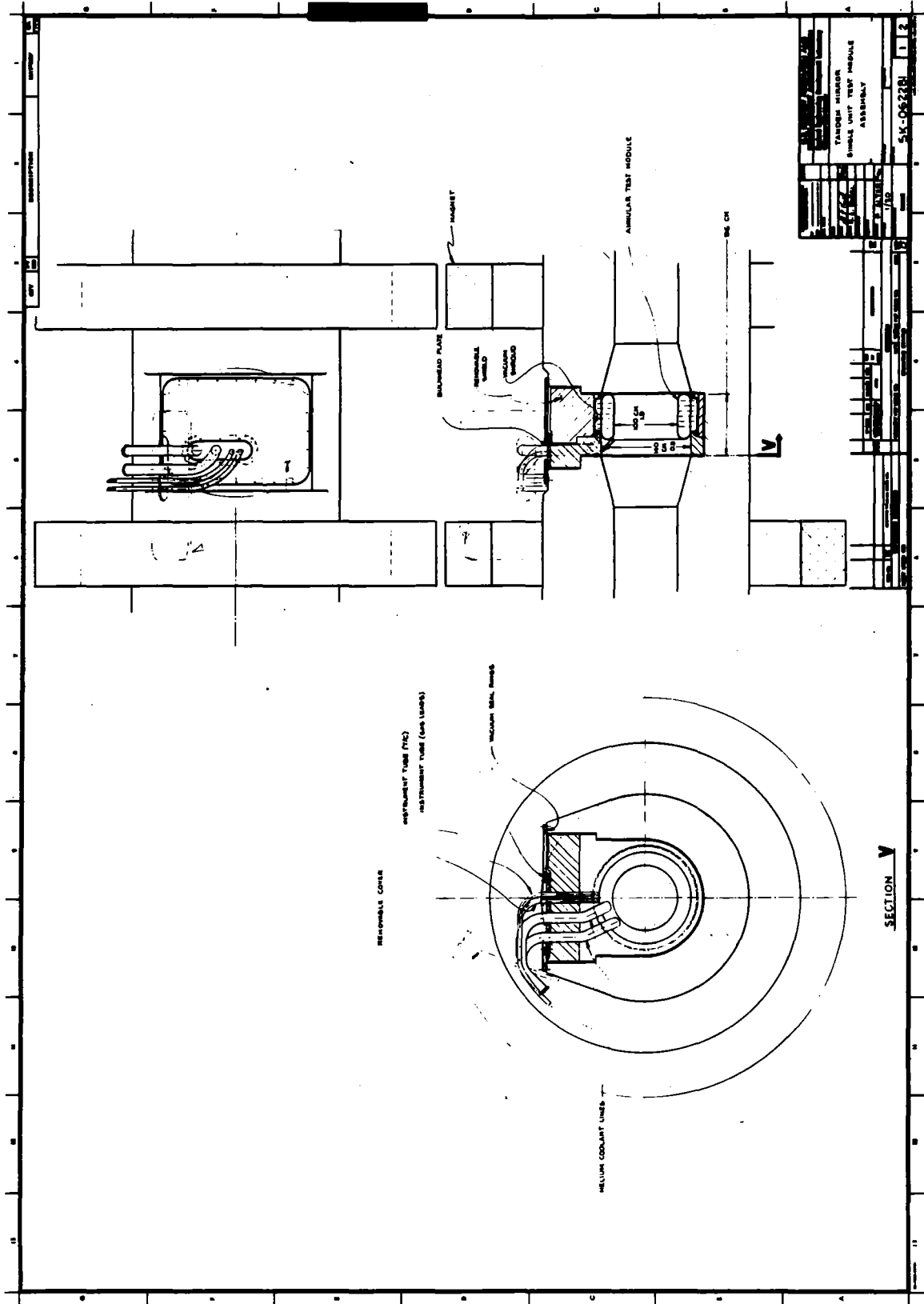
VII.2-74

VII.3   Test Module with Liquid Lithium Blanket

VII.3.1 General Consideration

Two basic blanket concepts were under consideration for TASKA

- a blanket with liquid material, where the breeding material lithium
  is pumped as a liquid through the blanket

- a blanket with solid material, where the breeding material is present
  as a solid and cooled by a gas stream

In both cases, the tritium must be separated from the breeding material
in an extraction process.

It was decided to work out the blanket concept with liquid material
for this TASKA study. The next section gives a detailed description of a
blanket module with liquid lithium as breeding material and of the
extraction process.

VII.3.2 Concept of a Test Module with Liquid Lithium Blanket
VII.3.2.1 Philosophy of the Concept

The test modules consist of three components:
- Blanket
- Reflector and shield
- Casing

The blanket is a hollow cylinder arranged around the plasma. It has an inner radius of 40 cm (first wall radius) and an outer radius of 140 cm.

Natural lithium is planned as breeding material and coolant for the test module with liquid metal blanket. The target coolant temperature in the blanket is in the range of 300 °C to 500 °C.

As lithium is liquid at temperatures higher than 180 °C, a blanket configuration is selected in which the lithium is pumped through tubes bent around the first wall cylinder. This tube bundle forms the structure of the blanket. The tubes are arranged inside the blanket volume in such a way that a large breeding material inventory is achieved.

The lithium flowing through the blanket permits a low tritium inventory in the blanket, continuous tritium extraction and simultaneous heat removal from the blanket. As the power is mainly deposited in the coolant itself, problems concerning heat transfer play only a secondary role. Due to the large surface of the blanket, caused by the tube construction, the blanket is enclosed in a casing for two reasons:

a) The pumping time required to evacuate the vacuum vessel is kept low, as the volume to be evacuated and the exposed surface are smaller,

b) The tritium permeation through the blanket tubes can be controlled by the build-up of a suitable casing atmosphere.

Furthermore, this casing serves to shield the wall of the vacuum vessel from direct neutron irradiation. This concept has, however, a disadvantage in that the cramped space conditions at the side walls of the casing and the first wall make the heat removal from these structures difficult linked with problems of the integration of the cooling facilities.

The part of the reflector and the shield which is integrated in the test module is also enclosed by the casing. Reflector and shield are designed as a plug to simplify handling and permit re-use. They are screwed on to the casing.

The modules must be exchanged from the central cell by means of remote control due to the high radiation level. For this reason, the module is not to be welded to the central cell, but rather is to be equipped with a flanged coupling joint. This means that stringent requirements are imposed on the flange sealings which must be able to maintain the vacuum in the central cell.

VII.3.2.2 Design

VII.3.2.2.1 Casing

The casing surrounds the blanket and the coolant piping and holds the reflector and shield plug. It is made of austenitic steel 1.4970. The side walls are graduated horizontally and vertically to prevent the vacuum wall being directly irradiated by 14 MeV-neutrons. The graduations (shielding edges) are arranged taking into account the thermal expansion of the casing and a linear material expansion rate of more than 4 % under neutron irradiation. Sufficient distance is thereby guaranteed between the neighbouring modules (Fig. VII.3-1). The width of the shielding edges amounts to 50 mm. When installed, the distance between the shielding edges of neighbouring modules is 50 mm and that between the side walls 40 mm. Fig. VII.3-2 contains a slide-in presentation of the modules in the central cell, in relation to the position of the base plates to each other.

With the exception of the base plate, which is 40 mm thick, the wall thickness of the casing amounts to 20 mm. The first wall is 10 mm thick and has an inner area of 2.54 m².

Table I of the Appendix contains a survey of the geometric data of the casing.

The wall thicknesses are dimensioned assuming low pressure differences and the integration of suitable support structures to retain the rigidity of the casing even after dismantling of the blanket and shield. Similarly, the installation of shielding structures takes into account the requirements for the shielding of the vacuum wall along the shielding edges.

Due to its cylindrical form, the first wall is sufficiently dimensioned against internal and external overpressure (max. 0.1 MPa) with a wall thickness of 10 mm. This pressure difference only occurs in the case of accident (leaky vacuum seals) or during short-term maintenance work in the blanket area without removal of the module.

During reactor operation, vacuum conditions ($\approx 10^{-3}$ Pa) are assumed both inside and outside the casing.
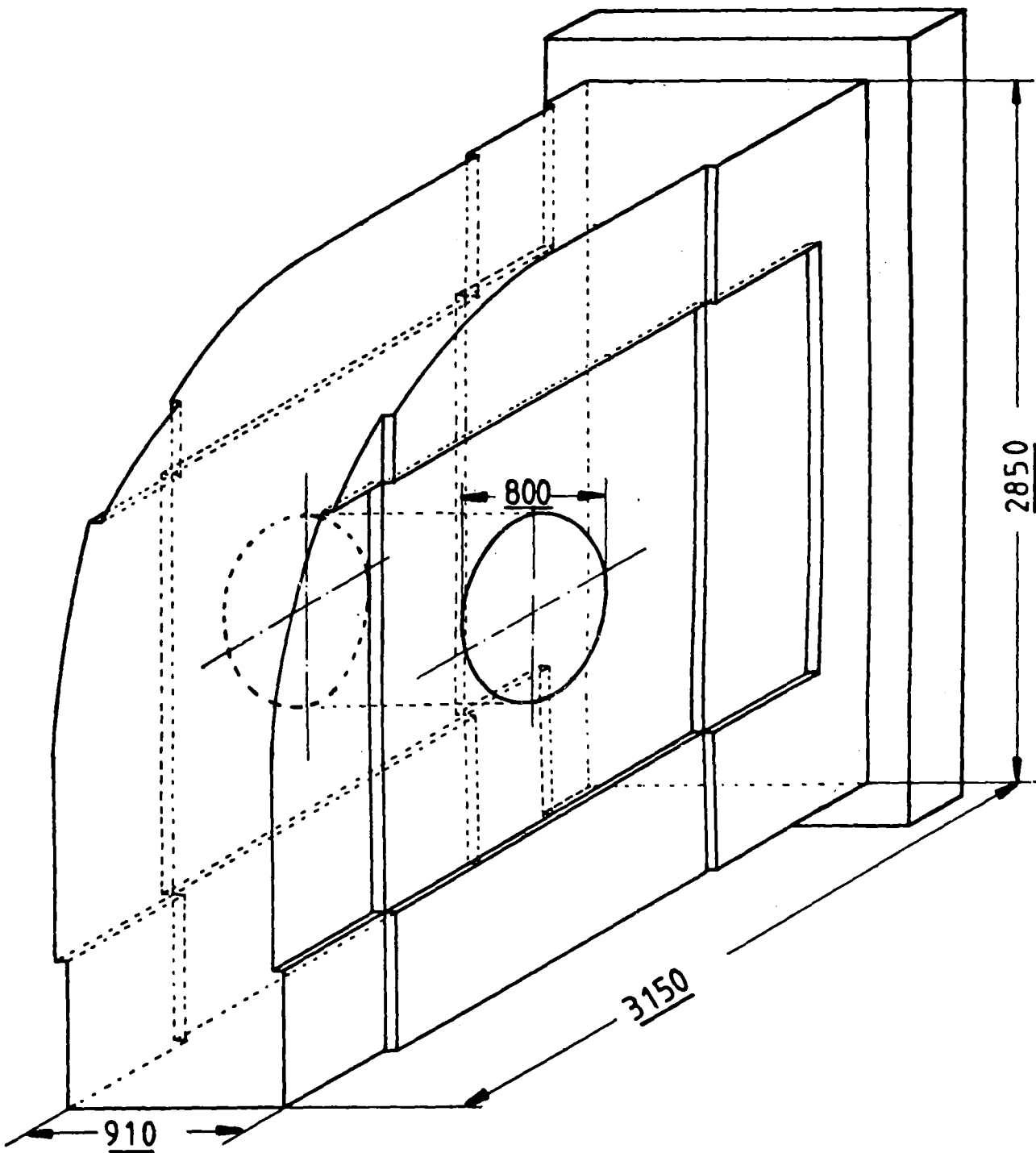
Fig. VII.3-1 TASKA test module casing

(Dimensions in mm)

VII.3-4

Central Cell

Test Module
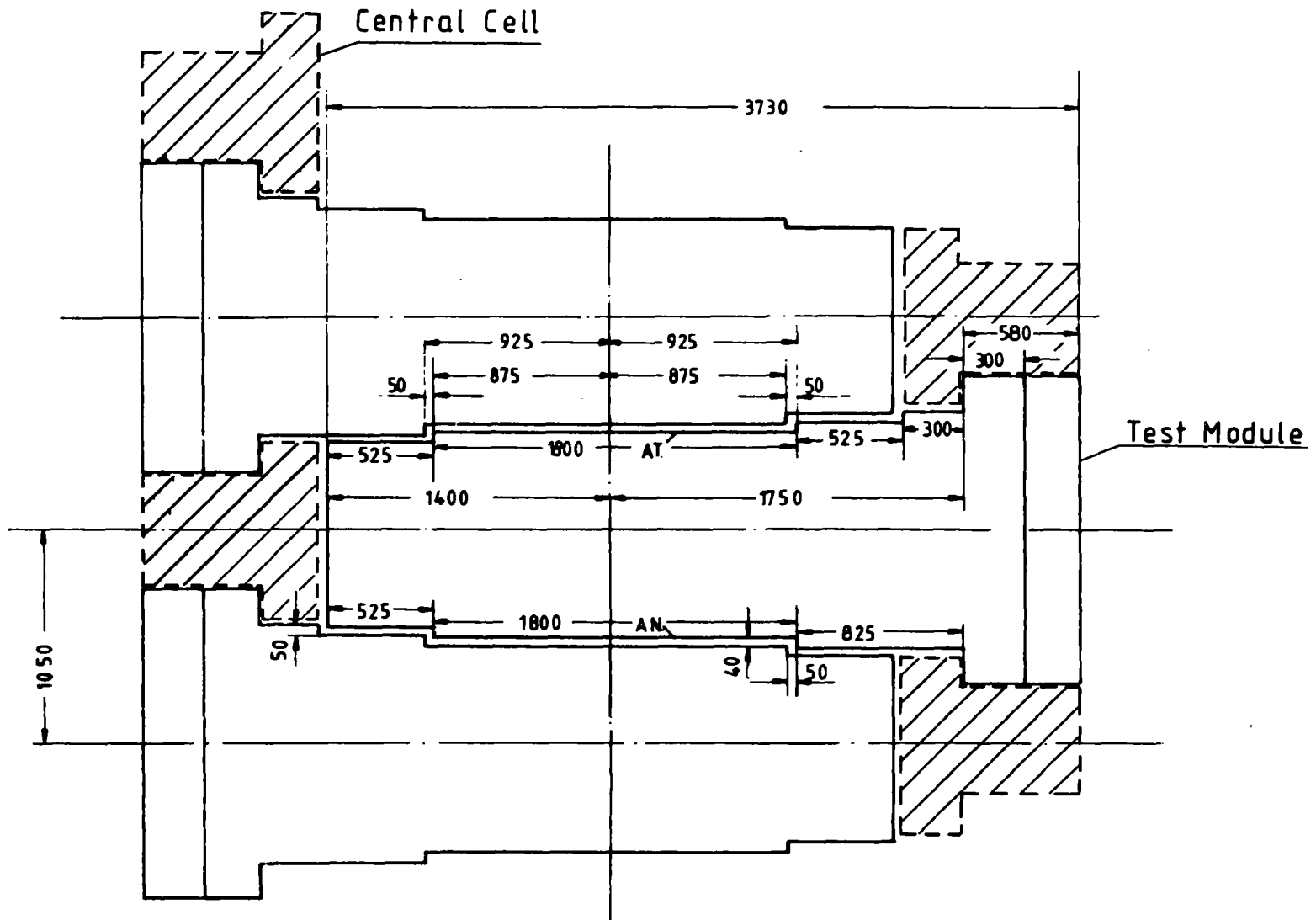
FIG. VII.3-2 Arrangement of the modules inside central cell

(Dimensions in mm)

For strength reasons, the maximum permissible temperature of first wall and the side walls of the casing has been fixed to 550 °C. Due to the heat production in these structures, they must be provided with cooling facilities. The cooling system of the first wall is dealt with in the following Chapter VII.3.2.2.2 as lithium is planned as coolant and the system is considered as an integral part of the blanket.

At this stage in the concept, we are trying to find a basic method of solving the cooling problem of the side walls.

The concept of a surface cooler, as illustrated in Fig. VII.3-3 is conceivable as a cooling system for the side walls. Thereby it is assumed that the heat production drops so drastically in the radial direction that only the area from r = 40 cm (first wall cylinder) to the first shielding edge needs to be cooled. This is realistic as the outer wall parts located behind are largely shielded by the blanket of the adjacent modules.

The inner side of the area to be cooled (approximately 3 m² per side) is covered by a plate in which coolant guides are imprinted. The plate is welded to the wall of the casing at the first wall and the shielding edges and is leak-proof.

With this configuration it is therefore possible to achieve a directed coolant guidance, which takes into account the gradient of heat production and should limit the average temperature in the wall structure to approximately 350 °C.

The coolant pressure has to be kept very low to avoid high additional wall stresses.

For handling the test module is guided along on support rails inside the central cell. The support rails are equipped with roller rails to improve the sliding ability of the module casing on the rails.

In order to simplify the remotely controlled exchange of the test modules, they are bolted to the central cell. This imposes high requirements on the flange sealing which must guarantee the vacuum conditions inside the central cell. The sealing is therefore a double O-ring seal with interspace evacuation. Viton or Inconel which is vapour deposited with silver can be used as sealing materials.

The maximum leakage rate of the flange should not exceed $10^{-3} \frac{Pa.1}{s}$.
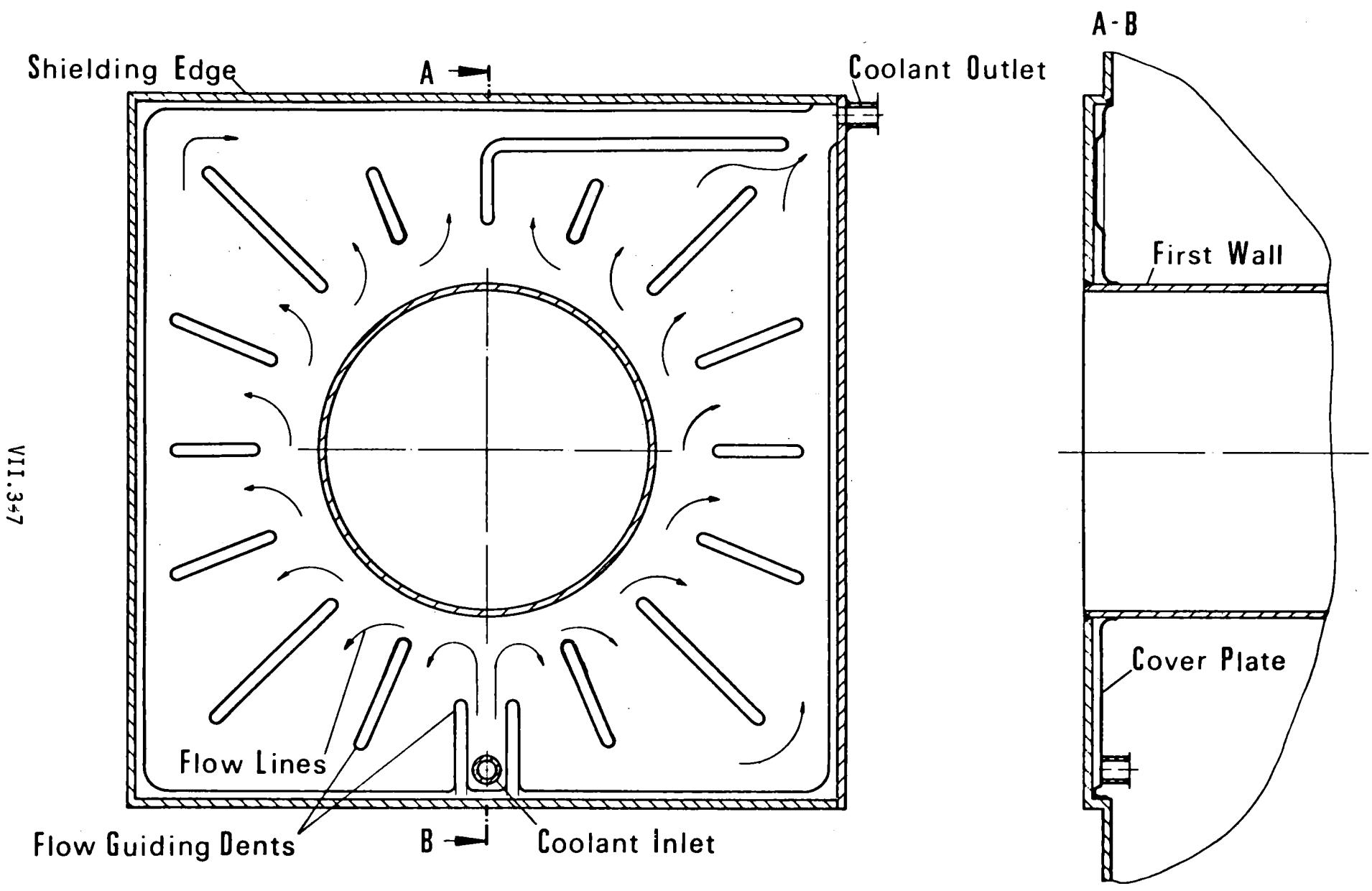
Fig. VII.3-3 Proposal for a cooling method for the casing wall

VII.3.2.2.2 First Wall/Blanket

VII.3.2.2.2.1 First Wall

From a construction point of view, blanket and first wall will be regarded as one unit here. The first wall must be cooled due to the power production in the structure of the first wall and the heat flow from the plasma. Liquid lithium which is planned as breeding material and coolant for the blanket, is to be used as coolant.

The basic arrangement of the first wall cooling system is presented in Fig. VII.3-4.

It consists of half-tubes welded on to steel bands which are arranged around the first wall cylinder. The half-tubes have an outer radius of 22.5 mm and should have a center distance of approximately 70 mm. The steel bands are pressed against the first wall cylinder by means of a holding fixture device, see Fig. VII.3-5, in order to attain the best possible heat transfer.

At the same time, this approach serves to prevent non-permissible high stresses in the cooling tubes, which can occur as a result of the thermal expansion of the first wall.

The temperature pattern in the first wall for a center distance of 70 mm between the cooling tubes which is illustrated in Fig. VII.3-6 shows that the maximum temperature difference between the inner side of the first wall and a cooling tube is approximately 10 °C per W/cm^3. This value can just be tolerated, but nevertheless calls for an optimization of the thickness of the first wall, taking into consideration the power production and the stability requirements for the specified pressure differences. The temperature difference between the first wall and the cooling tube plate amounts to approximately 35 °C for a heat transmission coefficient of 0.57 $W/°C\ cm^2$.

The cooling system of the first wall is connected to the coolant supply of the blanket.

VII.3.2.2.2.2 Blanket

The blanket is designed in such a way that an acceptable tritium breeding rate and power production are attained with the given breeding material.

It consists of tubes bent around the first wall cylinder which are made of austenitic steel 1.4970. They have a diameter of approximately 10 cm and a wall thickness of 2.6 mm (Fig. VII.3-7). The distance between the tubes amounts to approximately 5 mm. Spacers prevent the tubes from touching each other.
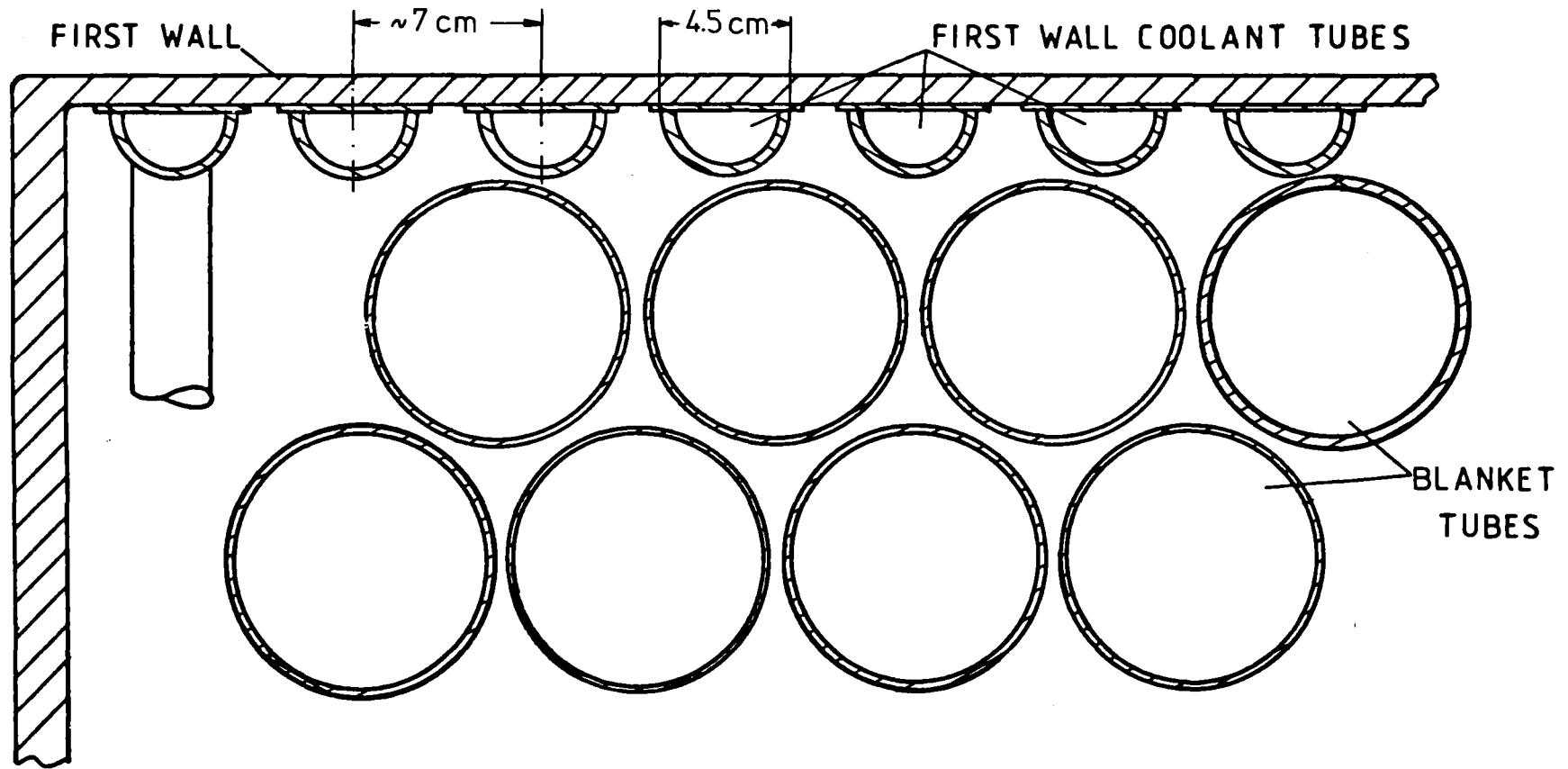
Fig. VII.3-4 Arrangement of the first wall coolant tubes
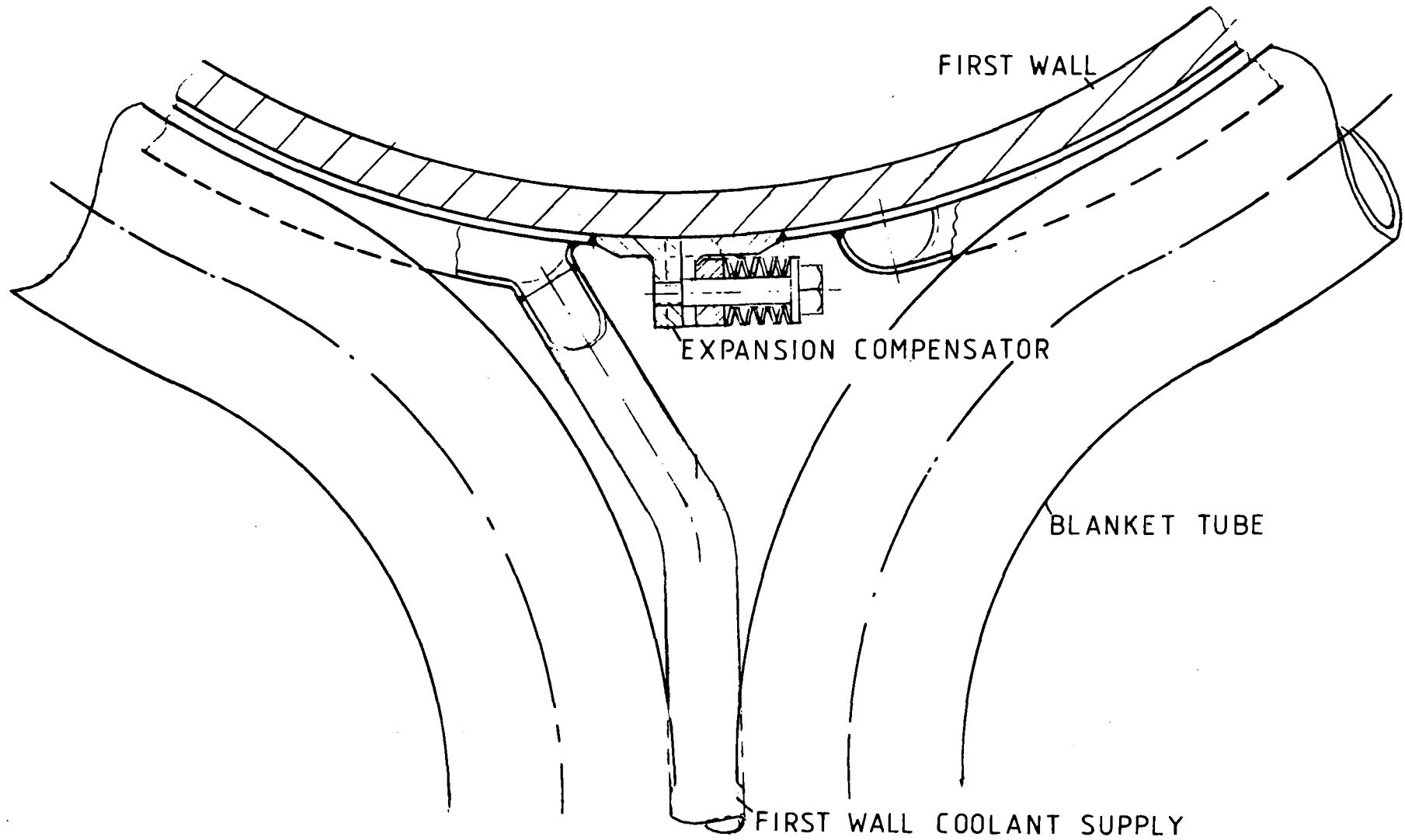
Fig. VII.3-5 Holding fixture of the first wall coolant tubes

Cooling Tube Plate

First Wall Element

$\Delta T = 10°C$

60°C

80°C

100°C   120°C   130°C

12.5 mm

35 mm
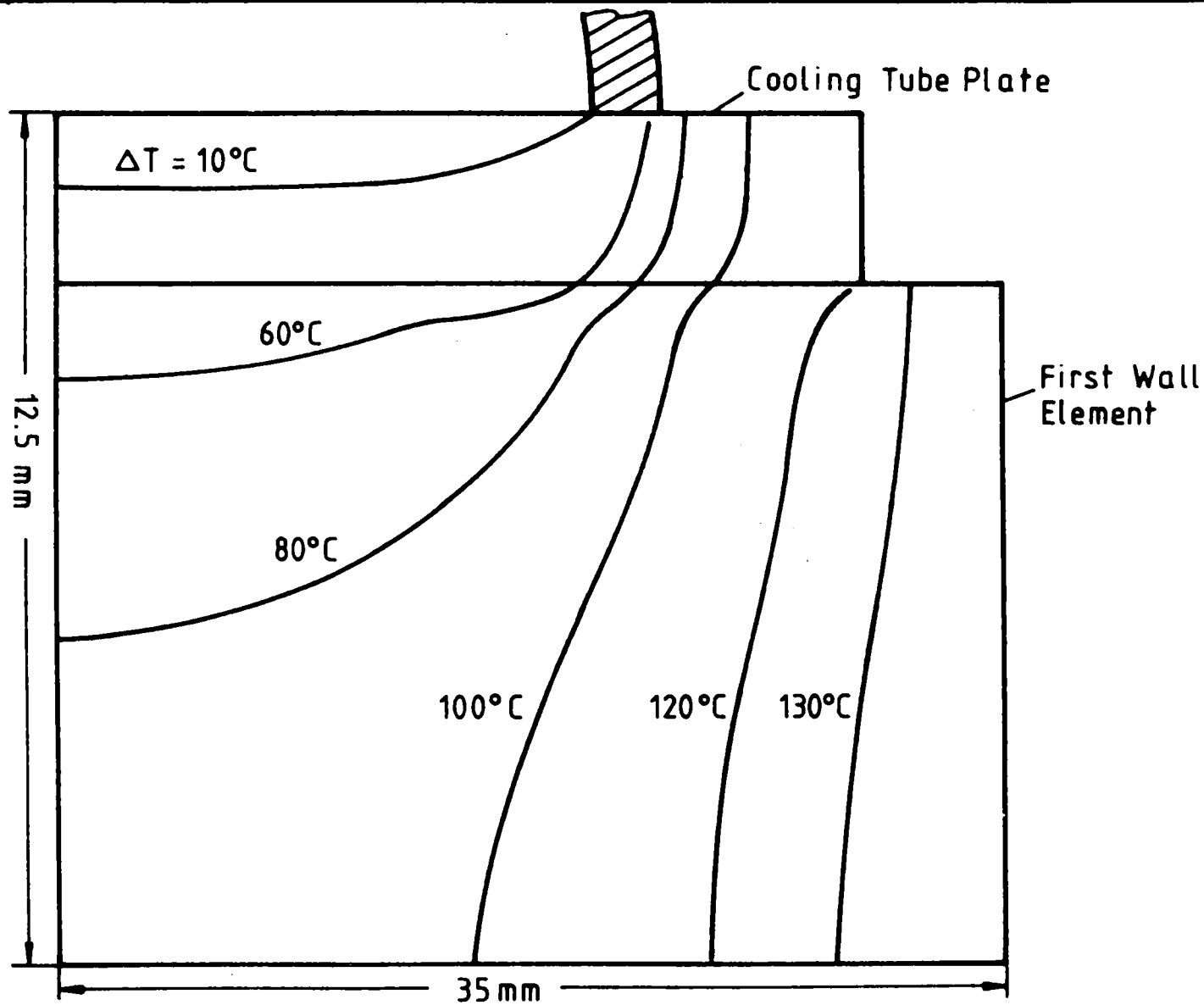
Fig. VII.3-6 Temperature distribution for the first wall cooling system $(p = 12 \text{ W/cm}^3)$

In the radial direction, ten layers of tubes are positioned in staggered form behind each other. The greatest possible utilization of the blanket volume with breeding material is attained as a result of this design. The fraction of breeding material in the blanket amounts to 73 % within the tube region.

The axial number of layers amounts to 4 rows of 8 tube bends and 6 rows of 7 tube bends from the inside to the outside caused by the geometry of the module casing. The average radius of the inner tube bend is 483 mm and that of the outer tube bend 1317 mm.

The liquid lithium is supplied via the coolant inlet pipe to the distribution header. This is connected to the blanket tubes by nozzles (Fig. VII.3-8). After it has flowed through the blanket area, the lithium is removed from the module via collecting header and outlet pipe. A different coolant mass flow is necessary in the tubes in accordance with the power distribution in the blanket. This is achieved by means of different tube lengths and the throttles in the nozzles which connect the blanket tubes to the headers.

The inner surface of the blanket which is exposed to fusion neutrons amounts to 2.3 m² or 91 % of the first wall area of the test module.

The important parameters of the TASKA blanket with liquid lithium as breeding material and coolant may be taken from Table VII.3-1.

The wall thicknesses of blanket tubes, nozzles, headers and coolant pipes were designed for a maximum coolant pressure of 0.7 MPa at T = 550 °C. Due to the very low coolant velocities in the bundle tubes (max. 7 cm/s), at this temperature the eroding corrosion which is to be expected during the maximum operating period of 2.5 years at load factor of 80 % has already been taken into account for the wall thicknesses. Austenitic steel 1.4970 which was used for the blanket tubes, is also used for nozzles, headers and coolant pipes. According to Larsen and Miller, its maximum permissible loading was estimated as being 110 N/mm² at 550 °C under neutron irradiation. After a first estimate, the stresses to be expected for blanket tubes, nozzles, headers and main coolant pipes are below this limit.
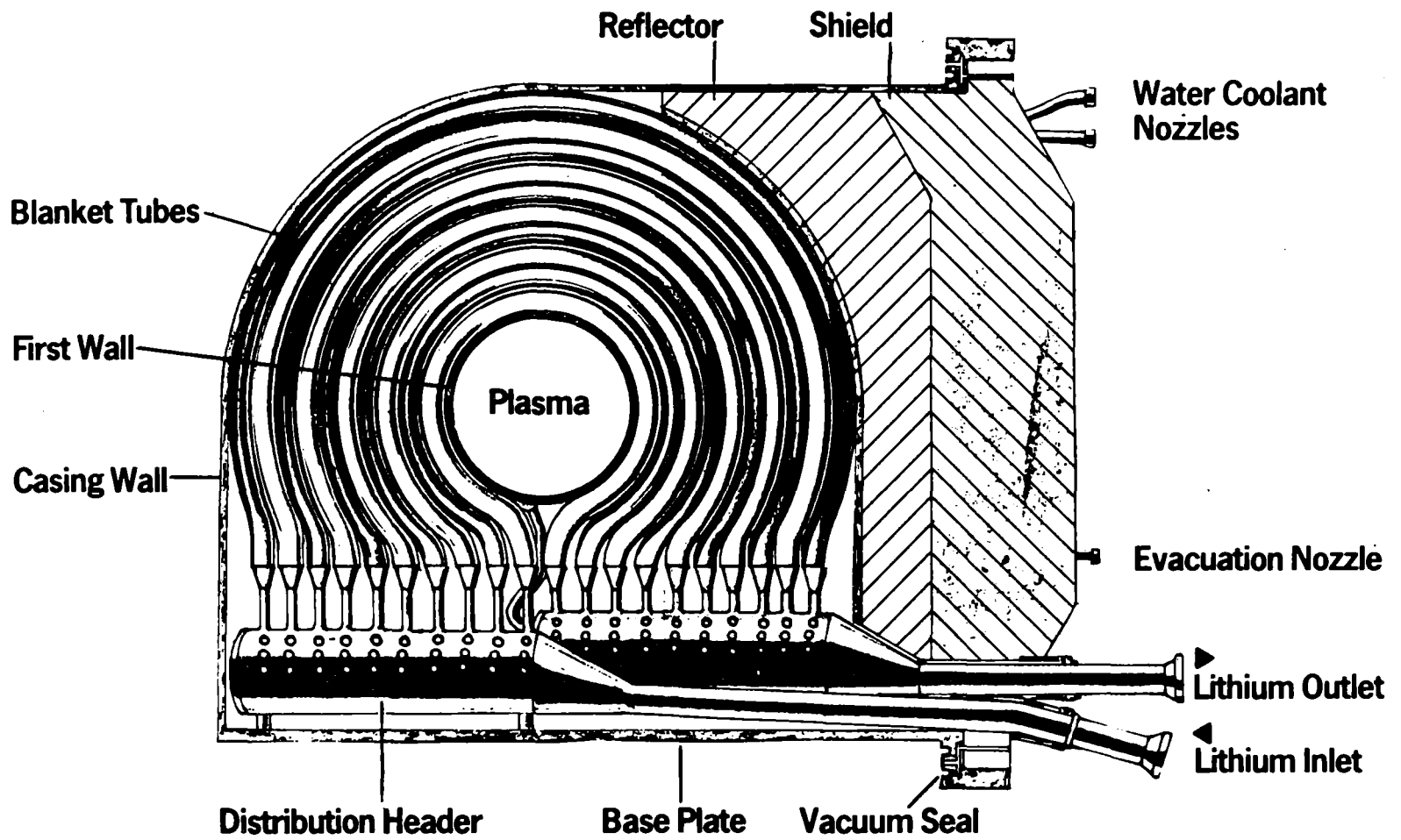
Fig. VII.3-7 TASKA test module blanket view

seal flange

first wall

blanket tubes

casing wall

distribution header
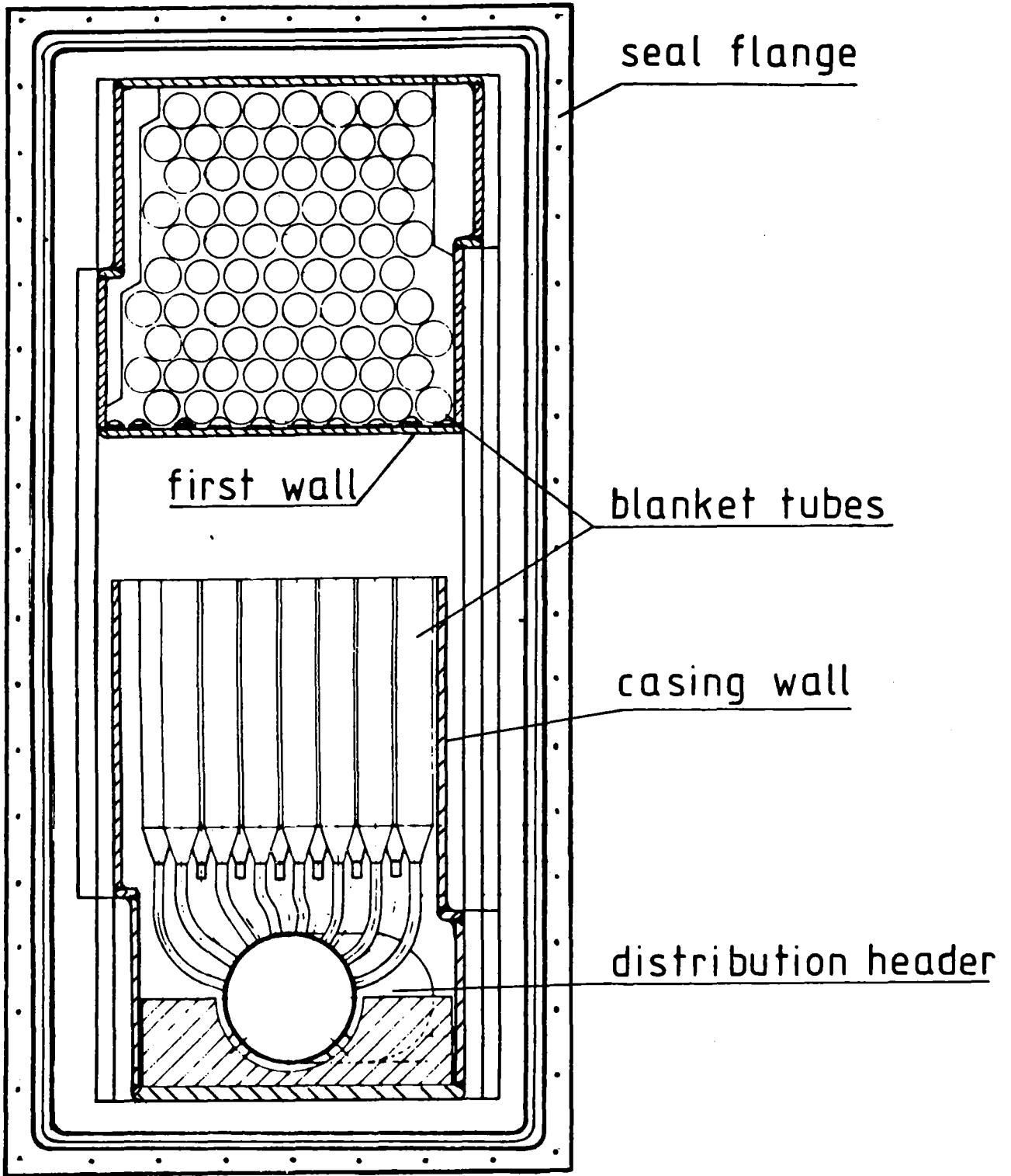
Fig. VII.3-8 TASKA test module vertical cut

Table VII.3-1: Data of the TASKA Liquid Lithium Blanket

Breeding material and coolant	Natural Lithium
	(92.5 % Li7, 7.5 % Li6)

Radius of the First Wall	40 cm

Thickness of the blanket	96 cm
Length of the blanket	
r = 42 cm	92 cm
r = 138 cm	82 cm

Composition (tube region)	73 % Lithium
	7 % Structure
	20 % Void

Structural material	Austenitic Steel 1.4970

Diameter of the blanket tubes	10 cm

Number of blanket tubes	74

VII.3.2.2.3 Reflector and Shield

VII.3.2.2.3.1 Design

Reflector and shield are designed as a plug which is inserted into the module casing behind the blanket as one component. Fig. VII.3-9 shows the schematic composition of reflector and shield.

The reflector is made of austenitic steel 1.4970 and is provided with cooling holes, through which water flows with an average temperature of approximately 80 °C and a pressure of approximately 0.5 MPa. The average power density in the reflector amounts to approximately 0.1 W/cm³.

The purpose of the shield is to guarantee sufficient protection against the neutron radiation and the secondary gamma radiation during reactor operation and shield also against the γ-radiation of activated structures after reactor shutdown.

In contrast to this, there is a demand for the thinnest possible shield, as this keeps the quantity of shielding material required low.

Furthermore, the thickness of the shield influences the inner diameter of the superconducting magnet coils, the size of which also greatly affects the costs of the plant.

The shield construction, which comprises 3 layers of $Pb/B_4C/$ steel structure, was specified.

The shield is cooled by water to remove the heat produced in the structure and in the boron layers. The maximum structural temperature is limited to 200 °C.

The reflector and shield plug is hermetically bolted to the casing (leakage rate $< 10^{-3} \frac{Pa.l}{s}$). A double O-ring seal with interspace evacuation, the suction channel of which is attached to the seal of the casing flange, is envisaged as the seal.

VII.3.2.2.3.2 Shield Calculations

The calculations dealt with the shielding effect with reference to the neutron and gamma dose rates during reactor operation and the -dose rates from the activated structures after plant shutdown in the case of an installed test module.

The two dimensional calculation of the neutron flux distribution (26-groups-ABBN-structure) was performed using the INTERATOM computer code DLS in accordance with the diffusion method, whereby the Removal Sources were taken into account. The INTERATOM computer code DLS-GAMMA was used to calculate the gamma dose rate during operation and after reactor shutdown. This program works according to the Point-Kernel method and takes the build-up factor into consideration.

R ⟵ [CM] ⟶ R

| Blanket | Blanket | Reflector | Shield

140 138   41 40 27   27 40 41   138   173 177 183   207 209 215 224 228 232 233

B   A PLASMA A   B   D   E F   D   F D E F

C   C   C   E   C
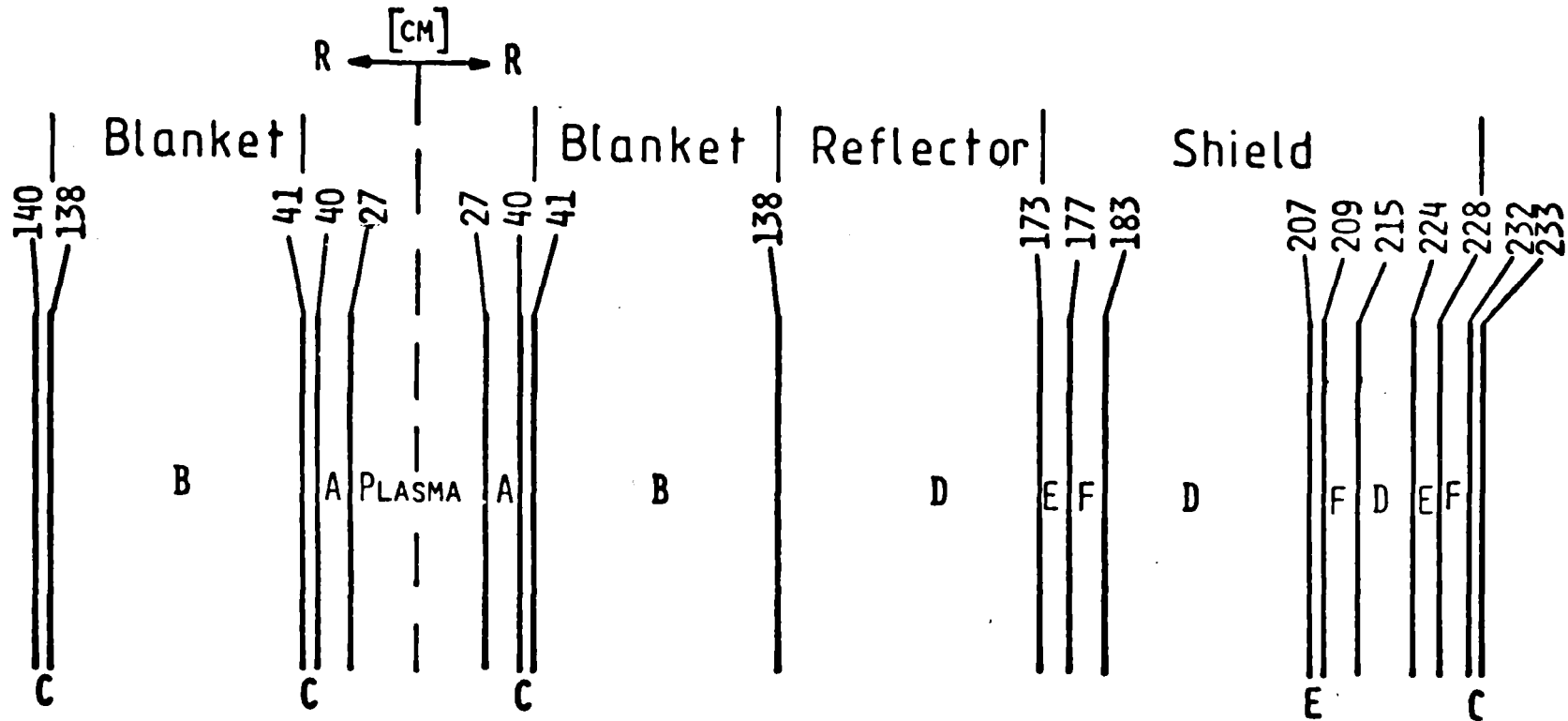
A = VACUUM

B = 73% Li_{NAT}; 7% SS 1.4970; 20% VOID

C = 100% SS 1.4970

D = 95% SS 1.4970; 5% H_2O

E = 95% PB

F = 87% B_4C

Fig. VII.3-9 TASKA blanket, reflector and shield composition

The 26-groups-flux at the outer blanket boundary of the KfK-INR-neutron transport calculations / 1 / was used as boundary flux for DLS.

The calculations resulted in a neutron dose rate of 4,000 rem/h and a gamma dose rate of 1 rem/h at a distance of 1 m from the outer edge of the module during reactor operation. The neutron flux distribution is shown in Fig. VII.3-10.

After reactor shutdown, the dose rate due to structure activation of the reflector/shield plug amounts to 12 mrem/h at the outer edge of the module and to about 6 mrem/h at a distance of 1 m. Only the long-lived isotopes Co60 ($T_{1/2}$ = 5.3 a), Ta 182 ($T_{1/2}$ = 115 d) and Fe59 ($T_{1/2}$ = 44 d) were considered in these calculations.

The concentration of the precursors in steel was assumed to be:

    500 ppm   Co 59
    500 ppm   TA 181
    3100 ppm Fe 58

In the case of a cyclic mode of operation over a period of 30 months with a load factor of 80 % / 2 / the fraction of the saturation activity achieved at the end of the operating period is as follows:

    23 % for Co 60
    89 % for Ta 182
    98 % for Fe 59

Table VII.3-2 contains a summary of the results calculated.

With reference to the sandwich construction of the shield, it is recommended that this be reduced to 3 layers. This could lead to a simpler construction with lower manufacturing and material costs.

Furthermore, the thicknesses of the absorber layers and the reflector should be optimized.
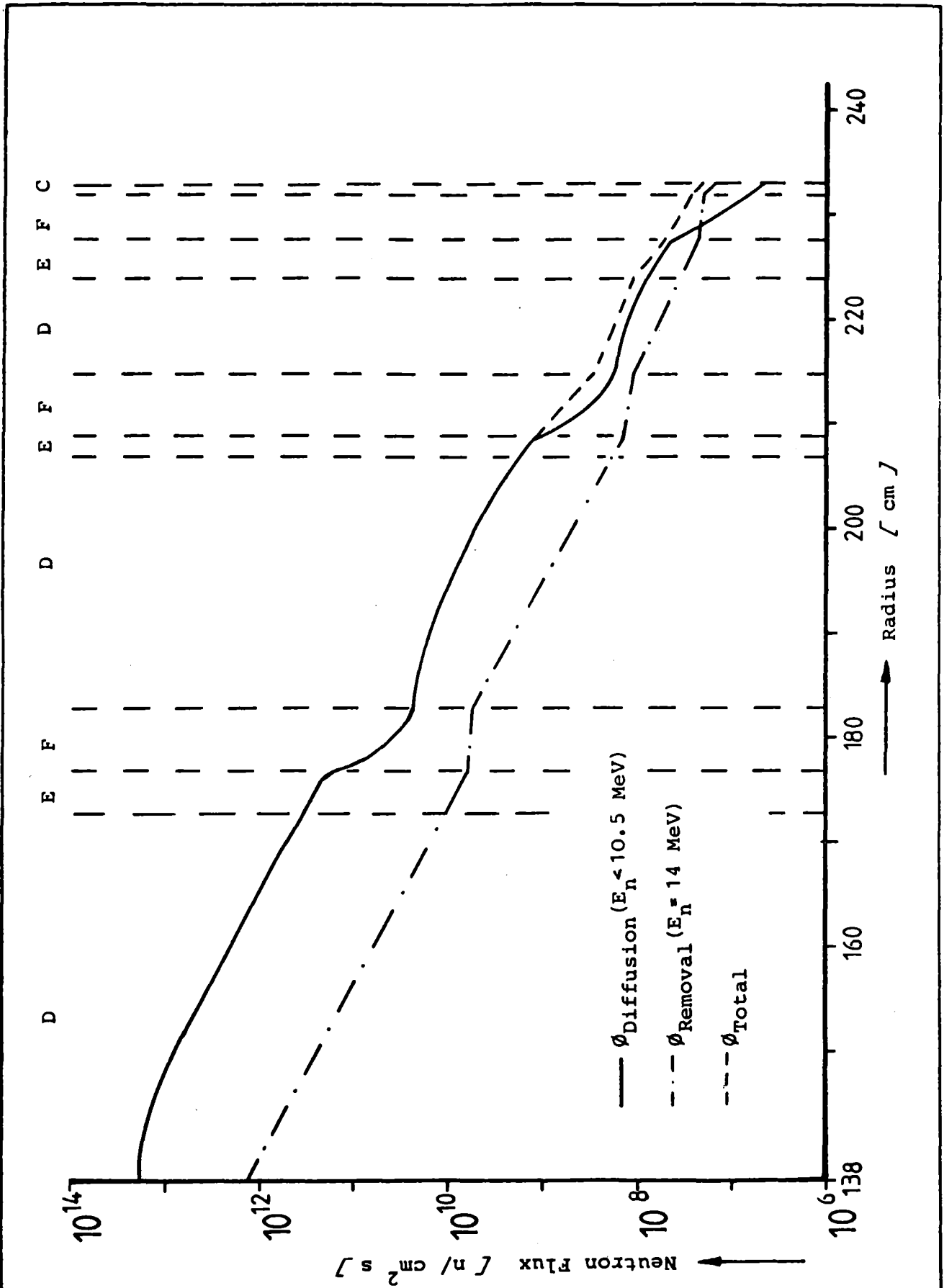
VII.3-18

Fig. VII.3-10 Neutron flux distribution inside reflector and shield plug at 1MW/m^2 neutron wall loading

Table VII.3-2: Radiation Exposure at the TASKA Test Module with Liquid Metal Blanket

Dose rate during operation:
at a distance of 1 m

due to neutrons $\dot{D}_n$ = 4000 rem/h
due to gammas $\dot{D}_\gamma$ =   1 rem/h

Dose rate after reactor shutdown
(T > 1d):

$T_{operation}$ = 2.5 years, LF = 80 %

Nuclide concentrations

500 ppm Co 59
500 ppm Ta 181
3100 ppm Fe 58

| Nuclide | $\dot{D}_{radial}$ / mrem/h / | |
	Module outer edge	1 m Distance
Co 60	1.1	0.6
Ta 182	10.0	5.0
Fe 59	0.5	0.3
Total	11.6	5.9

VII.3-20

VII.3.2.3 Cooling Loop

VII.3.2.3.1 Power and Coolant Balance

The power generated in the test module is made up of the power generated in the first wall and in the cooling system of the first wall and the blanket power.

Fig. VII.3-11 illustrates the radial power distribution in the first wall and in the blanket for a neutron wall loading of 1 MW/m^2. A homogeneous blanket composition of 73 % natural lithium, 7 % structure and 20 % void was assumed for the calculation.

The power generated per test module amounts to 3.5 MW for an average power density of approximately 0.9 W/cm^3 in the blanket. The neutron wall loading for TASKA is 1.53 MW/m^2 / 3 /.

The blanket energy multiplication factor is 0.9. This results in a blanket power of 3.2 MW.

The blanket energy multiplication factor has been estimated as follows.

From the one dimensional (1-D) neutronics calculations, a blanket multiplication factor (M_{1D}) of 1.02 was obtained. However, the true energy multiplication factor (M) of the blanket must take into account the fact that the blanket composition, structure and void fractions are different in different radial directions across the blanket (see Fig. VII.3-7). A first approximation to M may be obtained by weighting the 1-D computation of the multiplication factor by the ratio of the blanket volume fraction to the blanket volume fraction plus the headers volume fraction. Therefore,

$$M \approx M_{1D} \frac{V_{Blanket}}{V_{Blanket} + V_{Headers}}$$

where M_{1D} is the multiplication factor from the 1-D blanket neutronics calculation

$V_{Blanket}$ is the volume faction of the blanket (≈ 3.6 m³)

$V_{Headers}$ is the volume fraction of the headers region (≈ 0.5 m³)

Table VII.3-3 contains the power to be removed per tube row of the blanket. The inlet temperature of the coolant amounts to 300 °C and the outlet temperature should be varied between 400 °C and 500 °C. An average coolant outlet temperature of 450 °C was taken as the basis for the coolant balance. The corrosion at this temperature leads to a material deduction of approximately 10^{-5} m/a / 4 /, and is an acceptable value for the operating period maximum of 2.5 years as planned for the TASKA test modules.
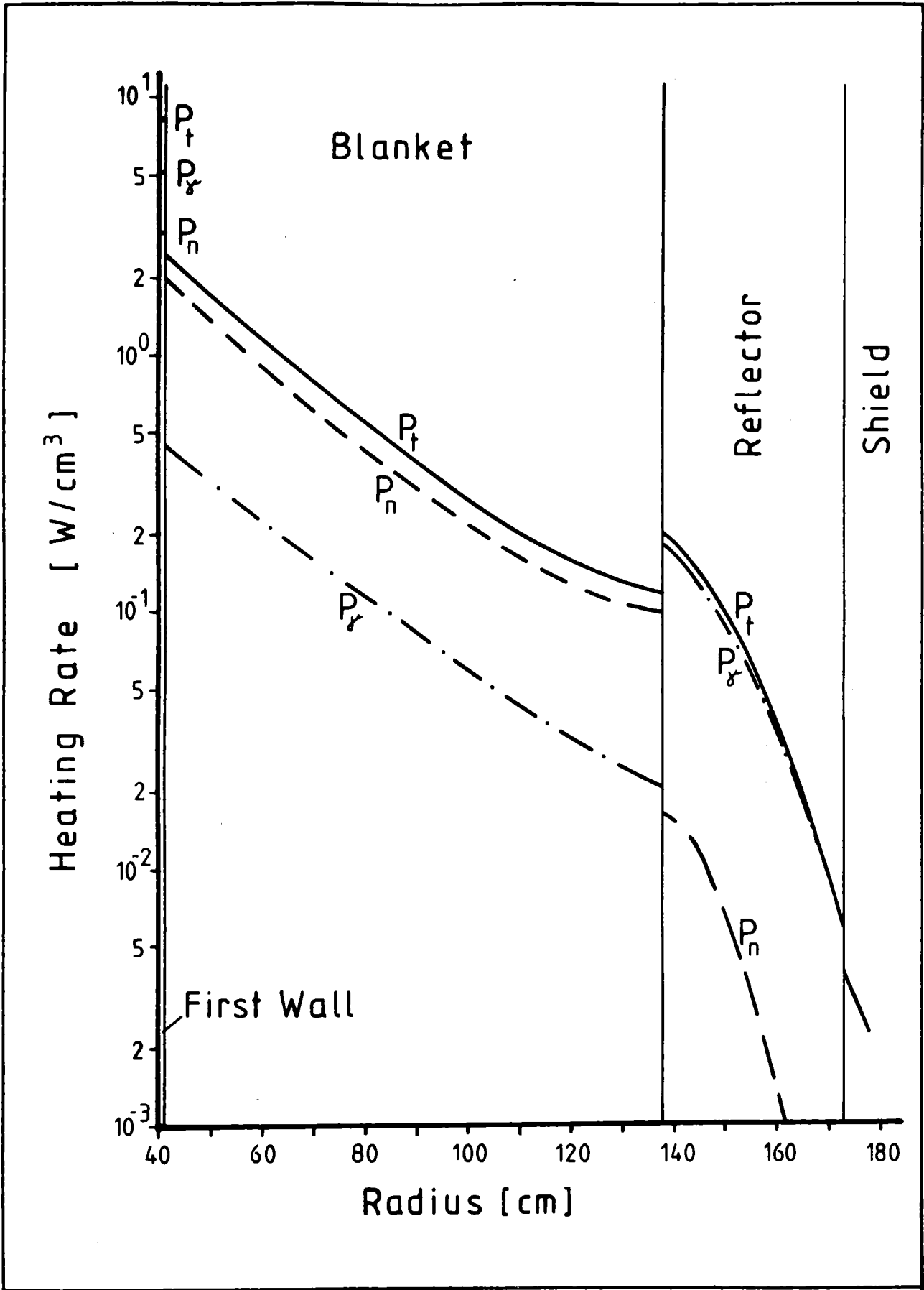
Fig. VII.3-11 Radial heating rate distribution at 1MW/m² neutron wall loading

A linear temperature increase in the coolant was assumed from the tube beginning to the end of the tube.

The main data concerning the balance of power and coolant for a test module may be taken from Table VII.3-4.

The calculations were based on the material data for lithium, which are listed in Table II of the Appendix.

Table VII.3-3: Tube Row Power in the TASKA Liquid Lithium Blanket

Tube Row	$\bar{r}$ / cm /	$\bar{p}$ / W/cm³ /	Power per Row / MW /	Number of Blanket Tubes
1	48	2.9	0.86	8
2	57	2.0	0.61	8
3	.67	1.4	0.46	8
4	76	0.95	0.36	8
5	85	0.7	0.27	7
6	95	0.5	0.19	7
7	104	0.38	0.15	7
8	113	0.3	0.11	7
9	122	0.24	0.10	7
10	132	0.2	0.09	7

VII.3-23

Table VII.3-4: Power and Coolant Balance of a TASKA Test Module with Liquid Lithium Blanket

Neutron wall loading	1.53 MW/m^2
Module power	3.5 MW
Average power density in the blanket	0.9 W/cm^3
Blanket energy multiplication factor	0.9
Power peaking factor $\dfrac{P_{max}}{P_{average}}$	≈ 4
Coolant	Liquid Lithium
Coolant temperatures	
Inlet nozzle	300 °C
Outlet nozzle	450 °C
Coolant pressure	0.5 MPa
Coolant mass flow	6 kg/s
Coolant inventory in the cooling loop	approx. 3.5 t
Max. coolant velocity at inlet nozzle	2 m/s
Max. coolant velocity in the blanket tubes	7 cm/s

VII.3.2.3.2 General Design

This presents a survey of the general design of the primary coolant loop for a test module. In principle this survey may only be transferred to a plant loop, as no statement is made concerning the extrapolation to larger power and units to be supplied.

The primary coolant loop for a test module with liquid metal blanket essentially consists of the following components, when viewed in the direction of the coolant flow (Fig. VII.3-12):

- module
- main coolant pipes
- degasification system
- purification system
- intermediate heat exchanger
- balancing tank
- primary pump
- drain system

The coolant leaves the test module with a maximum temperature of 500 °C, and a pressure of approximately 0.4 MPa. Thereby, a pressure loss of about 0.1 MPa is assumed in the module.

The gas bubbles present in the coolant are removed in the degasification system which must be located at the highest point in the geometry.

Approximately 10 % of the coolant flow in the primary loop is led through the purification system, which is situated in the hot leg of the loop. The purification system also contains the cold trap system required for the tritium extraction.

The intermediate heat exchanger must be designed for a power of approximately 3 MW per module. In order to keep the coolant pressure and the pumping capacity as low as possible, the pressure loss in the heat exchanger should be less than 0.1 MPa. Approximately 100 m^2 are assumed as heat exchanger area.

The purpose of the balancing tank is to balance any lithium losses which might occur due to leakage and purification as well as any alterations in the volume of the coolant caused by temperature.

Degasification System

Test Module

IHX

Purification System

Primary Lithium Loop

Secondary Sodium Loop

Balancing Tank

Primary Pump

Drain System
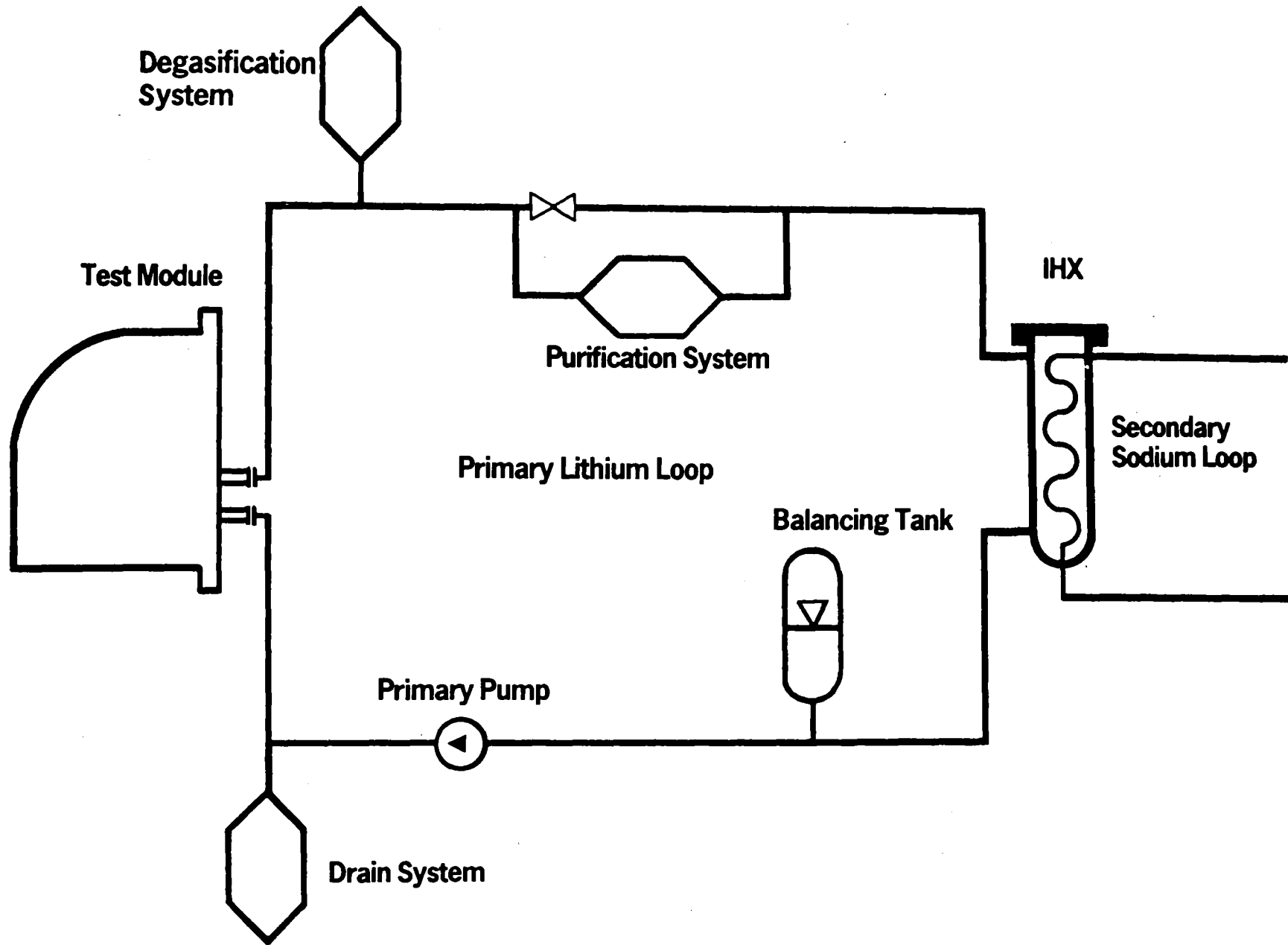
Fig. VII.3-12 TASKA primary coolant loop

The primary coolant pump transports a maximum of 12 kg/s lithium at a pressure difference of approximately 0.2 MPa per test module.

The temperature at the inlet nozzle of the test module amounts to approximately 300 °C at 0.5 MPa pressure.

The drain system is located between the primary coolant pump and the test module. Its capacity must be at least the inventory of one loop (3.5 t). The drain system is required for the exchange of the module and in the case of repairs to the cooling loop.

The components of the cooling system, in particular all the tanks, must be equipped with heating systems to ensure that the lithium temperature in the loop is higher than the melting temperature of 180 °C.

VII.3.2.4 Tritium
VII.3.2.4.1 Tritium Production

The calculation of the tritium production rate is based on the neutronic calculation performed by the KfK / 1 /. A tritium breeding factor of 1.32 was determined for the blanket assembly given in Chapter VII.3.2.2 using natural lithium as breeding material. Li6-enrichment is not necessary.

An estimation for a 90 % Li6-enrichment resulted in a 20 % lower breeding factor.

Fig. VII.3-13 illustrates the radial distribution of the tritium production rate in the blanket. It is evident that approximately 75 % of the tritium is produced in the blanket zone up to r = 90 cm.

Taking a tritium breeding factor of 1.32, one obtains a tritium production rate of 280 g/a at 1.53 MW/m^2 neutron wall loading.

The inventory of breeding material in the test module amounts to approximately 1.4 t. This is approximately 40 % of the lithium inventory stipulated for the cooling loop of one module.

The tritium inventory in the entire cooling loop is limited to 16.6 g as a result of continuous extraction in the purification system.

Table VII.3-5 presents the essential parameters for the production of tritium.

Table VII.3-5: Main Parameters for the Production of Tritium

Breeding material	nat. Lithium (92.5 % Li7; 7.5 % Li6)
Neutron wall loading	1.53 MW/m^2
Tritium breeding factor	1.32
Tritium production rate	280 g/a $= 3 \cdot 10^6 \text{ Ci/a}$
Inventory of breeding material per test module	1.4 t
Tritium inventory in the blanket	6.6 g
Tritium concentration in the breeding material	4.75 ppm
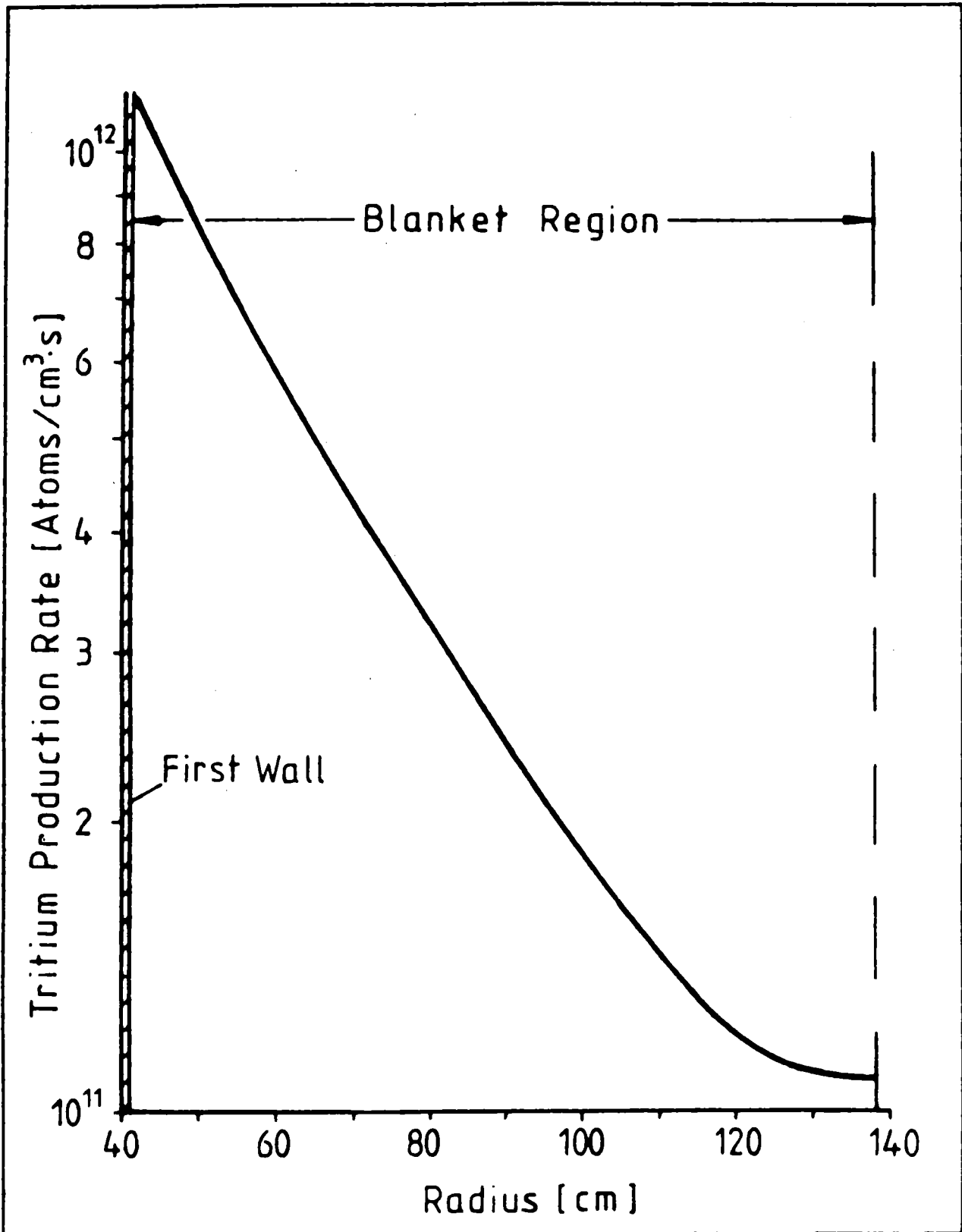
Fig.VII.3-13 Radial breeding rate distribution at 1MW/m^2 neutron wall loading

VII.3.2.4.2 Tritium Extraction

A concept was designed for an extraction process which applies the separation of hydrogen isotopes from sodium loops using cold traps to lithium systems. For sodium this process has already been tested on a large technical scale. The calculations show that such a process is promising. The majority of the tritium produced in the blanket is separated out in the cleaning section of the lithium loop.

It is necessary to interpose a sodium loop between the lithium and water/ steam loop as a tritium barrier.

The following contains a survey of the tritium balance within the heat transport system and an explanation of the extraction method.

As shown in Fig. VII.3-14, the heat transport system consists of a lithium primary loop, a sodium secondary loop and a water/steam loop.

VII.3.2.4.2.1 Tritium Balance in the Lithium Primary Loop

According to Chapter VII.3.2.4.1 the tritium production rate was calculated as being $1.8 \cdot 10^{18}$ T-atoms/s corresponding to about $3 \cdot 10^6$ Ci/a.

The tritium concentration in the lithium is determined by the cold trap operated at 185 °C. According to Fig. VII.3-15, the total solubility S (saturation concentration) of the hydrogen isotopes at this temperature is $3.06 \cdot 10^{-2}$ mol % for hydrogen and $1.12 \cdot 10^{-2}$ mol % for deuterium / 5 /.

An additional external injection of hydrogen, which is higher by a factor of 10 than the tritium production rate, will lead to a tritium concentration of

$$C_T = 4.75 \text{ ppm} = 9.44 \cdot 10^{17} \text{ atoms } T/g_{Li}$$

in the lithium loop. This is due to the simultaneous precipitation of hydrogen and tritium in the cold trap and takes into account the mass dependence of the solubility.

The resulting hydrogen concentration is:

$$C_H = 2.5 \cdot 10^{19} \text{atoms } H/g_{Li} = 42.8 \text{ ppm}$$

The T_2-partial pressure which is decisive for the tritium losses from the lithium loop is given by:

$$\sqrt{P_{T_2}} = \frac{C_T}{K_T}$$

$I_c = 6 Ci/a$

$I_c = 0.3 Ci/a$

TEST MODULE

T-Inventory = 17 g

T-Inventory = $2 \cdot 10^{-4}$ g

IHX

STEAM GENERATOR

$I_p = 1.6 Ci/a$ $\dot{T} = 3 \cdot 10^6 Ci/a$

$I_{HX} = 97 Ci/a$

$I_{SG} = 1.6 Ci/a$

$I_{Decay} = 9 \cdot 10^3 Ci/a$

$I_{Decay} = 0.1 Ci/a$

LITHIUM LOOP

SODIUM LOOP

STEAM/WATER LOOP

$I_{CT} = 3 \cdot 10^6 Ci/a$

$I_{CT} = 95 Ci/a$

COLD TRAP

COLD TRAP

(185 °C)

(115 °C)
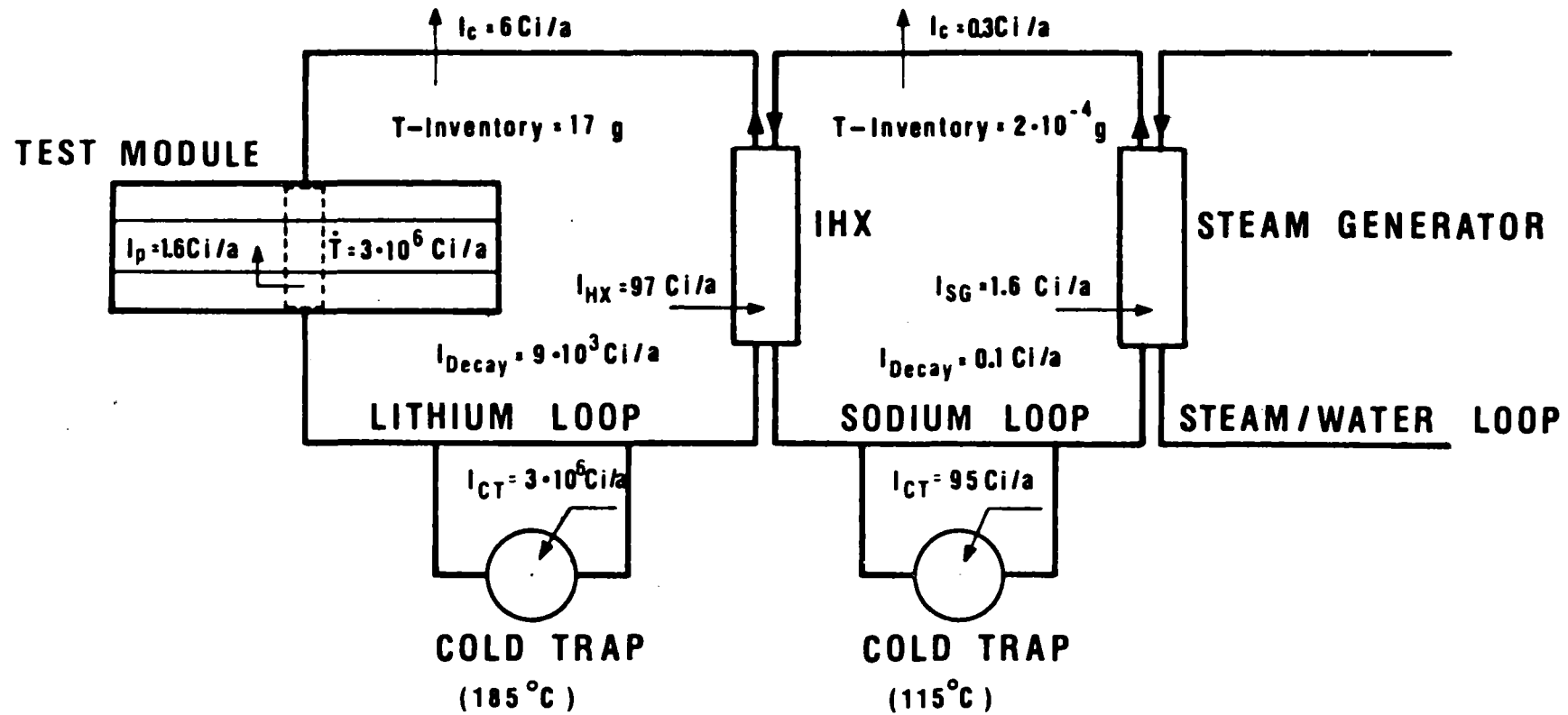
Fig. VII.3-14 Tritium balance of the TASKA heat transport system

(I refers to tritium loss rates)
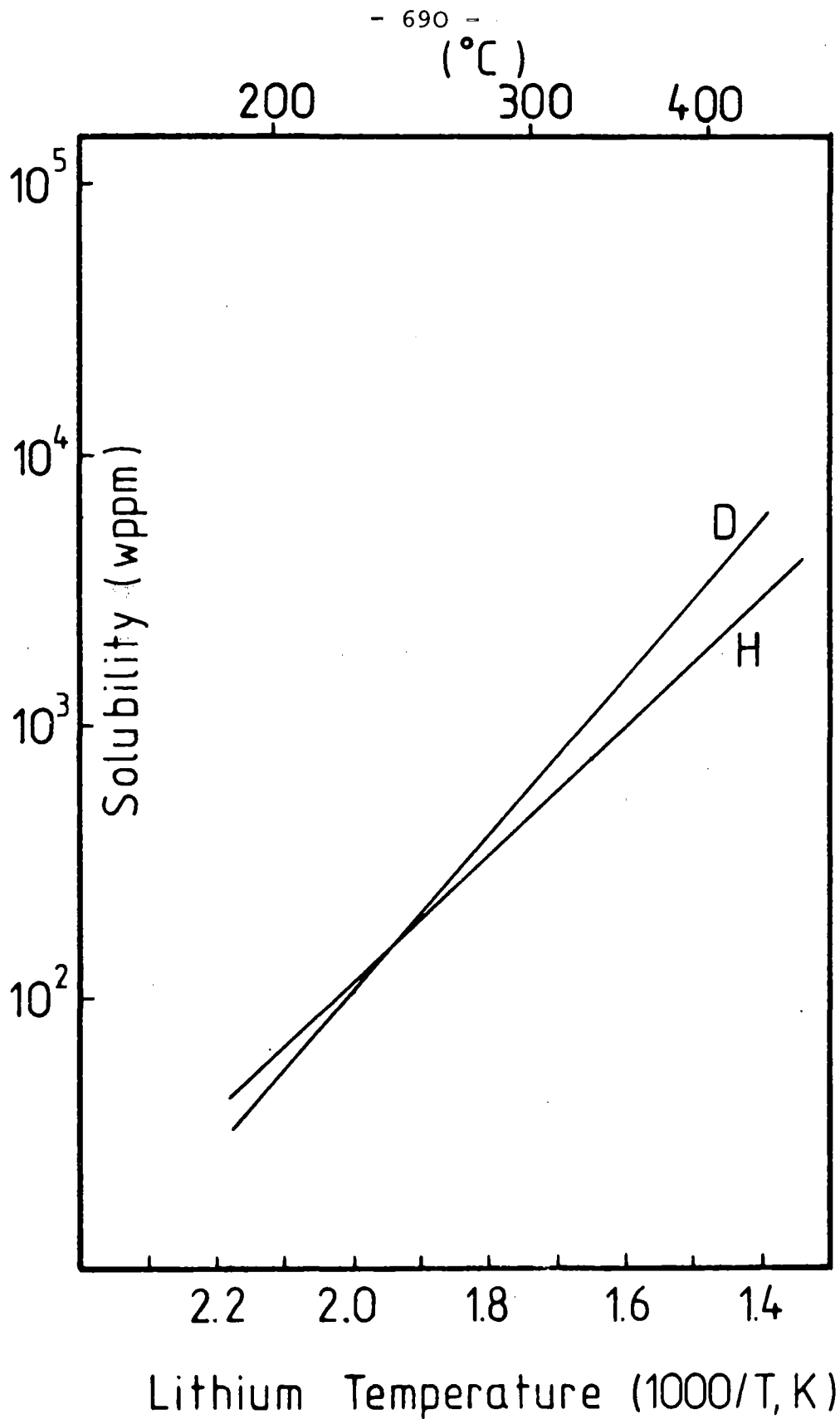
Fig.VII.3-15 Solubtility of Hydrogen Isotopes in Lithium

c_T : tritium concentration, ppm

K_T : Sievert's constant, ppm . $mbar^{-1/2}$*

Assuming an average lithium temperature of $\overline{450}$ °C,

$$K_T = 4.64 . 10^4 \text{ ppm . } mbar^{-1/2} \qquad / 6 /$$

As a result,

$$\sqrt{p_{T_2}} = 1.02 . 10^{-4} \text{ mbar}^{+1/2}$$
$$p_{T_2}^2 = 1.05 . 10^{-8} \text{ mbar}$$

In case of the calculated tritium partial pressure of $1.05 . 10^{-8}$ mbar, the tritium losses via the steam generator (SG) would attain non-permissible high values if the lithium loop were directly coupled to a water/steam loop. At present, approximately 2 Ci/a . MWe may be considered as a recommendation for the tritium discharge in the water/steam loop / 7 /. When transferred to the available reactor concept, the tritium loss rate per test module may amount to approximately 4.6 Ci/a in the water/steam loop. If the lithium loop and the water/steam loop are directly coupled, this value is exceeded by about a factor of 8. For this reason, the interposition of a sodium loop is deemed a suitable means of reducing the tritium discharge rate.

Under equilibrium conditions, the residual tritium inventory m_T in the lithium is:

$$m_T = m_{Li} . c_T$$
$$= 16.6 \text{ g} \cong 1.62 . 10^5 \text{ Ci}$$

The main tritium losses from the primary loop are:

- Tritium losses from the blanket tubes, headers and coolant pipes in the test module
- Tritium permeation into the sodium loop through the intermediate heat exchanger (IHX)
- Tritium losses through the pipe walls of the primary loop
- Tritium losses due to radioactive decay

* 1 mbar = 10^{-4} MPa

The tritium losses due to permeation are calculated according to the equation:

$$I_{i \to j} = \frac{\emptyset \cdot F}{X} \left(\sqrt{p_{T_2}}, i - \sqrt{p_{T_2}}, j \right) \qquad \text{(VII.3-1)}$$

whereby

$\emptyset$	=	permeability of the component material
F	=	permeation area
X	=	wall thickness
p_{T_2}	=	tritium partial pressure in the medium
i	=	discharge medium
j	=	inlet medium

A value of 250 Ci/a was calculated for the tritium losses through the walls of the blanket tubes, headers and main pipes in the test module.

This value is 2.7 times higher than the permeation rate through the intermediate heat exchanger.

This is an unsatisfactory result, as, according to the present state of the concept, the permeation flow through the structure walls of the blanket would not enter the plasma but rather the vacuum space of the casing.

We therefore do not suggest evacuating this space. Instead, it is proposed that a pressure balance between the tritium and the hydrogen in this space and the pressures in the lithium be permitted. After the pressure balance, a T_2-partial pressure of

$$p_{T_2} = 1.05 \cdot 10^{-8} \text{ mbar}$$

would result in the vacuum space.

If one takes the simultaneous hydrogen permeation and recombination to HT into consideration, the resulting tritium inventory present in this vacuum space amounts to 68 μCi (available as T_2 and HT), and is negligible. It is therefore not necessary to pump the tritium out of the vacuum space. At the same time, this means that the tritium can now diffuse into the plasma. The total pressure in the vacuum space amounts to $3 \cdot 10^{-7}$ mbar.

The tritium flow into the plasma via the first wall and the side walls of the casing was estimated as being approximately 1.6 Ci/a. The area of the casing walls relevant for tritium permeation (T > 300 °C) was estimated as being 6 m^2. The tritium losses as a result of permeation from the entire primary loop amount to 105 Ci/a. Including the losses due to radioactive decay, the total tritium losses are 9 . 10^3 Ci/a (Table VII.3-6).

Fig. VII.3-14 presents a survey of the tritium losses from the primary loop.

Table VII.3-6 Tritium Losses in the Primary Loop

Components	$\emptyset$ /T-atoms/s.cm.mbar$^{1/2}$/	I / Ci/a /
Test module		
First wall	$3.98 . 10^{11}$	1.3
Casing wall	$6.1 . 10^{10}$	0.28
Main coolant pipes	$3.98 . 10^{11}$	6.16
Intermediate heat		
exchanger	$3.98 . 10^{11}$	96.8
Radioactive decay	-	$8.9 . 10^3$
Total	-	$9.00 . 10^3$

Table VII.3-7 Tritium Losses in the Secondary Loop

Components	$\emptyset$ /T-atoms/s.cm.mbar$^{1/2}$/	I / Ci/a /
Steam generator	$2.4 . 10^{11}$	1.6
Main coolant pipes	$2.4 . 10^{11}$	0.3
Radioactive decay	-	0.1
Total		2.0

The quantity of tritium to be separated in the cold trap of the lithium loop results from the difference between the tritium production rate $\dot{T}$ and the tritium loss rate and amounts to 99.7 % of the tritium production rate or 280 g/a. Whether this separation rate can be achieved still has to be clarified experimentally. At present, we are not aware of any criteria which would negate this, especially as it is possible to connect more than one cold trap in series.

VII.3.2.4.2.2 Tritium Balance in the Sodium Intermediate Loop

As a result of comparisons of the primary and secondary coolant masses in sodium cooled reactors, one can assume that a sodium mass of

$$m_{Na} = 3 . 10^6 \ g$$

will be necessary for this concept. In this order of magnitude, this value can be considered relevant. On the whole, however, this is not a critical parameter for the tritium balance.

At an average sodium temperature of 420 °C, the Sievert's constant for tritium is:

$$K_T = 9.627 \ ppm . mbar^{-1/2} \qquad / \ 8 \ /$$

Due to corrosion of the steam generator (SG) on the water side, a hydrogen flow enters the sodium loop from this side. As a result of comparison with the conditions in sodium-cooled reactors, one can assume that, in the case under question, the ratio of the flows of hydrogen (via SG) to tritium (via IHX) entering the sodium loop is about $10^3/1$, whereby this can be considered a conservative assumption.

The cold trap in sodium is operated at 115 °C. According to Fig. VII.3-16, the total solubility of the hydrogen isotopes at this temperature is:

$$S = 2.357 . 10^{-2} \ ppm \qquad / \ 9 \ /$$

The following tritium and hydrogen concentrations result from this:

$$C_T = 7.03 \cdot 10^{-5} \text{ ppm} = 1.397 \cdot 10^{13} \text{ atoms } T/g_{Na}$$

$$C_H = 2.35 \cdot 10^{-2} \text{ ppm} = 1.397 \cdot 10^{16} \text{ atoms } H/g_{Na}$$

The tritium partial pressure is therefore:

$$\sqrt{p_{T_2}} = 7.302 \cdot 10^{-6} \text{ mbar}^{1/2}$$

$$p_{T_2} = 5.33 \cdot 10^{-11} \text{ mbar}$$

The residual tritium inventory in the sodium is:

$$
\begin{aligned}
m_T &= m_{Na} \cdot C_T \\
&= 3 \cdot 10^6 \cdot 7.03 \cdot 10^{-11} \text{ g} \\
&= 2.11 \cdot 10^{-4} \text{g} = 2.02 \text{ Ci}
\end{aligned}
$$

and is therefore negligible in contrast to the tritium inventory in the lithium primary loop.

When calculating the tritium losses from the secondary loop, no attention is paid to oxide barriers on the water side of the steam generator. Firstly, it is well known that the tritium barrier effect produced by oxidation on the secondary side is not very large and, secondly, such a barrier effect cannot be guaranteed for all operating conditions of the reactor.

The tritium losses from the indermediate loop result from the tritium concentration in sodium determined by the cold trap.

As in the outer lithium loop, all components are manufactured in austenitic steel.

The tritium losses from the sodium secondary loop comprise the following:
- Permeation losses via the steam generator
- Permeation losses from the pipes
- Losses due to radioactive decay
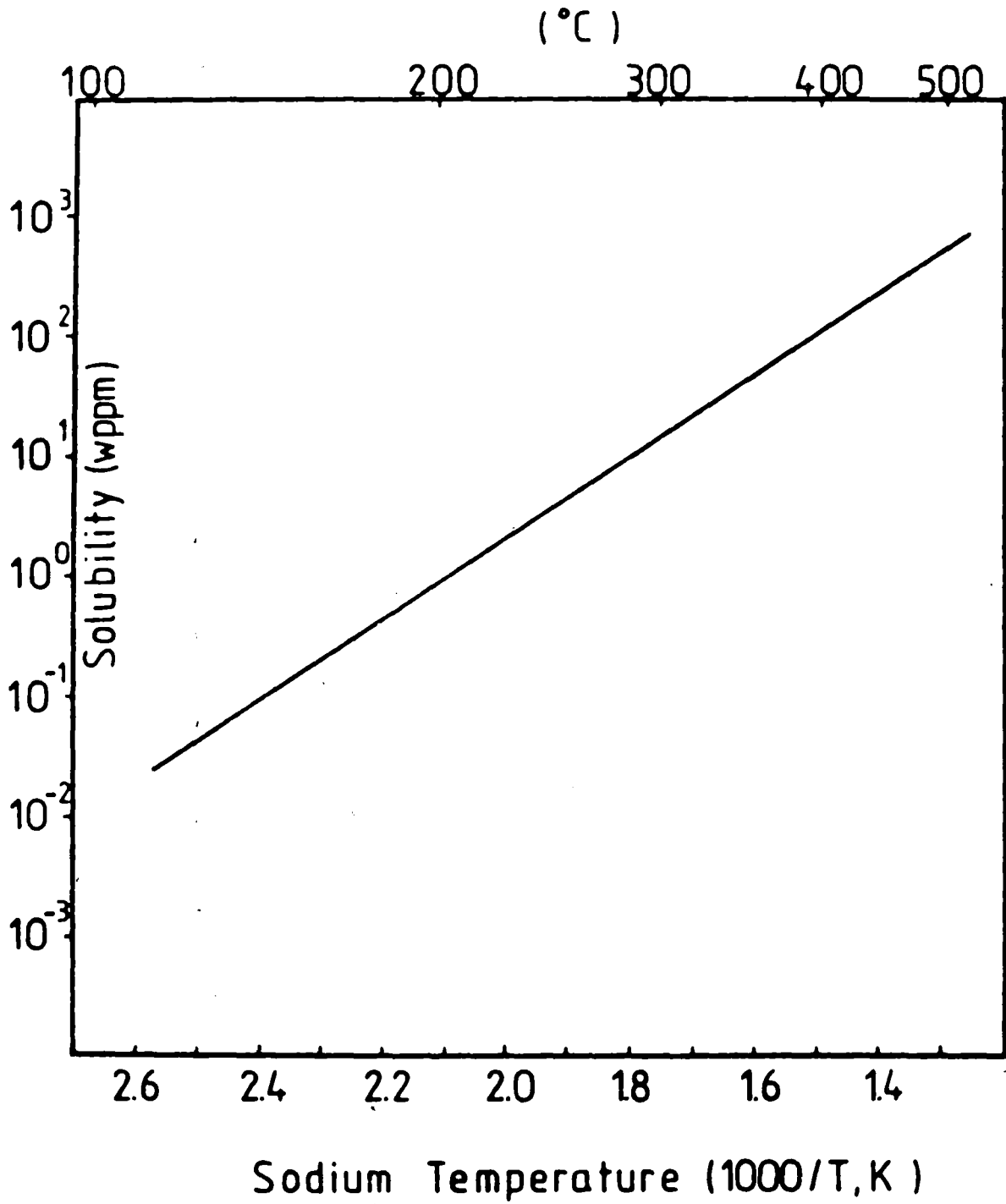
Fig.VII.3-16 Solubtility of Hydrogen Isotopes in Sodium

The loss rates listed in Table VII.3-7 were calculated in accordance with the calculation method given in equation VII.3-1. The total tritium losses from the secondary loop amount to approximately 2 Ci/a.

The tritium overflow rate of 1.6 Ci/a into the water/steam loop is an acceptable value for a fusion reactor.

Fig. VII.3-14 contains a survey of the tritium losses from the secondary loop.

The tritium separation rate in the cold trap of the sodium loop results from the difference between the tritium flow via the intermediate heat exchanger, and the tritium losses, and is:

$$6.25 \cdot 10^{13} \text{ atoms T/s} = 94.8 \text{ Ci/a}$$

This is approximately 98 % of the tritium flow entering the intermediate loop.

VII.3.2.4.2.3 Tritium Recovery from Cold Traps

The tritium recovery from the cold traps of the primary and secondary loop is effected after the dismantling of the cold traps. In principle, it is possible to reprocess the cold trap and therefore to extract the tritium gained before the maximum capacity of the cold trap has been attained, thus obtaining a quasi-continuous tritium extraction. For this reason, only the quantity of tritium necessary for reactor operation until the next extraction interval should be stored.

As the extraction intervals for TASKA have not been established to date, it is assumed that the tritium will be recovered after the maximum capacity of the cold trap has been attained.

Primarily the capacity of cold traps is determined by the hydrogen source strengths. Operating experience gained with sodium systems shows that the capacity of cold traps for hydrogen amounts to about 10-20 % of the active volume. If one assumes that the capacity of cold traps in lithium is determined by the same effects as in sodium, a comparison with a sodium cold trap having a volume of 1 m^3 leads to the assumption that the capacity of a lithium cold trap with the same volume corresponds to a separated hydrogen mass of about 2 kg.

Taking the primary tritium and hydrogen source strengths

$$S_T = 1.8 \cdot 10^{18} \text{ atoms/s}$$

$$S_H = 1.8 \cdot 10^{19} \text{ atoms/s}$$

the cold trap in the lithium loop has a service life of about 590 full load days $\cong$ 1.5 FPY. The tritium activity separated in this period is $4.5 \cdot 10^6$ Ci.

Due to the lower source strengths of the hydrogen isotopes in the secondary system, the service life of the sodium cold trap is greater than the service life of the reactor itself. The tritium activity to be regenerated amounts to $2 \cdot 10^3$ Ci for a service life of approximately 20 full load years. At this point in time, only a small proportion of the capacity of the cold trap is exhausted.

These considerations presuppose normal operating conditions. Disturbances of normal operation, which are linked with an increase in the hydrogen inlet rate, shorten the service life of the cold traps.

With reference to the lithium cold trap, greater requirements are made on the regeneration system than in case of the secondary cold trap. At present, no experimental experience is available on the regeneration of lithium cold traps, but one can assume that the same processes are suitable for these as for sodium cold traps.

The cleaning of sodium cold traps has been tested on a large technical scale. There are two ways of extracting the hydrogen isotopes from the coolant. This is either effected by continually evacuating the gas space above the coolant or by blowing argon scrubber gas over the surface. In both methods, the hydrogen partial pressure above the coolant is greatly decreased, and, as a result, metal hydride precipitated in the cold trap continuously dissolves and becomes gaseous. The kinetics of this process have been investigated in detail for sodium / 10, 11 /.

The efficiency of both processes increases greatly with increasing temperature. The vacuum extraction is more efficient than the scrubber gas extraction. The efficiency is increased if turbulences are generated in the coolant.

In the lithium systems, the gas discharge to be attained is lower by several orders of magnitude than in sodium at the same temperature due to the lower equilibrium pressure of the hydrogen isotopes. In order to obtain comparable extraction efficiencies, higher lithium temperatures and larger free surfaces are required. By extrapolating the data from / 10, 11 /, it is to be expected that, when these are transferred to lithium, bearing in mind the lower steam pressure, it will be possible to regenerate the lithium cold trap with a hydrogen extraction rate of about 30 cm^3 (STP)/s. (This value is based on a lithium temperature of 650 °C and a 1 m^2 free surface in the cold trap).

The resulting regeneration time amounts to approximately 400 h.

Depending on the inventory, it is possible to regenerate the sodium cold trap in a shorter time.

The gas which occurs during the regeneration of the cold traps consists of tritium and hydrogen. In order to close the fuel cycle, it is necessary to separate these two isotopes. The most promising separation method is considered to be a permeation process in the gaseous phase, in which the mass-dependent diffusion after the diffusion step causes an enrichment of the hydrogen in relation to tritium. In order to attain sufficiently high separation factors, it is necessary to apply a cascade separation with several subsequent permeation steps. The strength of the occuring gas flows necessitates the use of materials with high permeability and working temperatures around 500 °C. For example, niobium with a permeability of 9.78 . 10^{-5} cm^3 (STP) /cm.s.mbar$^{1/2}$ is suitable for hydrogen at 500 °C. In order to achieve the permeation of a gas flow of 30 cm^3/s (gas production when regenerating the lithium cold trap) the surface area of a 2 mm thick permeation diaphragm must amount to approximately 1900 cm^2.

VII.3.2.4.2.4 Tritium Storage

The tritium recovered from the cold traps of the primary loop and, if necessary despite the low inventory, of the secondary loop must be stored externally. In principle there are two methods of doing this. One method is to directly confine the gaseous tritium in a steel tank. The other method is to bind the tritium to hydride forming metals, e. g. titanium sponge.

If one assumes one regeneration process of the cold traps per operating year, 52 mol tritium from the lithium loop must be stored externally.

In the interest of safety, the storage of tritium in a steel tank should be effected at slight underpressure. At 0.1 bar underpressure in the tank this must have a volume of 1.4 m^3 for storage at room temperature. Due to the high activity inventory in this tank (3 . 10^6 Ci), however, the second form of storage is more advantageous in the interests of safety, as any leakages in the tank are not directly connected with serious radiological consequences due to the considerably lower tritium pressure above the titanium sponge.

The partial pressure of the tritium above the getter material is $< 10^{-3}$ mbar, if the getter material is cooled down to room temperature after being loaded with tritium at 300 °C.

10 kg titanium are required to store the tritium at titanium sponge.

VII.3.2.4.3 Safety Considerations

The use and handling of tritium require special safety measures, as it has a very good diffusivity and permeates through steel at high temperatures. This applies to the lithium primary loop in particular, as a constant tritium level has already formed in the entire loop after a short time.

The components of the primary loop must have as good integrity as possible for the tritium containment. Connections should be welded and tested using helium leak tests.

In order to improve the tritium containment, the application of double-walled pipes and permeation inhibiting pipe coatings could be investigated. However, double-walled pipes are only prudent at high tritium discharge rates, as the high manufacturing costs for the pipes and the extra costs for scrubber systems could make up a large part of the construction costs.

Similarly, the use of permeation-inhibiting coatings is only of slight importance, as only complete coating of the loops leads to verifiable tritium retention. It is, however, impossible to guarantee complete coating at the junction points for example, or because of cracks in the coating as a result of different thermal loadings.

Furthermore, it is impossible to prevent tritium contamination of the room atmosphere, as, for example, tritium diffuses through the flange sealings of the module or permeates through the walls of the coolant pipes.

More important, however, are the losses from the reactor fuel supply system
and the plasma heating system which also contribute to room contamination. In
order to keep the tritium discharge to the environment as low as possible,
those parts of the plant transporting tritium must be enclosed in a second con-
tainment. This second containment is formed by the rooms of the plant, which
are hermetically sealed off and for which the following measures must be pro-
vided:

- Monitoring of the room atmosphere with detectors
- Scrubbing the gas inventory of the rooms
- Build-up of an underpressure in tritium
  contaminated rooms
- Sealing the walls of the containment to impede
  tritium diffusion

The rooms must be supplied with locks for the transportation of compo-
nents.

As the handling processes are essentially determined by the activation
of the components and, for the most part, are remotely controlled, no further
essential measures are necessary with regard to the external radiation exposure
due to tritium. If contaminated rooms are entered for service or repair work,
respiratory equipment should be worn, or if manipulator cabins are used, these
should be equipped with a separate ventilation system in order to prevent a
non-permissible high radiation exposure of the personnel due to the incor-
poration of tritium. Nevertheless, all free volumes of dismantled components
should be checked for a possible tritium contamination before being removed
from the containment.

VII.3.2.5 Cost Estimates

With reference to the costs which are up to completion   of a test module for:

- planning
- manufacturing design
- manufacturing plus test and TÜV acceptance costs
- material costs,

only those costs for the supply of material can be realistically estimated.

The material costs listed in Table VII.3-8 were determined on the basis of 1981 prices. Based on a test module with liquid metal blanket, they amount to a total of approximately 700 TDM, excluding the material costs for the shield. These material costs essentially depend on the specification of the B_4C layer. The costs for B_4C can be estimated as amounting to approx. 150 DM/kg according to Chapter XI.

Table VII.3-8: Estimated Material Costs for a Test Module
             with Liquid Metal Blanket (basis 1981)

Component	Quantity	Material	Unit Value	Total Costs TDM
Blanket tubes	320 m	1.4970	170 DM/m	55
Nozzles and headers	approx. 0.5 t	1.4970	25 DM/kg	12
Cooling lines				
Casing	approx. 8 t	1.4970	30 DM/kg	240
Reflector	approx. 12 t	1.4970	30 DM/kg	360
Shield	approx. 20 t	1.4970	30 DM/kg	
		Pb	~ 5 DM/kg	
		B_4C	150 DM/kg	
Total (without shield)				667

At this point in the investigation, it is only possible to make tendentious estimates regarding the anticipated planning costs and the manufacturing documents which have to be prepared up to construction maturity.

The cost expenditure can be considerably reduced if it is possible to make use of already available knowledge, as, in this case, the sodium technology.

At present, however, this new technology is accompanied by problem points caused by the difficulties of the lithium technology, which cannot be summarized as yet, the compatibility of liquid lithium with the austenitic steel 1.4970 planned as structural material and the suitability of this material as structural material at high neutron fluxes and high temperature due to the unfavourable fatigue behaviour. If one considers the experience gained in the sodium technology with reference to the costs for the planning of comparable components, for example heat exchangers, the costs for planning and manufacturing design will probably be in the order of magnitude of the material costs estimated here.

At this point in the concept, it is very difficult to estimate the manufacturing costs without the costs for licensing and TÜV acceptance. After a first estimate, however, these should be approximately twice the material costs. Further detailling of the concept would be necessary for more exact cost data.

Table VII.3-9 shows an overview of the cost-estimates for one test module.

Table VII.3-9 Survey of the Costs for a Test Module (basis 1981)

Planning	approx.	200 TDM
Manufacturing design	approx.	800 TDM
Manufacturing without test and TÜV costs	approx.	2000 TDM
Material costs	approx.	700 TDM

(excluding shield)

Total	approx.	4000 TDM

VII.3.2.6 Operating and Other Peripherical Systems

VII.3.2.6.1 Operating Systems

A large number of auxiliary systems, instrumentation and control systems as well as measuring systems are required to ensure authorized operation of the test module. The survey compiled here essentially includes those systems in the primary loop mainly necessary for normal operation. It does not take into account any protective systems which may be additionally requested during the necessary licensing procedure or those which are additionally required for accident control. In addition to the main cooling and tritium systems already described in the preceding Chapters VII.3.2.3 and VII.3.2.4, the following auxiliary and secondary systems are also necessary for normal operation.

VII.2.6.1.1 Cooling Systems

A   Cooling loop for the reflector and shield plug

Task

Heat removal from the reflector and shield structures by means of water cooling.

Requirements

- Provision of the necessary quantity of coolant with the values specified for pressure and temperature
- Installation of devices to monitor the tritium contamination and the contamination with activated corrosion products

B   Emergency cooling systems

Task

Heat removal mainly from activated structures after failure of the main cooling systems

Requirements

- Design for the removal of decay heat even after accidents such as explosions or earthquakes
- Redundancy and diversity of the systems
- Energy supply ensured even in the case of an accident

VII.3.2.6.1.2 Evacuation Systems

A   Evacuation system for the flange sealings

Task

Evacuation of the space in the double sealing to prevent leakages into the plasma volume and the casing.

Requirements

- Provisions of the pumping capacity required for evacuation
- Provisions for monitoring of leakages and tritium contamination

B   Evacuation system for the module casing

Task

- Evacuation of the volume of the casing to approximately 10^{-3} Pa
- Injection of hydrogen to lower tritium permeation from the blanket into the casing

Requirements

- Provision of the pumping capacity required for evacuation
- Connection to a hydrogen supply system
- Monitoring of the tritium inventory in the casing possible
- Integration of a tritium cleaning system or connection to the fuel cycle cleaning system

VII.3.2.6.1.3 Cover Gas Systems

A   Cover gas system

Task

- Guarantee of a cover gas atmosphere above free surfaces in components carrying lithium e.g. Li-pumps, Li-tanks
- Build-up and control of the system pressure in the tanks
- Loading of sealing gas and pressure gas at seals
- Supply of the handling stations

Requirements

- Provision of the necessary quantity of cover gas even under accident conditions
- Monitoring of the tritium inventory in the cover gas possible
- Installation of a tritium and lithium aerosol cleaning loop

B   Inerting System

Task

Inerting and cooling of certain main and secondary facilities such as buildings or handling systems, if this is required by precise safety requirements or specifications from the regulatory commissions.

Requirements

-    Installation of gas loops to scrub and reinert containment cells
-    Installation of cooling loops to control the temperature in the rooms and to cool the gas inventories of certain handling components

VII.3.2.6.1.4 Component Heating Systems

Task

Maintenance of a given lithium temperature > 180 °C in components such as leak pans, cleaning pipes etc.

Requirements

-    Separate gas heating (e.g. He) to heat components such as blanket, headers, intermediate heat exchanger before filling with lithium
-    Electrical heating of the components (trace heating)
-    Connection to emergency power supply

VII.3.2.6.2 Measuring and Control Systems

VII.3.2.6.2.1 Measuring Systems of the Test Module (Survey)

-    Neutron flux
     Radial and axial distribution of sensors which in conjunction with a slide-in technique could be replaced without dismantling the entire test module.
-    Temperature
     Measurement of the temperatures of:
     - Blanket structure
     - First wall
     - Reflector and shield
     - Casing walls
     - Coolants
     - Breeding material
     The sensors must exhibit good radiation resistence due to the high-energy neutron flux.

- Monitoring of lithium leakage inside the test modules in connection with the evacuation system of the casing.
- Mass flow

  Measurement of the mass flow quantity of breeding material and coolant. Due to the magnetic field of the fusion plant, it is difficult to apply inductive measuring techniques. Only hydraulic measuring methods can be used.
- Magnetic field

  Measurement of the magnetic field in axial and radial distribution by means of inductive measuring methods.

VII.3.2.6.2.2 Measuring Systems Primary Loop

- Pressure

  Measurement of the coolant pressure using diaphragm, pressure and differential pressure measuring techniques
- Mass flow

  Measurement of the lithium mass flow using hydraulic flow meters, or permanent magnetic flow meters at a sufficient distance from the magnetic field of the plant
- Temperature

  Measurement of the coolant temperature by means of sensors
- Impurities

  Determination of the impurity level of the lithium in the cleaning circuit using plugging meters
- Leakage

  Determination of leakages from pipes and components by means of
  - electrical short circuit technique
  - photo diodes
  - measurement of the radiation level

VII.3.2.6.2.3 Control Systems

- Temperature

  Control of the coolant outlet temperature of the test module within the range 400 - 500 °C by controlling the pumping capacity

- Afterheat

    The structural temperature is limited by control of the mass flow within the emergency cooling system in the case of failure of the main cooling system.

VII.3.2.6.3 Handling Systems

The requirements for the handling systems of the test modules are essentially determined by the type of activities to be performed, the radiation level in the working area and the room conditions.

All activities must be performed using remote handling due to the high radiation level mainly resulting from the activated structures and considering the tritium contamination.

With reference to the test modules, the main activities to be performed with the handling facilities are:

- Insertion and withdrawal of the test modules
- Unscrewing of screwed connections
- Disconnecting and connecting of the supply lines of the modules
- Insertion and dismantling of the reflector and shield plug
- Transport of the modules
- Visual inspection of the module casing and blanket area after removal of the reflector and shield plug
- Cutting and welding of the pipes in the blanket area

These activities can either be performed using remotely controlled manipulator facilities equipped with television cameras, or using manipulators attached to shielded cabins.

In general, the handling methods should be based on the following provisions:

- All handling processes are carried out after the reactor has been shut down
- Free lithium surfaces are covered with a protective gas atmosphere, e.g. argon, in order to prevent the lithium reacting with the air in the room
- If cooling of the components to be handled is necessary, this is carried out by forced circulation of the cover gas or by means of heat conduction and thermal radiation.

VII.3.2.6.4 Buildings and Infrastructure

The requirements for the buildings are essentially determined by the distribution of the facilities and components to the rooms. Fundamentally, the requirements of the valid safety regulations and, in the case of operation as a nuclear plant in the Federal Republic of Germany according to § 7 AtG or as a plant according to § 11 AtG, those of the Radiation Protection Regulation must be fulfilled. The following comments therefore only provide an overall view and do not include any additional requirements compiled by the licensing and surveillance authorities.

For example, the following requirements for buildings can generally be taken into consideration:

- Sealing of rooms containing activity to prevent penetration or leakage of water
- Gas-proof penetrations of pipes and cables
- Decontaminable paintwork in rooms containing activity
- Ventilation facilities designed to remove large quantities of heat (accident)
- Installation of fire-protection facilities, in particular in rooms containing lithium and sodium
- Separation of rooms into rooms possibly containing activity and rooms with conventional plant components

Rooms containing activity can be grouped together into one control area. This comprises for example:

- Reactor hall
- Plant rooms of the primary loop
- Plant rooms of the tritium system
- Rooms for the repair of activated components

Furthermore, it should be planned to separate rooms containing facilities with lithium or sodium from those containing water-bearing facilities.

The reactor hall is subjected to special safety requirements.

The walls of the hall (radiation protection walls) must limit the radiation level outside the hall to the value permitted for that area (for example, operational surveillance area 500 mrem/a).

Tritium contamination of the atmosphere of the hall is to be expected. This requires gas-proof enclosure of the volume of the hall (containment). Accesses to adjoining rooms must be provided with locks. The atmospheric pressure in the hall should be lower than the ambient pressure to prevent a gas flow to the outside. The atmosphere of the reactor hall must be monitored for a non-permissible high tritium level, and the gas volume must be regularly scrubbed.

The ventilation facilities must be designed to remove any possible activity leakages by suction.

The infrastructure refers to the site of the plant and its supply with connections required for operation. Based on the operating concept of the plant as a test facility, the following supply connections must generally be available

- Access to the road network or to an equivalent waterway via a well-constructed communication road for the delivery of large components weighing several tons
- Cooling, domestic and waste water
- Mains electric connection for the energy supply to operate the plant and for the general supply
- Connections to communication systems (telephone, telex)
- Possibilities for the removal and final storage of waste material (radioactive and conventional)
- Facilities for monitoring radioactive emissions (meteorological stations, activity measurements in the settling tank etc.)

VII.3.2.7 Problems Regarding Development and Technology

The considerations of the problems arising in the development and technology of tritium breeding blankets with liquid lithium as breeding material and coolant may be divided into general points, which are valid for all liquid metal blankets and specific problems concerning the blanket concept applied here.

VII.3.2.7.1 General

The general problem points include the reliability of the cross section data which are at present available for natural lithium for the calculation of the tritium breeding rate, the compatibility of lithium with austenitic steel (corrosion rate, mass transport) on a large technical scale and the improvement of austenitic steel for use in fusion plants.

When calculating the tritium breeding ratio for fusion facilities, which use natural lithium as breeding material, a deviation of 20 to 30 % was assumed for one-dimensional calculations of the tritium breeding ratio, and, as a result, a breeding factor of 1.2 to 1.3 was sufficient to obtain a facility breeding factor of 1.

With reference to the Li7 cross sections, which made up approximately 30 % of the total breeding factor in the TASKA calculations, newer estimations / 12 / resulted in values in the relevant energy range which were approximately 26 % lower than the ENDF/B data used to date. As a result of the neutron multiplication effect of the Li7 (n, n'$\propto$) T-reaction, this does not only influence the Li7 contribution to the breeding factor but also the tritium ratio from Li6.

At present, the compatibility of lithium with austenitic steel is only being examined in small loops on bench scale. In addition to lithium corrosion, the experimental programme also includes mass transport and the effect of impurities in lithium.

It is only fundamentally possible to transfer the experimental results to the requirements and effects in plants with larger dimensions, higher temperatures and, above all, using materials under neutron irradiation. Detailled investigations of this point are therefore necessary and should be performed before a reactor-relevant blanket concept is determined in test facilities.

The same is valid for the application of austenitic steel in fusion reactors. Taking the special lithium characteristics into consideration, it is possible to make use of the experiences gained from the liquid metal technology in breeder reactors when selecting the material for loop components. In addition to the problems found in the liquid lithium technology, problems caused by radiation damages (swelling, He-production) also arise in areas with high neutron fluxes. These have a considerable effect on the operating behaviour (temperatures approximately 450 °C, low plant efficiency), and therefore call for the improvement of austenitic steels by means of suitable manufacturing processes and compositions or the development of new materials, whereby the time required to develop new materials up to production on a large technical scale (approximately 30 years) must be taken into consideration.

VII.3.2.7.2 Special Problems Concerning the Blanket Concept
        and Tritium Extraction

The special problems of the blanket concept refer to:

-    The cooling of the first wall and the side walls of the casing
-    The welds of the blanket tube nozzles
-    The welding design of the casing
-    The coolant distribution on the blanket tubes

Concept proposals for the cooling of the first wall and the side walls of the module casing were presented in Chapter VII.3.2.2.

As regards the cooling system of the first wall, the problems are not so much to be found in the choice of coolant - in addition to lithium, it is also possible to use helium - as in the temperature gradient between the inner side of the first wall and the cooling tubes, which is due to the power production in the first wall. For this reason, it is necessary to optimize the first wall in a further concept step with reference to the wall thickness necessary for the stability and the lowest possible power production. Due to the radial temperature gradient in the first wall, the temperature differences between the cooling tubes and the first wall, and the resulting diverse expansion, welding of the cooling tubes to the first wall, which could achieve better heat transmission should, nonetheless, be rejected.

The pressing of the cooling tubes on to the first wall calls for the examination of suitable materials, in order to improve the heat conductivity between cooling tubes and the first wall with the available contact pressure.

The cooling system of the side walls calls for further examinations of the power production in the structure and the heat transport out of the first wall area, as well as the stress-free welding of the guiding dents to the wall structure.

The welding design of the casing and blanket areas should be detailled within the framework of further consideration of the concept.

This includes the welding of the nozzles between blanket tubes and the headers, in particular with reference to remotely-controlled maintenance and repair in the blanket area at a later date, as well as the design and production of the shielding edges of the casing for vacuum tight welding and stable reinforcement of the casing structure.

Another problem point requiring further consideration is the coolant distribution in the blanket tubes, taking into consideration the radial gradient in the power production of the blanket. Due to the low hydraulic pressure loss in the blanket tubes, the sole use of restrictors and similar throttle devices would not be able to attain the required mass flow distribution, in particular because of the influence exerted by the magnetic field on the coolant flow. Examinations using flow models are therefore considered necessary.

Some important problem points regarding the extraction and storage of tritium have already been dealt with in Chapter VII.3.2.4. To summarize, one can say that the extraction concept for tritium using cold traps is theoretically very promising, and that lithium purification by means of cold trap operation is being investigated / 13 /. It is, however, necessary to carry out further extensive experimental investigations, in particular with reference to the separating effect of the cold trap before this concept is used on a large technical scale.

References

1. L. Buth, private communication

2. A.Suppan, W. Köhler, KfK
   TASKA-Overall Machine Design
   TASKA Review Meeting, Madison, Wisconsin, 2./3. Nov. 1981

3. TASKA List of Parameters, dated 6/15/71

4. Smith, D.L. et al:
   Fusion Reactor Blanket/Shield Design Study
   ANL/FPP-79-1, July 1979

5. Pulham R.J. et al:
   Reaction Rates and Electrical Resistivities of the Hydrogen Isotopes with,
   and their Solubilities in Liquid Lithium
   CONF 750 989, 1975

6. Smith F.J. et al:
   The Solubility of Hydrogen Isotopes in Lithium
   Proc. 9th Symp. on Fusion Techn. 1976, p. 325 ff

7. Länderarbeitsgemeinschaft Wasser (LAWA):
   Richtlinien für das Einleiten radioaktiver Stoffe
   aus kerntechnischen Anlagen in die Gewässer
   Dezember 1973

8. Skladzien S.B. et al:
   Tritium Meters for Use in LMFBR Sodium Coolant
   ANL-78-30, 1978

9. A.C. Whittingham:
   An Equilibrium and Kinetic Study of the Liquid Sodium-
   Hydrogen Reaction and its Relevance to Sodium-Water
   Leak Detection in LMFBR Systems
   Journ. Nucl. Mat. 60 (1976), 119-131

10. J.R. Gwyther, A.C. Whittingham:
    The Kinetics of Hydrogen Removal from Liquid Sodium;
    C. E. G. B. Berkeley Nuclear Laboratories, Berkeley,
    Glos GL 13 9 PB

11. J.R. Gwyther et al:
    Developments in Plugging Meters and Cold Traps for LMFBRs
    CONF 800 401-P2, (1980), 16-47

12. Swinhoe, M. T and Uttley, C.A.:
    Tritium Breeding in Fusion
    Proc. Int. Conf. on Nuclear Cross Sections
    for Technology 1979

13. Down, M.G., private communication

14. Maroni, V.A. et al:
    A Review of the Chemical, Physical and Thermal
    Properties of Lithium that are Related to its Use
    in Fusion Reactors
    ANL-8001, 1973

Appendix

TASKA Test Module

Parameter list for the liquid lithium blanket

Table I

I   Casing

     1.   Geometric data:

Length (incl. reflector and shield plug)		3730 mm
Width	max.	1160 mm
	min.	910 mm
Graduations		50 mm
First wall diameter		800 mm
First wall length		1010 mm
First wall area		2.54 m^2
Width of coating and clearance resp.		1800 mm
Wall thicknesses:		
First wall	approx.	10 mm
Casing wall		20 mm
Base plate		40 mm

     2.   Flange construction

Height		3250 mm
Width		1520 mm
Depth		300 mm
Flange width	horizontal	180 mm
	vertical	200 mm
Design	Double O-ring seal with interspace evacuation	
Sealing material	Viton or Inconel vapour deposited with silver	

     3.   Pressure conditions

Casing inner pressure	approx. 10^{-3} Pa
Max. loading of the casing wall	0.1 MPa

4. Material   Austenitic steel 1.4970
                             (X10 Cr Ni Mo Ti B 15 15)

5. Weight of the casing   approx. 8 t

II   Blanket

1. Composition
    Structural material: Austenitic steel 1.4970
                             (X10 Cr Ni Mo Ti B 15 15)
    Coolant   Liquid lithium
    Breeding material   Natural lithium (92.5 % Li7,
                                              7.5 % Li6)
    Blanket composition   73 % Li_{nat}
                                              7 % steel
                                             20 % void

2. Dimensions
    Length   r = 48 cm   920 mm
                             r = 138 cm   820 mm
    Thickness   960 mm
    First wall radius   400 mm
    First wall area   2.54 m^2

3. Design
    General   rows of tubes arranged round
                             the first wall cylinder
    Number of blanket tubes   74
    Dimensions of the blanket tubes
    Outer diameter   101.6 mm
    Wall thickness   2.6 mm
    Length   min.   3300 mm
                                   max.   5500 mm
    Total length of the blanket tubes   320 m
    Tube material   Austenitic steel 1.4970
                             (X10 Cr Ni Mo Ti B 15 15)
    Rupture strength of 1.4970 for
    t = 20.000 h, T_{max} = 550 °C   110 N/mm^2
    Weight of the blanket tubes   6.4 kg/m

4. Power balance

Fusion power   86 MW

Neutron wall loading   1.53 MW/m^2

First wall heat loading   0.8 W/cm^2

Blanket energy multiplication (1-D)   1.02

Power production of the first wall   0.3 MW

Blanket power   3.2 MW

Blanket volume   3.6 m^3

Max. power density in the blanket   3 W/cm^3

Energy output per 14.1 MeV-neutron
Blanket:

Neutrons   11.47 MeV

Gammas   2.84 MeV

Total   14.3 MeV

5. Cooling

Coolant temperature

                inlet   300 °C

                outlet   450 °C

                            (max. 500 °C)

Coolant velocity

Inlet pipe   max. 2 m/s

Blanket tube   approx. 7 cm/s

Pressure loss in the module   approx. 0.1 MPa
(without MHD losses)

Coolant pressure   0.5 MPa

Coolant inventory
per loop   3.5 . 10^6 g

6. Tritium

Breeding material   nat. lithium (92.5 % Li7;

                                   7.5 % Li6)

Mass flow   6.0 kg/s

Temperatures

Lower boundary   300 °C

Upper boundary   500 °C

Average value   450 °C

Breeding material in the blanket $1.4 \cdot 10^6$ g

Breeding factor   1.32

Production rate $1.8 \cdot 10^{18}$ atoms/s

                      = 282 g/a

Tritium concentration in the
lithium   4.75 ppm

Tritium inventory in the primary
loop   approx. 16.6 g

Extraction process   Purification loop with cold
traps at 185 °C

7. Costs (Base 1981)

Material   Austenitic steel 1.4970

   Blanket tubes   approx. 170,-- DM/m

   Header   approx. 25,-- DM/kg

   Primary coolant pipe   approx. 350,-- DM/m

   Casing walls   approx. 30,-- DM/kg

   Reflector material   Austenitic steel 1.4970

                      approx. 30,-- DM/kg

III Reflector

Design   see Chapter VII.3.2.2

Material   Austenitic steel 1.4970

Coolant H_2O

Reflector power   0.12 MW

Average power density   0.12 W/cm^3

Reflector temperature   max. 200 °C

Coolant mass flow   approx. 1 kg/s

Coolant pressure   0.5 MPa

Coolant temperature

             Inlet   approx. 70 °C

             Outlet   approx. 100 °C

Average reflector thickness   350 mm

Weight   approx. 12 t

IV   Shield

Design	see Chapter VII.3.2.2
Material	Austenitic steel 1.4970
	Pb
	B_4C
Coolant	H_2O

Temperatures:

Structure		max.	200 °C
Coolant			
	Inlet	approx.	70 °C
	Outlet	approx.	100 °C
Coolant pressure			0.5 MPa
Weight		approx.	20 t

V   Radiation exposure

1. During operation
   Dose rate at a distance of 1 m

due to neutrons	$4 . 10^3$ rem/h
due to secondary gammas	1 rem/h

2. Dose rate from structure activation of reflector and shield

Operating period	2.5 years
Load factor	0.8

   Dose rate radial

at the surface	11.6 mrem/h
at a distance of 1 m	5.9 mrem/h
Isotopes considered	Co 60
	Ta 182
	Fe 59
Nuclide concentrations	500 ppm Co 59
	500 ppm Ta 181
	3100 ppm Fe 58

3. Radiation damage

First wall	8.61 dpa/a
(at 1 MW/m^2)	

Table II: Material Data of Lithium from Ref. 14

Composition of nat. Lithium	92.5 % Li7; 7.5 % Li6

Melting Point   180.6 °C
Boiling Point   1342 °C

Density / g/cm^3 /
$$\vartheta = 0.515 - 1.01^{-4} \, (t-200)$$
(t / °C / = temperature)

Heat Capacity / J/g . °C /
$$c_p = 4.53 - 8.37 \cdot 10^{-4} \, t$$
$$t < 422 \, °C$$
$$= 4.21 - 7.24 \cdot 10^{-5} \, t$$
$$t > 422 \, °C$$

Thermal Conductivity
/ J/s . m . °C /
$$\lambda = 42.3 + 12.3 \cdot 10^{-3} \, t$$

Electrical Resitivity
/ $\mu\Omega$. cm /
$$R = 18.33 + 3.339 \cdot 10^{-2} \, t$$
$$- 6.795 \cdot 10^{-6} \, t^2$$

VIII End Plug Design

VIII.1 General Features

The end plug region consists of the barrier, "c", and yin-yang magnets, their support structure and dewar, shielding penetration for neutral beam injection and ECRH heating, neutral beam dumps and the electron and ion thermal dumps at the end walls. There is also provision for testing of direct convertor modules. The details of the magnet design are given in Chapter V. Three-dimensional Monte Carlo calculations of neutron streaming through the various penetrations of the end plug shield are presented in Section VIII.2. The beam dumps for the various neutral beams are discussed in Section VIII.3. A conceptual design of a single stage plasma direct convertor module is given in Section VIII.4. The thermal hydraulics aspects of the thermal dumps is treated briefly in Section VIII.5. The surface erosion aspects of the direct convertor and thermal dumps is discussed in Section VIII.6. The overall arrangement of the various components is treated in Section VIII.7. Assembly and maintenance considerations are discussed in Chapter X.

VIII.2 Neutron Environment

A primary objective of this work is to determine the neutron and gamma-ray streaming into the NBI and ECRH ducts. This will be of great importance in evaluating the radiation effects in these penetrations.

Evaluation of the radiation flow into the ducts requires an accurate knowledge of the neutron source, and the geometrical configuration of the shield, as well as the size of the ducts.

The neutron source distribution in the reactor is shown in Fig. VIII.2-1. The D-T reaction rate drops to a negligible value at the center of the end-plug region. The distribution is characterized by two relative peaks in the barrier and plug regions. The first peak occurs in the barrier region at a distance of 16.5 m from the center of the reactor, and the second peak is in the end-plug region at a distance of 25 m. Fortunately, the NBI and ECRH ducts are not in direct line of sight of the source neutrons at these peaks.

In the shield design of the barrier and end-plug regions, the shield wall follows the plasma envelope. The vertical and horizontal plasma envelopes are shown in Fig. VIII.2-2.

The distance between the plasma and the wall differs from one region to another according to the magnetic field strengths, and can easily be calculated as explained below.

The total magnetic flux is, in general, given by

$$F = \pi r^2(z) \, B(z) \, \sqrt{1-\beta(z)} + \pi[r_w^2(z) - r^2(z)] \, B(z) \qquad \text{(VIII.2-1)}$$

where r is the plasma radius, B is the vacuum magnetic field, r_w is the wall radius, and β is the ratio between the plasma and magnetic field pressures.
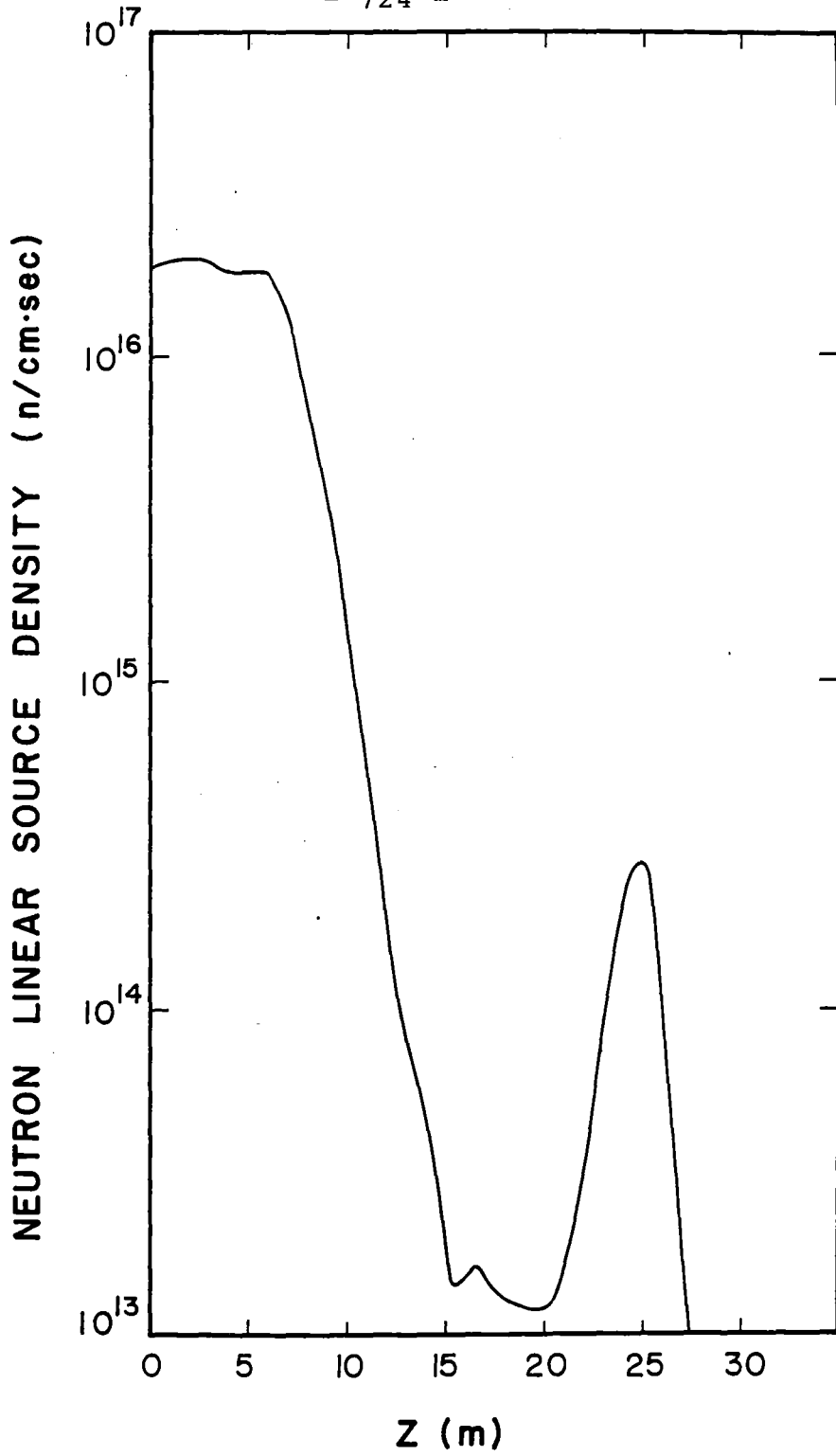
VIII.2-1

Fig. VIII.2-1   Variation of the neutron linear source density along the z axis.

FRAME 8, GFUN LDSN1   DATE 10/29/81 TIME 23:59:08RUN FOR BLANKET(HOMG.)
34 CONDUCTOR ELEMENTS (O)IRON ELEMENTS
Z-Y PLANE

B-LINE RO (0.0, 32.0, 0.0)ZY, HO (0.00, 0.00, 2.97) 2.97TES
B-LINE RO (0.0, 32.0, 0.0)ZY, HO (0.00, 0.00, 2.97) 2.97TES
B-LINE RO (-32.0, 0.0, 0.0)ZX, HO (0.00, 0.00, 2.97) 2.97TES
B-LINE RO (-32.0, 0.0, 0.0)ZX, HO (0.00, 0.00, 2.97) 2.97TES

NO BLANKET
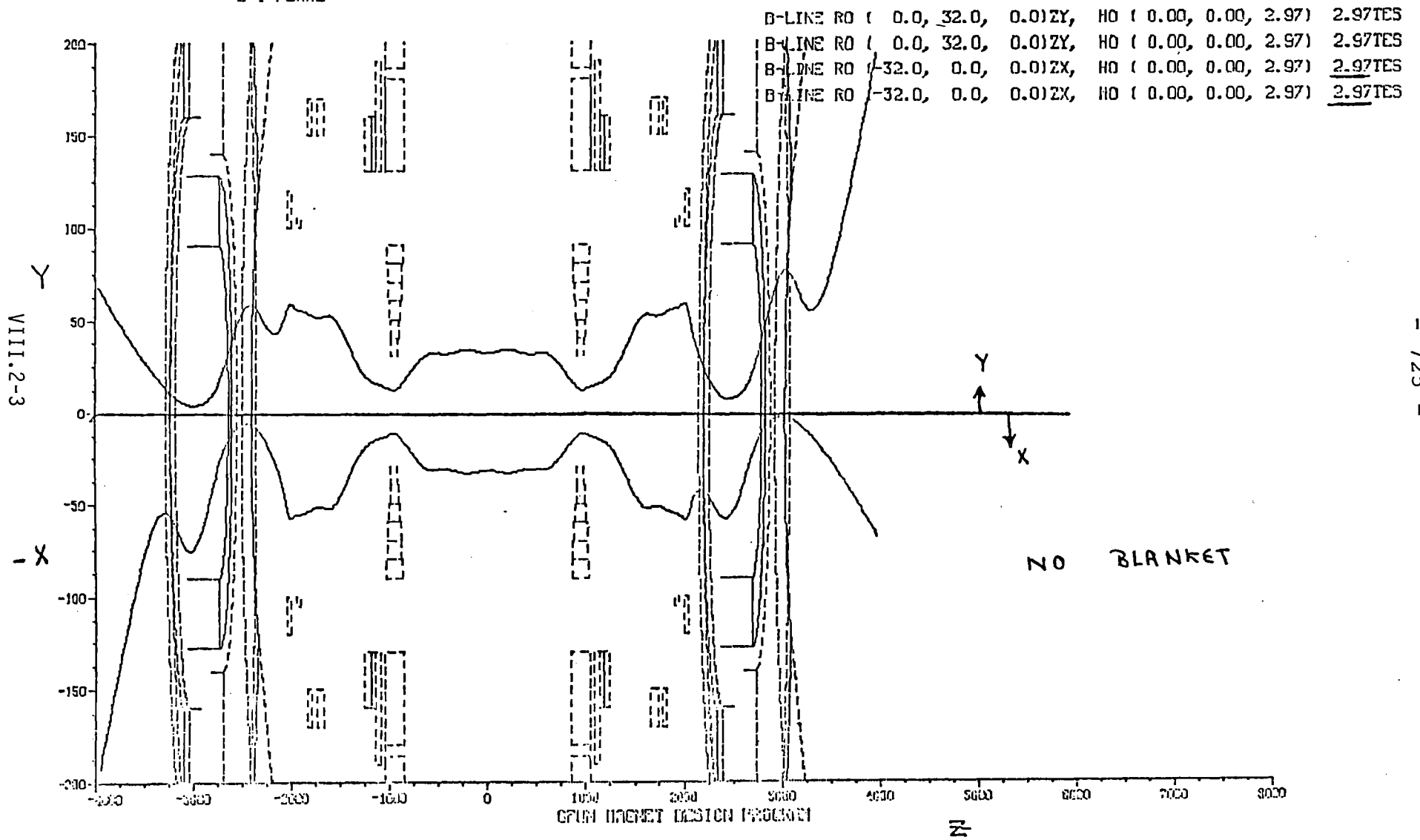
Fig. VIII.2-2   Vertical and horizontal plasma envelopes along the z axis.

The first term on the right-hand side is the contribution from the plasma, and the second is from the halo region.

By flux tube conservation, the plasma radius for a circular flux tube is given by

$$r(z) = r_c \left(\frac{B_c \sqrt{1-\beta_c}}{B(z)\sqrt{1-\beta(z)}} \right)^{1/2} \qquad (VIII.2-2)$$

where r_c is the central cell (cc) plasma radius, $B_c = 2.7$ T is the cc magnetic field, and $\beta_c = 0.5$ is the cc beta.

From Eqs. VIII.2-1 and VIII.2-2 the distance between the plasma and the wall $(r_w - r(z))$ can be calculated at any point along the z-axis. The distance has an average value of 10 cm in the end-plug region and a maximum value of 30 cm in the barrier region.

The shield thickness in the barrier and end-plug regions has been determined from one-dimensional calculations. In these calculations, the peak source density in the appropriate region was used. In order to reduce the radiation damage in the field shaping, transition, and yin-yang coils to an acceptable level, the shield has been designed to have the thicknesses of 20-30 and 60 cm in the barrier and end-plug regions, respectively. Also, a 20 cm thick shield is used in the direct convertor region.

To deal with the three-dimensional geometrical configuration of the shield, the Monte Carlo code MCNP[1] was used for the treatment of the problem. Figures VIII.2-3 and VIII.2-4 are elevation and plan views, respectively, of the MCNP model from the midplane of the barrier to the end of the reactor. The model contains the NBI and ECRH ducts and the figure illustrates the geometrical relationship of these ducts to the reactor.
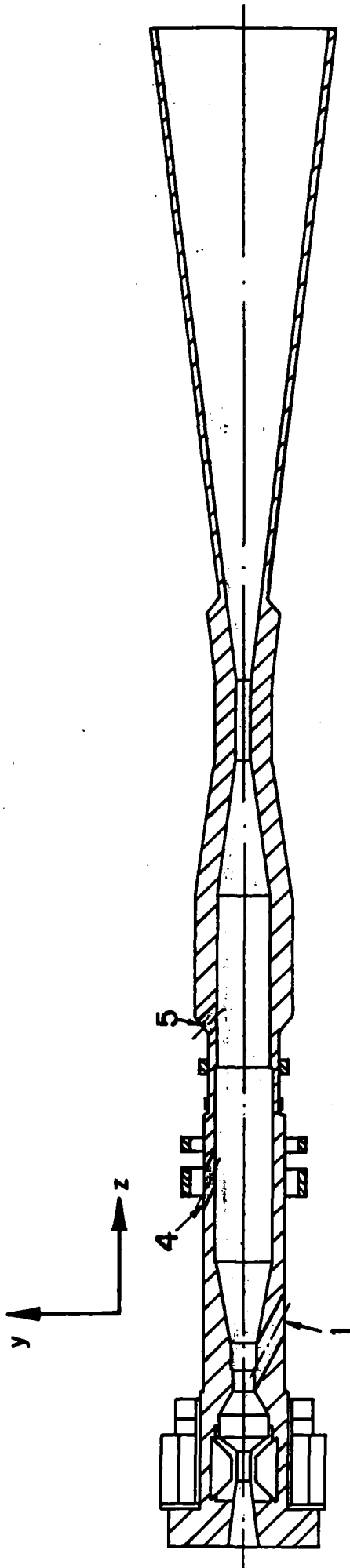
VIII.2-4
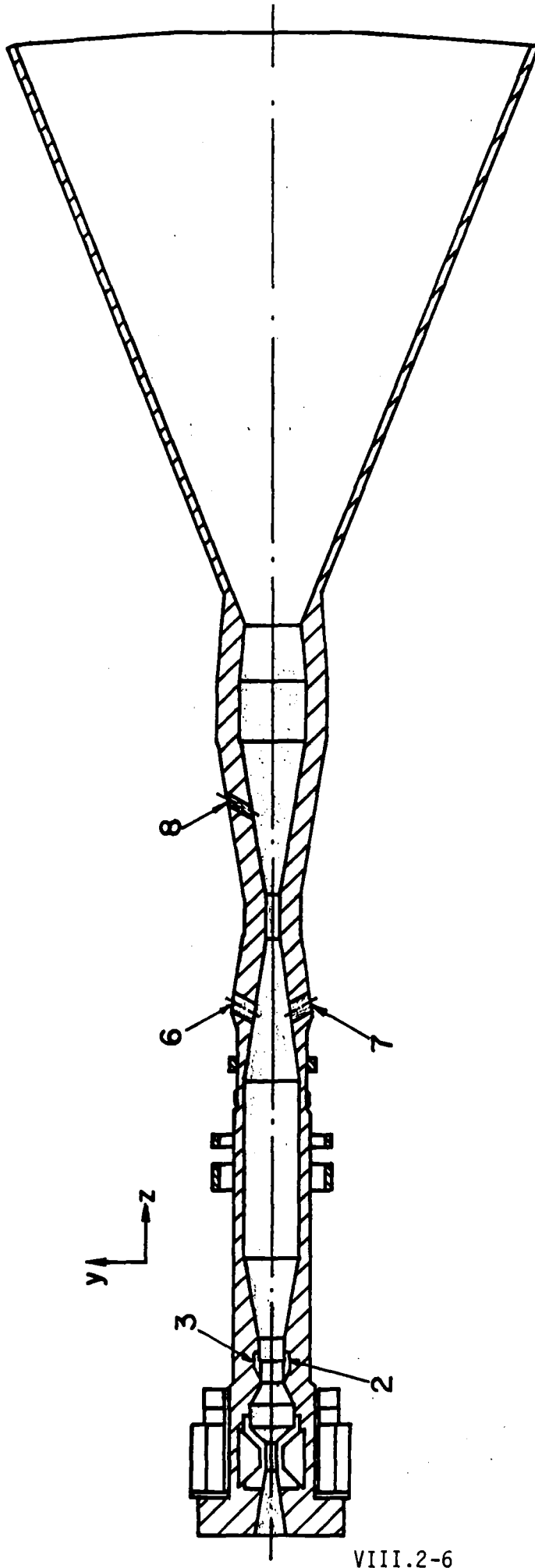
Fig. VIII.2-3

VIII.2-5

Fig. VIII.2-4

VIII.2-6

Details of the geometrical model in the vertical plane are given in Figs. VIII.2-5, VIII.2-6, VIII.2-7, VIII.2-8 for the axial zones 9.5-20.30, 20.30-31.10, 31.10-41.90, 41.90-50 m, respectively. The geometrical model details in the horizontal plane are given in Figs. VIII.2-9 - VIII.2-11, for the axial zones 9.5-20.30, 20.30-31.10, 31.10-38.30 m, respectively. Figure VIII.2-12 shows, on a different scale, the axial zone 34.4-50 m of the horizontal plane. This model will be used to evaluate radiation effects in these regions.

The model shown on these figures is entered into the MCNP input. Trapping surfaces are located at the entrance surfaces to eight ducts shown on Figs. VIII.2-3 and VIII.2-4. At these surfaces all particles entering the ducts are counted according to angle and energy bins. The results are stored to serve as source distributions in later modeling of the ducts themselves. These results were obtained by sampling the source distribution separately in the central cell and barrier and end plug regions. The source strengths are given in Table VIII.2-1. As the source in the barrier and plug are dominant, a run was made using 20,000 source particle hisotries from that part of the source distribution between 9.2 m and 14.5 m from the reactor midplane. A second run of 20,000 histories are sampled from axial position 14.5 m to 26.7 m. The data from all runs are combined according to a total source of 1.47 E19 neutrons/sec to axial position 9.2 m and 2.71 E17 and 8.33 E16 nuetrons/sec in the two regions described above.

The number of particles crossing each trapping surface is given in a per fusion and on a per second basis along with the energy per fusion in Table VIII.2-2.

The tabulated results can be interpreted qualitatively by observing the energy current density in MW/m^2 in the right hand column. This corresponds to
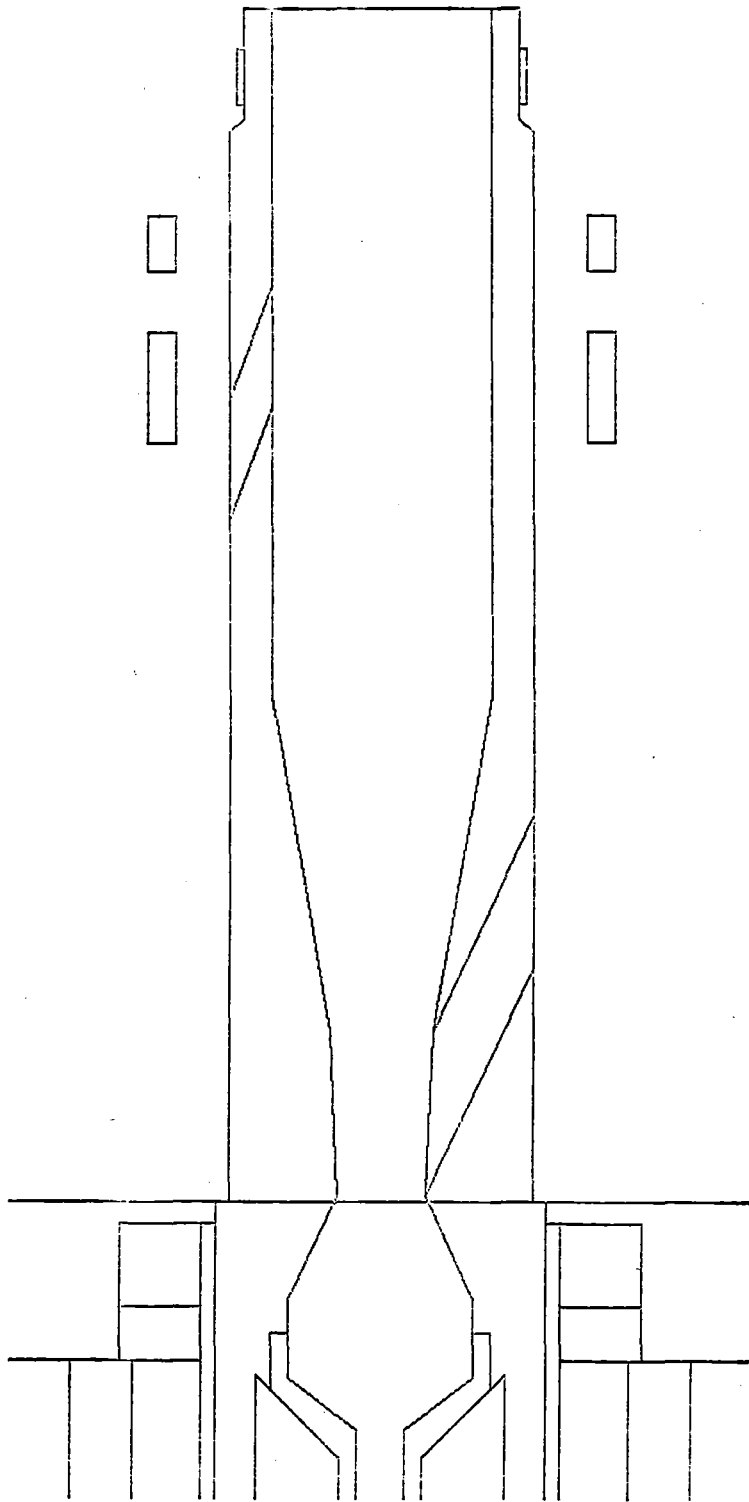
VIII.2-7

Fig. VIII.2-5 Vertical plane, z = 9.5 - 20.3 m.
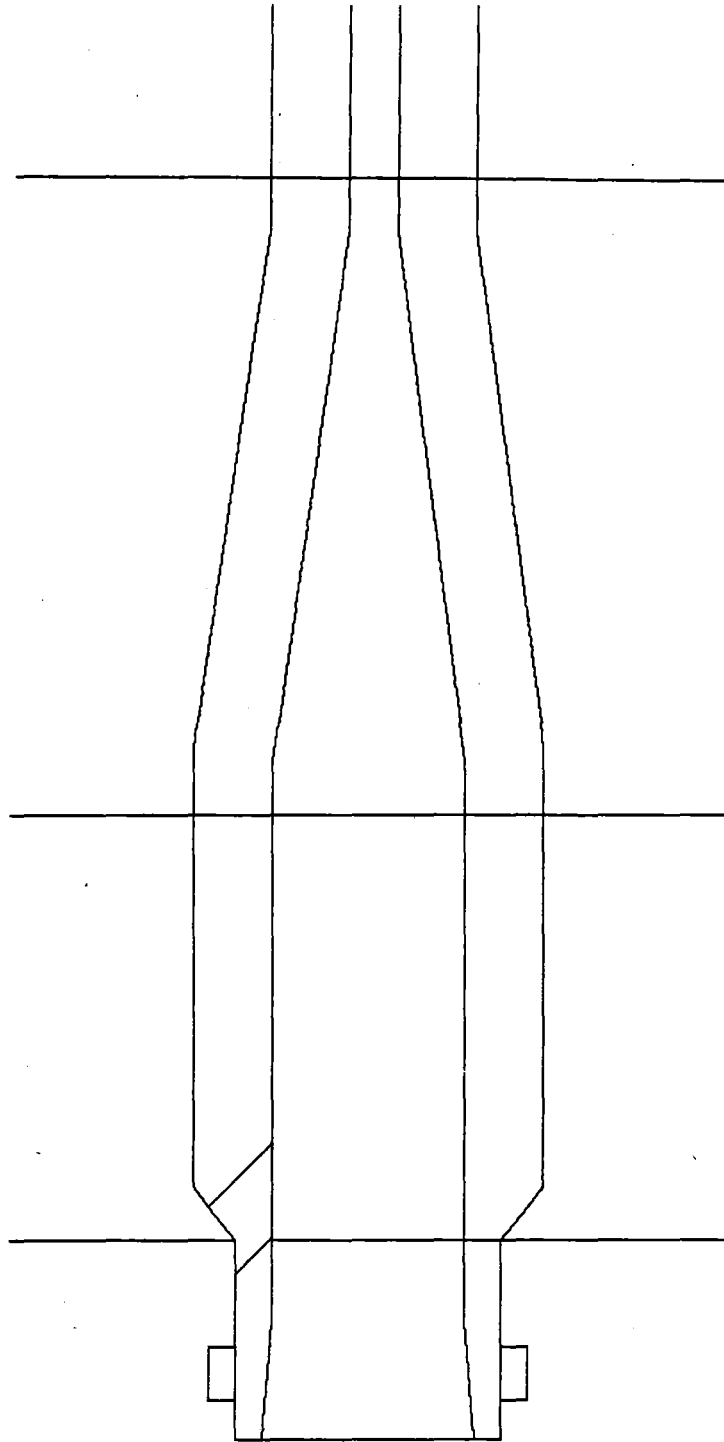
VIII.2-8

Fig. VIII.2-6 Vertical plane, z = 20.3 - 31.1 m.
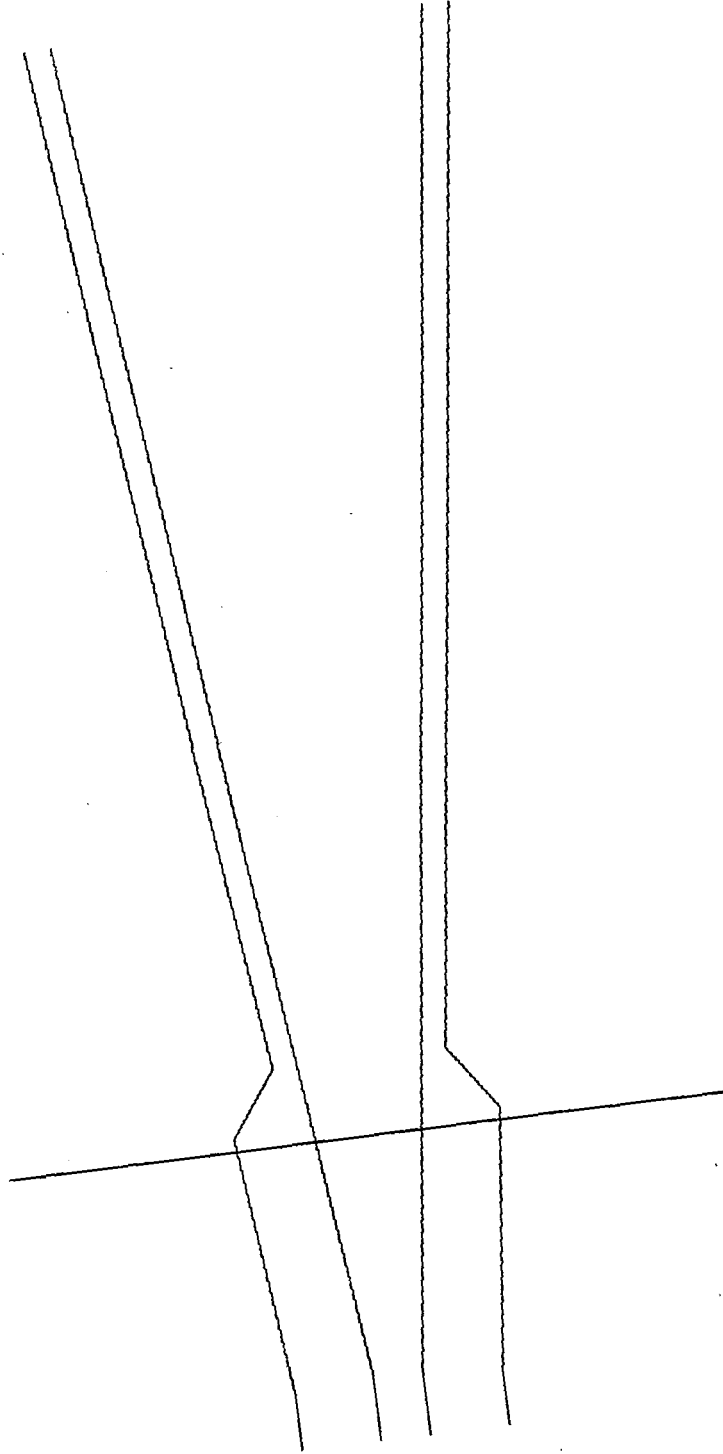
VIII.2-9

Fig. VIII.2-7 Vertical plane, z = 31.1 - 41.9 m.

VIII.2-10
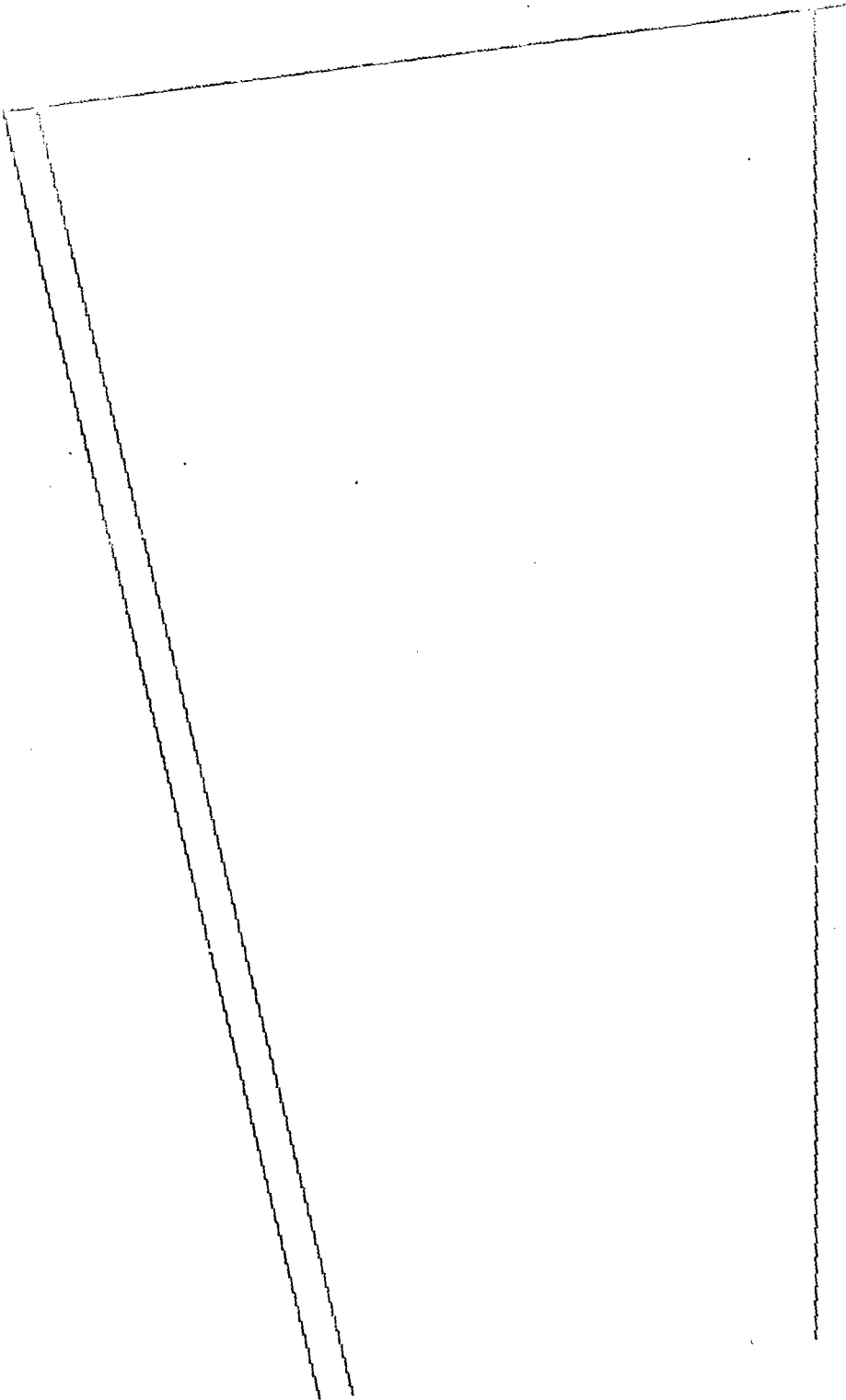
Fig. VIII.2-8 Vertical plane, z = 41.9 - 50 m.
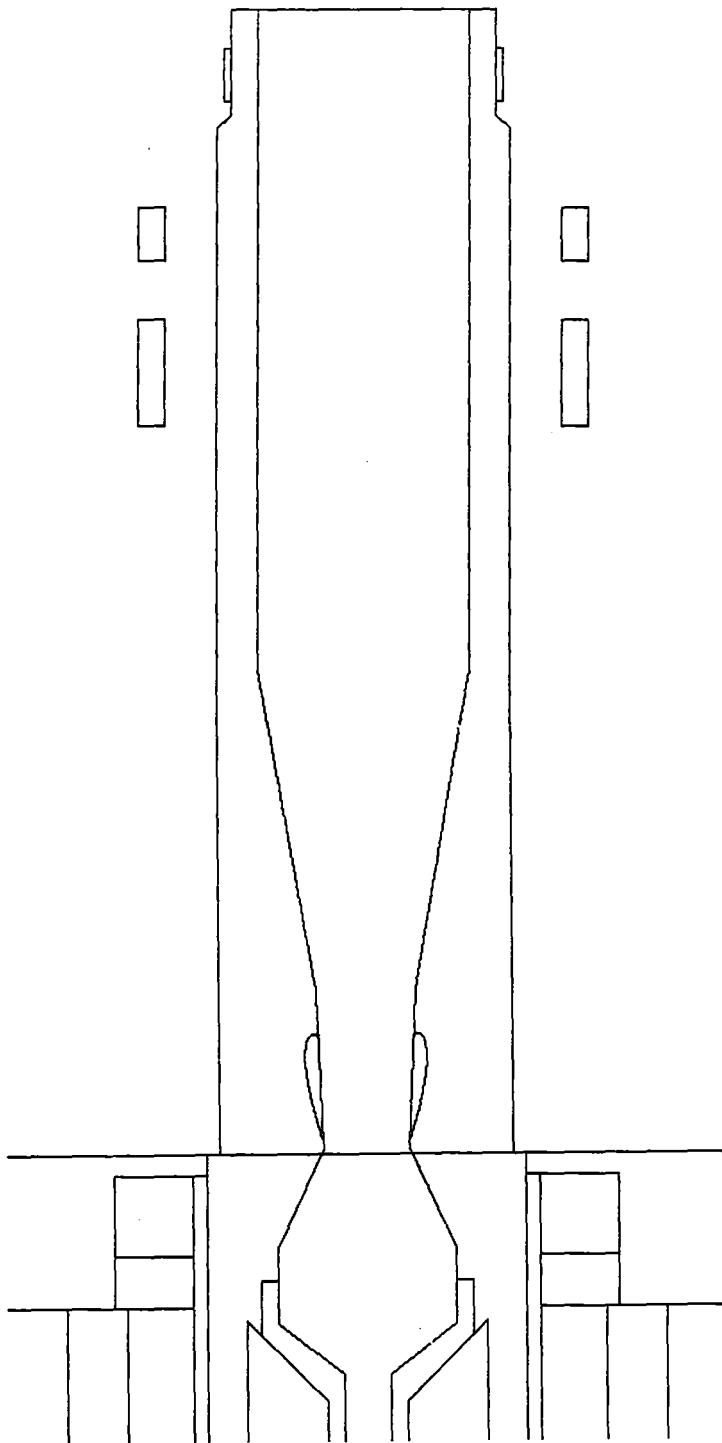
VIII.2-11

Fig. VIII.2-9 Horizontal plane, z = 9.5 - 20.3 m.
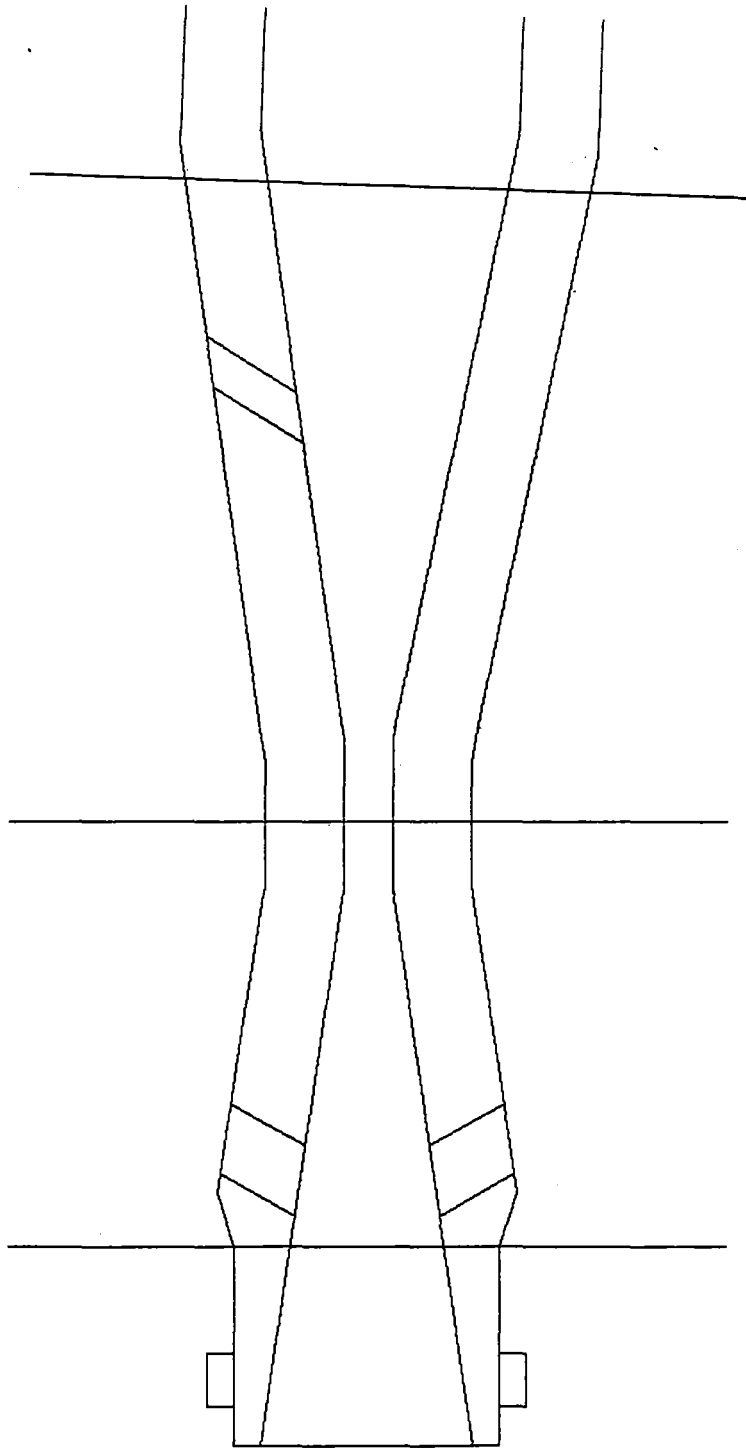
VIII.2-12

Fig. VIII.2-10 Horizontal plane, z = 20.3 - 31.1 m.
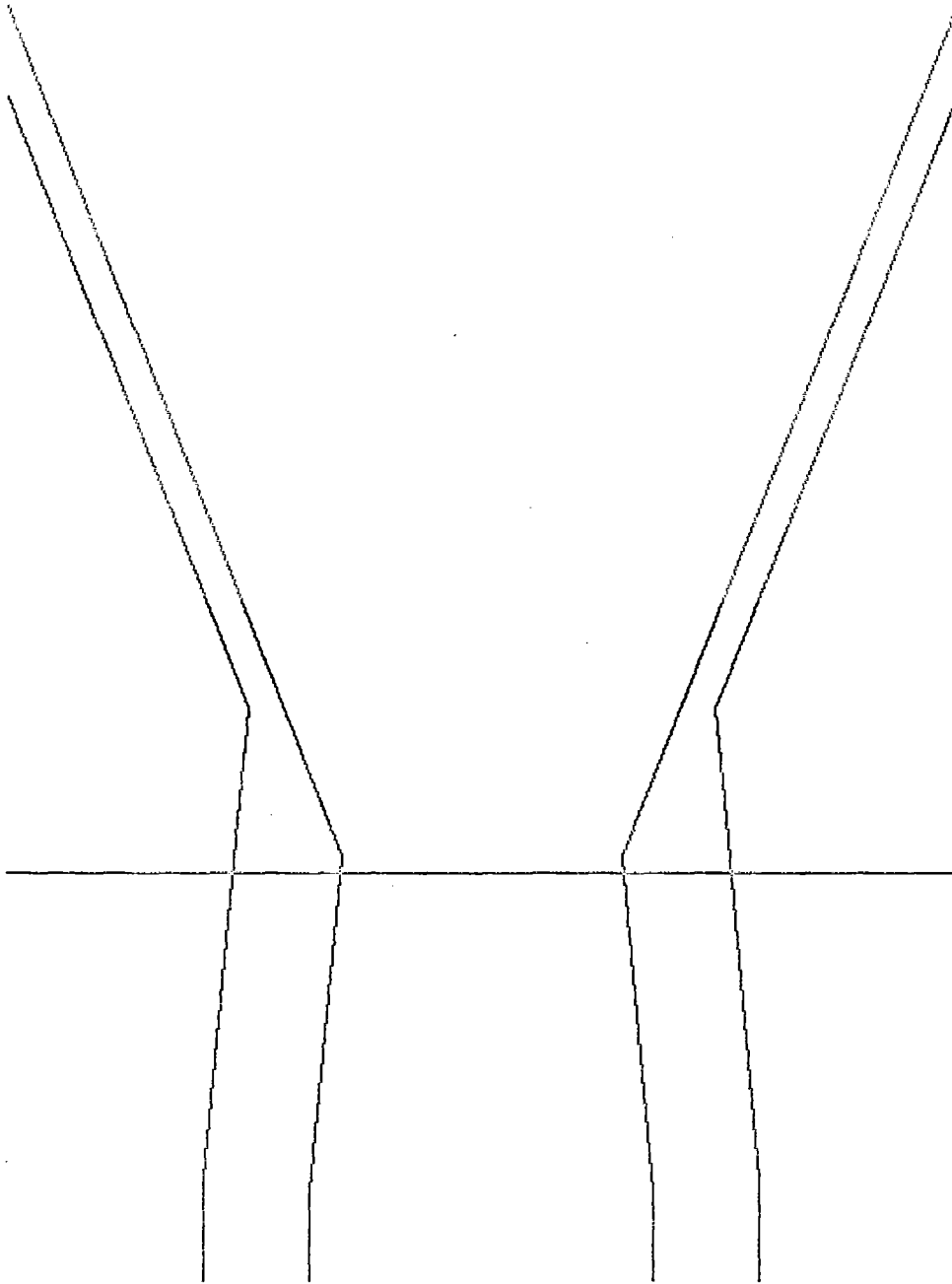
VIII.2-13

Fig. VIII.2-11 Horizontal plane, z = 31.1 - 38.3 m.
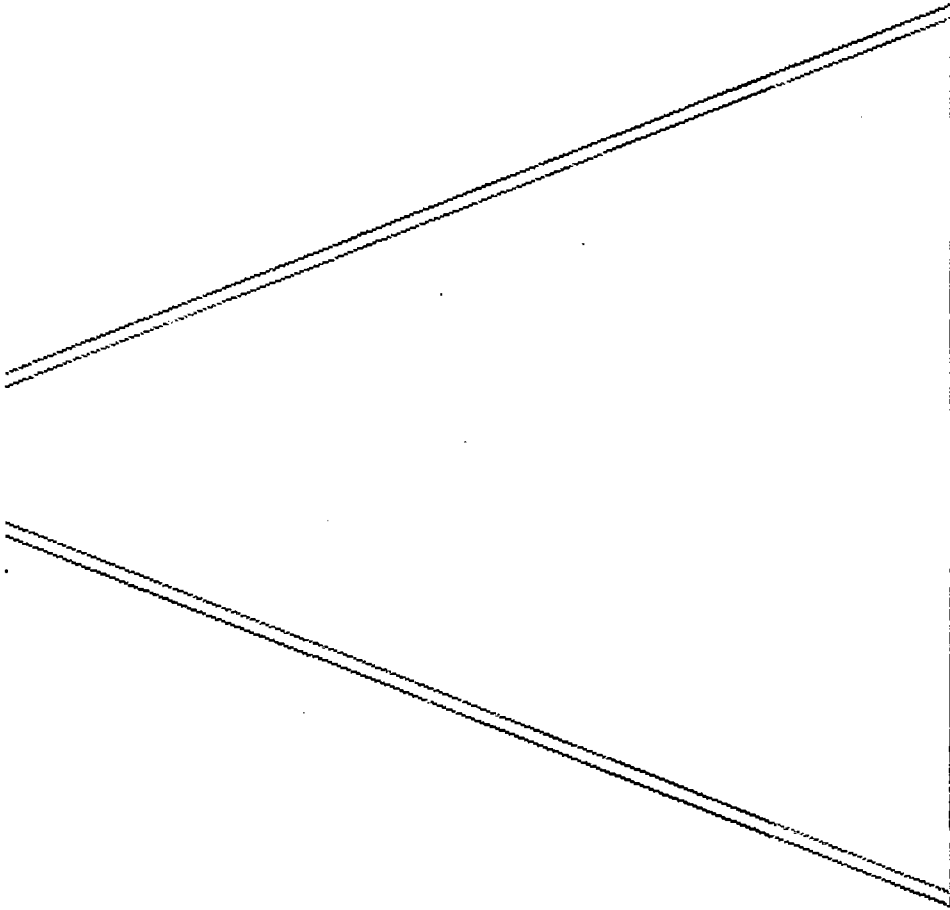
VIII.2-14

Fig. VIII.2-12 Horizontal plane, z = 34.4 - 50 m.

Table VIII.2-1

Region	Source (n/sec)	Power (MW)
C.C.	2.94 E19	82.914
B&EP (2)	7.08 E17	1.998
Total	3.01 E19	84.912

Table VIII.2-2

Duct	Neutrons		Gammas		Energy		Energy Current (MW/m^2)
Number	Per Fusion	Per Sec	Per Fusion	Per Sec	keV/Fusion	kW	
1	2.96 E-4	8.90 E15	4.79 E-5	1.44 E15	2.101	10.136	2.236 E-2
2	2.77 E-4	8.39 E15	4.66 E-5	1.40 E15	1.833	8.842	1.950 E-2
3	2.75 E-4	8.27 E15	4.40 E-5	1.32 E15	2.029	9.788	2.159 E-2
4	5.48 E-6	1.65 E14	8.80 E-7	2.65 E13	0.042	0.202	9.779 E-4
5	2.80 E-5	8.43 E14	5.32 E-6	1.60 E14	0.190	0.917	3.302 E-3
6	1.94 E-5	5.84 E14	4.13 E-6	1.24 E14	0.122	0.587	2.587 E-3
7	2.15 E-5	6.47 E14	4.68 E-6	1.41 E14	0.162	0.781	3.444 E-3
8	1.89 E-6	5.69 E13	4.54 E-7	1.37 E13	0.005	0.025	2.677 E-4
Total into 16 Ducts	1.85 E-3	5.57 E15	3.08 E-4	9.25 E15	12.968	62.556	

~ .02 MW/m^2 or less compared to ~ 2 MW/m^2 for the first wall of a fusion chamber or about 2 orders of magnitude less at the entrance to our penetrations. Further, the energy is less directed here; so the actual source to the back of the ducts will probably be at least another order of magnitude less than in similar fusion chamber penetrations.

The neutron and gamma energy spectra and singular distributions are obtained and since duct 1 is the most severe case and duct 6 is representative of the other ducts their spectra are shown in Figs. VIII.2-13 to VIII.2-18. An inspection of Fig. VIII.2-15 shows the angular distribution of the source particles peaks at normal incidence while the center line is appreciably off normal and most particles will go into the shield of the duct near the first wall. This is also true of duct 6.

Duct 1 is the medium energy neutral beam injector and is modeled as shown in Fig. VIII.2-19. The radiation problem of greatest concern here is the effect on the insulating electrode support structure which is a cylindrical shell, designated 1 on the figure, of the ceramic material MACOR. The composition of MACOR and other materials in the model are given in Table VIII.2-3. The model is an idealization and adaptation of a neutral beam system design provided us by John Osher.

The neutral beam duct model problem employs neutron and gamma surface sources at the duct opening of 8.9 x 10^{15} and 1.44 x 10^5 particles/second respectively, as obtained from the previous model. Only the central ion source was considered as radiation damage effects in adjacent ion sources are expected to be less severe. An MCNP run of 50,000 histories was carried out resulting in relative standard deviations of less than 10% for the quantities of interest. The energy deposition and dose rate in the insulating electrode
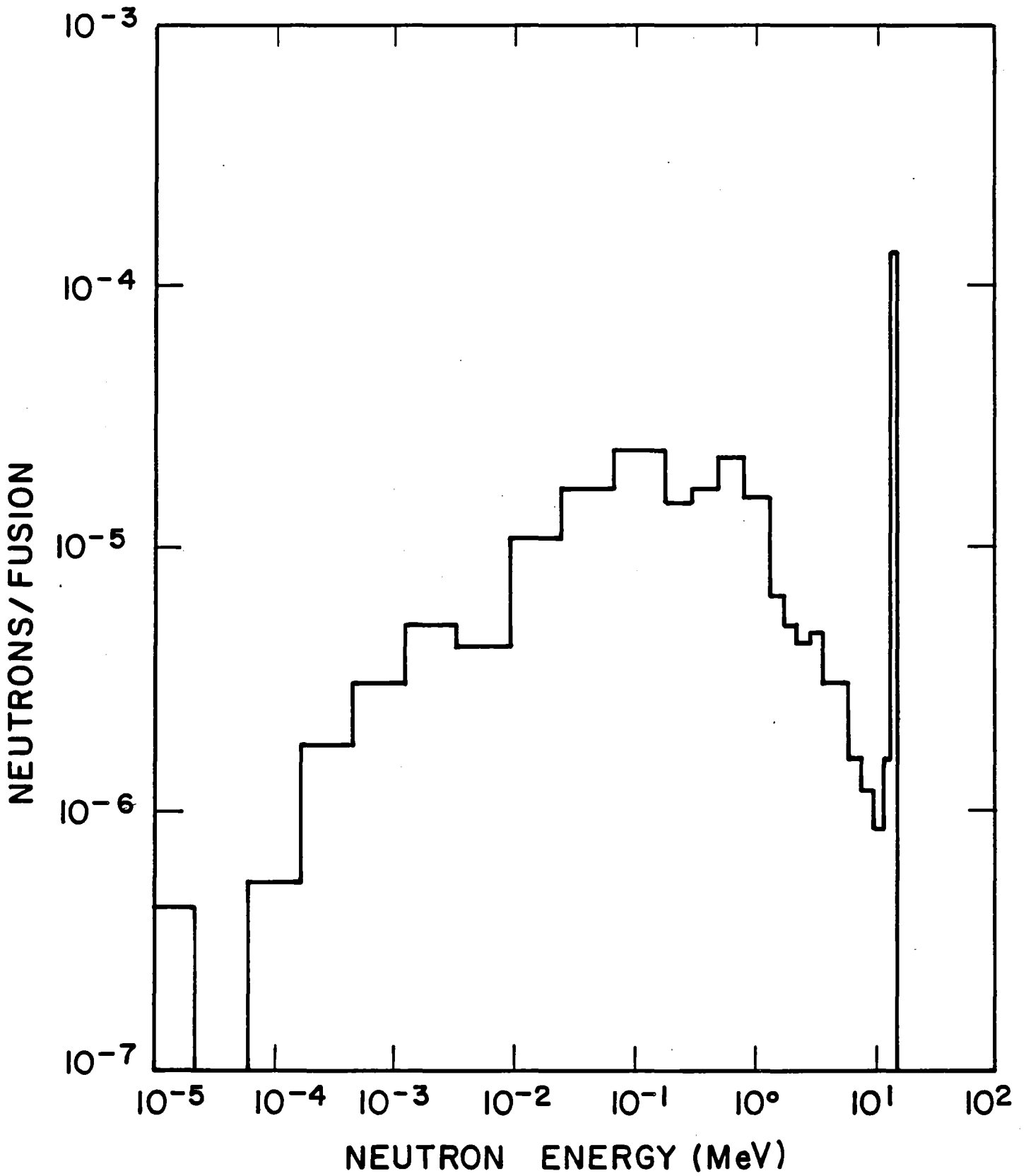
Fig. VIII.2-13. Neutron energy spectrum entering Duct 1.
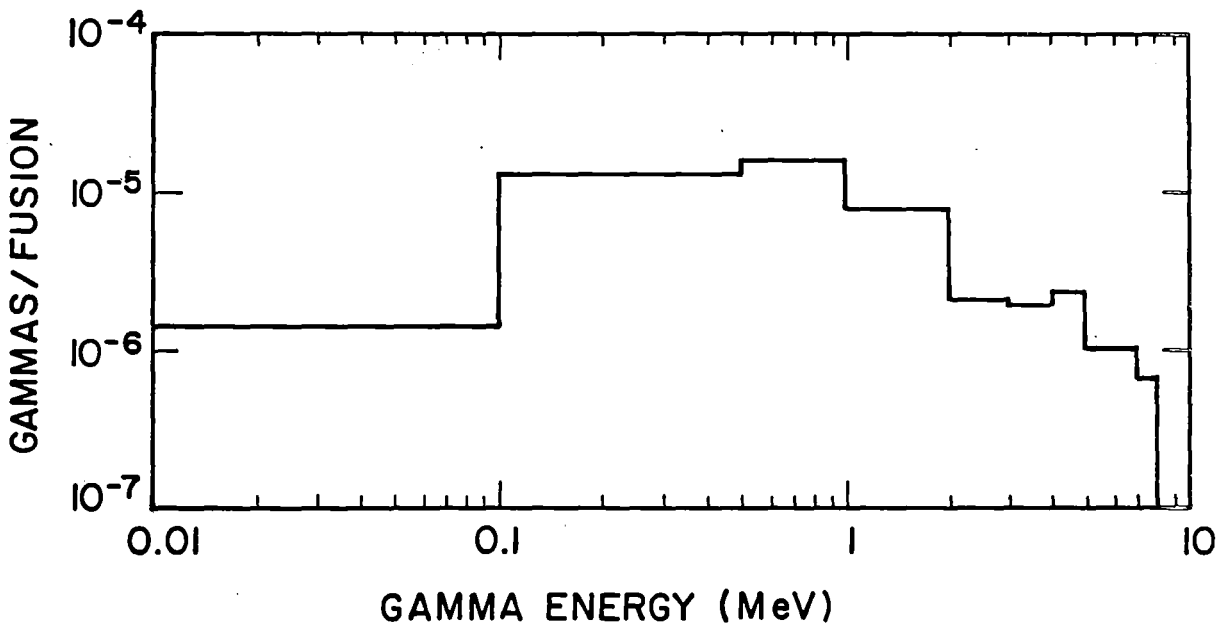
VIII.2-19

Fig. VIII.2-14. Gamma energy spectrum entering Duct 1.
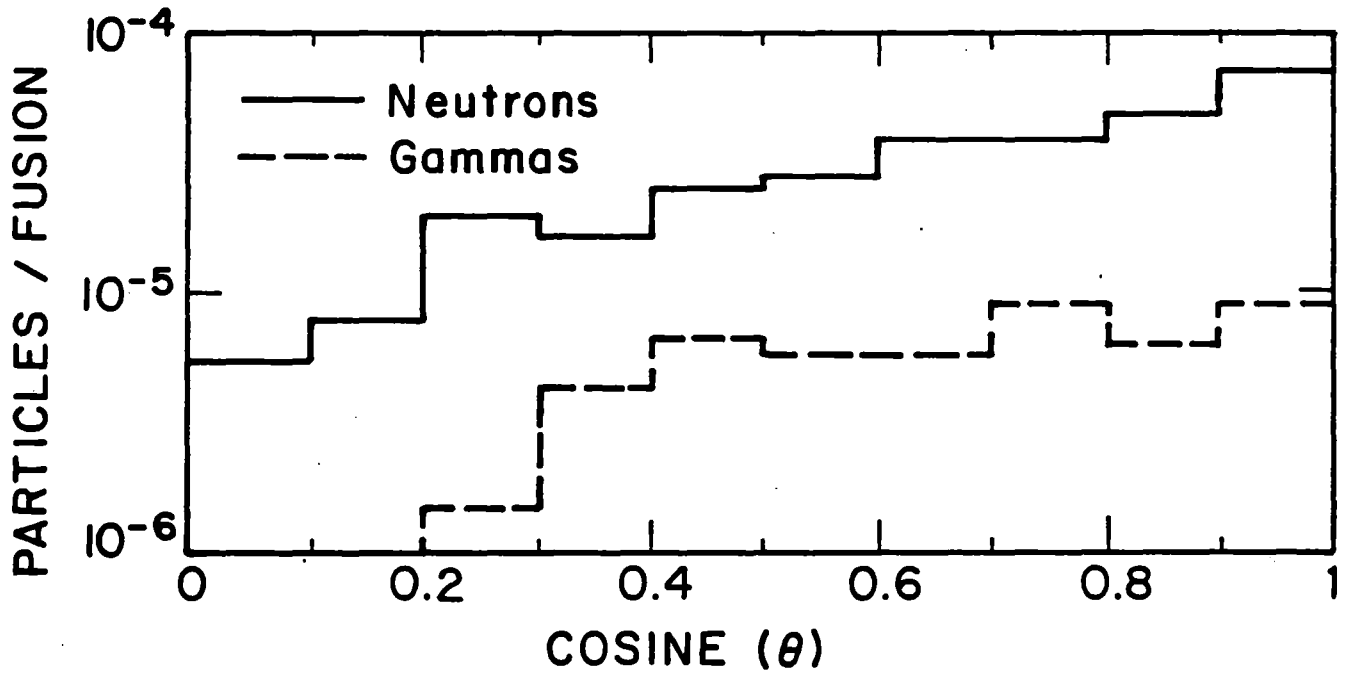
Fig. VIII.2-15. Angular distributions of neutrons and gammas entering Duct 1.
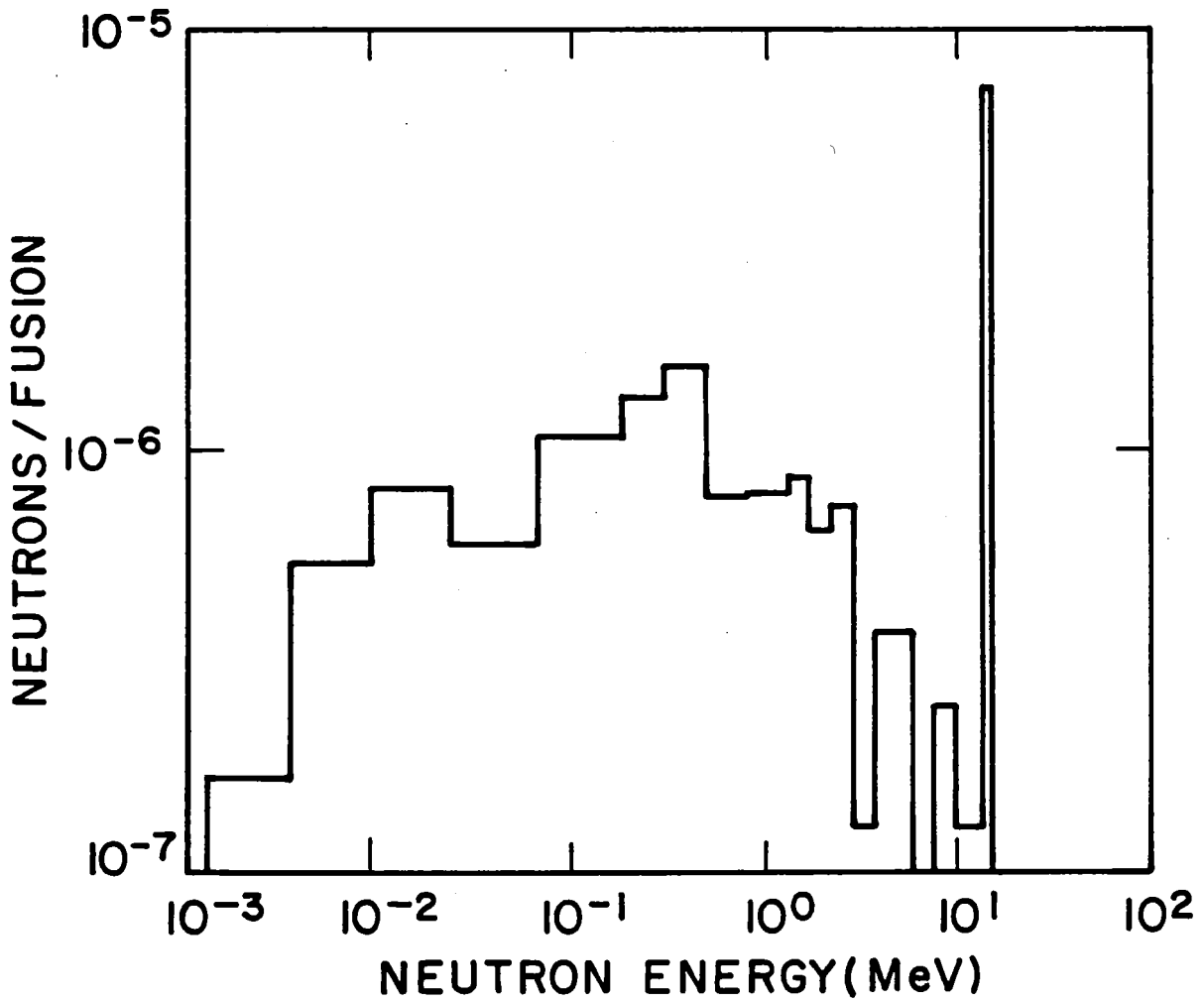
Fig. VIII.2-16. Neutron energy spectrum entering Duct 6.
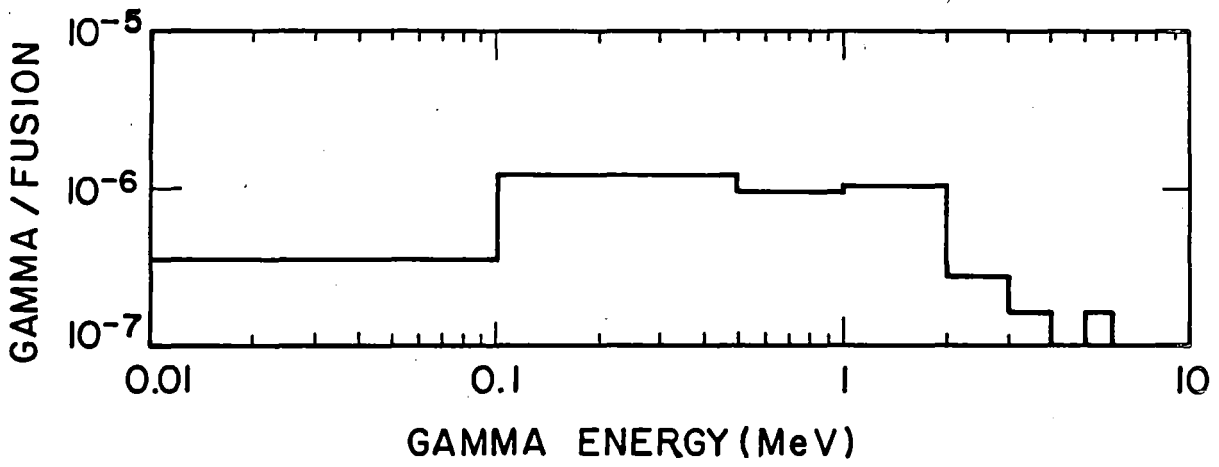
Fig. VIII.2-17. Gamma energy spectrum entering Duct 6.
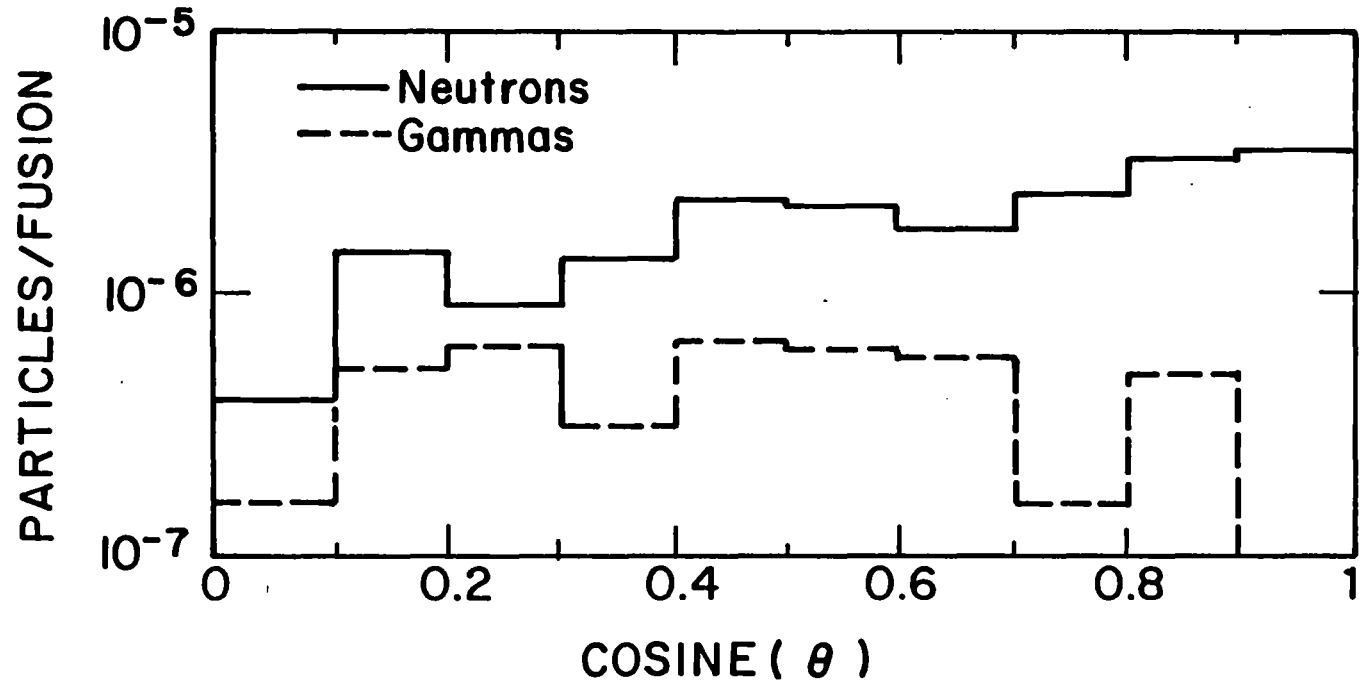
Fiq. VIII.2-18. Anqular distribution of neutrons and qammas entering Duct 6.
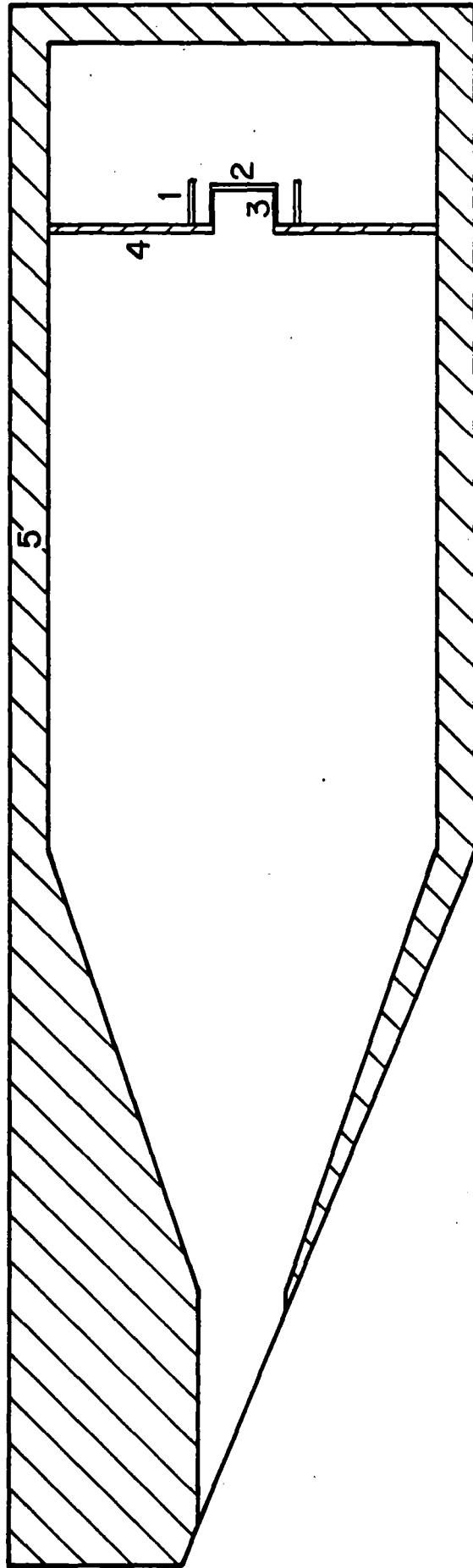
Fig. VIII.2-19

VIII.2-25

Table VIII.2-3. Composition of Region in Model of the NBI Duct 1

Region	Thickness (cm)	Material	Composition
1	1.5	MACOR	46 w/o SiO_2
			16 w/o Al_2O_3
			17 w/o MgO
			10 w/o K
			4 w/o F
			7 w/o B_2O_3
2	2	Copper	Cu
3	0.5	Copper	Cu
4	4	SS-316	68 w/o Fe
			17 w/o Cr
			12 w/o Ni
			3 w/o Mo
5	20	Shield	56 v/o Fe 1422
			26 v/o B_4C (87%)
			14 v/o Pb
			4 v/o H_2O

support structure due to gammas, neutrons, and totals are given in Table VIII.2-4. The flux (and heating rate) at the end of the insulator is higher at the end than elsewhere by the order of 50% due to direct streaming from the opening.

An experimental study of radiation effects in MACOR (Ref. VIII.2.2) indicated slight damage by 14 MeV neutrons at a fluence of 10^{22} neutrons/m^2 which was estimated to correspond to a dose of 6×10^8 Rad. Comparing this with the result of 5×10^7 Rad per full power year from the table, it would appear that the insulators would last 10 FPY's as far as radiation is concerned. Note however that a fusion chamber source strength two orders of magnitude higher would indicate possible problems after about one month.

This points up the need for more definitive damage data in insulators. The data used were post-irradiation and give no indication of performance under irradiation where electrical conductivity and electric breakdown phenomena may be important. Thus our results, while favorable regarding insulator performance, must be used with some caution.

Reference for Section VIII.2

1. "MCNP", Los Alamos National Laboratory Report LA-7396-M, April 1981.

Table VIII.2-4. Energy Deposition and Deposition Rate in the MACOR

Insulating Electrical Support Structure in NBI Duct 1

	Neutron	Gamma	Total
Energy deposition per 14.1 MeV neutron (eV/fusion)	2.176 E-2	1.152 E-2	3.328 E-2
Nuclear heating rate (w/cm^3)	4.051 E-5	2.144 E-5	6.195 E-5
Dose rate (rad/sec)	1.608	0.851	2.459
Dose Rate (rad/FPY)	5.070 E7	2.683 E7	7.753 E7

VIII.3 Beam Dumps

VIII.3.1 Introduction

In the process of neutral beam heating of the plasma, the trapping of the various incident neutral species is not, unfortunately, one hundred percent efficient. It is the purpose of the neutral beam dumps to provide an effective heat sink for these residual neutral beam fractions which are not absorbed by the plasma. It is interesting to note that, although the beam dumps comprise only a small part of the overall engineering design of TASKA, they nevertheless present some novel technology problems which warrant equally novel solutions.

The salient features of these technology problems may be summarized as follows:

1. <u>Power Absorption - Heat Transfer</u>

The maximum power density of the TASKA neutral beams at the plasma footprint approaches a steady state value of $\sim$ 30 kW cm^{-2} for the case of the medium energy D/T beam into the barrier. This should be compared with power densities encountered in current state-of-the-art designs of dumps for high heat fluxes, where maximum power densities of only $\sim$ 4 kW cm^{-2} can be tolerated, and then only for short periods of < 0.5 s [see, for example, Harbaugh,[1] Moir, et al.[2]]. It can be seen, therefore, that the power absorption - heat transfer aspects of the beam dump design require careful study in order to reduce the residual beam power densities to acceptable limits.

2. <u>Sputtering of the Dump Surfaces From Beam Impact</u>

For the range of beam energies encountered from the neutral beam injectors in TASKA (i.e., 5 to 250 keV), the sputtering yield of

materials considered as candidates for the dump surfaces is typically in the range 10^{-1} to 10^{-4} atoms per incident particle [see, for example, Roth, et al.[3]]. This has two important consequences. Firstly, the phenomenon of surface erosion must be considered with regard to the lifetime of each beam dump. Secondly, the prevention of this sputtered high-Z surface material from entering the plasma region dictates some complex pumping requirements.

3. Tritium Absorption and Diffusion Into the Dump Coolant

The 50 keV medium energy pump beam in the barrier coil also performs the central cell fueling by virtue of its mixed D/T composition. However, this latter feature results in a large residual tritium particle flux to the dumps. Under equilibrium conditions, there is a steady state distribution of tritium within the dump matrix yielding a constant flow rate of tritium from both the front and rear (coolant) surfaces of each dump. This can result in an unacceptably large tritium inventory within the dump coolant itself.

4. DD and DT Neutron Generation Within the Dump Surfaces

As will be demonstrated later, the beam dumps for all four types of neutral beams in TASKA will contain, under equilibrium conditions, an internal steady state distribution of their respective incident neutral species. In the case of the dumps for the high and low energy beams into the barrier region, a pure deuterium distribution results. Subsequent D neutrals incident on these dumps are, therefore, capable of generating DD neutrons at any depth from the surface down to their implantation depth. In the case of the dumps for the mixed D/T medium energy beams into the barrier coil region, subsequent D and T neutrals

are similarly capable of generating DD and DT neutrons from D on D, D on T and T on D reactions. This, therefore, requires consideration of neutron source intensities and angular distributions from the beam dumps and attention to resulting shielding requirements.

5. Vacuum Pumping of the Dump Chambers

In addition to pumping considerations for the high-Z sputtered surface material, attention must also be given to the re-emission of cold neutral gas from the dump surfaces. Although in the steady state there is a constant flow of neutral particles from both the front and rear (coolant) surface of each dump, it will be demonstrated later that the flow rate from the front surface is much larger than that from the rear surface and approaches the incident neutral beam implantation rate. Sophisticated vacuum techniques are, therefore, required to prevent this large backflow of cold gas from entering the plasma chamber.

In considering the above points, it is interesting to note that the ion dumps internal to the neutral beam injectors are subject to similar but usually more severe operating constraints. In the case of the medium energy D/T beam, for example, approximately 20% of the original charged particle beam from the ion source escapes neutralization and must be directed to an internal ion dump within the injector. The external beam dump, on the other hand, is only exposed to that fraction of the neutral beam which is not trapped in the plasma. For this medium energy beam, the ratio of the ion beam power on the internal dump to the neutral beam power on the external dump is approximately a factor of five.

VIII.3-3

VIII.3.2 Design Philosophy

Table VIII.3-1 illustrates those aspects of the TASKA neutral beam para-
meters which are of relevance to the engineering design of the beam dumps.
The parameters of prime importance in this respect are the neutral beam power
and the fraction of the beam absorbed in the plasma (i.e., the trapping
fraction). In the case of the 250 keV H beam into the plug, for example, only
21% of the incident beam is absorbed in the plasma. Therefore, the dump for
the residual beam must be capable of dissipating 79% of the original beam
power!

Current designs for high heat flux dumps employ a suitable metal sub-
strate (e.g., copper or a refractory metal) in either tubular form or in the
form of a thin plate with etched channels on the rear surface. High pressure
water is then forced through these tubular or etched-channel passages. Maxi-
mum (pulsed) power densities for these designs are ~ 4 kW cm^{-2}, above which
the nucleate-boiling to film-boiling transition occurs resulting in catas-
trophic burnout of the dump.

It is important to note that current dump designs envisaged for use up to
~ 4 kW cm^{-2} are at present only being designed for, and tested under, a pulsed
mode of operation. Thus, in their "Thermoskan" design for Lawrence Berkeley
Laboratory, United Technologies[4] has developed a photo-etched copper dump
plate with dimensions of ~ 50 x 50 cm, capable of absorbing 2 kW cm^{-2} for
20,000 shots. In a similar design,[1] RCA has achieved successful test
results for 2.5 - 3 kW cm^{-2} over 1000 cycles (0.5 seconds on, 0.5 seconds
off). At present, the 36 x 110 cm tubular-array beam dumps for the Mirror
Fusion Test Facility-B at Lawrence Livermore National Laboratory are being
designed[4,5] for 2 kW cm^{-2}. If currently planned tests are successful, the

Table VIII.3-1
TASKA Neutral Beam Parameters
of Relevance to Beam Dump Design

	PLUG NEUTRAL BEAM	HIGH ENERGY NEUTRAL BEAM	MEDIUM ENERGY NEUTRAL BEAM	LOW ENERGY NEUTRAL BEAM
LOCATION	Plug	Barrier	Barrier coil	Barrier
NEUTRAL SPECIES	H	D	T (56%) D (44%)	D
NUMBER OF NBI IN EACH END CELL	1	1	3	1
NUMBER OF ION SOURCES PER NBI	1	1	3	1
BEAM ENERGY (keV)	250	76	50	5
BEAM POWER PER NBI (MW)	2.7	3.3	8.27	0.25
RADIUS OF PLASMA FOOTPRINT (cm)	~ 8	~ 12	~ 9.3	~ 38 (unfocussed)
PLASMA TRAPPING FRACTION	0.21	0.42	0.95	0.99

design will be upgraded to ~ 4 kW cm^{-2}. Although MFTF-B will be a pulsed device,[6] the relatively long burn time of 30 s means that the beam dumps will be operated in a quasi-steady state mode (or, at least, with a beam-on time which is much greater than the thermal time constant of the dump material).

The main engineering problems in the design of high power density beam dumps are the very large pumping powers required for efficient coolant flow and the structural integrity of the dump substrate. Thus, for power densities in excess of those above 2-4 kW cm^{-2}, there is a rapid and unacceptable increase in pumping power (values in the region of hundreds of kW per m^2 of dump area are required) coupled with a rapid decrease in the structural safety factor. It is possible to withstand very high power densities by utilizing very short test sections coupled with very high pressure drops. Gambill and Green,[7] for example, report a high heat-flux dump consisting of a 2.3 cm long tube with a 0.6 cm inside diameter and 3.4 MPa differential pressure drop, capable of absorbing 11 kW cm^{-2}. However, such a performance cannot be achieved for long tubes and reasonable dump areas due to excessive pressure drop and associated excessive pumping power requirements. Further considerations of pumping power requirements for high heat flux surfaces may be found in a recent paper by Moir et al.[2]

Recently, there have been several novel designs of large area high heat-flux dumps for operation at around 10 kW cm^{-2}, including a liquid lithium metal dump[8] and a high-velocity-flow circumferentially-cooled dump of semi-circular cross section.[2] However, besides presenting volume limitation constraints, such dumps are currently only in the conceptual stage and could not, therefore, be considered for use in the present TASKA design.

VIII.3.3 Engineering Design

Further reference to Table VIII.3-1 indicates that maximum incident beam power densities at the plasma footprint are ~ 30 kW cm^{-2}, with maximum residual power densities for the untrapped beam fractions of ~ 10 kW cm^{-2}. However, reference to the present dump designs described above implies that maximum attainable power densities for such dumps are ~ 4 kW cm^{-2} and then only for quasi-steady state operation. Accordingly, the following design criterion was defined: the neutral beam dumps for TASKA must be capable of withstanding a maximum steady state power density of 1 kW cm^{-2} under normal operation of full plasma density.

Figure VIII.3-1 is a schematic of the representative design for the TASKA beam dumps. The 1 kW cm^{-2} maximum power density criterion has been accommodated by inclining the dump surface at an angle relative to the beam direction so that the beam is dispersed over a larger effective area. Furthermore, the lower section of the dump has been inverted to form a V-shape. This yields two important advantages. Firstly, sputtering of the dump surface is reduced due to the phenomenon of "cross-sputtering", whereby a fraction of the beam-sputtered material from one plate will now tend to plate-out on the opposing plate (see Section VIII.3.5). Secondly, the overall volume occupied by the dump is reduced by a factor of two. This latter factor is especially important for the medium energy beam dumps situated in the barrier coil, where there are severe space constraints. Further reduction in volume would be possible by employing a multiple-V design.[9]

Two candidates were examined for employment as the dump substrate. The first consisted of a copper plate of approximately 3.5 mm thickness with an explosively-bonded molybdenum layer on the front surface. The rear surface of

θ ⊣ Inclination Angle

⌐Molybdenum (TZM) Tubing

Force–Swirl Water Cooling

NON– TRAPPED NEUTRAL BEAM FROM PLASMA
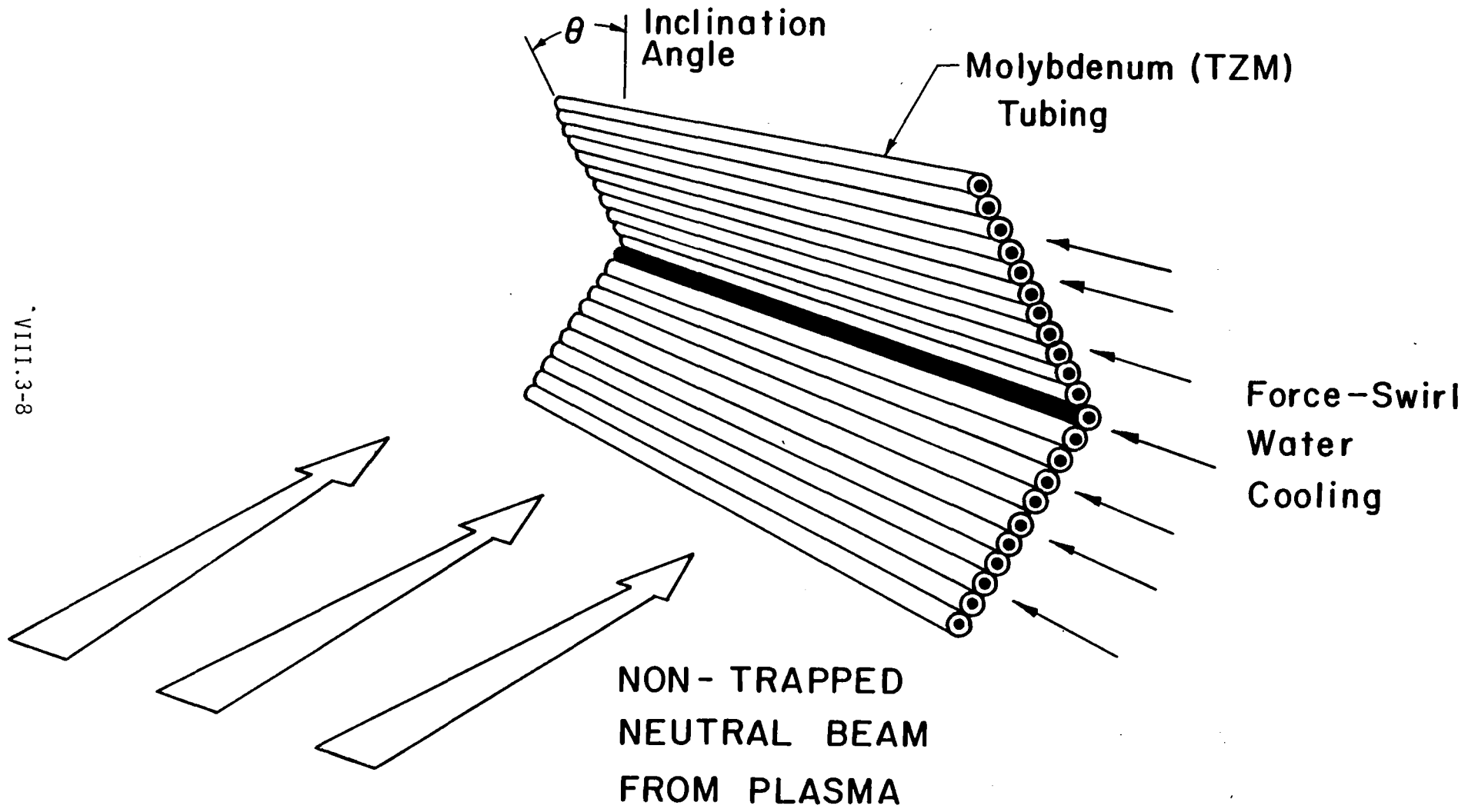
Fig. VIII.3-1   Schematic design of the V-configuration beam dump.

the copper plate contained machined channels of approximately 1.5 mm depth for improved water cooling.

The second dump substrate design, and the one chosen for use in TASKA, consists of a parallel array of TZM molybdenum alloy[10] tubes of approximately 10 mm OD and 2 mm wall thickness, the precise value of the latter parameter depending on the particular beam dump under consideration - see later. The tubular dump design is shown in Fig. VIII.3-1 and was chosen in preference to the copper plate design mainly from considerations of ease of construction and of current operating experience with this type of dump design.[4] The tubular dump is cooled by the "force-swirled" technique, by which water is forced along the tube length in a swirl vortex motion induced by an internal twisted tape. Such a motion of the water yields virtually forced-convection cooling of the tube inner wall and increases the heat transfer coefficient of the system over that of a conventional flow system by up to 1.5. Typical coolant conditions for this system are a pressure of 5.4 MPa, a flow rate of 5.14×10^4 ℓ/minute per square meter of surface area and an outlet temperature of 150°C.

The selection of TZM molybdenum alloy (Mo, 0.5 w/o Ti, 0.08 w/o Zr, 0.02 w/o C) as a dump material is attributable to four main factors: it is commonly available in thin walled tubing; it is a refractory metal and can, therefore, withstand high temperatures; it has a long lifetime with respect to stresses; it has relatively low sputtering properties.

Table VIII.3-2 gives the major design parameters for the TASKA neutral beam dumps. Fuller details of these design values are given in an associated publication.[9] It can be seen that no actual dump is required for the low energy barrier beam since the opposing first wall is easily capable of

Table VIII.3-2
TASKA Beam Dump Parameters

	PLUG NEUTRAL BEAM (250 keV p)	BARRIER HIGH ENERGY NEUTRAL BEAM (76 keV D)	BARRIER MEDIUM ENERGY NEUTRAL BEAM (50 keV D/T)	BARRIER LOW ENERGY NEUTRAL BEAM (5 keV D)
DUMP POWER DENSITY - NORMAL OPERATION (kW cm^{-2})	1.0	0.58	0.2	4×10^{-4} (at first wall)
DUMP POWER DENSITY - NO PLASMA CONDITION (kW cm^{-2})	1.27	1.0	4.0	4×10^{-2} (at first wall)
DUMP CONFIGURATION	Rectangular-V	Rectangular-V	Circular-V	No dump required. (Opposing first wall is capable of withstanding power density)
DUMP DIMENSIONS (cm)	29.4x44.1x62.5 (hxwxd)	50.1x71.6x47.5 (hxwxd)	60.1,23.0,33.5 (or,ir,d)	
INCLINATION ANGLE θ	76.7°	61.9°	58.1°	
DISPLACEMENT FROM Z-AXIS (cm)	125.4	587.1	99.5	
MOLYBDENUM SURFACE THICKNESS (cm)	0.2	0.5	0.6	
OUTER SURFACE TEMPERATURE (°C)	510	495	277	
INNER SURFACE TEMPERATURE (°C)	350	265	190	
EFFECTIVE BEAM AREA OVER DUMP (cm^2)	2131	2068	3300	

withstanding the beam power density. However, this opposing first wall region will require recessing due to gas pumping constraints - see below.

It should also be noted from Table VIII.3-2 that the beam dumps for the plug H beam and the high energy barrier beam are single rectangular-V structures as shown in Fig. VIII.3-1, whereas the medium energy barrier coil beam dump is a one piece dump having circular symmetry about the z-axis and accommodates all three beams directed into each barrier coil. Dimensional safety factors have been included for each dump in that their linear dimensions are 50% greater than the expected beam imprints under normal operation.

The dump surface temperatures in the table were obtained from heat transfer calculations on the basis of forced convection and conduction through the substrate. Any effects of burn-out, vibration and erosion on the heat transfer coefficient were not included in these calculations.

It can also be seen from Table VIII.3-2 that the beam dumps have been designed to withstand a maximum steady state power density of 1 kW cm^{-2} under the normal operating conditions of full power density and appropriate plasma trapping fractions shown in Table VIII.3-1. If the plasma should be lost, the power densities of the plug beam and the high energy barrier beam at their respective dumps are still in the region of the maximum design criterion. However, during such an excursion, the power densities for the medium energy beams on the barrier coil dump would rise to 4 kW cm^{-2} which is unacceptable under steady state conditions. Therefore, a significant loss of plasma density in the barrier region would necessitate that these latter neutral beam injectors trip out. Typical shut-off time for the beam injectors is ~ 0.5 ms and, therefore, is much less than the passive thermal inertia of the dump.

VIII.3-11

Steady state testing of the medium energy barrier coil beams could be accomplished in an external test stand with associated large area beam dumps. In situ testing of the beam optics, etc., under plasma conditions would be performed in short (e.g., 10-50 ms) pulses, which again can be accommodated by the thermal inertia of the dump.

VIII.3.4 Dump Location and Vacuum Pumping Considerations

Although methods for vacuum pumping of the beam dump spaces have been described elsewhere in Section IV.5, it is necessary to consider how the pumping requirements can be ameliorated by strategic location of the dumps. In this connection, impact of the residual neutral beams with the dump surfaces has two detrimental effects. Firstly, neutral beam impact causes sputtering of the dump surface with the resulting emission of molybdenum atoms. Secondly, under equilibrium conditions, there is a large backflow of cold neutral gas from the front surface of each dump.

With regard to the sputtered molybdenum atoms, their eventual fate is not clear. They will be emitted from the dump surface as neutral atoms with certain angular and energy distributions. The region in front of each dump will contain a cold plasma region of uncertain density. Therefore, due to either this cold plasma or subsequent incident neutral particles, the molybdenum atoms will eventually undergo ionization. The resulting Mo^{n+} ion will then be directed along a field line in the system which will act as a guiding center for the particle. Depending on the original mean free path (mfp) for ionization, there are now three possibilities. For a short mfp, the molybdenum ion will impact the vacuum wall in the region of the dump, thus initiating the release of impurities from the wall. For a larger mfp, the molybdenum atom will escape the dump space region and, on ionization, will either be

directed to the end of the machine due to the self-cleaning action of the tandem mirror or may become trapped as a deleterious high-Z impurity in the main plasma.

Therefore, with regard to both sputtered Mo atoms and cold gas backflow from the dumps, it is necessary to locate the dumps as far back from the plasma as possible. In the case of the dumps for the plug beam and the high energy barrier beam, this has been accomplished by recessing them a distance of ~ 1 m into the opposite vacuum wall. In the case of the low energy barrier beam, no separate dump is required as described above. However, that portion of the opposite vacuum wall impacted by the residual low energy beam is also recessed by 1 m, thus forming a re-entrant cavity which can be conveniently pumped.

Location of the dump for the three medium energy beams directed into the barrier coil presents a much more complex problem due to the severe space constraints in this region. Figure VIII.3-2 is a cross section of the barrier coil region and shows the location of this dump. The section taken at B - B' is shown as an end-elevation in this figure and illustrates the intersection of the three medium energy beam lines and the dump vacuum pumping ports with the reactor vessel. The section taken at A - A' in Fig. VIII.3-2 is shown in end-elevation in Fig. VIII.3-3; note that the dump is a one piece construction with circular symmetry about the z-axis. If this dump were to be positioned nearer the plasma, pumping of the dump space becomes very difficult; in addition the three individual beam imprints will overlap in the x-y plane, thus increasing the power density at the dump. However, positioning the dump any further back means that the radiation shielding for the normal conducting copper insert coil becomes seriously jeopardized; as it is tungsten shielding

Vacuum pumping port

Vacuum wall

NBI entry duct

SECTION B-B'

Beam dump

B

B'

A

A'
(Fig.VIII.3-3)

SC solenoid

Normal insert coil

Shielding

VIII.3-14
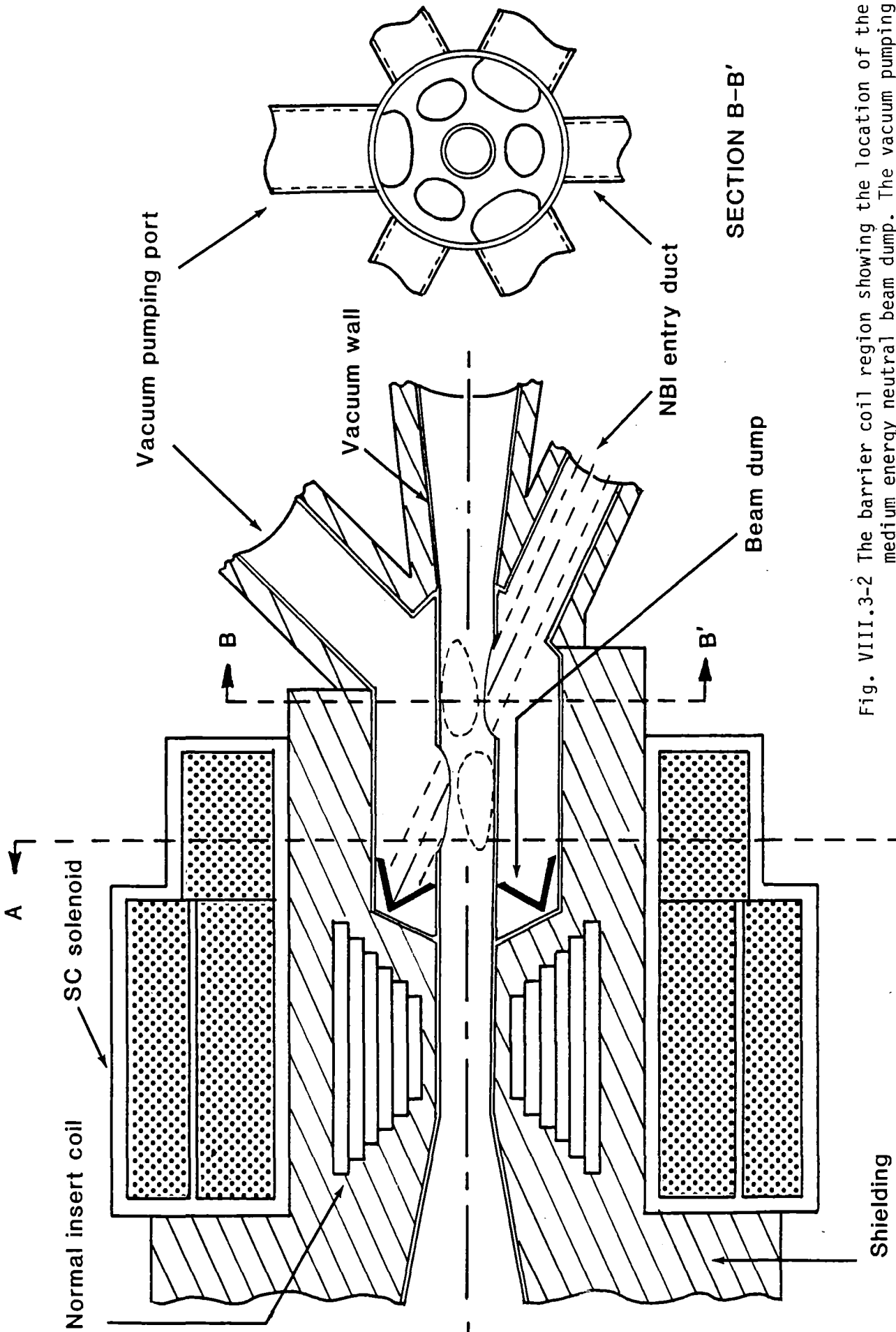
Fig. VIII.3-2 The barrier coil region showing the location of the medium energy neutral beam dump. The vacuum pumping ports for the cold gas backflow from the dump surface are also shown. The section at A-A' is illustrated in Fig. VIII.3-3 .

BARRIER COIL

SHIELD

VACUUM PUMPING DUCT

INSERT COIL

VACUUM CHAMBER

9,5 m   10,15 m   11,55 m   12,6 m
11,3 m

NEUTRAL BEAM INJECTOR DUCT

ION DUMP

0   1   2   3 m

BARRIER REGION WITH ION DUMP

SC coil

Dewar

Shield
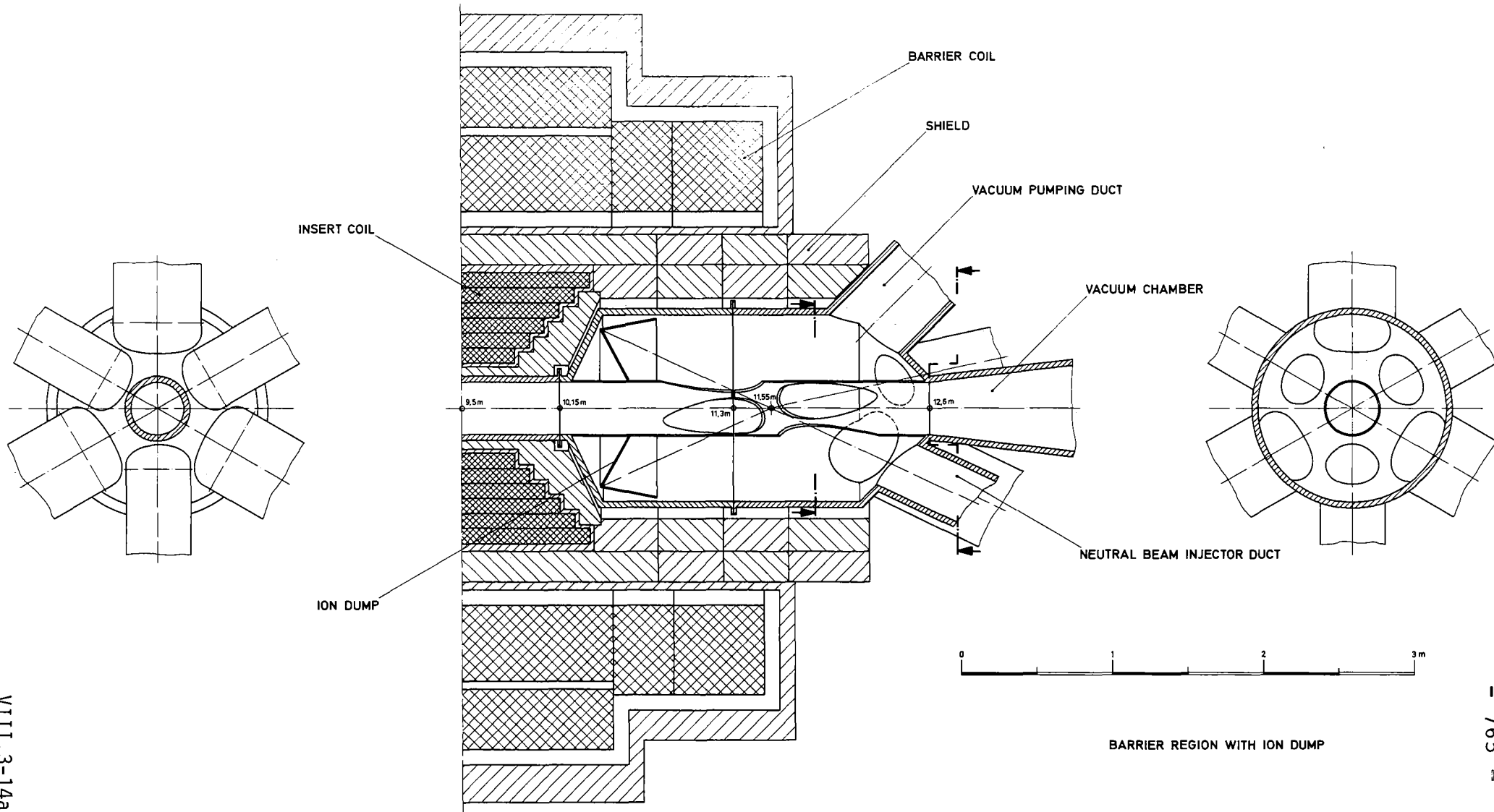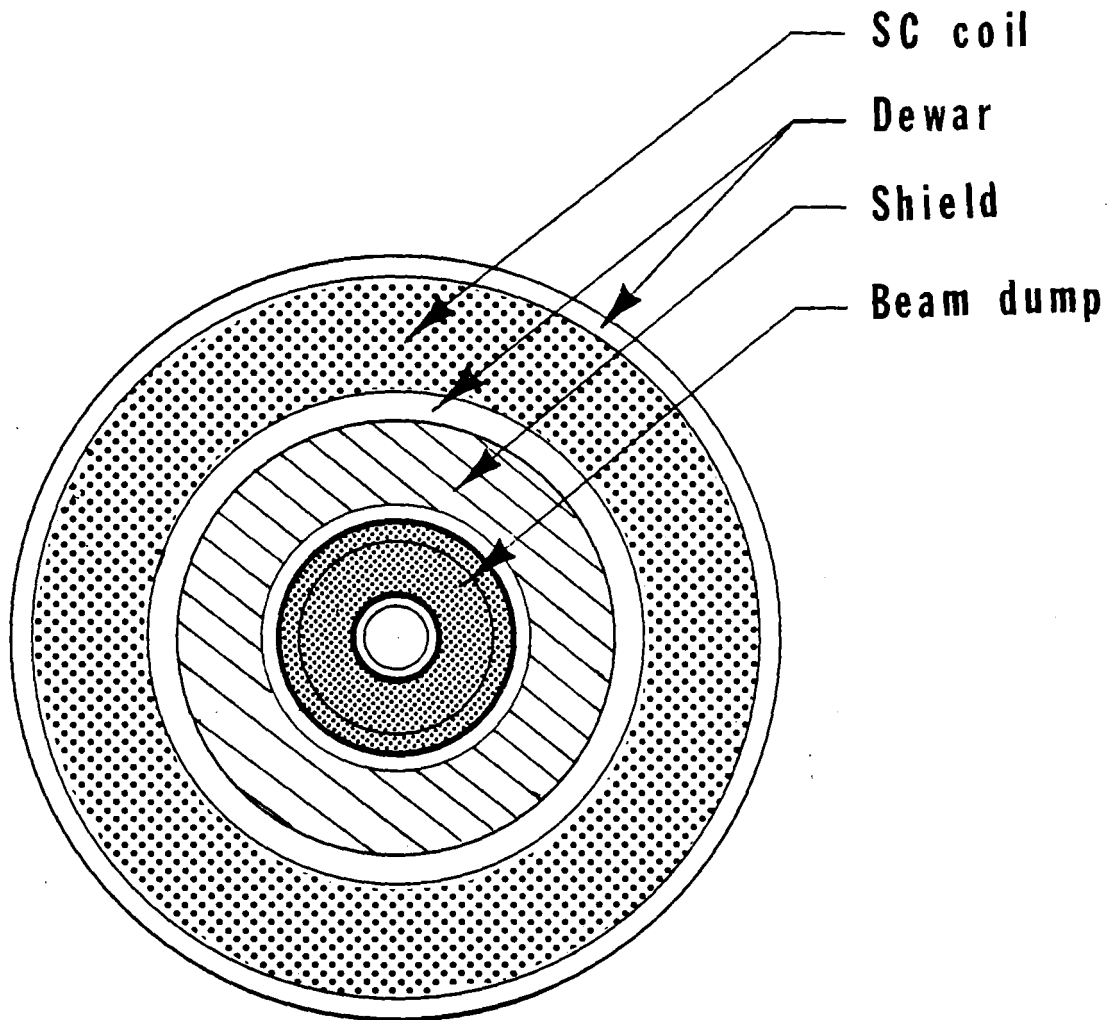
Beam dump

Fig. VIII.3-3 Cross section of the barrier coil region showing the circular-V medium energy neutral beam dump. This is section A-A' from Fig. VIII.3-2 .

must be employed in this region. The location of this dump is, therefore, a compromise between two opposing constraints.

VIII.3.5 Sputtering and Lifetime Considerations

Continual bombardment of the beam dumps by the incident neutral beams produces a gradual erosion of the dump surfaces due to sputtering of the molybdenum substrate. Requirements for estimates of dump lifetimes therefore arise. This is especially important for the medium energy beam dump in the barrier coil since disassembly of the coil assembly due to dump failure is a complex operation with an associated long machine downtime.

Figure VIII.3-4 illustrates the energy dependence of the sputtering yield (in atoms/ion) of molybdenum for H, D, T and ^{4}He ions of normal incidence. The data for H, D and ^{4}He below 10 keV were taken from Roth et al.,[3] while the data above this energy came from an, as yet, unpublished source.[11] Values for tritium were taken from Bay, et al.[12] These curves are not a function of the temperature of the dump surface, since the sputtering of elements by light ions does not increase with temperature providing no chemical reactions occur.[13]

It should be stressed that the data in Fig. VIII.3-4 are for normal incidence. As seen above, the beam dumps are inclined at an angle θ with respect to the incident beam in order to reduce the beam power density by a factor of cosθ. However, as the angle of incidence θ between the incident beam and a normal to the surface is increased to values greater than zero, a significant increase in sputtering yield occurs over those values for normal incidence shown in Fig. VIII.3-4. Sigmund[18] has determined the dependence of the sputtering yield Y(θ) on θ to be
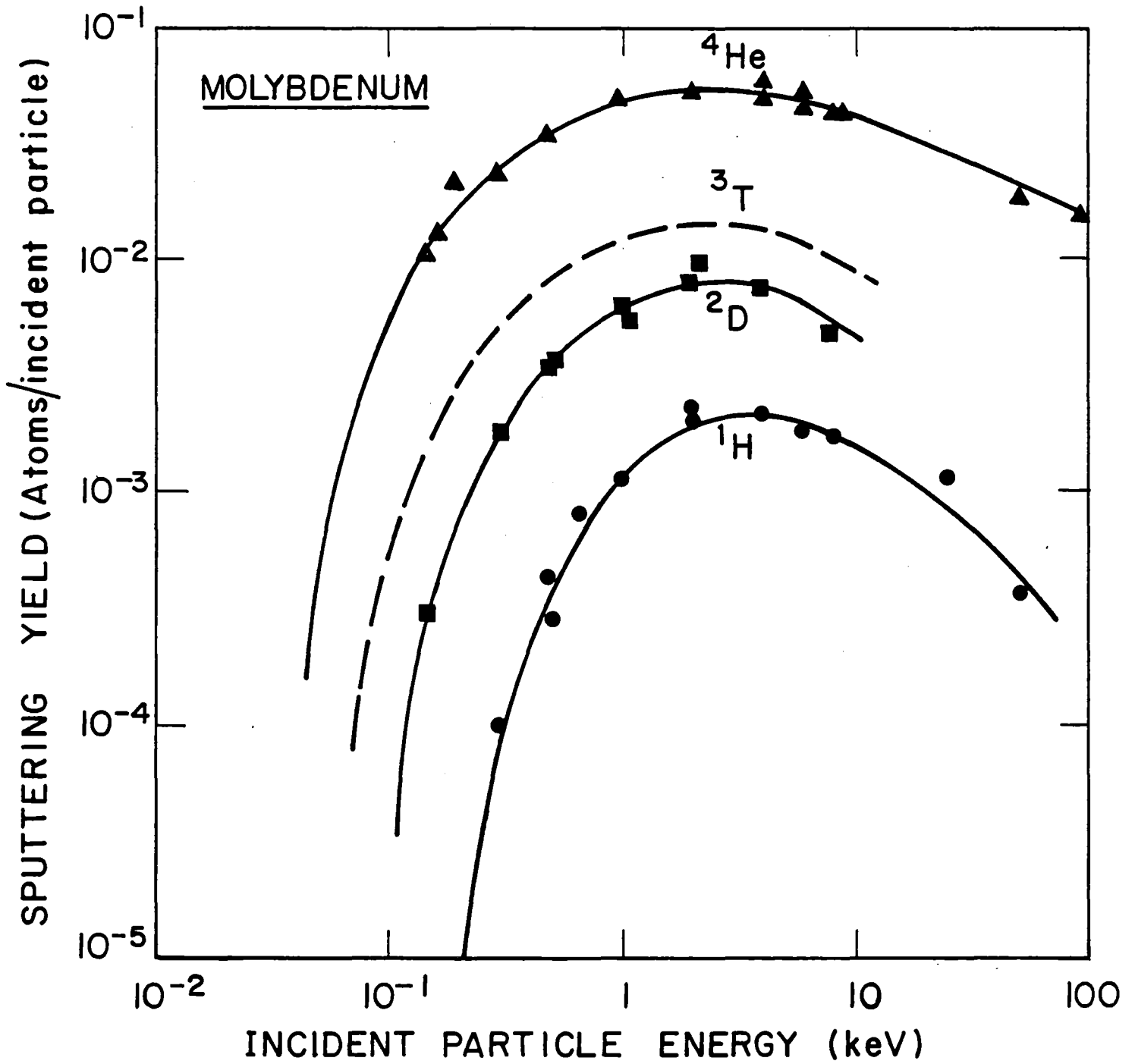
Fig. VIII.3-4 Energy dependence of the sputtering yield for molybdenum at normal incidence.

$$Y(\theta) = Y(o) \cos^{-n}\theta \qquad\qquad (VIII.3-1)$$

where: θ = angle of incidence

Y(o) = sputtering yield at normal incidence

and where n is a factor between 1 and 2 and is a function of the mass ratio of the incident and sputtered particles.

In addition to increasing the sputtering yield, impact of the neutral beam with the dump surface at non-normal incidence has an interesting effect on the angular distribution of the sputtered molybdenum atoms. At normal incidence, the angular distribution of sputtered atoms is diffuse and follows a cosine distribution [actually slightly "over-cosine" due to the contribution of reflected incident ions.[13]]. As the incident beam moves away from normal incidence, the sputtered angular distribution changes from diffuse and becomes increasingly specular with increasing angle of incidence. The peak in the sputtered product distribution, therefore, occurs at an angle of "reflection" approximately equal to the angle of incidence. It can be seen, therefore, that increasing the angle of inclination θ of the V-configuration beam dump, with respect to the incident beam, causes a greater portion of the sputtered molybdenum from one V-plate to be emitted in the direction of the adjacent plate. Thus, in this phenomenon of "cross-sputtering", sputtered material from one surface will tend to plate out on the adjacent surface and thus reduce the overall erosion of the dump surfaces. Note, however, that it is not clear that the redeposited material is as good as the original surface in respect of the latter's relatively low sputtering properties.

It should be noted that self-sputtering yields for molybdenum on molybdenum are considerably greater than the corresponding yields for light ion

sputtering shown in Fig. VIII.3-4. In fact, for incident energies greater than ~ 1 keV, the molybdenum self-sputtering yield becomes greater than unity.[14] In such a case, cross-sputtering would actually be detrimental to dump lifetime. Fortunately, in the energy regime of the TASKA neutral beams, sputtered Mo atoms are emitted in the eV range of energies,[9] thus cross-sputtering enhancement of dump lifetime will occur.

One serious obstacle to an accurate calculation of the beam dump lifetimes due to the sputtering process is that, at angles away from normal incidence, the data base for sputtering is rather deficient, especially at higher energies $\gtrsim$ 10 keV. The paucity of data for angular and energy distributions of sputtered products is particularly marked. For this reason two calculations of the estimated dump lifetimes were performed. Firstly, a worst case lower bound for each dump lifetime was computed by assuming that the increase in sputtering due to non-normal incidence followed a $\cos^{-2}\theta$ dependence. This is the upper limit of current estimates since the factor n in Eq. (VIII.3-1) lies between 1 and 2. In addition, no allowance was made for cross-sputtering in that all initial atoms sputtered from the dump surfaces were assumed to be lost from the system.

In the second, more formal, analysis the current (and rather sparse) data for the actual angular dependence of sputtering yields were taken into account. Also, data on angular and energy distributions of emitted atoms were included, so that some estimation of cross-sputtering enhancement could be obtained. Further details of these calculations may be found in an associated publication.[9]

Table VIII.3-3 documents the results of the above calculations, showing the sputtering rates and estimated lifetimes for the TASKA beam dumps. The

TABLE VIII.3-3
Beam Dump Sputtering
Rates and Estimated Lifetimes

	ESTIMATION FROM FORMAL ANALYSIS			WORST CASE LOWER BOUND		
	DEPTH SPUTTERING RATE OF Mo (cm/s)	DEPTH OF Mo SPUTTERED OVER MACHINE LIFE[1] (cm)	ESTIMATED DUMP LIFETIME[2] (FP YEARS)	DEPTH SPUTTERING RATE OF Mo (cm/s)	DEPTH of Mo SPUTTERED OVER MACHINE LIFE[1] (cm)	ESTIMATED DUMP LIFETIME[2] (FP YEARS)
PLUG NEUTRAL BEAM	5.73×10^{-10}	0.096	> machine life	1.59×10^{-9}	0.27	3.14
BARRIER HIGH ENERGY NEUTRAL BEAM	1.34×10^{-9}	0.22	> machine life	4.79×10^{-9}	0.80	2.65
BARRIER MEDIUM ENERGY NEUTRAL BEAM	8.53×10^{-10}	0.14	> machine life	2.91×10^{-9}	0.49	4.36
BARRIER LOW ENERGY NEUTRAL BEAM	No dump required. (Lifetime of opposing first wall is > machine life).			No dump required. (Lifetime of opposing first wall is > machine life).		

[1] Machine life = 5.3 FP years

[2] Time required to reduce surface thickness to 20% of its original value

lifetime of a particular dump has been defined as the time required to reduce the surface thickness of the dump, by sputtering, to 20% of its original value. This is a rather arbitrary definition of lifetime, but it gives a reasonable safety margin on dump performance, especially since the inner diameter of the molybdenum tubing cannot be assumed to be perfectly regular.

From the table, it is seen that all three dumps will outlast the life of the machine (5.3 full power years) under the results from the formal analysis. In the case of the worst case lower bound estimates, the lifetime of the medium energy beam dump in the barrier coil is seen to be 4.36 which is slightly less than the machine life. However, this is certainly longer than the estimated changeout period for the normal conducting insert coil in the barrier (2.3 FPY) and is, therefore, satisfactory.

The worst case lower bound lifetime estimates for the plug beam dumps and the high energy beam dumps are 3.14 and 2.65 FPY, respectively. Therefore, under this estimation they would require renewing at least once during the operating life of the machine. However, unlike the medium energy beam dump in the barrier coil, they are easily accessible. Lifetimes of this order are, therefore, acceptable.

VIII.3.6 DT and DD Neutron Generation From the Dump Surfaces

VIII.3.6.1 Nature of the Problem

The production of fusion neutrons from the dump surfaces themselves arises from the interaction of incident D or mixed D/T neutral beam particles with the equilibrium deuterium or deuterium/tritium distributions in the respective dump substrates. The neutral species in the plug heating beams are pure protons, thus considerations of neutron production from these dumps clearly do not apply. The high (76 keV) and low (5 keV) energy beams into the

barrier region consist of pure deuterium and thus are capable of DD neutron generation at their dump surfaces. The three medium energy (50 keV) beams into the barrier coil region each comprise a mixed deuterium-tritium species with atomic proportions of 44% and 56%, respectively. Thus, interaction of the D/T beams with the steady state D/T distributions in the dump gives rise to neutron generation via the separate reactions of D on D, D on T and T on D, respectively.

Neutrons resulting from the interaction of incident deuterons with tritium generated in-situ by the other branch of the DD reaction (i.e., D(d,p)T) may be neglected. This is due to the low equilibrium concentration of such tritium compared to the main equilibrium deuterium and tritium concentrations implanted by the incident beams.

Neutrons will also be generated in the medium energy beam dumps via the TT reaction (T(t,2n)^{4}He, Q = 11.33 MeV). Preliminary studies show[19] that the magnitude of the TT neutron-producing cross section in this energy range (i.e., tens of keV) is comparable to that for the DD reaction -- for example, at 50 keV $\sigma_{DD}/\sigma_{TT} \sim 1.34$. However, due to the current paucity of data for this reaction, especially with regard to neutron angular distributions, TT neutron generation was not formally computed in this study; approximate estimates of TT yields will be presented in Section VIII.3.6.3. Work is continuing on this effect.

Accurate computation of neutron production from the dump surfaces, including source intensities and angular distributions of emission, consists of two distinct stages. Firstly, it is necessary to determine the steady state distribution of the neutral D/T species within each dump substrate from consideration of temperature and concentration profiles in the dump surface.

Secondly, computation of neutron production is performed by integration of all DD, DT and TD incremental neutron sources, ranging from the dump surface down to the implantation depths for each D or T neutral particle incident on the dump. Physically, this results in a very complex problem due to the nature of the processes occurring in the dump surface.

Accordingly, formal solution for neutron generation from the dumps required extensive computational effort and resulted in the evolution of the computer code "BDUMP". The code BDUMP computes neutron source and angular distributions resulting from the interaction of D, T or D/T beams with solid or liquid surfaces. It can also be used to compute neutron emission spectra from conventional tritiated or deuterated neutron-producing targets. BDUMP will shortly be available for general use on the U.S. National Magnetic Fusion Energy Computer System at Lawrence Livermore National Laboratory, and further information can be obtained in references 15 and 16.

A brief discussion of the physical mechanisms contributing to neutron generation within the dumps will now be given. Complete details will be given in an associated publication[15], while a concise overview may be found in Ref. 20.

VIII.3.6.2 Substrate Equilibrium Particle Distributions and Tritium Loss Rates

The incident D neutrals, or D/T neutrals for the medium energy barrier coil beams, slow down in the dump substrate and stop at their respective implantation depths. This latter parameter is a function of the energy of the particles and their specific energy loss (dE/dx) in the medium. For example, the implantation depth of 50 keV deuterium atoms in pure molybdenum is ~ .5 µm. Once brought to rest, the D or D/T atoms diffuse, both forward and backwards, from their implantation site under the action of the resulting concentration

gradients. However, the resulting concentration profiles cannot be accurately computed from a simple one region diffusion problem for two reasons. Firstly, for high neutral beam intensities, the stopping power for incident particles depends on the dE/dx parameters for both the substrate atoms and those neutral atoms already implanted in the dump plate. Thus, as the number density of implanted atoms becomes comparable to that of the substrate, the implantation depths for subsequent incident particles tends to decrease, moving towards the surface. Note that, in addition, the implantation depths for the incident D and T particles in the barrier coil dump will be different due to the different energy per unit mass of these ions. Secondly, under normal operation there is an appreciable temperature gradient between the front and rear (coolant) surfaces of each dump; therefore, the diffusion coefficient $D_j(x)$ of each particle type j is a function of position in the material.

Once equilibrium has been reached, there will be a steady state profile of D or D/T within each dump and a constant flow rate of cold D or D/T particles from both the front and rear surfaces equal to the particle implantation rate from the beam.

The formal solution to the diffusion equation for this medium, where the diffusion coefficient is a function of position, is given in the associated publications.[9,15] It is shown there that the ratio R_j of the flow rate of particles of type j from the rear coolant surface of the dump to the flow rate from the front surface of the dump is given by

$$R_j = \frac{\left| F\left(\frac{k_j}{m\delta_j + c}\right) - F(k_j/c) \right|}{F\left(\frac{k_j}{m(\delta_j - t_1) + c}\right) - F(k_j/c)}$$

(VIII.3-2)

VIII.3-24

where

$$F(x) = -\frac{e^x}{x} + \ln x + \sum_{n=1}^{\infty} \frac{x^n}{n \cdot n!}$$

$$m = (T_f - T_r)/t_1 \ ,$$

$$c = T_f + \frac{\delta_j}{t_1} (T_r - T_f)$$

$$R_j = \Delta H_j / R$$

and where

t_1 = dump thickness

δ_j = implantation depth of particle type j

T_f = absolute temperature of front surface of dump

T_r = absolute temperature of rear (coolant) surface of dump

R = gas constant

ΔH_j = diffusion activation energy for particle type j (assuming that the temperature dependence of the diffusion coefficient follows $D_j(T) = D_{0_j} \exp(-\Delta H_j/RT)$).

VIII.3-25

Computing the tritium flow-rate ratio to the rear (coolant) and front

surfaces of the barrier coil beam dumps yields a value of $R_j = 2.09 \times 10^{-5}$.

This translates to a total tritium loss to the dump coolant of 5.68 kCi per

year which is very large. It is interesting to note that had the relatively

small temperature gradient across the plate ($T_f = 277°C$, $T_r = 190°C$) been

neglected, the resulting tritium flow to the coolant would have been

overestimated by a factor of ~ 4.

It should also be noted here that the inclusion of a thin metal surface

of low tritium diffusivity between the molybdenum substrate and the coolant

can promote a drastic improvement in the tritium retention of the dump.

Aluminum is a candidate material for this "tritium-buffer zone" and could

possibly be applied by vapor deposition or similar process. If the

positional/temperature dependence of the diffusion coefficients within each

zone is neglected here for simplicity, then the equation for the flow rate

ratio becomes

$$R_j = \frac{\delta_j}{(D_{1_j}(x)/D_{2_j}(x)) \, t_2 + t_1 - \delta_j} \qquad \text{(VIII.3-3)}$$

where:

δ_j = implantation depth of particle type j

t_1 = thickness of dump surface

t_2 = thickness of tritium-buffer material

$D_{1_j}(x)$, $D_{2_j}(x)$ = diffusion coefficients of particle j in regions 1 and 2.

Thus, neglecting the positional dependence of D_{1_j} and D_{2_j}, a backing

region of aluminum of thickness in the range 10-100 μm would reduce the

tritium diffusion to the coolant in the range 0.36% - 0.036% of its former

value at a dump surface temperature of $\sim 200^\circ$C. This is a significant decrease!

VIII.3.6.3 Neutron Production

Once the equilibrium particle distributions have been ascertained, the BDUMP code proceeds to determine the neutron production distributions. These are computed by discretizing the implantation range in the dump substrate for each incident particle type into a finite number of slowing down bins. The differential neutron yield at any specified energy and emission angle (i.e., neutrons cm^{-2} s^{-1} per unit solid angle) originating from each incremental depth/energy bin is then a function of the local equilibrium D or D/T number density and the respective differential cross sections for that bin. The total number of neutrons per steradian which originate from energy bin E_i and emerge from the dump at a laboratory angle θ with energies between E_n and $E_n + dE_n$ per incident (D or T) particle is

$$\sum_{i,j} N_{ij} (\theta, E_n) dE_n = \sum_{i,j} \frac{\frac{d\sigma_{ij}}{dw'} (E_i, \theta') \frac{dw'}{dw} (E_i, \theta) n_j (E_i) \frac{dE_i}{dE_n} (E_n, \theta) dE_n}{-dE_i/dx}$$

$$\text{(VIII.3-4)}$$

where i = incident particle (D for high and low energy beams, D or T for medium energy beams)

j = target particle (D for high and low energy beams, D or T for medium energy beams)

E_i = instantaneous energy of incident particle i at a specific depth in surface

θ = neutron emission angle in lab frame

θ' = neutron emission angle in cm frame

$d\sigma_{ij}/dw'$ = differential cross section in cm for reaction of particle i with j

dw'/dw = ratio of solid angles in cm and lab frames

$n_j(E_i)$ = number density of target particle j in dump where incident particle has energy E_i

dE_i/dx = specific energy loss for incident particle i at energy E_i in surface (contributions from both dump substrate material and target particle distribution).

The neutron energy E_n at a lab emission angle θ is related to the instantaneous incident particle energy E_i at a specific depth by considerations of the kinematics of the j(i,n) neutron-producing reaction. The total neutron yield at a given lab angle θ is then given by the integral of Eq. (VIII.3-4) with respect to the instantaneous energy E_i of the incident particle, from its maximum value at the surface of the dump down to zero at the implantation depth. In BDUMP, this is equivalent to summing the angular yields from each incremental energy/depth bin in the implantation range. Further details of these processes may be found in Ref. 15.

Figure VIII.3-5 illustrates the BDUMP computed neutron yields arising from the interaction of each medium energy neutral beam (56% T, 44% D) with the beam dump in the barrier coil. Neutrons are seen to result from the DD reaction (D on D) and the DT reaction (D on T and T on D). The yields shown in Fig. VIII.3-5 should be multiplied by three for the total yield from each dump. The neutron yields for each reaction type are plotted as a function of the surface temperature of the dump. The strong dependence of the neutron source strength on this latter parameter is attributable to the temperature
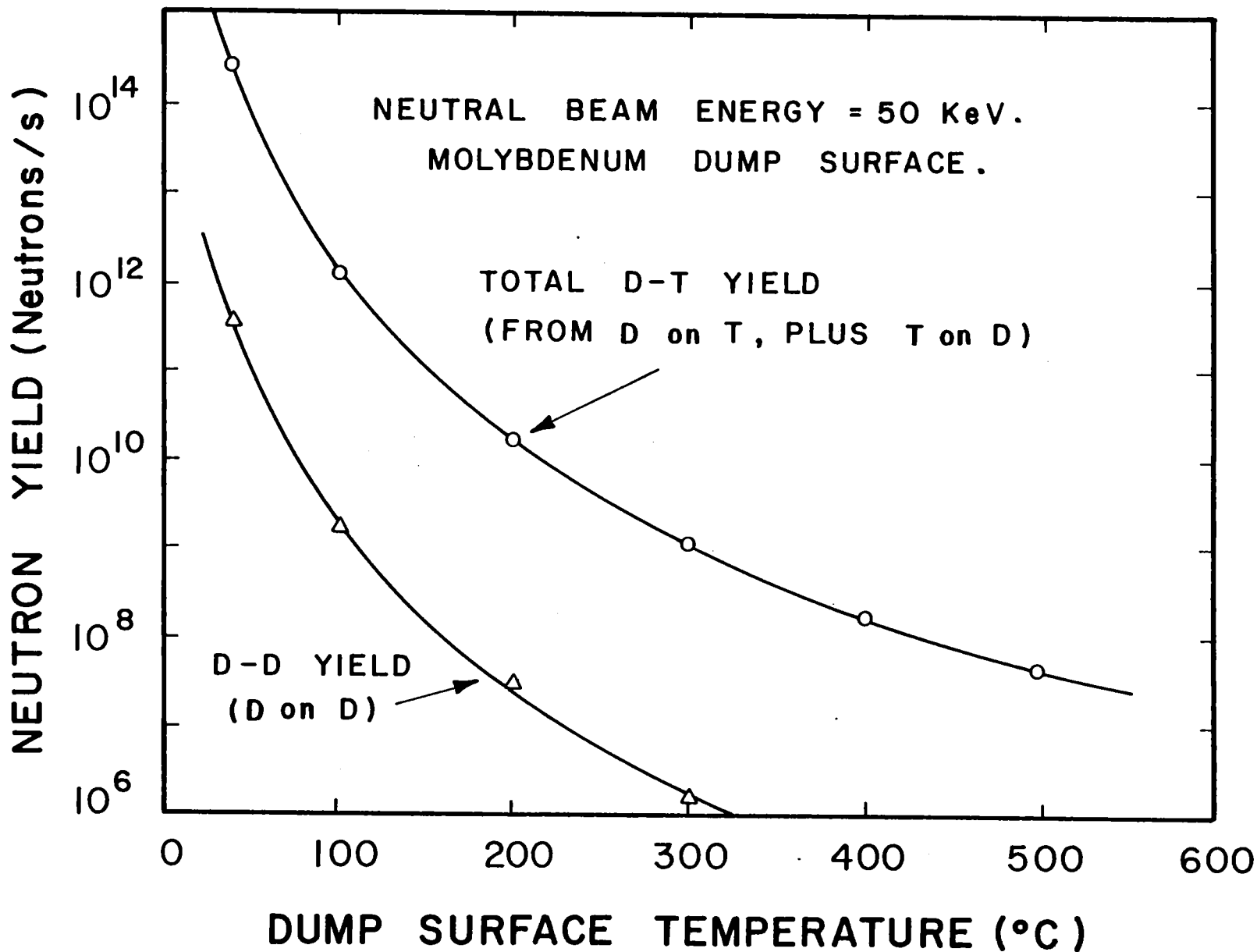
Fig VIII.3-5 Beam-induced neutron production from the medium energy neutral
beam dump (via the code BDUMP). The incident beam current and
energy are 8.27 A and 50 keV, respectively, and consist of 56%
T and 44% D neutrals.

dependence of the diffusion coefficients for tritium and deuterium in the molybdenum substrate. Note that for a fixed substrate equilibrium D/T number density, the neutron yield would be proportional to the incident beam current. However, this equilibrium D/T particle density in the dump is also proportional to the beam current. Therefore, the neutron yield from the beam dump is proportional to the square of the incident neutral beam current. See Refs. 15, 16, and 20 for further details.

As expected from Fig. VIII.3-5, the DD neutron yield is about two orders of magnitude smaller than the DT yield at any surface temperature. This is due to the relative magnitudes of the DD and DT cross sections for incident neutral D or T particles at these energies (50 keV at the dump surface through zero at the implantation depth).

Production of neutrons from the dump via the $T(t,2n)^4He$ reaction was discussed above in Section VIII.3.6.1. In view of the fact that the magnitude of the TT cross section is ~ 0.6 of the DD cross section at 50 keV[19] and that two neutrons are emitted per reaction, it may be expected that the TT yield for this dump is comparable to the DD yield shown in Fig. VIII.3-5. Since the TT reaction (Q = 11.33 MeV) involves a 3-body breakup, the reaction kinematics for the output neutrons are complex. In addition, angular distributions for this reaction are poorly known. For this reason, the reaction is not, at present, included in the BDUMP code. Work is, however, continuing on this effect.

In the case of the high (76 keV) and low (5 keV) energy deuterium neutral beams into the barrier, there is only the DD reaction to consider. For the high energy beam, the equivalent deuteron current to each dump is only approximately half that for each of the medium (50 keV) energy beams into the

VIII.3-30

barrier coil dump. However, the cross section for the DD reaction at 76 keV is ~ twice that at 50 keV and neutrons are produced for all deuteron energies ranging from these values down to zero at the respective implantation depths. Therefore, the total DD neutron yields from the high energy neutral beam dumps will be close to those shown in Fig. VIII.3-5 for the medium energy dumps.

In the case of the low energy deuterium neutral beam, the value of the DD cross section at the energy of the incident deuterons at the surface of the dump (i.e., 5 keV) is several orders of magnitude less than the cross section at 50 keV. Neutron yields are, therefore, similarly reduced by about this factor and may be safely neglected when compared with the contribution from the main fusion plasma in the end cell.

Given the results of Fig. VIII.3-5, it is interesting to compare the resulting neutron fluxes with those stemming from the main fusion plasma in this region. The barrier coil dump will be operated with a surface temperature in the range 200-300°C. Accordingly, at the edge of the tungsten shield facing the circular beam dump, the flux of 14 MeV neutrons arising from neutral beam production within the dump is ~ 1.5×10^7 cm^{-2} s^{-1}. To compute the equivalent flux due to the plasma, a one-dimensional neutron transport calculation was performed across the mid-plane of the barrier coil employing the discrete-ordinates code ONEDANT[17] in cylindrical geometry. At the outer surface of the normal-conducting insert coil in the barrier (an x-y displacement from the z axis comparable to that for the beam dump), integrated neutron fluxes above a neutron energy E_n were determined to be ~ 2×10^8 cm^{-2} s^{-1} for $E_n \geqslant 1$ MeV and ~ 6.4×10^7 cm^{-2} s^{-1} neutrons per second for $E_n \geqslant 10$ MeV.

It can be seen, therefore, that, in the vicinity of the dump space, the neutron production from neutral beam dumps can be within an order of magnitude

of the neutron production from the main plasma itself, especially in the case of mixed deuterium-tritium beams. In general, therefore, in the case of neutral beam dumps for deuterium and deuterium-tritium neutral beams which are situated outside of the shielding for the main fusion neutron/gamma ray fluxes, appropriate shielding precautions should be taken against DD and DT neutrons emanating from the dumps themselves.

In conclusion, the following question should be posed: Given a D or D/T neutral beam of fixed specifications (i.e., fixed energy, power, trapping fraction, etc.), how can the resulting neutron production at the beam dump(s) be minimized? One very effective way to achieve this is to operate the dump at the highest possible surface temperature consistent with heat transfer constraints. From Fig. VIII.3-5, for example, increasing the surface temperature of the medium energy beam dump from 200°C to 400°C (i.e., a factor of two) decreases the DT neutron yield by more than two orders of magnitude.

A second method of reducing the neutron yield is to select a substrate material possessing a high tritium diffusion coefficient in that temperature range envisaged for dump operation. It was shown in Eq. (VIII.3-3), that the tritium flow rate from the dump surfaces is a function of the variation of the diffusion coefficient with the temperature gradient across the dump. The magnitude of the equilibrium D, T or D/T number density n_j, on the other hand, is a strong function of the absolute value of the diffusion coefficient for the substrate (see the associated publications in Refs. 9 and 15). Therefore, from Eq. (VIII.3-4), so is the resulting neutron yield.

Figure VIII.3-6 illustrates the above dependence of neutron yield on the tritium diffusion coefficient of the dump substrate where the neutron yields from the medium energy beam dumps are shown for the cases of a molybdenum
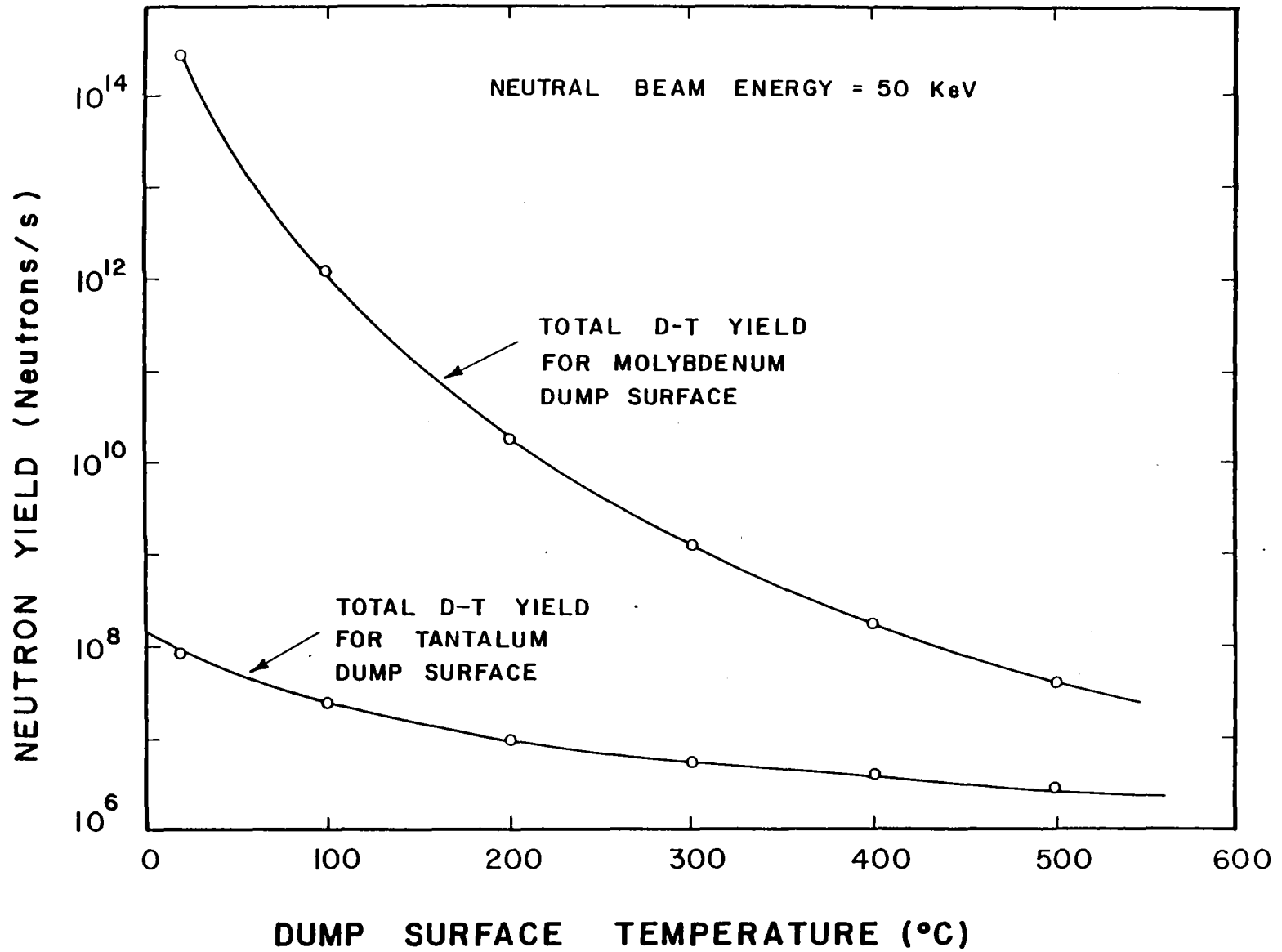
Fig. VIII.3-6 A comparison of beam-induced DT neutron production from molybdenum
and tantalum dump surfaces (via the code BDUMP).

(reference design case) and tantalum dump surface. Tantalum has a very high tritium diffusivity relative to molybdenum and can be seen to result in a reduction in neutron yield of almost three orders of magnitude.

Although tantalum is also a refractory metal and thus has high heat load and stress capabilities, it was not considered to be a suitable material for the barrier coil beam dump in place of molybdenum for three reasons. Firstly, it has inferior sputtering (and thus lifetime) properties; secondly, the action of a tritium-buffer layer such as aluminum is much less successful when incorporated with a dump substrate material of high intrinsic tritium diffusivity; thirdly, there is little or no current operating experience of high heat flux dumps employing tantalum substrates. In addition, the barrier coil dump is situated in a well-shielded environment and thus high neutral-beam-induced neutron yields are of less consequence than in the case of a remote dump. An example of the latter situation can be seen in the case of the ion dumps internal to the medium energy neutral beam injectors. Here, careful thought should be given to the choice of the dump material, especially with regard to neutron production.

References for Section VIII.3

1. W.E. Harbaugh, "The Development of a High Energy Density Heat Sink," Proc. 8th Symp. on Engineering Problems of Fusion Research, IEEE Publication 79CH1441-5 NPS, (1979) p. 996.

2. R.W. Moir, C.E. Taylor, and M.A. Hoffman, "New Concept for a High Power Beam Dump," UCRL-83696, Lawrence Livermore Laboratory (1981).

3. J. Roth, J. Bohdansky and W. Ottenburger, "Data on Low Energy Light Ion Sputtering," IPP 9/26, Max Planck Institut für Plasmaphysik (1979).

4. R.R. Stone, Lawrence Livermore National Laboratory, private communication (1981).

5. C.C. Thompson, D.H. Polk, D.J. McFarlin, and R.R. Stone, "Heat Exchanger Concepts for Neutral Beam Calorimeters", Proc. 9th Symp. on Engineering Problems of Fusion Research, Chicago, Oct. 1981, IEEE (to be published 1982).

6. K.I. Thomassen, "The Tandem Mirror Fusion Test Facility," Energy and Technology Review UCRL-52000-80-8, 1 (1980).

7. W. Gambill and N. Green, "A Preliminary Study of Boiling Burnout Heat Fluxes for Water in Vortex Flow," ORNL CF-58456, Oak Ridge National Laboratory (1958).

8. R.W. Moir, Lawrence Livermore National Laboratory, private communication (1981).

9. L.J. Perkins, "High Power Neutral Beam Dumps for the TASKA Tandem Mirror Fusion Test Facility," University of Wisconsin Fusion Engineering Program Report UWFDM-451 (to be published, 1982).

10. "Molybdenum for Nuclear Energy Applications - A Perspective," (Climax Molybdenum Co., NY, 1964) p.46.

11. J. Roth, Max Planck Institut für Plasmaphysik, Garching, private communication (1981).

12. H.L. Bay, J. Roth and J. Bohdansky, "Light Ion Sputtering Yields for Mo and Au at Low Energy," J. Appl Phys., 48, (1977) 4722.

13. J. Bohdansky, "Important Sputtering Yield Data for Tokamaks: A Comparison of Measurements and Estimates," J. Nucl. Mater., 93, (1980) 44.

14. D.L. Smith, "Physical Sputtering Model for Fusion Reactor First-Wall Materials," J. Nucl. Mater., 75 (1981) 20.

15. L.J. Perkins, "DT and DD Neutron Production from High Power Neutral Beam Dumps," University of Wisconsin Fusion Engineering Program Report UWFDM-435 (to be published, 1982). Also to be submitted to Nucl. Tech./Fusion in 1982.

16. L.J. Perkins, "BDUMP: A Code for the Computation of Beam-Induced DT and DD Neutron Production from High Power Neutral Beam Dump Surfaces," University of Wisconsin Fusion Engineering Program Report UWFDM-452 (to be published, 1982). This will also be availabe with the code package itself from MFECC, Lawrence Livermore National Laboratory.

17. R.D. O'Dell, F.W. Brinkley, Jr., and D.R. Marr, "Users Manual for ONEDANT: A Code Package for One-Dimensional, Diffusion-Accelerated, Neutral-Particle Transport", Los Alamos National Laboratory Report (to be issued 1982).

18. P. Sigmund, Phy. Rev. 184 (1969) 383.

19. G.M. Hale, Los Alamos National Laboratory, private communication (1981).

20. L.J. Perkins, "Generation of DT and DD Neutrons from High-Power Neutral-Beam Dumps," Trans. Am. Nucl. Soc. (to be published, June 1982).

VIII.4 Direct Convertor

A single-stage plasma direct convertor module has been incorporated into the TASKA design to provide direct conversion of the escaping ion kinetic energy to electricity. A direct convertor is required only at one end since the ion end loss can be directed out one end. This is accomplished by lowering the potential of one plug slightly relative to the other plug. As central cell ions upscatter in energy, they escape out the lower potential plug before acquiring enough energy to escape out the other plug. The electron end loss can be directed out the end opposite to the direct convertor by biasing that end wall slightly positive relative to the ground potential at the entrance of the direct convertor. The main benefit of directing the electrons out the end opposite to the direct convertor is that the heat load on the entrance grid of the direct convertor is drastically reduced; it only has to handle the power carried by the small fraction of ions intercepted by the grid and not the entire electron power.

The obvious way to design a tandem mirror reactor with a direct convertor is then to put the direct convertor at one end and to use a simple thermal dump for the electron heat load at the other end. This configuration was used in the Livermore tandem mirror reactor design[1] and in WITAMIR-I.[2] A unique feature of the tandem mirror is the narrow energy distribution of the ions entering the direct convertor. This is because they have fallen through the potential $\phi_c + \phi_e$ (see Section III.2) which is many times the ion temperature in the central cell. Consequently, a single stage plasma direct convertor (PDC) provides adequate efficiency.

The purpose of the direct convertor module is to provide testing of direct convertors; the direct convertor is not required for operation of TASKA.

VIII.4-1

A single module which intercepts only a fraction of the magnetic flux at the end wall is used. The module can be attached to the end wall by a gate valve and removed without disturbing the vacuum in the main chamber. When the module is removed, the port hole is covered by a cooled plate. This plate and the rest of the end wall receive a heat flux of 100 W/cm^2 and must be cooled. A schematic is shown in Fig. VIII.4-1. An on-axis port allows testing the direct convertor in the radiation environment due to neutrons streaming down the axis. An off-axis port allows testing in a reduced radiation environment. The cooled plate at the same end as the direct convertor is referred to in this section as the ion thermal dump. The cooled end wall at the other end of the machine is referred to as the electron thermal dump.

A contributor to energy loss in the PDC is the high energy alpha particles. About 5% of the alpha particles are born inside the loss-cone of the central cell and immediately escape out the ends. Because their energy is much greater than the potential, they go equally out both ends. Approximately 30% of the fusion-born alphas scatter into the loss-cone while downscattering in energy; these also go equally out both ends unless one makes the peak field of the barrier at one end higher than that at the other end. Of the alpha particles entering the direct convertor, only a small amount of their energy is converted to electric power; they enter the PDC with a kinetic energy substantially greater than twice the PDC voltage.

The TASKA direct convertor is described in the following sections. The composition of the power incident on the thermal dump and entering the direct convertor is given in Section VIII.4.1. The details of the various grids and collector plates in the direct convertor are described in Section VIII.4.2.

DIRECT CONVERTOR MODULE

CRYOPANEL

COOLED END WALL

DIRECT CONVERTOR MODULE

CRYOPANEL

GATE VALVE
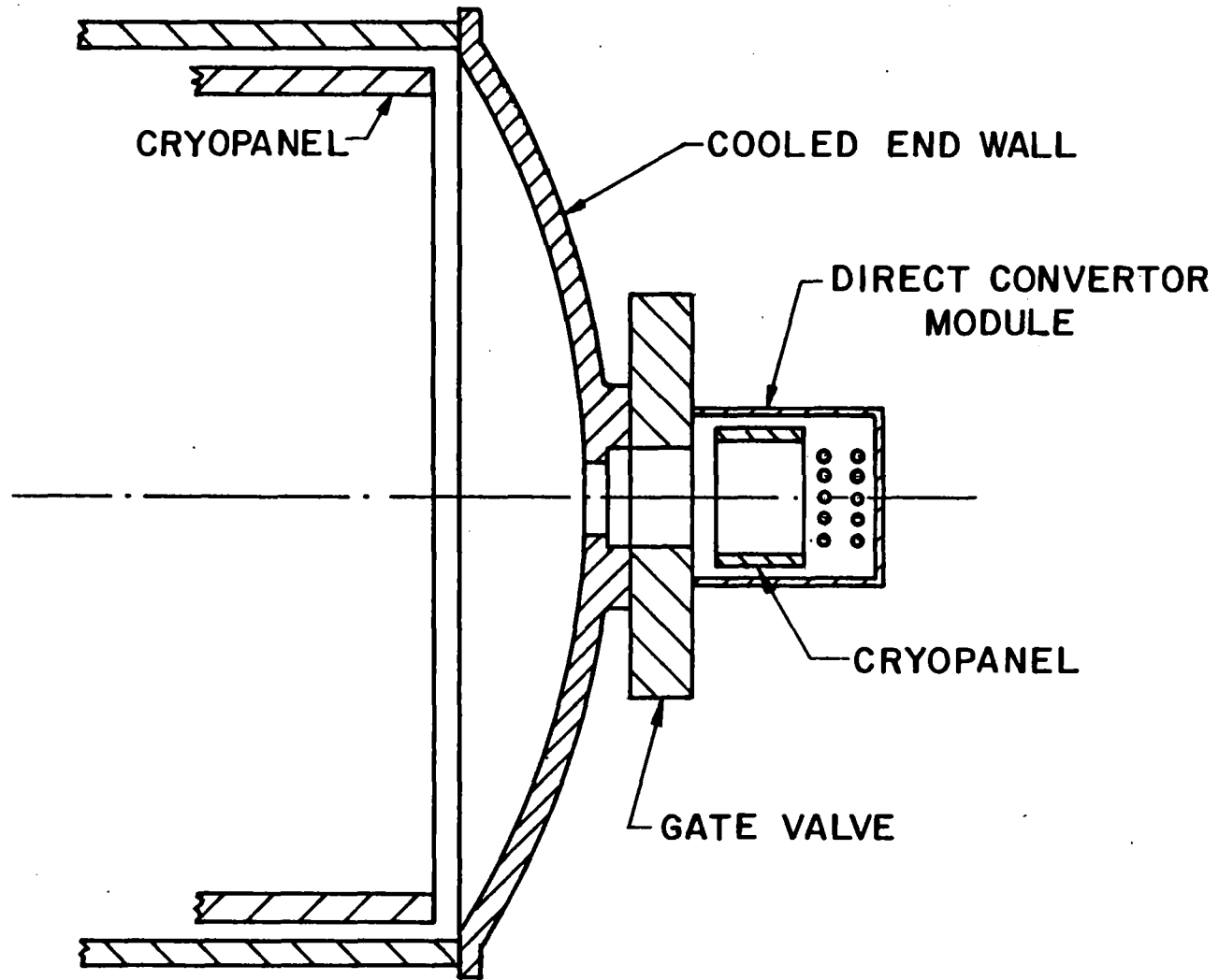
Fig. VIII.4-1

Finally, a comparison of the module to the WITAMIR-I direct convertor is made in Section VIII.4.3.

VIII.4.1 Particle and Energy Flow to the Direct Convertor and Thermal Dumps

The basic parameters describing the central cell plasma, the end loss rates, and the electrostatic potentials are given in Section III.4. These parameters determine the species mix and energy spectrum of the particles entering the direct convertor at one end and incident on the electron and ion thermal dumps.

The central cell ions escaping through the end plug have essentially zero parallel kinetic energy as they pass over the plug potential and are accelerated by the potential $(\phi_c + \phi_e)$ before entering the direct convertor. They also carry with them a certain amount of perpendicular kinetic energy which is roughly T_{ic}, the central cell ion temperature. Consequently the mean energy of the central cell ions entering the PDC is 139 keV, while the minimum energy is 109 keV. This relatively narrow energy spectrum is advantageous for the direct convertor. The mean energy coupled with the ion loss rate gives a power of 78 MW approaching the ion end wall. In addition, the plug ions (protons) leave the plug with an energy of about 198 keV. This contributes another .6 MW to the power approaching the ion end wall.

The remaining ionic species are the fusion born alpha particles. These see a mirror ratio (determined by the barrier peak field and the beta-corrected central cell field) of 10. Since the alphas are born isotropically in velocity space, 5% are in the loss-cone and leave the central cell immediately with an energy of 3.5 MeV. They are then accelerated by the electric field and approach the ion end wall with an energy of 3.7 MeV, which corresponds to .4 MW of power. The remaining 95% of the alphas are magnetically

trapped in the central cell and slow down, first by electron drag and then by scattering off ions when their energy is lower. Approximately 31% are estimated to enter the loss-cone with an energy of approximately 680 keV. These alpha particles contribute 1.2 MW. One half of the alpha particles are assumed to exit at the ion end and the other half to go to the thermal dump. The remaining 64% of the alphas are electrostatically as well as magnetically contained in the central cell. They thermalize with the central cell ions and are lost axially. Because of the relatively low value of $\phi_c/T_{ic} \simeq 1.46$, the axial confinement time of thermal alphas is sufficiently short so that their equilibrium fraction in the central cell is $\simeq 1\%$.

The central cell electrons are confined axially by the potential ϕ_e; those electrons reaching the dump have little parallel kinetic energy and a perpendicular kinetic energy of about T_{ec}. This represents a power of 6.6 MW incident on the electron thermal dump. The plug electrons enter the central cell electron population upon upscattering in energy to above their confining potential of $\phi_c + \phi_b$; this is not an additional loss from the system.

In addition to the energy carried by charged particles out the ends, energy leaves the plasma by energetic neutral atom transport, mostly in the barrier, and by synchrotron and bremsstrahlung radiation. This is estimated to contribute 9 MW. This is relevant for the blanket and shield design, but not for the direct convertor or thermal dumps, since they would receive only a minute portion of that power.

The power approaching the ion end wall is given by the sum of the central cell ion power, half the plug ion power, and half the energetic alpha power, which adds up to 81 MW. The electron thermal dump receives the central cell electron power, and the other half of the energetic alpha and plug ion power.

The total power incident on the electron thermal dump is then 8.2 MW. The electrical current approaching the ion end wall is given by the particle loss rate and charge for each species entering the PDC. The total current is 569 amps. The efficiency of the direct convertor is calculated in Section VIII.4.4. These results are summarized in Tables VIII.4-1 and VIII.4-2.

Table VIII.4-1   Input Power and Current to Ion End Wall

	Power, MW	Average Energy, keV	Current, A
Central Cell Ions			
(50% D-T)	78.3	139	563.
Plug Ions	.6	307	2.1
Prompt Alphas	.4	3,630	.1
Scattered Alphas	.6	808	.7
Thermal Alphas	.8	248	3.1
TOTAL	80.7		569.

Table VIII.4-2   Input Power and Current to Electron Thermal Dump

	Power, MW	Average Energy, keV	Current, A
Central Cell Electrons	6.6	11.5	-576.
Plug Ions	.6	307	2.1
Prompt Alphas	.4	3,630	.1
Scattered Alphas	.6	808	.7
TOTAL	8.2		-573.

VIII.4.2 Grid and Collector System

The minimum ion energy entering the direct convertor is 109 keV; hence the collector voltage relative to ground (the thermal dump) is set just below this value to collect all ions. We chose 100 kV in order to allow some loss of energy between the end plug and the collector; this could be due to scattering by neutrals or deflection by the non-planar electric fields near the grids. In front of the collector plate are the entrance grid and electron repeller grid, as shown in Fig. VIII.4-2. The potential of the ion thermal dump and entrance grid are taken to be zero; this defines the machine ground potential. The potential of the electron thermal dump at the opposite end of the machine is set to be slightly positive (~ 1 kV) in order to assure electron collection at that end. The electron repeller grid prevents low energy electrons near the entrance grid from reaching the collector plate. If they were allowed to reach the collector plate, the electrons would hit it with high energy. This would generate heat and reduce the collected current. The second grid (electron repeller grid) is set more negative (-9 kV) to correct for the non-planar electrostatic potential surfaces near the grids. The system is analogous to a triode vacuum tube, as noted by Barr.[4] The repeller grid voltage is set so that the system operates in the cut-off condition; electrons reaching the entrance grid are prevented by the repeller grid from reaching the collector plate.

The grids intercept a fraction of the ion current entering the PDC. This produces a heat load which must be removed by cooling. The ion end wall also experiences the same heat load. Its cross sectional area is set so that the peak power density does not exceed 150 W/cm^2. This gives a radius of 415 cm and requires expansion of the magnetic field to 110 G at the end wall. The

GRIDS AND COLLECTOR IN THE DIRECT CONVERTOR
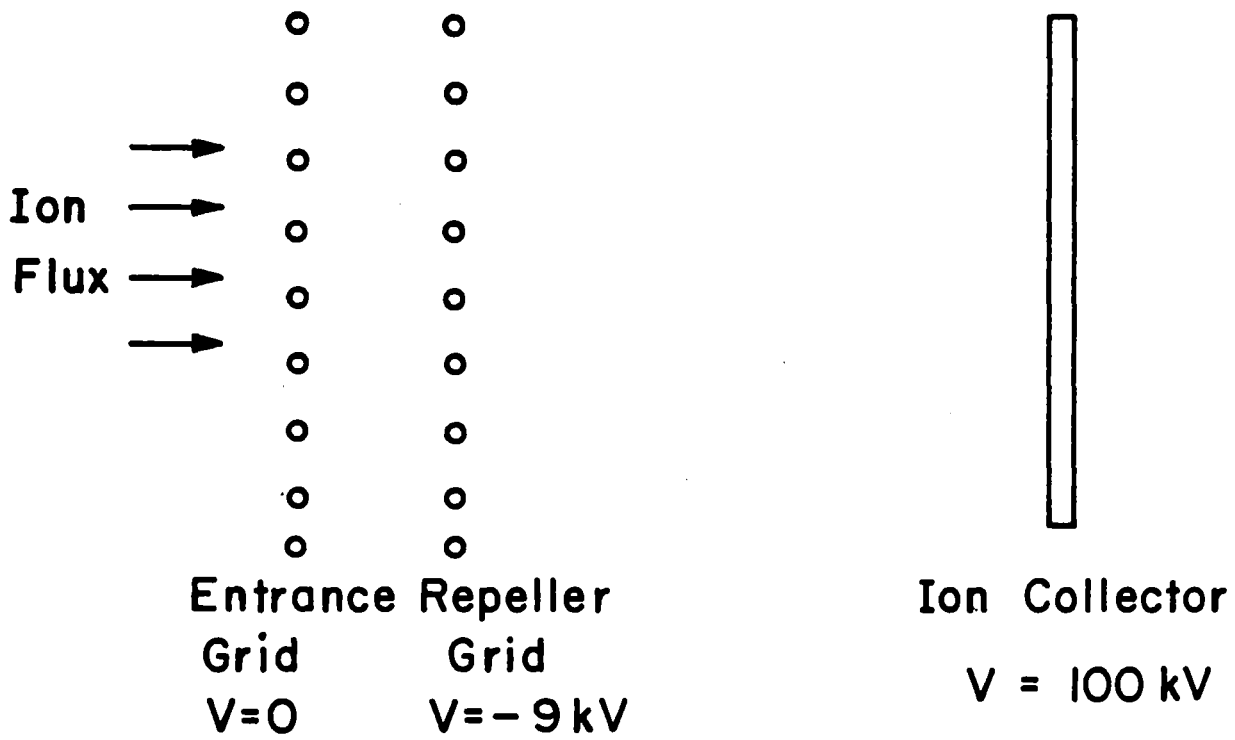
Fig. VIII.4-2

ion current density is then 10.5 amps/m^2. The grid-collector spacing in the PDC is set by the requirement that the current density be less than the space-charge-limited current density, J_ℓ, in a plane diode,[3]

$$J_\ell = \frac{4\varepsilon_0}{9} \sqrt{\frac{2q}{m}} \frac{V^{3/2}}{d^2} \quad , \qquad \text{(VIII.4-1)}$$

where V is the voltage across the diode of spacing d, q is the charge, m is the mass, and ε_0 = 8.85 x 10^{-12} farads/meter. For the repeller grid-collector voltage, this gives a maximum d of 31 cm. We choose this spacing to be 25 cm. Equation (VIII.4-1) assumes the ions have zero speed at the collector. Since the ions approach the collector with finite kinetic energy (average = 39 keV), using Eq. (VIII.4-1) to set an upper limit on d is actually conservative.

The spacing, a, between the tubes forming the grids is chosen to be small compared with d, so that the potential surfaces are reasonably planar. We take a = .2 d,[4] so that the spacing is 5 cm. The tube diameter then determines the transparency of the grids and hence the total heat load on the grids. We choose a tube diameter of .5 cm, which yields a transparency per grid of 90%. The radius of the PDC then determines total power incident on the PDC and the length of the grids, assuming they are not segmented in the module. For a 1 MW incident power, the module radius is 46 cm. Hence, the longest tube is ~ 100 cm, which is 200 times its diameter. This tube "aspect ratio" is similar to that in the direct convertor for a reactor. In a reactor, the tubes forming the grid are typically 1 cm in diameter and ≈ 2-5 m long.[1,2]

In a full size power reactor, the grid system is segmented with each segment electrically isolated to minimize the electrical energy that can be

dissipated in a spark. The typical design value for the electrostatic energy per segment is ≈ 10 Joules. In the PDC module above, the total electrostatic energy is .1 Joules, so segmentation is not required.

Each grid is 90% transparent. Hence, a total of 20% of the ion current entering the PDC is intercepted by the grids. In addition, secondary electron emission at the electron repeller grid produces a beam of electrons which travel back through the plasma and strike the electron thermal dump at the other end of the reactor. Assuming three secondary electrons per incident ion, the -9 kV power supply for the electron repeller grid needs to supply 2.8 amps, or 25 kW. Of this power, 3/4 is deposited as heat at the electron thermal dump and 1/4 at the grid by ion bombardment. A total of 100 kW of heat is generated at each grid and 224 kW at the collector plate because the ions are collected with finite kinetic energy. These parameters are summarized in Table VIII.4-3. Table VIII.4-4 gives the fluxes of various energy components of ions incident on the electron and ion thermal dumps, the grids, and the collector plate. In calculating the particle flux to the electron thermal dump, it has been assumed that the radius (= 1.4 m) has been chosen so that the heat load there is also 150 W/cm^2. One could place the electron thermal dump further back and increase its area to reduce the particle flux incident on it if blistering due to energetic alpha particle bombardment is a problem. The wall erosion aspects of the direct convertor and thermal dumps are discussed in Section VIII.6. The heat transfer aspects are discussed in Section VIII.5. The vacuum pumping aspects of the direct convertor and the thermal dumps are discussed in Section IV.4. The required neutral pressure is taken to be 10^{-5} torr[4] in the direct convertor in order to minimize

Table VIII.4-3   Heat Generation in the PDC and Thermal Dumps

Entrance Grid	100 kW
Repeller Grid	100 kW
Collector Plate	224 kW
Ion Thermal Dump	80 MW
Electron Thermal Dump	9 MW

Table VIII.4-4   Ion Energy and Particle Flux Incident

on PDC Components and Thermal Dumps

Particle Species	Mean Energy keV	Energy Spread keV	Particle Flux #/cm^2-sec
Grids and Ion Thermal Dump			
D	139	109-170	3.2×10^{15}
T	139	109-170	3.2×10^{15}
p	307	150-600	2.4×10^{13}
He	248	218-280	3.6×10^{13}
He	808	300-1,500	8.9×10^{12}
He	3,630	2,700-4,300	1.4×10^{12}
PDC Collector Plate			
D	39	9-70	3.2×10^{15}
T	39	9-70	3.2×10^{15}
p	207	50-500	2.4×10^{13}
He	48	18-80	3.6×10^{13}
He	608	100-1,300	8.9×10^{12}
He	3,430	2,600-4,200	1.4×10^{12}
Electron Thermal Dump			
p	307	150-600	2.2×10^{14}
He	808	300-1,500	8×10^{13}
He	3,630	2,700-4,300	1.2×10^{13}

VIII.4-12

interactions between the escaping plasma and the neutral gas. The neutral

pressure near the thermal dumps is taken to be 5×10^{-5} torr.

VIII.4.3 Comparison to a Full Scale Reactor Direct Convertor

In order to be a viable test of direct convertor technology, the module

has to have characteristics similar to direct convertors for full size tandem

mirror power reactors. The incident power density is 150 W/cm^2, which is half

the design value for WITAMIR-I.[2] The incident DT ion flux in the module is

6×10^{15} cm^{-2}sec^{-1}, which compares favorably with the WITAMIR-I value of 4.6 x

10^{15} cm^{-2}sec^{-1}. The DT particle flux is higher in the module because the

average energy of the ions approaching the PDC (139 keV) is less than in

WITAMIR-I (358 keV). Consequently, one can expect a somewhat higher rate of

sputtering of the grids in the module. The average energy at which the DT

ions bombard the plate is the same (39 keV) in both devices.

The most significant difference with the particle-surface interactions

between these two devices is the energetic helium flux to the PDC. The

fractional burnup in TASKA is much less than in WITAMIR-I, but the "thermal"

alpha component was assumed to be absent in the WITAMIR-I direct convertor.

This is because the value of ϕ_c/T_{ic} in WITAMIR-I was much higher; consequently

the thermal alphas are well-confined axially in WITAMIR-I and had to be

"pumped" from the central cell by some other means. In TASKA, the fusion-born

alpha particles can escape axially since $\phi_c/T_{ic} \simeq 1.4$. The fluxes for the

various energy groups of alpha particles reaching the direct convertor are

compared in Table VIII.4-5 for TASKA and WITAMIR-I. The module has a much

lower flux of the more energetic (E > 600 keV) alphas, but has a substantial

thermal (E = 250 keV) component. The total helium flux into the TASKA module

Table VIII.4-5 Comparison of Helium Fluxes at PDC Entrance

Device	Mean Energy keV	Energy Spread keV	Flux #/cm^2-sec
TASKA	248	218-280	3.6×10^{13}
WITAMIR	---	---	---
TASKA	808	300-1,500	8.9×10^{12}
WITAMIR	1,000	650-2,000	4.9×10^{13}
TASKA	3,630	2,700-4,300	1.4×10^{12}
WITAMIR	3,950	3,200-4,800	3.4×10^{13}

is about half the flux into WITAMIR-I. This will have an impact on wall erosion due to blistering.

Mechanically, the TASKA module and the WITAMIR-I PDC are similar. The tubes forming the grids in the module have a smaller diameter (1/2 cm vs. 1 cm) but similar length to diameter ratio. The feeder pipes and support structure needed to segment the WITAMIR-I PDC are not exposed to the plasma beam in the TASKA module, since it is not segmented.

The efficiency of the PDC module is computed to be 53%, which compares with the 65% value for the WITAMIR-I PDC. The sources of the various losses are somewhat different. The grid loss is higher in TASKA because of the reduced transparency, but the energetic alpha contribution to the loss is less because of the reduced fractional burnup.

In most respects the module and a reactor PDC are sufficiently similar so that the module should be a meaningful test of plasma direct convertor technology.

References for Section VIII.4

1. G.A. Carlson et al., "Tandem Mirror Reactor with Thermal Barriers," Lawrence Livermore National Laboratory Report, UCRL-52836 (1979), Chapter 7.

2. B. Badger et al., "WITAMIR-I - A Tandem Mirror Reactor Study," University of Wisconsin Fusion Engineering Program Report UWFDM-400 (1980).

3. J.D. Cobine, "Gaseous Conductors," Dover Press (1958), p. 123.

4. W.L. Barr and R.W. Moir, "Measured and Projected Performance of Plasma Direct Convertors," Lawrence Livermore National Laboratory Report, UCRL-86026.

VIII.5   Ion and Electron Thermal Dumps

VIII.5.1   Thermal Hydraulics

The power approaching the ion end wall is given by the sum of the central cell ion power, half of the plug ion power, and half of the energetic alpha power, which adds up to 81 MW. The power is distributed to an area of 54 m^2, resulting in a heat flux on the dump of 150 W/cm^2. This heat flux is picked so that forced convection water can be used as the coolant. Forced convection is more desirable than boiling heat transfer because of its larger safety margin. The thermal hydraulic and tritium diffusion aspects of the power dump are discussed in this section. The sputtering and blistering problems caused by the high energy ions are discussed in Section VIII.6.

A forced convection water stream with a velocity of 2.5 m/sec is used as the coolant of the power dump. The inlet and exit coolant temperatures are 60° and 110°C, respectively. With a coolant tube diameter of 0.5 cm, a coolant heat transfer coefficient of 1.6 watt/cm^2 °C is available. The film temperature drop is 90°C for a heat flux of 150 watt/cm^2. The front tube wall is .4 cm thick, which results in a temperature difference across the wall of 346°C. Therefore, at the exit end, the coolant wall temperature is

$$T = 865 \, x + 473^0K \qquad\qquad (VIII.5\text{-}1)$$

in which x is the distance from front surface. This temperature equation will be useful in the tritium diffusion calculations.

The total thermal power to the power dump is 81 MW. The coolant flow rate is, therefore, 1.4×10^6 kg/hr. The coolant flow length is 1 m. The pressure drop is .04 MPa. The pumping power required is 1 MW. The important parameters of the power dump are listed in Table VIII.5-1.

Table VIII.5-1 Thermal Hydraulic Parameters for Power Dump

Total Power	81 MW
Energy Flux	150 W/cm^2
Coolant	H_2O
Structural Material	316 SS
Coolant Tube Diameter	.5 cm
Coolant Tube Length	1 m
Coolant Velocity	2.5 m/sec
Coolant Inlet Temp.	60°C
Coolant Exit Temp.	110°C
Coolant Flow Rate	1.4 x 10^6 kg/hr
Coolant Pumping Power	1 MW
Maximum Structural Temp.	546°C
Minimum Structural Temp.	60°C

VIII.5.2 Tritium Considerations

High energy tritium ions impinge on the surface of the power dump area. The tritium will penetrate to a certain distance, δ, from the front surface and will either diffuse backward to the vaccum cavity or forward to the coolant. Since water is used as the coolant, it is important to calculate the tritium leakage rate to the coolant.

The penetration depth of 139 keV tritium is calculated to be .4 x 10^{-4} cm. It can be assumed that the tritium is deposited uniformly within this depth. It is further assumed that the back diffusion rate is much higher than

the forward diffusion rate. Therefore, the back diffusion can be calculated by a stationary diffusion system with uniform mass deposition, or

$$C(x) = \frac{\dot{M}}{2D} [\delta^2 - (\delta-x)^2] \qquad\qquad \text{(VIII.5-2)}$$

$$\text{and} \quad \dot{M} = m/\delta \qquad\qquad \text{(VIII.5-3)}$$

in which C is concentration, g/cm^3

$\dot{M}$ is mass generation rate, g/cm^3-sec

D is diffusivity, cm^2/sec

δ is the penetration depth, cm

x is distance from the front wall, cm

m is the particle flux, g/cm^2-sec

Diffusivity of hydrogen in 304 SS is reported to be[1]

$$D = 1.8 \times 10^{-2} e^{(-14000/RT)} . \qquad\qquad \text{(VIII.5-4)}$$

Within the penetration depth of δ, the temperature is almost constant and has been calculated to be 546°. The incoming tritium particle flux is $3.2 \times 10^{15}/sec$-cm^2. The maximum tritium concentration at $x = \delta$ is, therefore, 10^{-7} g/cm^3.

The tritium concentration beyond $x = \delta$ can be calculated by the solution for an infinite plate facing a constant concentration in front. The mass transfer can be calculated by

$$G = - D \frac{dc}{dx} \qquad\qquad \text{(VIII.5-5)}$$

or

$$\frac{C(o) - C(x_o)}{G} = \int_0^{x_o} \frac{dx}{D} \qquad\qquad \text{(VIII.5-6)}$$

VIII.5-3

in which G is the mass transfer rate, g/cm^2 sec.

The temperature profile is

$$T = 865 \, x + 473 \; ^0K \qquad\qquad (VIII.5-7)$$

and

$$D = 1.8 \times 10^{-2} \, e^{-14000/RT} \; . \qquad\qquad (VIII.5-8)$$

The left side of eq. VIII.5-6 can be integrated numerically from 0 to x_0 = .4 and equals 6.72×10^6 sec/cm. The mass transfer rate can then be calculated by assuming $c(x_0) = 0$ and $C_0 = 10^{-7} \, g/cm^3$:

$$G \cong \frac{C_o}{6.72 \times 10^6}$$

$$= 1.5 \times 10^{-14} \, g/cm^2 \; sec \; .$$

The total dump area is 54 m^2. Therefore, the total tritium leakage rate to the coolant is 7 curies/day. With any effect of oxide layers as a diffusion barrier, the tritium leakage rate can be reduced to <1 curie/day. The integration of $\int_0^{x_0} \frac{dx}{D}$ can be transferred into a summation of $\sum_{i=1}^{10} \frac{\Delta x}{D(T)}$. Each term in the summation indicates the resistance to the diffusion of tritium for this particular zone. The magnitude of the resistances are shown on Table VIII.5-2. It is clear that the last zone provides almost 2/3 of the total resistance. The tritium concentration in the wall is shown on Fig. VIII.5-1. The total tritium inventory in the structure is less than .05 g.

Table VIII.5-2 Resistance to Tritium Diffusion from Each Zone

Zone No.	Resistance $[\frac{1}{D(i)}]$, $\frac{sec}{cm^2} \times 10^{-5}$
1	3.64
2	5.42
3	8.36
4	13.47
5	22.80
6	40.91
7	78.58
8	163.61
9	375.25
10	967.62

Fig. VIII -5-1   TRITIUM CONCENTRATION IN
POWER DUMP WALL
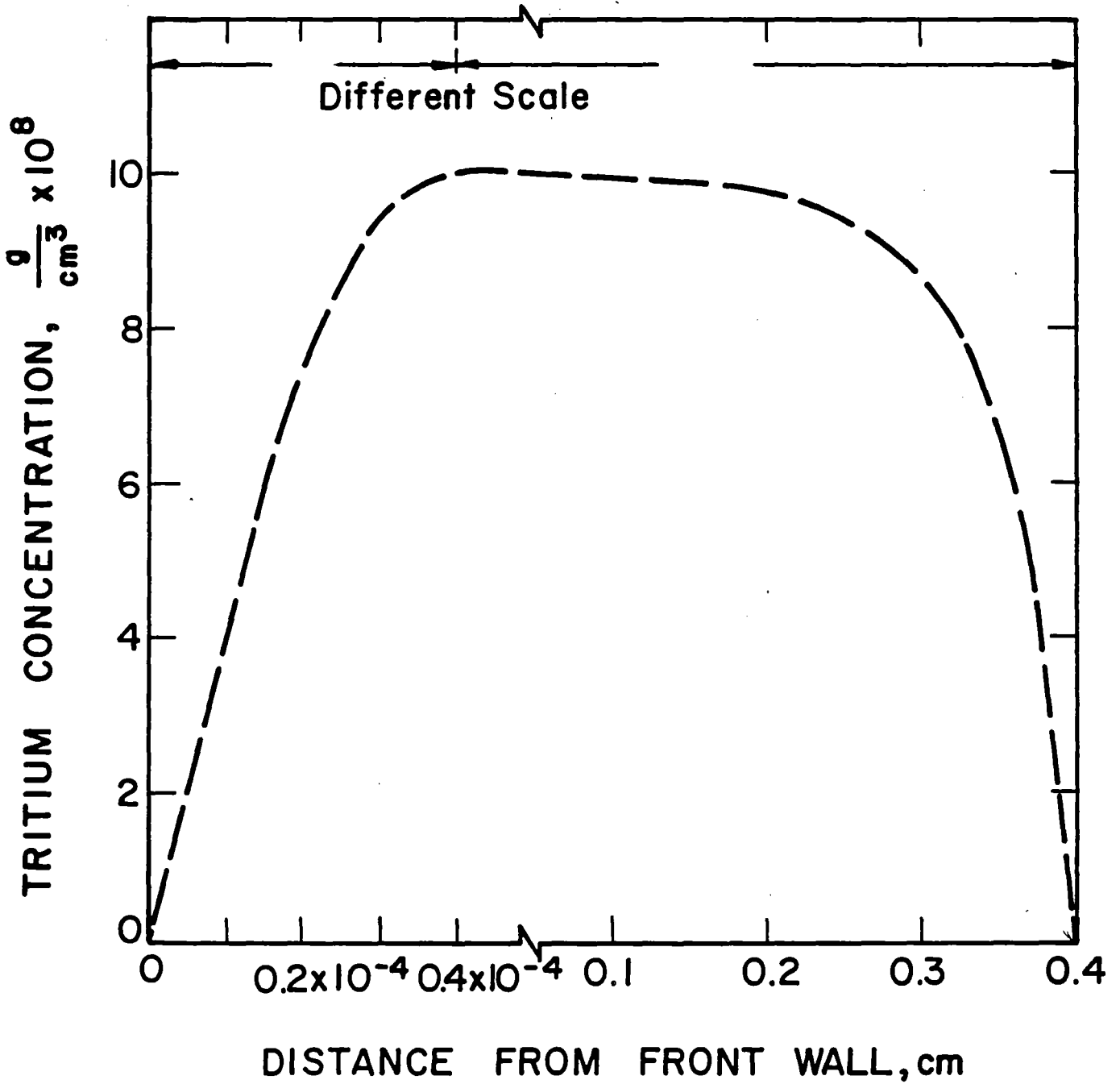
VIII.5-6

References for Section VIII.5

1. H. K. Perkins et al., "Tritium Hold Up Due to Coatings on the First Wall of Fusion Reactors," Radiation Effects and Tritium Technology for Fusion Reactors, Gatlinburg, TN (Oct. 1975).

VIII.6 Surface Erosion on Components of the Plasma Direct Convertor and

Thermal Dump

VIII.6.1 Introductory Remarks

The energies carried by plasma particles which impinge on the components of the plasma direct convertor (PDC) are in the range where both sputtering and blistering are of utmost concern. Blistering, if it occurs repeatedly, can lead to particularly high erosion rates. Whether or not repetitive blistering is possible, depends on a number of factors which have only recently been recognized. These factors are of central importance in our following assessment of surface erosion, and they will therefore be briefly reviewed.

There are four basic conditions for blistering or flaking to occur as a result of ion implantation in solids:

- A critical concentration of the implanted gas must be reached within the solid of the order of 10 to 50% of the metal atom density, depending on temperature and material (see Fig. VIII.6-1).

- Erosion by sputtering must not remove more material during the time to reach a critical gas concentration than the ion range.

- The depth distribution of the implanted gas must be such that the critical concentration is first reached below the surface rather than at the surface.

- The creep strength of the material must be sufficiently high to contain within small bubbles a gas pressure of the order of 10^{-3} * shear modulus of the solid.

The last two conditions provide ways to avoid blistering altogether. The surface temperature of the solid must be kept above a temperature of about half the melting point.[1] In this case, only blister holes form, and the gas
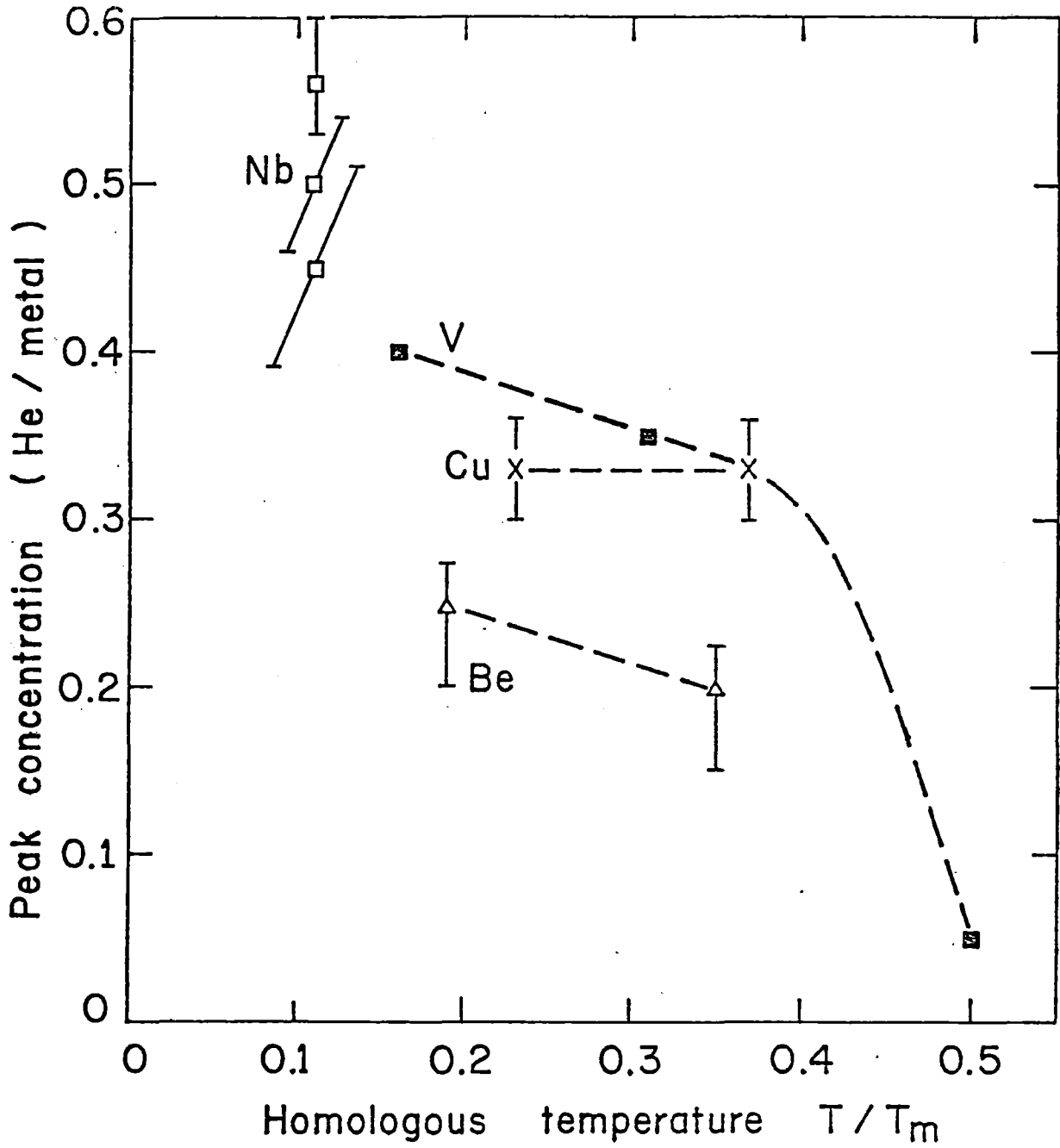
Fig. VIII.6-1. Critical helium concentration for blistering.

is released without further erosion. Or, the other strategy is to implant the solid with ions having a sufficiently wide spectrum of energies that a broad gas distribution is obtained in the solid which intersects the surface. For this strategy it must be noted that sputtering may erode a sufficient amount of material so that the critical concentration is first reached at the receding surface.

Terreault[2] has recently studied the repeated appearance of blistering or flaking upon monoenergetic helium bombardment in greater detail and derived the following empirical rules. If R_p is the projected range of ions in the solid, and FWHM the full width at half maximum of the implantation concentration profile, then

- repetitive blistering or flaking occurs when $FWHM/R_p < 0.7$;

- blistering gradually disappears when $FWHM/R_p$ is between 0.7 and 1.0;

- blistering occurs only once when $FWHM/R_p \gtrsim 1.0$;

- blistering is likely to happen not at all when $FWHM/R_p \gtrsim 1.5$.

Figure VIII.6-2 from Ref. (2) shows the range of implantation energies and atomic numbers for which the various blistering processes take place.

Multiple energy implantations of helium ions into nickel and stainless steel have recently been carried out by Jaeger and Roth[3] in order to investigate the reasons why blistering does not occur. They found that a continuous distribution of small helium bubbles is formed under multiple energy implantations which reaches from the (receding) surface into the material. Upon reaching the critical gas concentration, interbubble fracture and bubble coalescence lead to an interconnected porosity up to the surface which provides microscopic channels for gas release. By implication, it can then be concluded that for monoenergetic ion implantation at sufficiently high
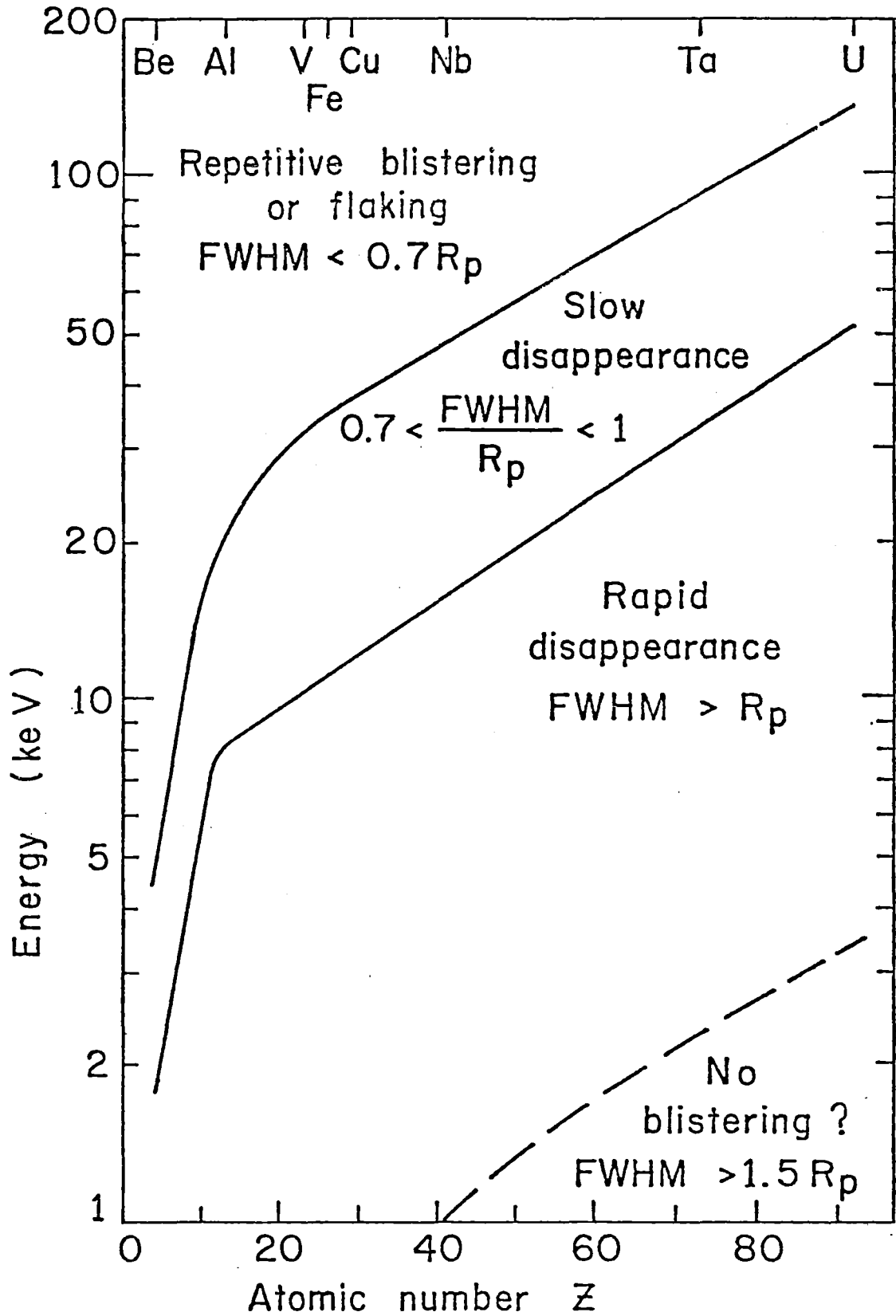
Fig. VIII.6-2. Blistering conditions.

energies such that $FWHM/R_p < 0.7$, the interconnected porosity does not reach the surface, and blistering or flaking will ensue.

VIII.6.2 Concentration Profiles of Implanted Ions

The collector plate, grids, and ion thermal dumps are exposed to ions which can be divided in six different groups. Each group is characterized by a range of energies listed in Tables VIII.6-1 and VIII.6-2. Their implantation ranges covers therefore certain depth intervals which were obtained from the compilation in Refs. (4,5) and which are also listed in Tables VIII.6-1 and VIII.6-2 for stainless steel. If we assume a uniform energy distribution within each group, the concentration of implanted ions within the corresponding depth interval will build up uniformly at rates given by the last columns in Tables VIII.6-1 and VIII.6-2. Figures VIII.6-3 and VIII.6-4 show the depth distribution of ions for both helium and hydrogen, assuming that no diffusion occurs. This assumption is certainly incorrect for hydrogen at elevated temperatures, but it does apply to helium trapped in vacancy clusters produced in connection with the ion bombardment.

In order to assess the possibility of blistering we assume that a critical concentration for implanted helium of 20% of the metal atom density must be reached.

For the case of the collector plate, the low energy group (18-80 keV) of the helium ions accumulates at the fastest rate, and a critical concentration is reached in about 1415 seconds.

However, both the low energy group of the helium ions and the flux of D and T give rise to sputtering erosion. Using an average sputtering yield of 0.03 for D and T, and a sputtering yield of 0.1 for the helium ions with energy between 18 and 80 keV, we find a sputtering erosion distance of 0.0325 μm

Table VIII.6-1. Flux of Particles, Range Distribution,

and Rate of Gas Concentration Buildup in the Collector Plate

Particle Species	Energy Spread (keV)	Flux $cm^{-2}s^{-1}$	Depth Range (μm) Without/With Straggling		Rate of Gas Buildup (atom fraction/sec)
D	9-70	3.2×10^{15}	0.065-0.4	0.06-0.52	2.25×10^{-3}
T	9-70	3.2×10^{15}	0.065-0.4	0.06-0.52	
H	50-500	2.4×10^{13}	0.27 -2.5	0.20-2.7	1.27×10^{-6}
He	18-80	3.6×10^{13}	0.09 -0.3	0.06-0.36	2.02×10^{-5}
He	100-1300	8.9×10^{12}	0.2 -2.0	0.14-2.1	5.83×10^{-7}
He	2600-4200	1.4×10^{12}	4.4 -8.0	4.3 -8.2	4.58×10^{-8}

Table VIII.6-2. Flux of Particles, Range Distribution, and Rate of Concentration Buildup in Grids and Ion Thermal Dumps

Particle Species	Energy Spread (keV)	Flux $cm^{-2}s^{-1}$	Depth Range (μm) Without/With Straggling		Rate of Gas Buildup (atom fraction/sec)
D	109-170	3.2×10^{15}	0.6 -0.8	0.45-0.95	3.77×10^{-3}
T	109-170	3.2×10^{15}	0.6 -0.8	0.45-0.95	
H	150-600	2.4×10^{13}	0.65-2.5	0.55-2.7	1.53×10^{-6}
He	218-280	3.6×10^{13}	0.6 -0.7	0.5 -0.8	4.24×10^{-5}
He	300-1500	8.9×10^{12}	0.7 -2.5	0.6 -2.6	5.83×10^{-7}
He	2700-4300	1.4×10^{12}	4.5 -8.0	4.4 -8.2	4.72×10^{-8}
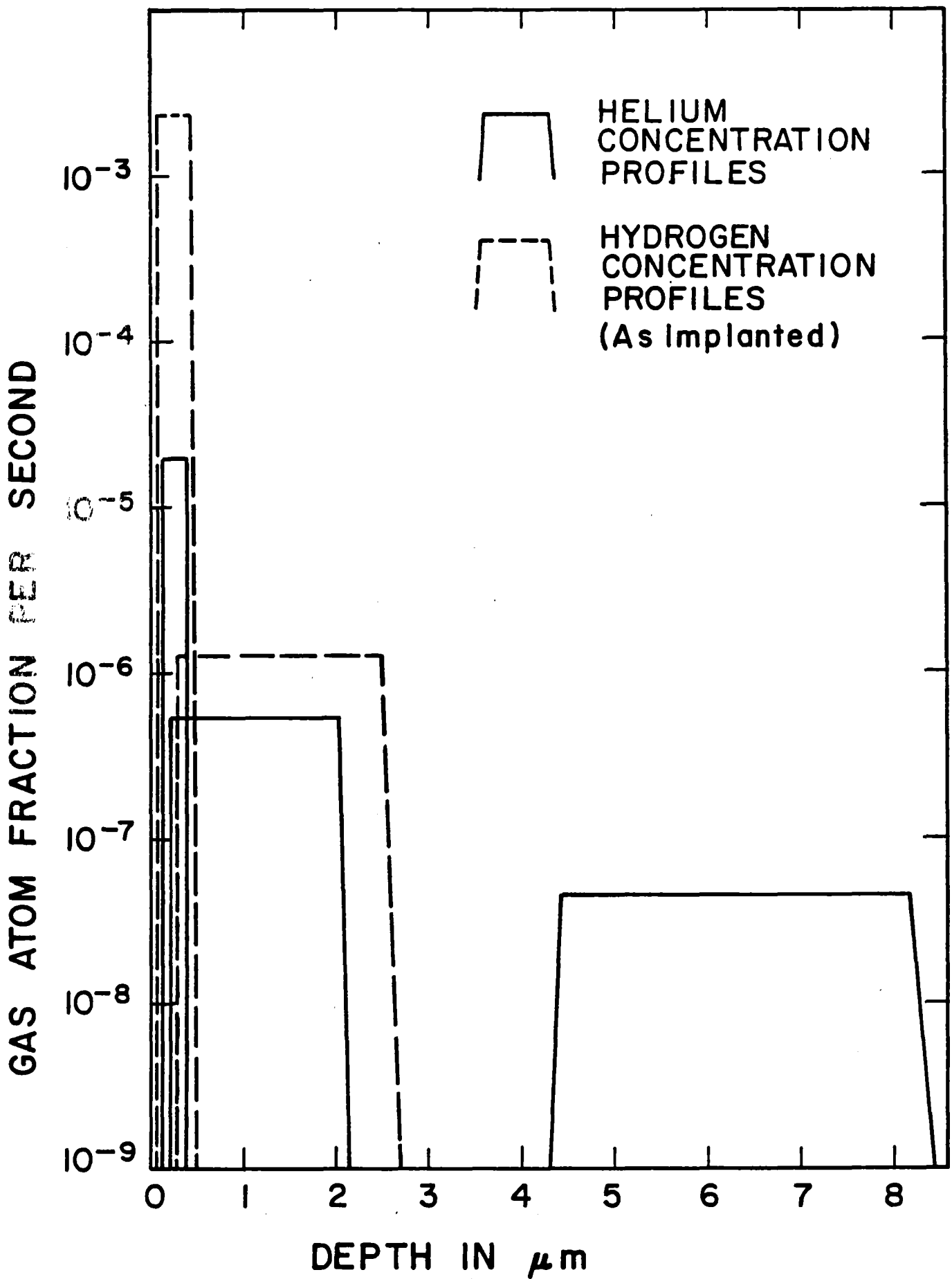
Fig. VIII.6-3. Depth distribution of implanted ions in the collector plate.
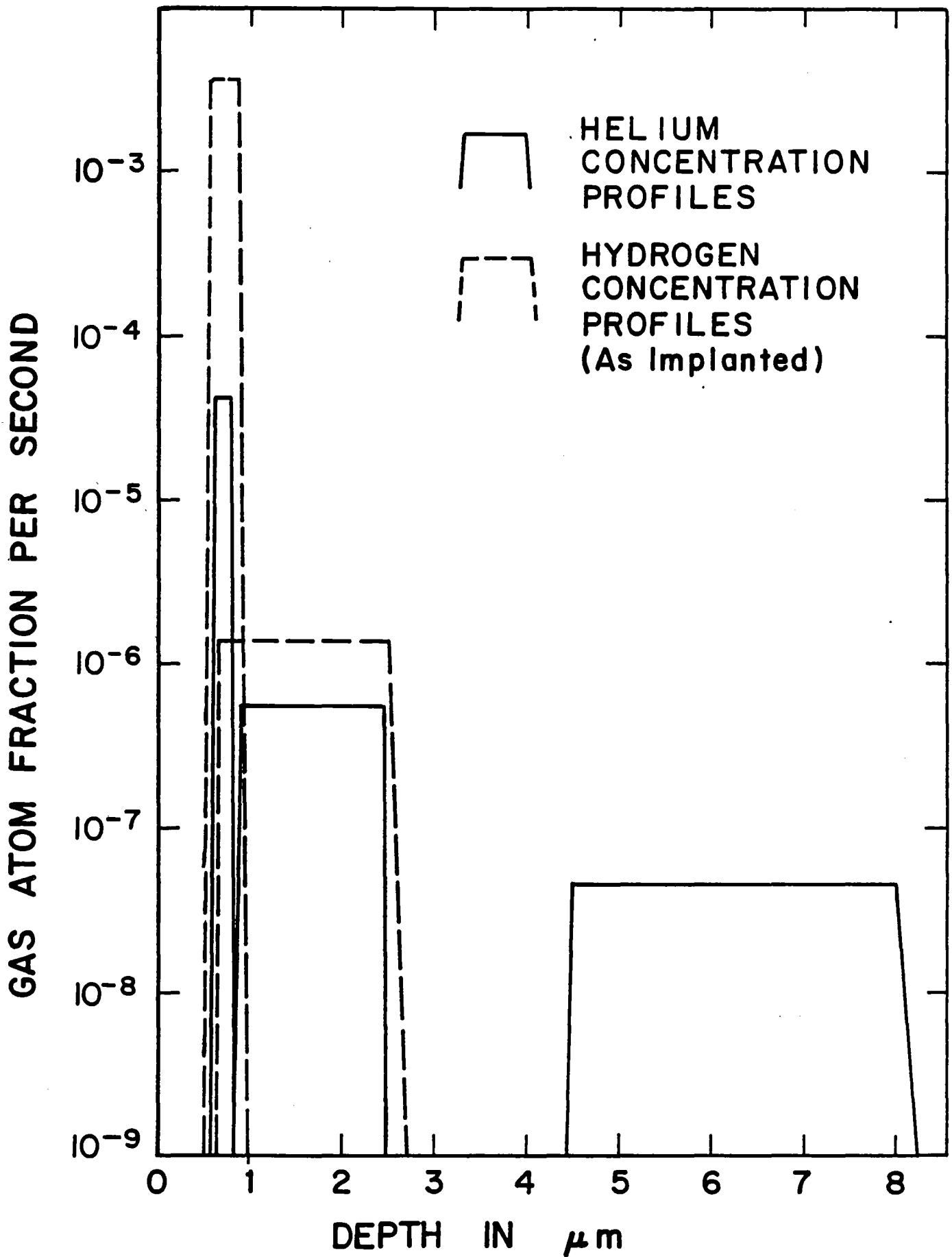
VIII.6-8

Fig. VIII.6-4. Depth distribution of implanted ions in grids and thermal dumps.

VIII.6-9

within the time interval of 1415 seconds. Since the helium depth distribution starts now at a distance of only 0.0275 μm below the surface (taking straggling into account) blistering is not expected to occur, or at most only once.

The second energy group of implanted helium (ranging from 100 to 1300 keV) overlaps with the first one, and reaches its critical concentration after the first one. Therefore, an interconnected network of pores will already exist for continuous helium release for this second group by the time it has reached the critical concentration. Hence, the second group will not lead to blistering either.

The third group, whose implantation depth extends initially from 4.3 to 8.2 μm, would require an implantation time of 4.8×10^6 seconds to reach a critical concentration. By that time, however, sputter erosion by the flux of D and T will have resulted in the removal of about 100 μm of material, i.e. many times more than the implantation depth of the high energy α-particles. Consequently, the critical concentration is never reached.

In conclusion, blistering or flaking by the implantation of helium into the collector plate will not occur. Instead, sputter erosion from the low energy flux of D and T is the dominant erosion mechanism, resulting in a total erosion rate of about 0.73 mm/FPY.

The situation with regard to erosion of the grids and thermal dumps for the PDC is somewhat different. As seen from Table VIII.6-2, the six different groups have energy spreads larger by about 100 keV. As a result, the implantation range for the low-energy D and T particles extends now from 0.45 and 0.95 μm.

The low energy group of helium ions is implanted between 0.6 and 0.7 μm, in which range a critical concentration of 20 at.% is reached within a time of

4.7×10^3 seconds. The thickness of the eroded surface layer by sputtering with the D and T particles is only 0.07 μm for this time interval, and therefore insufficient to expose the layer of helium saturated material. As a result, blistering will occur, removing about 0.7 μm.

The medium energy group of helium ions, whose implantation depth extended originally from 0.6 to 2.6 μm, has accumulated to a concentration of only 0.27 at.%, a negligible amount compared to the 20 at.% at saturation. Therefore, after the first blister generation, the low-energy group of helium ions will rapidly build up a second implantation profile, leading to the second blister generation after an additional time of 4.7×10^3 seconds.

Repetitive blistering will continue up to six generations or a depth corresponding to the original range of the high-energy group of α-particles. When this implantation profile is exposed, helium has been accumulated up to about 0.13 at.%. Again, this is negligible in comparison to 20 at.%, required to create the interconnected porosity necessary for gas release. It must therefore be concluded that repetitive blister erosion by the low-energy group of helium ions will occur, unless other remedial actions are taken.

As discussed above, there are two possibilities. The PDC could be designed such that the grids and the thermal dumps have surface temperatures in excess of 0.5 T_m (T_m is the melting temperature of the material in K) on all surfaces exposed to the particle flux.

The second choice is to precondition these components by implanting helium at energies ranging from 10 to 100 keV up to the critical concentration prior to using these components in the TASKA reactor. It may be possible to precondition a second set of grids first at the collector plate and then exchange them with the first set of grids. These preconditioned components

would release helium upon further bombardment in the same manner as it is released from the collector plate. The maximum rate of erosion would then be by sputtering, i.e. at a rate of 0.73 mm/FPY.

The electron thermal dump is bombarded by three groups of particles whose fluxes and depth distributions are listed in Table VIII.6-3. The medium energy helium flux reaches its critical implantation concentration after a time of 3.8×10^4 s. The sputtering erosion by both the hydrogen and the helium flux is estimated to be about 3×10^{-7} cm, i.e. much shorter than the implantation depth. As a result, blistering by the medium energy helium flux is again the dominant erosion mechanism unless the electron thermal dump is preconditioned or run at a surface temperature of about half the melting point or higher.

It should be noted that in the present assessment of blistering, it was assumed that the energy spectrum in each particle group is uniform. If, however, the spectrum is peaked at the low energies of the energy spread, the critical concentration would first be reached at the minimum range for that group. For example, if the medium energy helium flux is peaked at 300 keV, the blister thickness would be 0.7 μm, leaving a depth region of 1.3 μm where the helium concentration is high. After the first generation of blisters have been produced, the subsequent helium concentration buildup in the underlying material would be a superposition of the remainder of the old distribution plus the new one. The total distribution reaches now from the new surface into the material, and the next critical concentration may very well be produced at the surface. In this case, no further blistering would occur.

A detailed analysis of both the energy spectra of the plasma particle fluxes and the accumulated depth distributions of helium will be required to obtain a more reliable assessment of blistering. It appears that repetitive

Table VIII.6-3. Flux of Particles, Range Distribution,

and Rate of Concentration Buildup in the Electron Thermal Dump

Particle Species	Energy Spread (keV)	Flux $cm^{-2}s^{-1}$	Depth Range (μm) Without/With Straggling		Rate of Gas Buildup (atom fraction/sec)
H	150-600	2.2×10^{14}	0.65-2.5	0.55-2.7	1.40×10^{-5}
He	300-1,500	8.0×10^{13}	0.7 -2.5	0.6 -2.6	5.24×10^{-6}
He	2,700-4,300	1.2×10^{13}	4.5 -8.0	4.4 -8.2	4.05×10^{-7}

blistering can be avoided in a more detailed analysis or with proper tailoring

of the energy spectra of the impinging plasma particles.

References for Section VIII.6

1. S.K. Das and M. Kaminsky, "Radiation Blistering in Metals and Alloys," Chapter 5, in Radiation Effects on Solid Surfaces, ed. by M. Kaminsky, American Chem. Soc., (1976).

2. B. Terreault, J. Nucl. Matls. 93&94, (1980), 707-712.

3. W. Jaeger and J. Roth, J. Nucl. Matls. 93&94, (1980), 756-766.

4. H.H. Andersen, J.F. Ziegler, "Hydrogen, Stopping Powers and Ranges in all Elements," Pergamon Press, New York, (1977).

5. J.F. Ziegler, "Helium, Stopping Powers and Ranges in all Elements," Pergamon Press, New York, (1977).

8.7. End Plug Coils Arrangement

The end plug coils are composed of two transition coils and a pair of
Yin Yang coils. All are superconducting coils and therefore inserted
in a dewar vessel combined with a precooling of the magnets.

As can be seen in figure 8.7-1 the middle of the first transition coil
is arranged in a distance of 23.2 m from the test facility center. The
following Yin Yang coils with no common coil center are located at the
27.5 and 27.86 m points, the outer transition coil at 32.16 m. Also
located in this region are the ECRH units and the end plug neutral beam
injector, 22.0 m and 27.68 m distant from the test facility center. The
mentioned figure 8.7-1 shows also that all coils are surrounded by a
single common dewar vessel. Reasons for this concept are

- the proximity of the magnets to each other and to the vacuum
  chamber which in addition is enclosed by the shield;

- the fact that a common dewar vessel renders possible a favourable
  support structure of the coils in relation to magnetic forces acting
  upon the particular magnets and between them;

- the cold support structure between the coils prevents thermal heat
  transfer from otherwise outside the dewar vessel arranged support
  components to the magnets.

The dewar vessel design pays regard to assembling and dismantling problems
of coils and heating units. The difficulties are a consequence of the
special shape of the plasma and the consequently resulting shape of
vacuum chamber and shield as well as of the minimum of space between the
latter one and the magnets. Therefore the vessel is composed of three
obliquely divided parts welded and clamped together. Moreover, the outer
shell as well as the inner one of the dewar vessel are divided in
longitudinal direction too. A channel for the neutral beam injector duct
and the end parts of the vessel connect the outer and inner shell,
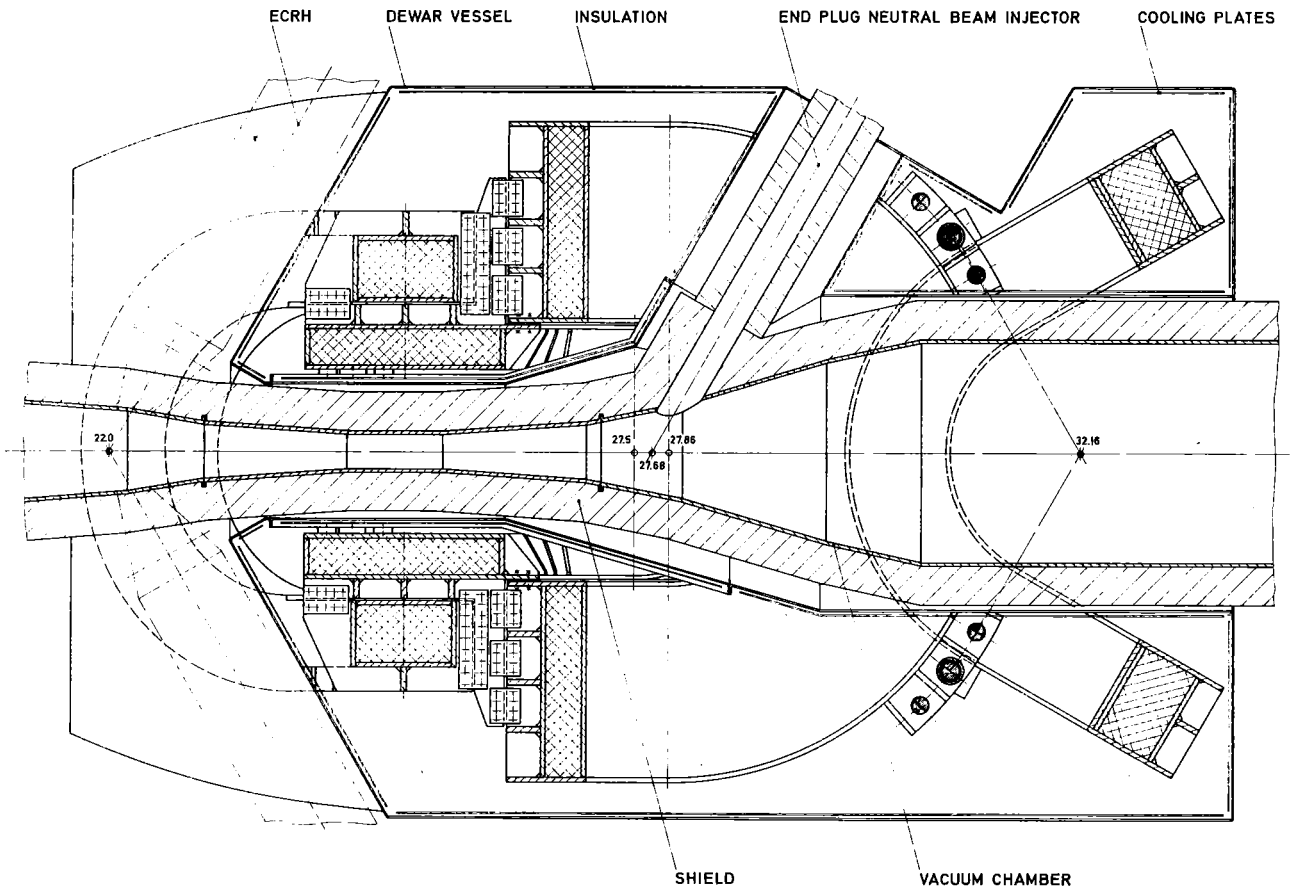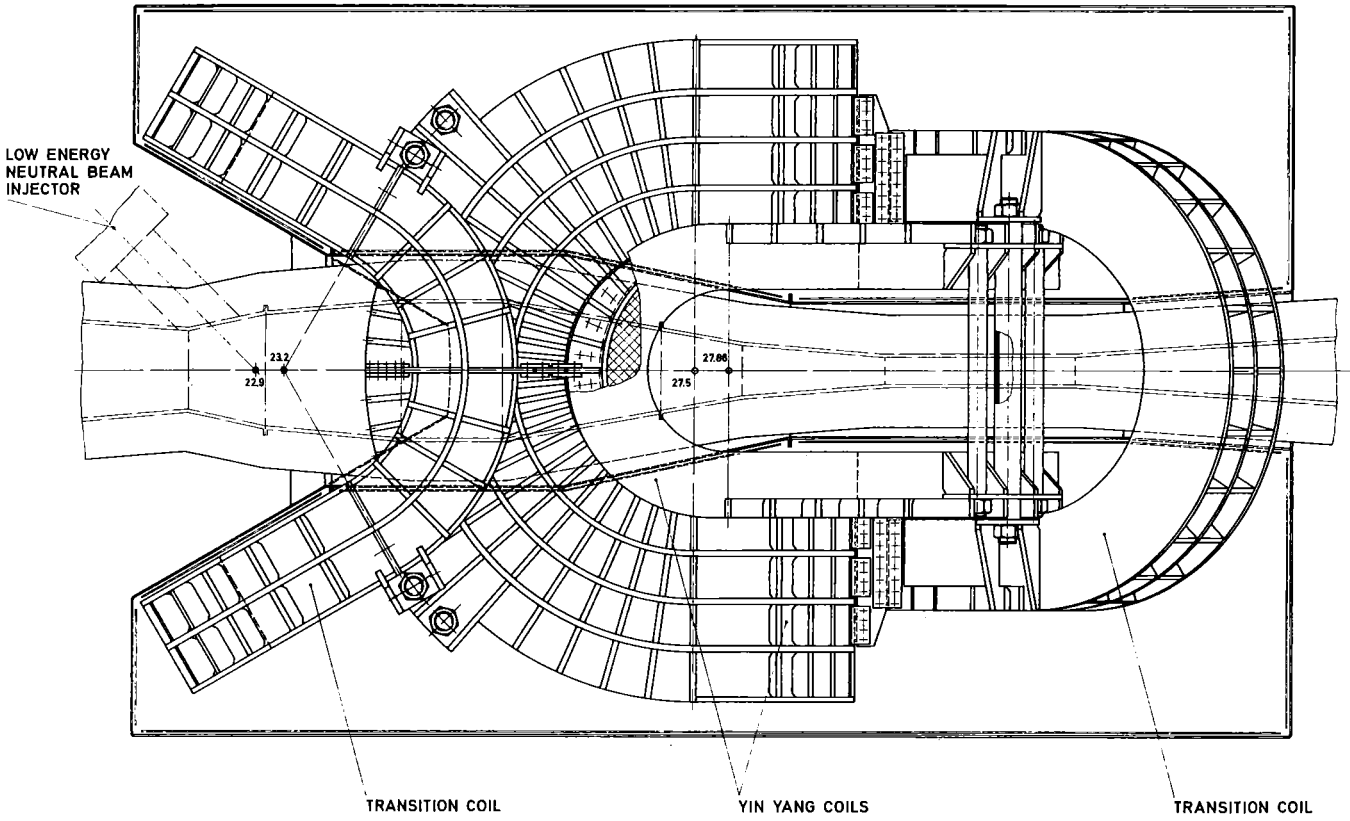
VIII.7-1

FIG. VIII.7-1   END PLUG COILS - ARRANGEMENT

while ECRH-units are located outside and do not penetrate it. Insulation
is attached to the inner side of the shell and cooling plates with liquid
nitrogen for cooling medium are arranged between magnet support structure
and shell. The difference pressure outside and inside the vessel is
assumed to be 760 Torr. From this the vessel thickness amounts to 2 cm
under consideration that the shell is reinforced by fins. The dewar vessel
material will be austenitic steel.

To support the end plug unit a special support structure, movable on rails
will be used. The necessary thermal insulation of the unit resting on the
structure will be obtained by application of carbon fibre synthetic resin.
The assembly of vacuum chamber, magnets and dewar vessel have to be
performed in one assembly schedule, for a subsequent mounting as well as
a later displacement of components along the chamber axis will be
prevented by the chamber shape.

The maintenance and replacement of end plug components have been checked.
The problems are soluble but further design investigations will be
necessary.

IX Operations

IX.1 Plasma Startup

IX.1.1 Introduction

The discussion of the plasma physics aspect of TASKA in Chapter III has been concerned with the steady state operating condition. Obviously, consideration has to be given to the problem of initiating the plasma and, by heating and fueling, bringing it to the desired operating condition. The startup sequence in tandem mirror experiments is to inject into the plugs a plasma stream from plasma guns in the end wall. The plug neutral beams are then turned on and the plug plasma is built up to its required density and mean ion energy. Gas is then injected into the central cell to build up the central cell density.

The startup sequence in a barrier tandem mirror is complicated by the additional sources from barrier pumping, and ECRH, and perhaps ICRF heating. Electron and ion power losses from the central cell or plug plasma scale as the appropriate collision frequency which, in turn, scales as $n/T^{1.5}$, where n and T represent the appropriate density and temperature. This suggests that, if one tries to heat the plasma at the full density, the power loss is greater when the plasma is cold. It takes more power to heat the plasma than to sustain it at the final temperature. The power sources, however, have been sized for the required steady state loads. It is expensive to have additional power available that is only required for startup. The solution to this is to start with a low density plasma and raise the density while heating the plasma in such a way as to not exceed the power available.

An additional complication arises from the variation of the neutral beam trapping efficiency with density. At too low a density, the beam is poorly

trapped and the plasma heats too slowly. Furthermore, the plug mirror ratio varies with beta, which affects the hot ion confinement time; this effect is stronger for a sloshing ion plug than for 90° injection. In addition, the absorption of the ECRH power is poor (for the O-mode) for electron temperatures less than a few keV. One could use the X-mode to heat the electrons at low T_e, but switching modes as the plasma heats complicates the ECRH delivery system. One possible scenario is to heat the plug plasma at moderate density with the neutral beam until the electron temperature gets to a few keV. One then applies ECRH to heat the electrons; whether one can simultaneously control the plug ion density in the appropriate manner is not yet established. Once a sufficiently hot and dense plug plasma is established, the central cell plasma can be built up by gas injection into the central cell; the hot ion plasma leaking out of the plug would act as a "seed" for ionization in the central cell. While the central cell plasma is building up, beam injection into the barrier region to establish the thermal barrier would be initiated.

We have developed a rate code to study various scenarios for plasma startup. This code solves the time dependent rate equations for the central cell and plug plasmas and includes the effect of the thermal barrier. The code is described in Section IX.1.3 and some results are given in Section IX.1.3.3.

IX.1.2 Initial Target Plasma

Each time TASKA is restarted after an interruption in operation, a startup sequence will need to be followed. One possible startup scenario is given here; other approaches are possible and may have advantages for barrier formation using ECRH.

<u>Step 1</u>. The machine is assumed to be under good vacuum and the magnetic field magnets have been energized. If the plasma has been opened to contaminants, then a glow discharge cleaning cycle to remove H_2O, CO_2, CH_4, etc. surface impurities is recommended. This entails insertion of several high power probe anodes, filling the machine with H_2 (or D_2) to a pressure of a few m torr, establishing a several hundred volt glow discharge to the chamber (cathode) walls at a current density of a few $\mu A/cm^2$, and pumping with sufficient H_2 gas flow to flush out the described impurity molecules. This should be continued for ~ 20-100 hours for surface cleaning to a depth of ~ 1000 Å. All cryopanels are to be warm and getter panels cool during the glow discharge cleaning cycle.

<u>Step 2</u>. The cryopanels are then cooled and the getter panels warmed to achieve the maximum H_2 pumping speed and specified low background pressure ($<< 10^{-6}$ torr).

<u>Step 3</u>. The fast plasma startup sequence is then initiated. A "cold" target plasma stream is created using approximately 10 MFTF-B type stream guns. The plasma stream becomes the target for "startup" neutral beam injection into the plugs. The required stream plasma is roughly 40 cm in order to provide a plasma halo beyond the required 28 cm hot plasma radius in the plugs. The required line density is ~ 2×10^{14} cm^{-2} in order to have at least 10% trapping of the startup neutral beams. The plasma stream is only required to last a few msec. Successful startup with a cold plasma stream injected into one plug was accomplished in TMX. This mode of startup is assumed here.

<u>Step 4</u>. A set of startup beams is injected into both plugs to rapidly replace the cold target plasma formed in Step 3. A high initial neutral beam current is required in each plug at an appropriate energy (~ 15 keV) such that

the hot ion trapping rate over the full radius of interest is at least equal to the charge exchange loss rate from cold impinging neutral gas. The startup neutral beam energy must also be high enough so that the collisional loss time of the hot plasma is longer than the plasma buildup time with the available neutral beams. For reasonable vacuum assumptions, this requires approximately 500 A at 15 keV in each plug. This can be accomplished by an array of ten 50 A beams split into three beam lines, with a fourth beam line reserved for the steady state 250 keV plug beam. A startup neutral beam pulse time ~ 10 msec appears adequate.

Step 5. The final step is the transition from a ~ 15 keV plug plasma to the desired operating conditions fueled by the steady state 250 keV H^0 beams, barrier pump beams on, ICRF heating in the central cell on, and ECRH heating of the plug plasma. The buildup of the plasma to this phase is described in the next section.

IX.1.3 Rate Code Calculations

A code based on a set of six coupled rate equations has been developed in order to make numerical simulations of the time evolution of the density and temperature of each species in the central cell and plug, as well as the time dependence of the central cell, plug, and barrier potentials. It is assumed in this code that a target plasma has already beem established; the task now is to bring the plasma to the desired operating point. The code is written for the TASKA configuration of an inboard thermal barrier with minimum-B plugs. The objective is to study scenarios for startup and to demonstrate a technique for attaining the steady-state operating conditions of the TASKA device by using a suitable programmed set of injected powers and particle

sources subject to constraints in the amount of sources required. This code is zero-dimensional but fully time dependent.

IX.1.3.1 Physics Model

The six coupled rate equations considered here describe the time evolution of density, mean ion energy, and electron temperature in the plugs, and the density, ion temperature, and electron temperature in the central cell region. The processes that have been taken into account in these equations are described below. Only those expressions that have not been specifically used and given in the power balance model (see Section III.2) are detailed here.

The plug ion density is given by

$$\frac{dn_p}{dt} = S_p - \frac{n_p^2}{(n\tau)_{ip}}$$

where the first term on the right side is the ion source due to ionization of the neutral beam, and the second represents the end losses.

The plug electron density evolution is given by

$$\frac{dn_{ep}}{dt} = S_p + \frac{n_{ep}n_b}{(n\tau)_{ep}} \left(\frac{T_{ep}}{T_{ec}}\right)^{\nu_c} \exp\left(\frac{\phi_b + \phi_c}{T_{ep}}\right) - \frac{n_{ep}^2}{(n\tau)_{ep}}$$

where the first term on the right side is the electron source due to ionization of the plug neutral beam; the second gives the source due to central cell passing electrons scattered into the plug; and the third simulates the end losses to the central cell over the potential barrier $(\phi_b + \phi_c)$. Also,

$$n_{ep} = n_{ew} + n_{e,passing} \simeq n_{ew} ;$$

this model neglects the central cell electron passing density in the plugs.

The central cell ion density evolution is given by

$$\frac{dn_c}{dt} = S_c + J_{TRAP} \frac{2V_b}{V_c} \frac{\langle\sigma v\rangle_{ionb}}{\langle\sigma v\rangle_{cxb}} - \frac{n_c^2}{(n\tau)_{ic}} - \frac{n_c^2}{(n\tau)_{xfi}} - \frac{1}{2} n_c^2 \langle\sigma v\rangle_{DT}$$

where the first term on the right-hand side corresponds to an external ion source which is only needed for startup; the second term accounts for the ionization of the barrier pumping neutral beams; the third represents the end losses over the potential barrier ϕ_c. The fourth gives the cross field diffusion; and the fifth is the sink due to fusion reactions.

The central cell electron density is given by

$$\frac{dn_{ec}}{dt} = S_c + J_{TRAP} \frac{2V_b}{V_c} \frac{\langle\sigma v\rangle_{ionb}}{\langle\sigma v\rangle_{cxb}} - \frac{n_c^2}{(n\tau)_{ec}} - \frac{n_c^2}{(n\tau)_{xfe}} - (\frac{dn_{ep}}{dt} - S_p) \frac{2V_p}{V_c}$$

where the first term on the right-hand side represents any external source; the second comes from ionization of barrier pumping neutral beams; the third gives the end losses over the potential barrier ϕ_e; the fourth simulates the cross field diffusion; and the fifth and sixth give the transfer of particles between the plug and central cell populations.

By quasineutrality, the ion and electron densities and their derivatives are equal everywhere. Therefore, only the ion density rate equations are integrated to obtain the time evolution of the plug and central cell densities. The integration of the electron density rate equations does not provide any new information. By equating the ion and electron currents in the central cell and plugs, two new independent equations are obtained which allow for the calculation of the confinement electrostatic potentials. The central electron

confinement potential follows from the equation

$$\frac{dn_{ec}}{dt} = \frac{dn_c}{dt} \ .$$

The central cell ion confinement potential follows from the equation

$$\frac{dn_{ep}}{dt} = \frac{dn_p}{dt} \ .$$

In order to evaluate the confinement parameters $(n\tau)_{ic}$, $(n\tau)_{ec}$, and $(n\tau)_{ep}$, generalized Pastukhov expressions are used. The Logan-Rensink model is used to calculate the plug ion confinement parameter $(n\tau)_{ip}$.

The four temperature rate equations are of the form

$$\frac{dT_j}{dt} = \frac{2}{3n_j} (S_j - L_j) - \frac{T_j}{n_j} \frac{dn_j}{dt}$$

where the subindex j indicates species; S_j and L_j are the sources and sinks of power as described in Section III.2; and dn_j/dt have been given above.

The expressions for the central cell beta, plug beta, plug radius, barrier parameters (potential, density, radius, beta, ion trapping current, and energy and angle required for the pumping neutral beams), as well as the formulas to calculate the neutral beam absorption fractions, fusion power, powers absorbed and injected into the plasma and amplification factor Q, are those described in Section III.2.

Plug fueling and heating are provided by neutral beam injection and ECRF power. The central cell fueling and heating are done by ionization of the barrier pumping neutral beams and ICRH power to ions. This time dependent

code also includes external fueling and auxiliary power to central cell electrons to be used during startup. The other source of power taken into account is the heating of central cell ions and electrons due to the thermalization of the alpha particles, but the code does not account for the detrimental effect on the ion density due to the accumulation of alpha particles.

The rate code approach to study transient phenomena has the benefit of simplicity and speed but contains the uncertainties inherent in the models. The electron and ion end loss expressions as well as the Logan-Rensink model used to find the plug ion confinement time are reasonably valid over the range of parameters used in this study. But the expressions for the barrier ion trapping rate are valid only for $\phi_b/T_{ic} \gg 1$ and intermediate values of the pumping parameter, g_b. No model has yet been developed which gives the barrier ion trapping current for all ranges of ϕ_b/T_{ic} and g_b. Unfortunately, during startup ϕ_b/T_{ic} can be less than one. The code assumes that the formula for the barrier trapping ion rate is valid for all obtainable values of ϕ_b, and a constant pumping parameter g_b is imposed. The same applies to the expression for the barrier passing ion density, which is only valid for $\phi_b/T_{ic} > 1$.

IX.1.3.2 Method of Solution

The system of six coupled rate equations can be written in the form

$$\frac{dy_i}{dt} = g_i(y_j, \phi) + a_i(y_j, \phi)\, S_i \qquad i,j = 1 \text{ to } 6 \qquad \text{(IX.1-1)}$$

where y_1, y_2, y_3 are the density, mean ion energy and electron temperature of the plug plasma and y_4, y_5, y_6 are the density and ion and electron temperatures of the central cell plasma. S_i represents the external sources and ϕ

represents the barrier, plug, and central cell potentials, which are given by instantaneous nonlinear equations of the form

$$f(y_j, \phi) = 0 \ .$$

The solution of this system of equations is calculated using one of the three possible modes of operation of the code:

1. Steady-state calculations in which, for a given set of y_i, the code calculates the sources S_i such that $dy_i/dt = 0$.

2. Starting with a set of initial conditions y_{io}, the code calculates the time evolution of y_i for given time dependent sources injected into the plasma. To integrate the system, a predictor-corrector method is used.

3. Starting with a set of initial conditions y_{io}, the code calculates the sources needed to maintain a certain kind of time variation of y_i. The profiles chosen are growing exponentials with constant asymptotic values and variable growth rate such that the sources can be kept within some specified limits. A schematic flow chart is given in Fig. IX.1-1.

In the steady state calculation it takes only a few time steps for a set of sources to converge to a stationary value. The convergence is not obtained in the first iteration since some of these sources influence the instantaneous equations which give the potentials at each time step, thus altering the coefficients of the rate equations. If care is used in choosing the input values for the set y_i, the obtained sources are also reasonable and the convergence is very fast. These calculations are useful in doing parametric studies and trying to obtain a reference case in which the power handled by every fuel and heating system is acceptable.

IX.1-9

FLOW DIAGRAM FOR THE RATE CODE
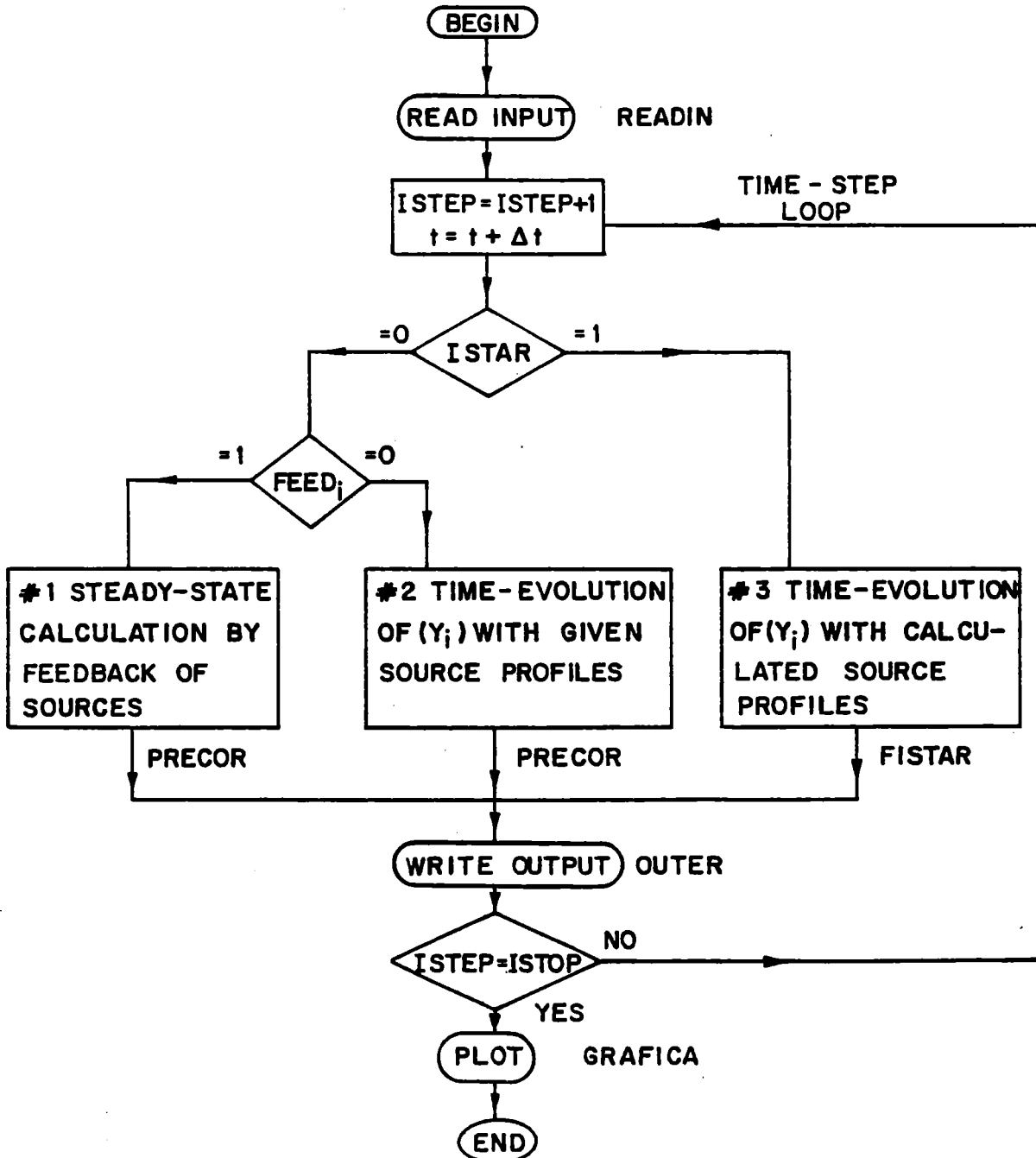
Fig. IX.1-1

The predictor-corrector method used in the second mode of operation is Heun's method. Figure IX.1-2 shows the scheme of the calculation. The predictor is Euler's formula and the corrector assumes that $y_i(t)$ is quadratic. The iterative procedure between the corrector formula and the corresponding differential equation continues until the convergence criterion is satisfied for all six equations simultaneously. There is a trade-off between the length of the time step and the number of corrector iterations. If Δt is chosen too large, an excessive number of iterative cycles may be needed for convergence or even the algorithm may not converge at all. Large differences between predictor and corrector outputs suggest reduction of the interval. On the other hand, very small differences between predictor and corrector outputs suggest increasing the time step length and perhaps speeding up the computation. The convergence criterion used is $\varepsilon = 0.001$ with maximum number of iterations ICMAX=10. If this number is reached the time step length is reduced and the time step repeated.

The time step length can be either specified or calculated at the beginning of each step. The code calculates characteristic times τ_i for the variation of each variable and the subsequent time step length is limited to 10% of the shortest characteristic time for density or temperature variations up to a specified maximum time step size as equilibrium is approached.

The numerical stability of this scheme has been studied by choosing a set of initial conditions and external sources known to form a stationary point, and running the code with different fixed time step sizes. It was found that for time steps < 0.1 ms, the differences obtained with respect to the stationary point, after a long enough simulation, were not significant. For time steps sizes > 1 ms, the departure from the stationary point was significant.

CALCULATIONAL SCHEME OF MODE # 2.

BEGIN TIME-STEP K

INITIALIZATION

SOURCE
ISYSTEM
TSYSTEM

REPEAT
TIME-STEP

CALCULATE PREDICTOR VALUES

$$Y_i^P(K+1) = Y_i(K) + \Delta t \cdot \frac{dY_i}{dt}\Big|_K$$

IC = IC+1

CORRECTOR LOOP

CALCULATE CORRECTOR VALUES

$$Y_i^{ic}(K+1) = Y_i(K) + \left(\frac{dy_i}{dt}\Big|_K + \frac{dy_i}{dt}\Big|_{K+1}\right)\frac{\Delta t}{2}$$

ISYSTEM
TSYSTEM

RECALCULATE
$\Delta t(K)$

$$\frac{\left|Y_i^{ic}(K+1) - Y_i^{ic-1}(K+1)\right|}{Y_i^{ic}(K+1)} \leq E$$

NO

IC=ICMAX

YES

=1

ITIMST

NO

YES

=0

YES

=1   ITIMST   =0

CALCULATE
$\Delta t(K+1)$

STOP

RETURN

Fig. IX.1-2

IX.1-12
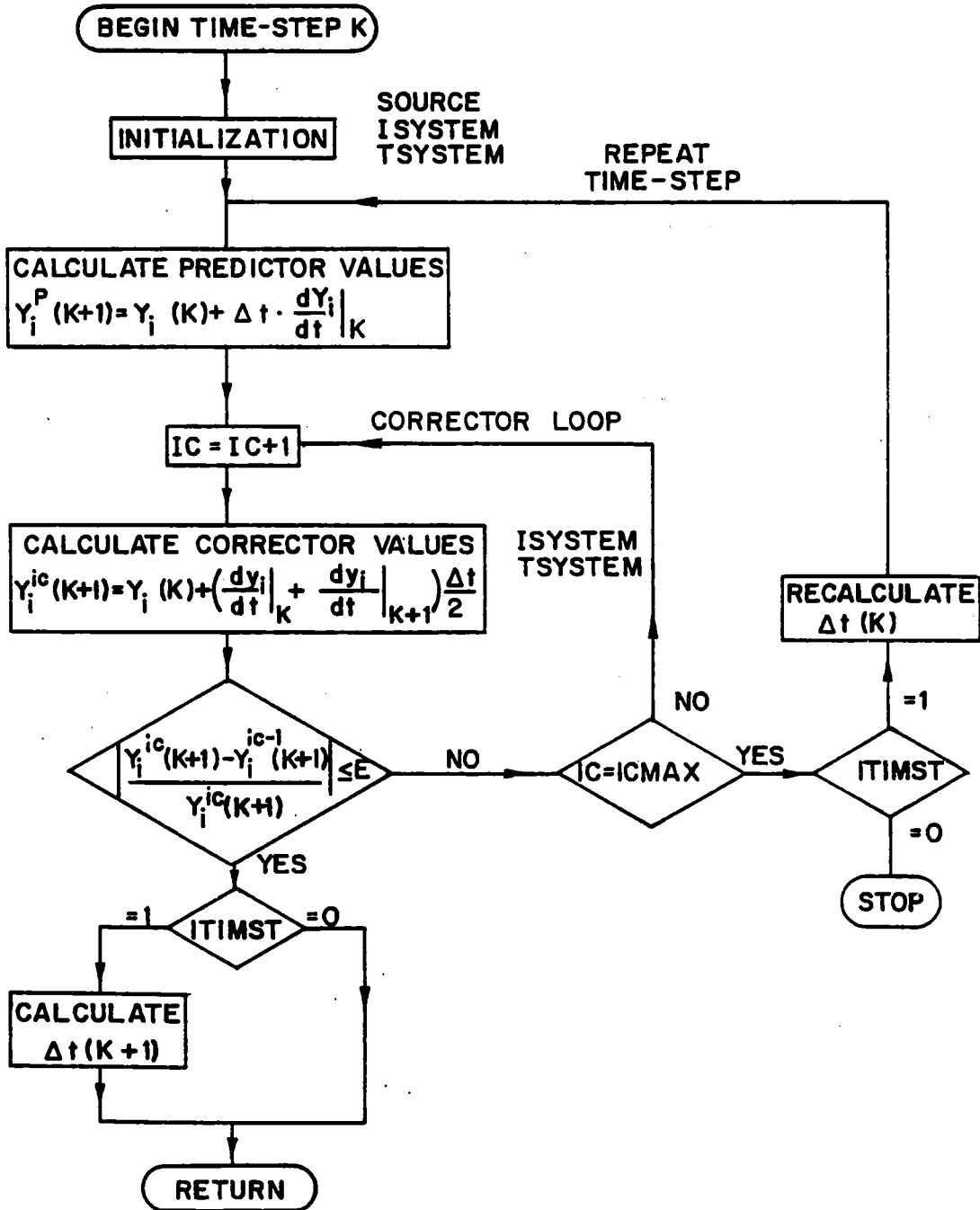
Therefore, Δt = 1 ms is the largest time step used in calculations near steady state values. For situations far from steady state a very small time step is initially taken ($\sim$ 1 μsec) and the option of variable time step is used.

The predictor-corrector method can be used in combination with steady state calculations in finding the time evolution of some of the variables and the sources required to keep the other variables constant. This method is helpful for doing steady state calculations in which any of the required powers becomes negative. This power can be set equal to zero and the corresponding variable is allowed to change. Also it can be used for startup calculations in which one of the cells (e.g., the plug) is initially built up and it is required to hold it in steady state.

The scheme of calculation of the third mode is represented in Fig. IX.1-3. At time step k, the iteration is started using the values of the exponential growth rates α_i^k and external sources S_i^k found in the preceding time step. The values of the variables at time $t + \Delta t^k$ are found from the equations

$$y_i^{k+1} = y_{iA} - (y_{iA} - y_i^k)\, e^{-\alpha_i^k \Delta t^k} \qquad i = 1 \text{ to } 6$$

where y_{iA} are the asymptotic values of the variables which coincide with the steady state operating point.

Now,

$$\frac{dy_i^{k+1}}{dt} = (y_{iA} - y_i^k)\, \alpha_i^k e^{-\alpha_i^k \Delta t^k} \quad . \qquad (IX.1\text{-}2)$$

However, from the rate Eq. (IX.1-1) the time derivative has the expression

CALCULATIONAL SCHEME OF MODE # 3.
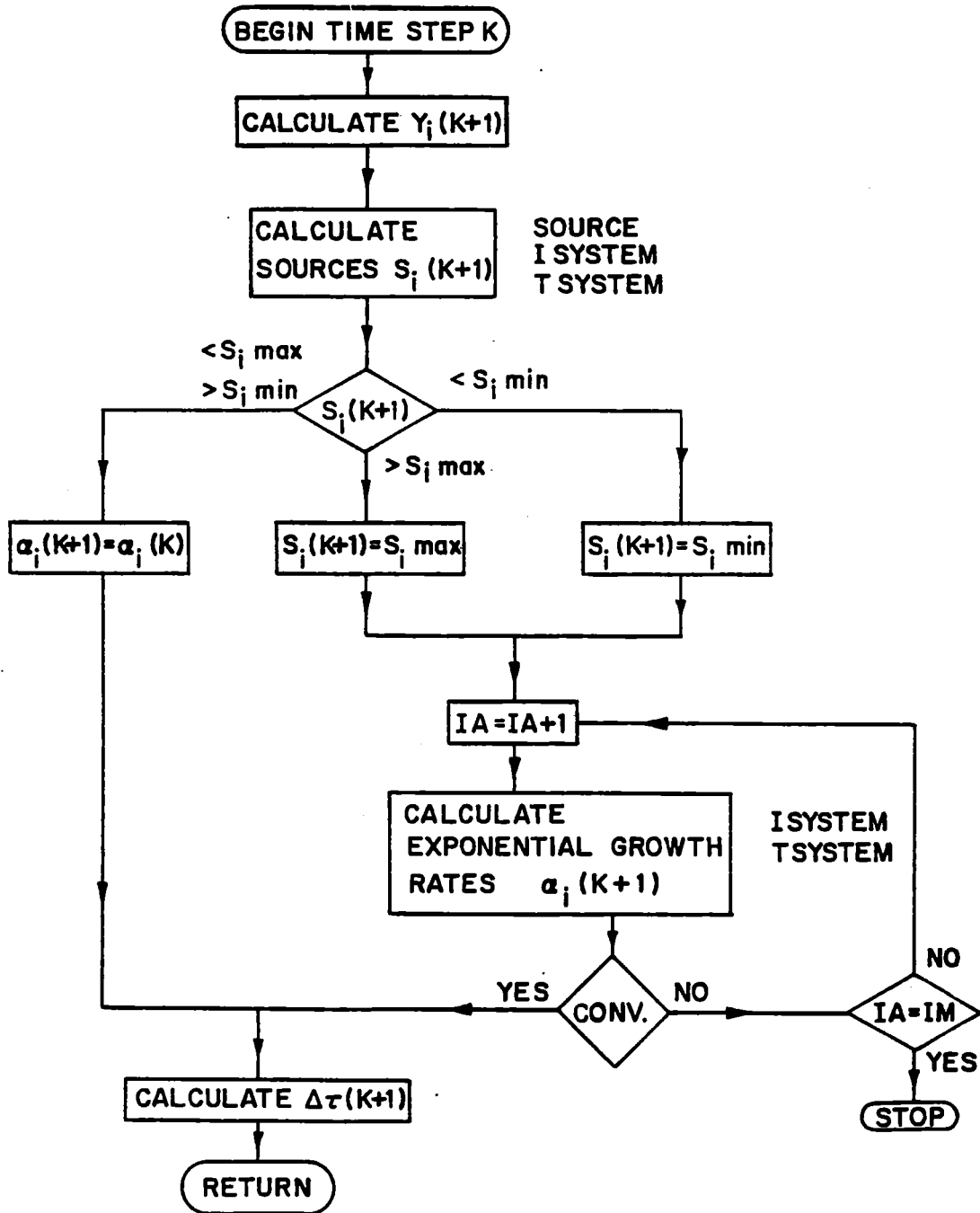
Fig. IX.1-3

$$\left(\frac{dy_i^{k+1}}{dt}\right) = g_i(y_j^{k+1},\phi) + a_1(y_j^{k+1},\phi) \cdot S_i^{k+1} \qquad j = 1 \text{ to } 6 \ . \qquad (IX.1\text{-}3)$$

This can be solved for the source strength,

$$S_i^{k+1} = \frac{\dfrac{dy_i^{k+1}}{dt} - g_i(y_j^{k+1},\phi)}{a_i(y_j^{k+1},\phi)} \ . \qquad\qquad , \quad (IX.1\text{-}4)$$

This source is now compared with specified maximum (S_{imax}) and minimum (S_{imin}) values of the source given as input data. If $S_{imin} < S_i^{k+1} < S_{imax}$, the values of y_i^{k+1} and S_i^{k+1} are those given by Eqs. (IX.1-2) and (IX.1-4), respectively, and the code takes $\alpha_i^{k+1} = \alpha_i^{k}$. If $S_i^{k+1} < S_{imin}$, the code sets $S_i^{k+1} = S_{imin}$ and the new values α_i^{k+1} are the solution of a nonlinear system of six coupled equations

$$(y_{iA} - y_i^k)\alpha_i^{k+1}e^{-\alpha_i^k \Delta t^k} = g_i(y_j^{k+1},\phi) + a_i(y_j^{k+1},\phi)S_{imin}$$

where

$$y_j^{k+1} = y_{jA} - (y_{jA} - y_j^k)e^{-\alpha_j^{k+1}\Delta t^k} \ .$$

It should be noted that all α_j^{k+1} are involved in the calculation of α_i^{k+1}. The loop is iterated until the convergence in all six α_i^{k+1} is obtained simultaneously. If $S_i^{k+1} > S_{imax}$, the same procedure is used, but now putting $S_i^{k+1} = S_{imax}$.

Once the values of y_i^{k+1}, α_i^{k+1}, and S_i^{k+1} are calculated, the code obtains the characteristic time τ_i for the variation of each unknown,

$$\tau_i^{k+1} = \frac{1}{\alpha_i^{k+1}} \left(\frac{y_{iA}}{(y_{iA} - y_i^k)e^{-\alpha_i^{k+1}\Delta t^k}} - 1 \right)$$

and the new time step is estimated as one-tenth of the minimum of these characteristic times.

The condition to reach the asymptotic values is that α_i^{k+1} be positive. If at any time step a negative α_i value is found the code changes it to the positive value that is specified as input data, and recalculates the source needed to sustain this growth rate, even if this implies going out of the allowed interval for the variation of sources. This feature has been included in the code in order to avoid the value of the variable going to $-\infty$ and the calculation being stopped due to numerical errors.

Another source of numerical error is due to those variables which reach values very near to the steady state values. This is corrected by assuming that when a variable reaches a value close enough to the desired asymptotic one, both are equal and the calculations related with that particular variable are skipped.

Finally, for this method to work, the initial set of α_i, S_{imin}, and S_{imax} must be chosen with care, since the loop that calculates α_i is highly non-linear, and has included in it the calculation of potentials which are also given by nonlinear equations. By using the predictor-corrector method of operation simulating a short excursion, a good estimation of the initial values of α_i and of the limiting values of the sources can be obtained.

Next the instantaneous calculations carried out at every time step are described. The code evaluates several parameters either for output purposes or for use in obtaining the coefficients for the rate equations. This

calculation is common for the three ways of solving the rate equations. The scheme is as follows. Magnetic field profile, central cell radius and length, and barrier length are held constant. First central cell beta, plug beta, and plug radius are calculated using densities and temperatures of the preceeding time step. The code now proceeds to find the barrier parameters by solving one of two possible barrier models which are based on the same equations, the difference between them being the input and output variables. In the first model, the pumping parameter g_b and the fraction of total pumping done for each one of the three pumping beams is given. Then, barrier beta, potential and density are calculated in a loop. Next the code obtains the trapping current and the pumping neutral beam currents. Injection energy and angle of the neutral beams can be either input or calculated; if they are input data the code checks that the injection point is in the appropriate region of velocity space. In the second model, the beam current profiles are given and the pumping parameter calculated. This last model seems more realistic in the sense that the beam currents can be externally controlled. The problem with this approach is that even though any kind of time dependent profile for the neutral beams can be specified, it is difficult to guess one that will obtain reasonable barrier parameters when compared with the parameters of other regions of the machine. The code also includes the possibility of doing the barrier pumping in two stages. In this option, the high energy pumping neutral beam does not pump ions directly to the central cell but rather it changes their energy in such a way that the resulting ions can be pumped by a very low energy neutral beam. After the barrier calculation the code obtains the central cell ion confinement potential, solves the Logan-Rensink model for

the plug and finally it calculates the central cell electron confinement potential.

In doing startup calculations, there is usually no difficulty in obtaining the time evolution using either one of the two integration schemes. But when the code is solving the instantaneous equations, it may occur, and often does, that for certain values of densities and temperatures the nonlinear equations that give the potentials do not have roots or they are out of the valid ranges. This happens more often with sets of values far from the stationary point or for situations in which one or more of the variables have grown at a much faster rate than the others. If this occurs, the calculation is stopped. This suggests that the physics model used only allows for the simultaneous buildup of the three regions of the machine.

The exponential growth method provides an easier way of simulating startup sequences than the predictor-corrector method does. In the latter method the sources specified at every time step have strong influence in the rate equations. Therefore, the set of densities and temperatures obtained as a result of the time integration may be such that the roots of the equations which give the potentials cannot be found. The exponential growth method does not have this inconvenience because the sources are not input data to the time integration. In order to obtain a complete startup sequence by the predictor-corrector method it would be necessary to adjust the input sources every few steps. The output consists of the time evolution of the most relevant parameters of the machine. This code is written to run on the MFECC CDC-7600 machine. Running time is approximately twenty seconds per one thousand time steps.

IX.1.3.3 Results

Startup studies are aimed at demonstrating a technique for attaining steady state plasma parameters starting from a set of initial conditions and trying to achieve this goal, while minimizing the amount of injected power. An ideal case would be to reach the stationary point using only the power supply needed at steady state operation. Unfortunately this goal seems impossible to accomplish, at least within the constraints of the physics model used here.

The results presented in this section are an example of the estimates of the amount of power and particle currents that are expected to be necessary to reach a steady state operating point in the machine. They have been obtained using the exponential growth method. The asymptotic values and input parameters correspond to the reference case (see Section III.4). The density and temperature of the initial target plasma are assumed to be one-tenth of the asymptotic values.

Graphs that give the time evolution of the more relevant plasma parameters and the required external sources are included. Densities are given in cm^{-3}; temperatures, potentials and energies in keV; currents in sec^{-1}; powers in MW; and time in seconds.

Figure IX.1-4 shows the time evolution of plug density, plug ion mean energy, plug electron temperature, central cell density, central cell ion temperature, and central cell electron temperature. Plug electron temperature is the first variable to reach steady state even though the ECRH power to plug electrons is less than nominal during startup. The rest of the variables, except the plug ion mean energy, reach the stationary point in ~ 300 msec. The plug ion mean energy reaches its steady state value at time ~ 1 sec.
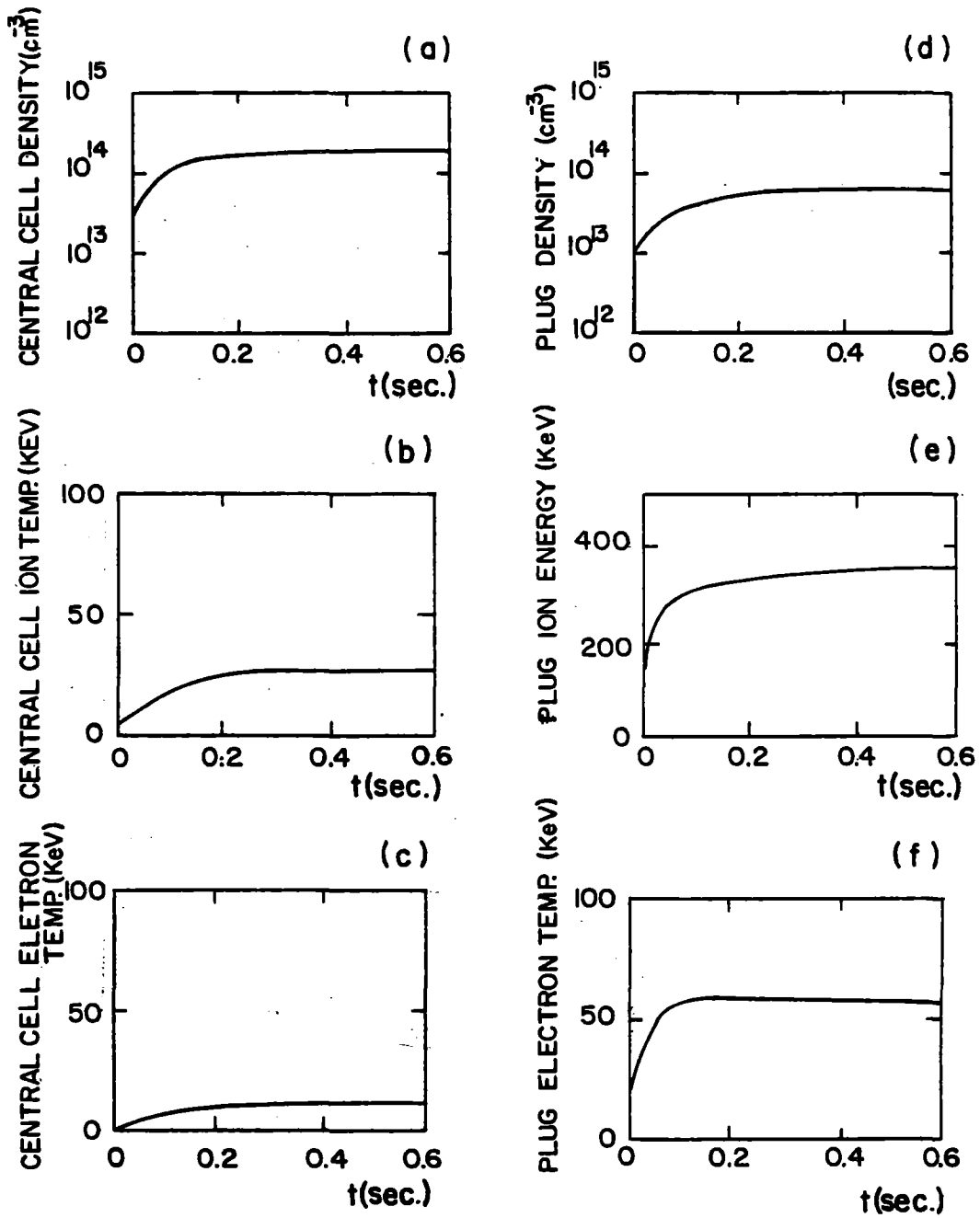
Fig. IX.1-4. Time-evolution of densities and temperatures in central
cell and plug.

Figure IX.1-5 shows the evolution of barrier, plug, and central cell potentials, and central cell, barrier and plug betas. The plug beta reaches the steady state value in ~ 1 sec. The other variables are stationary at time ~ 300 msec.

Figure IX.1-6 describes the medium energy barrier pumping neutral beam showing the time evolution of the power and current absorbed by the plasma; injection energy (held constant during this simulation); power and current injected into plasma and absorption fraction, respectively. The absorbed power needed for startup is smaller than that at steady state. This fact is compensated by the smaller absorption fraction; the end result is that the total injected power remains near the steady state value. Similarly, Fig. IX.1-7 describes the high energy barrier pumping neutral beam, and Fig. IX.1-8 shows the time evolution of the low energy barrier pumping neutral beam.

Figure IX.1-9 shows the evolution of the plug neutral beam: neutral beam power and current absorbed by the plasma, energy of the beam, neutral beam power and current injected into plasma and absorption fraction of the beam. During startup the absorbed plug neutral beam power is slightly above its steady state value. But when the absorption fraction is taken into account, the injected power needed grows dramatically.

Figure IX.1-10 shows the time evolution of the plug ECRH power and the central cell sources: ICRF heating to ions, particle source and auxiliary electron heating. The time evolution of the absorption coefficients for the several RF heating systems are not yet modeled in the code so total absorption is considered. ECRF heating of the plug must be supplied gradually or else the plug electrons overheat. Finally, Fig. IX.1-11 shows the total absorbed power in the plasma, amplification factor of the absorbed power, fusion power
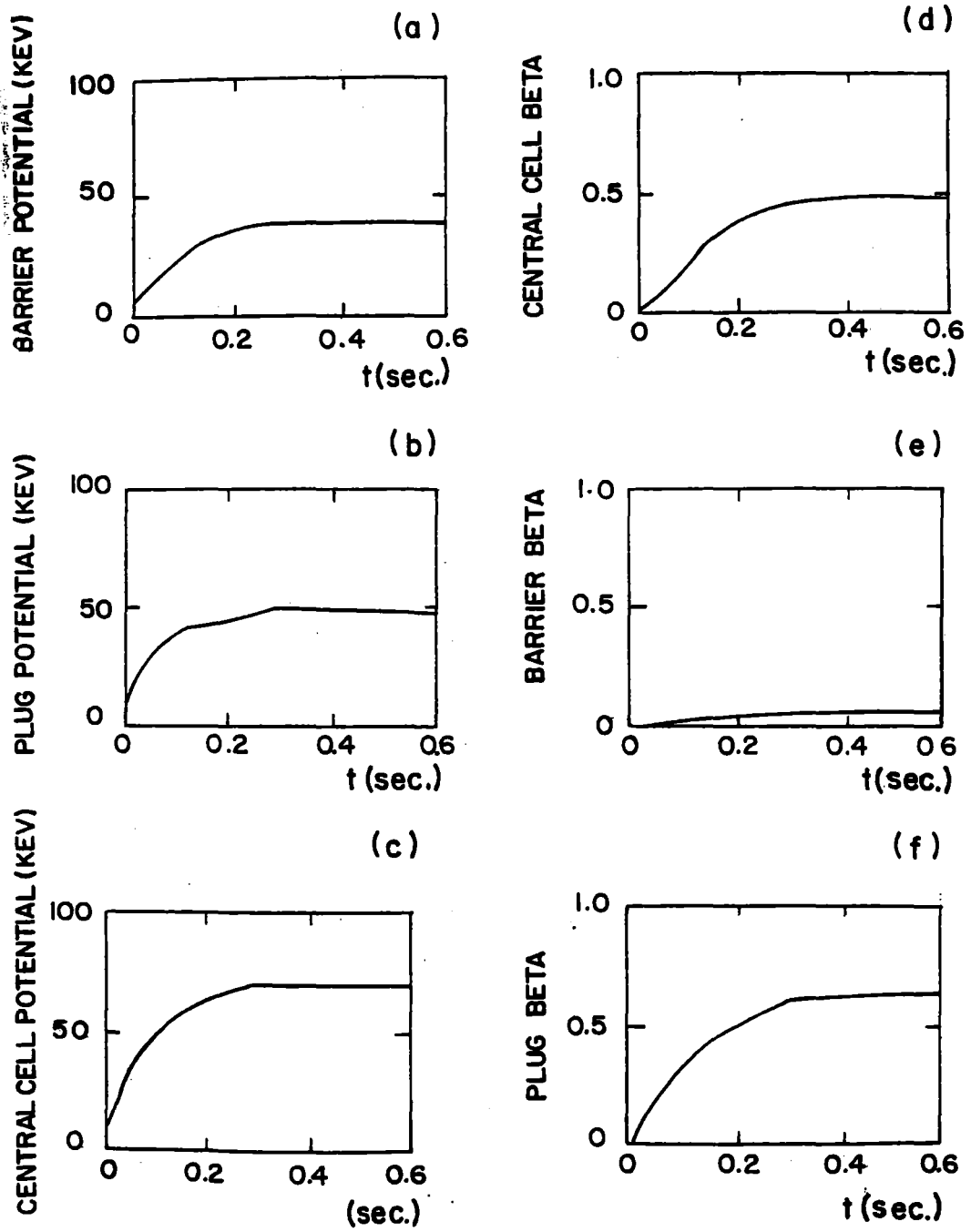
Fig. IX.1-5. Time-evolution of potentials and betas.
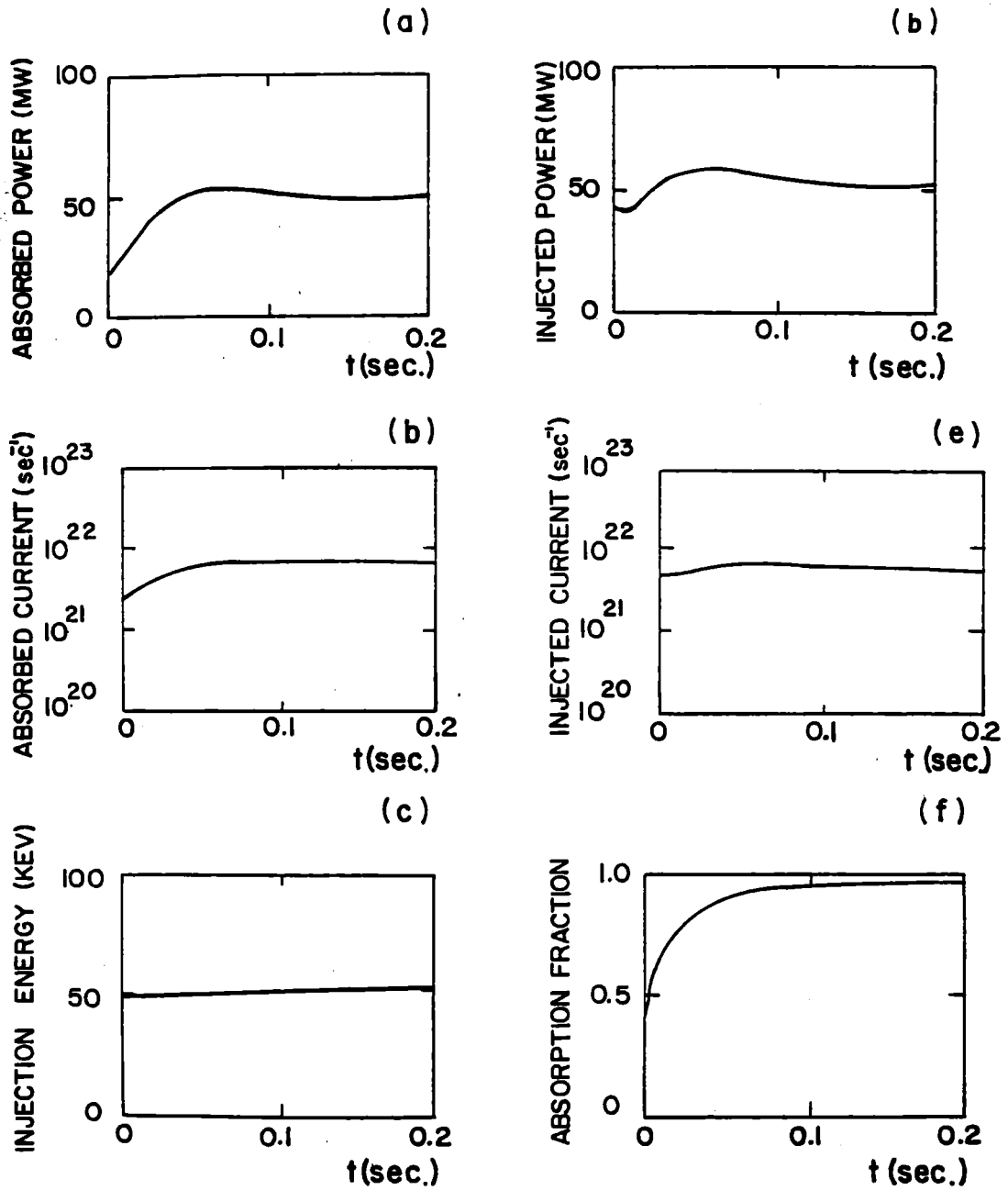
Fig. IX.1-6. Time-evolution of the medium-energy barrier pumping neutral beam.
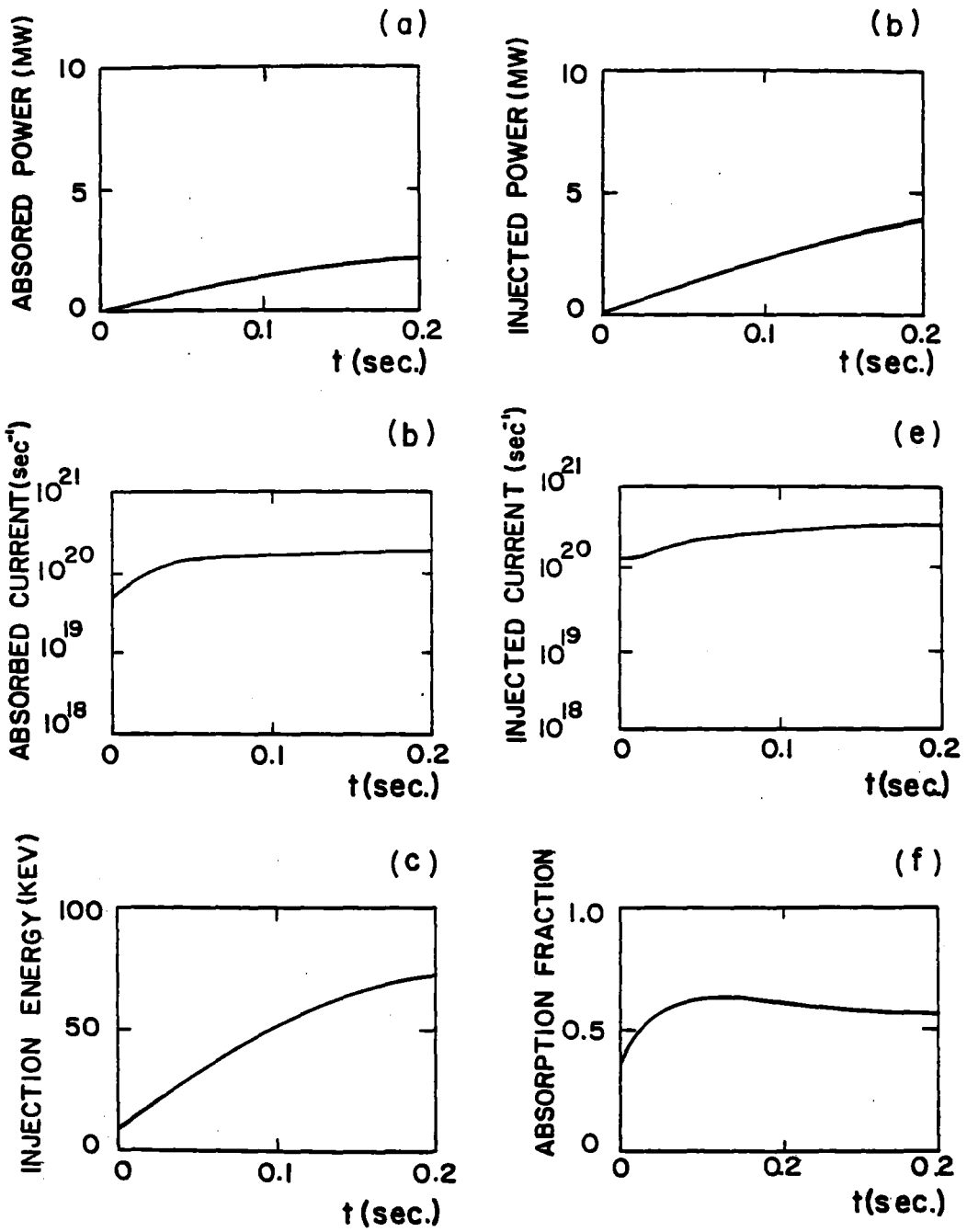
Fig. IX.1-7. Time-evolution of the high-energy barrier pumping neutral beam parameters.

(a) ABSORBED POWER(MW) vs t(sec.)

(b) ABSORBED CURRENT (sec⁻¹) vs t(sec.)

(c) INJECTION ENEGY(KEV) vs t(sec.)

(d) INJECTED POWER (MW) vs t(sec.)

(e) INJECTED CURRENT(sec⁻¹) vs t (sec.)

(f) ABSORPTION FRACTION vs t(sec.)
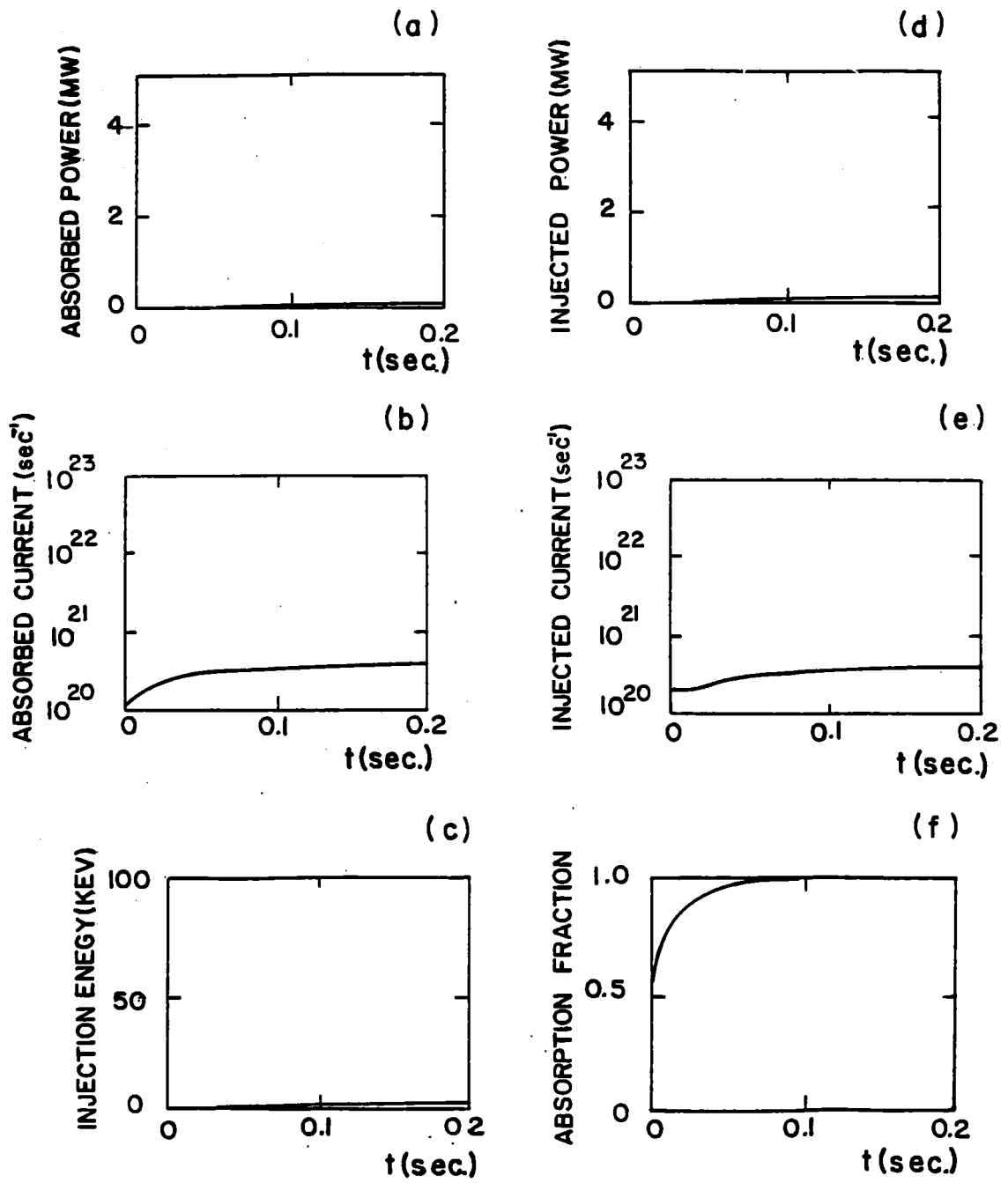
Fig. IX.1-8.   Time-evolution of the low-energy barrier pumping neutral beam parameters.
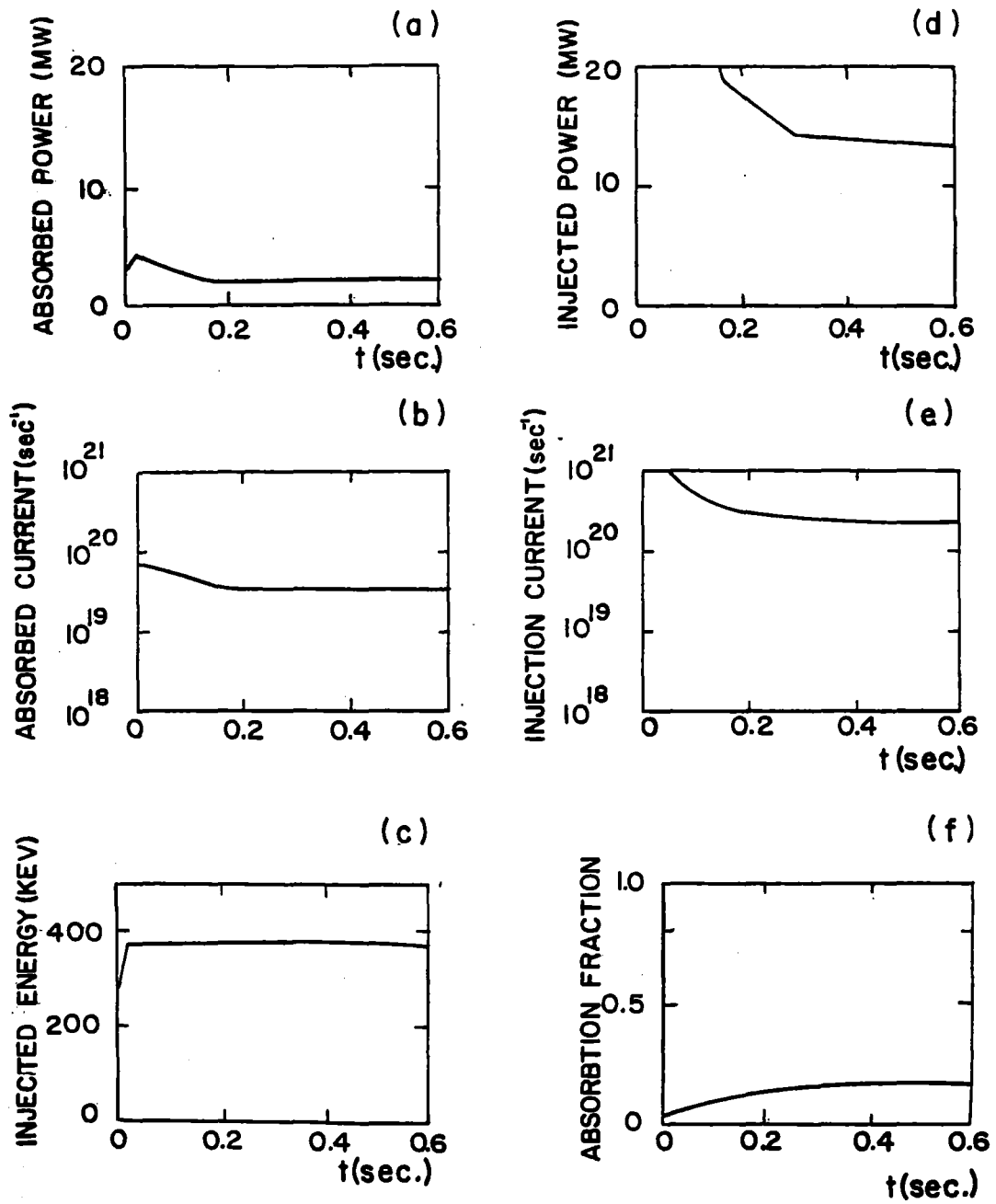
Fig. IX.1-9. Time-evolution of the plug neutral beam parameters.
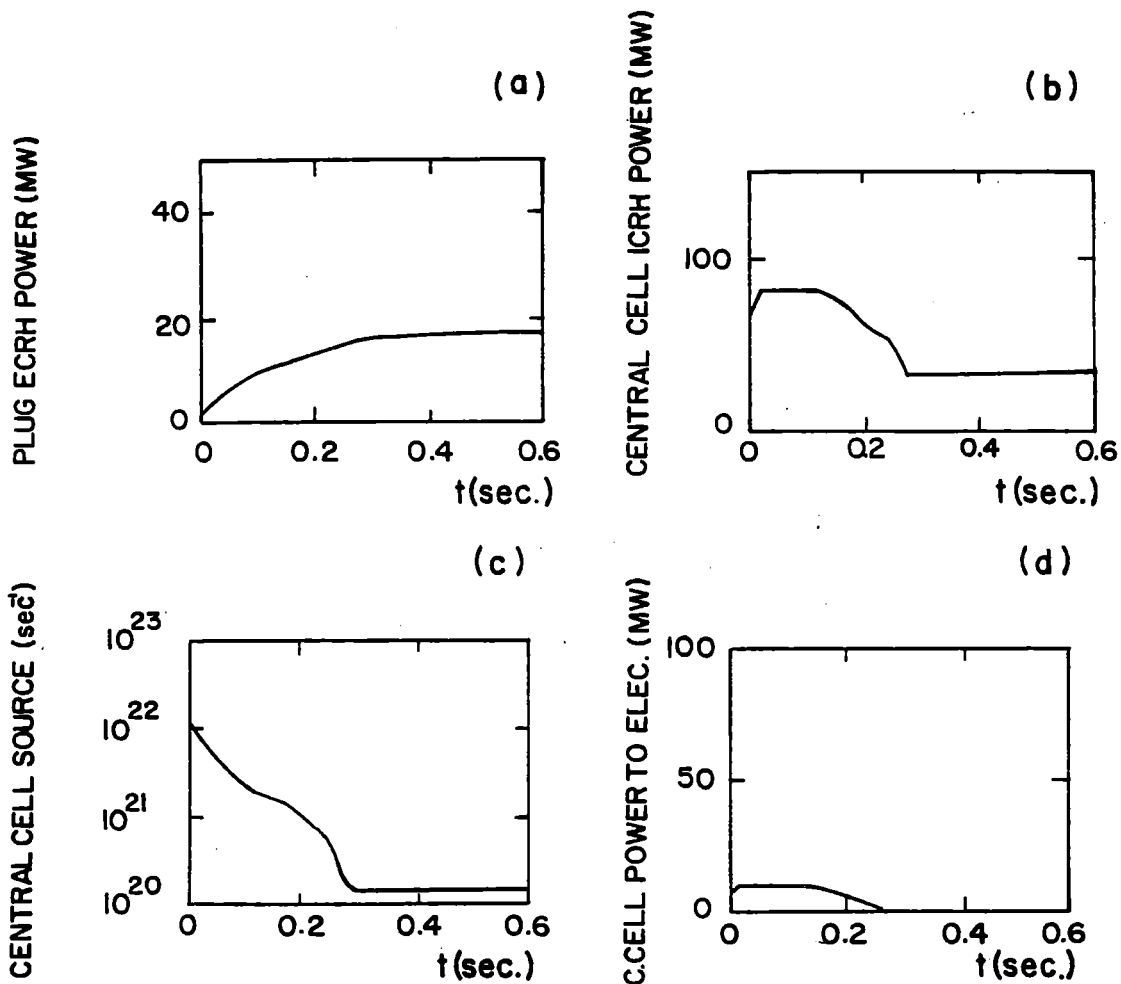
Fig. IX.1-10. Time-evolution of:

(a) ECRH power absorbed in the plug.

(b) ICRH power absorbed in the central cell.

(c) Central cell particle source.

(d) Auxiliary power absorbed by central cell electrons.
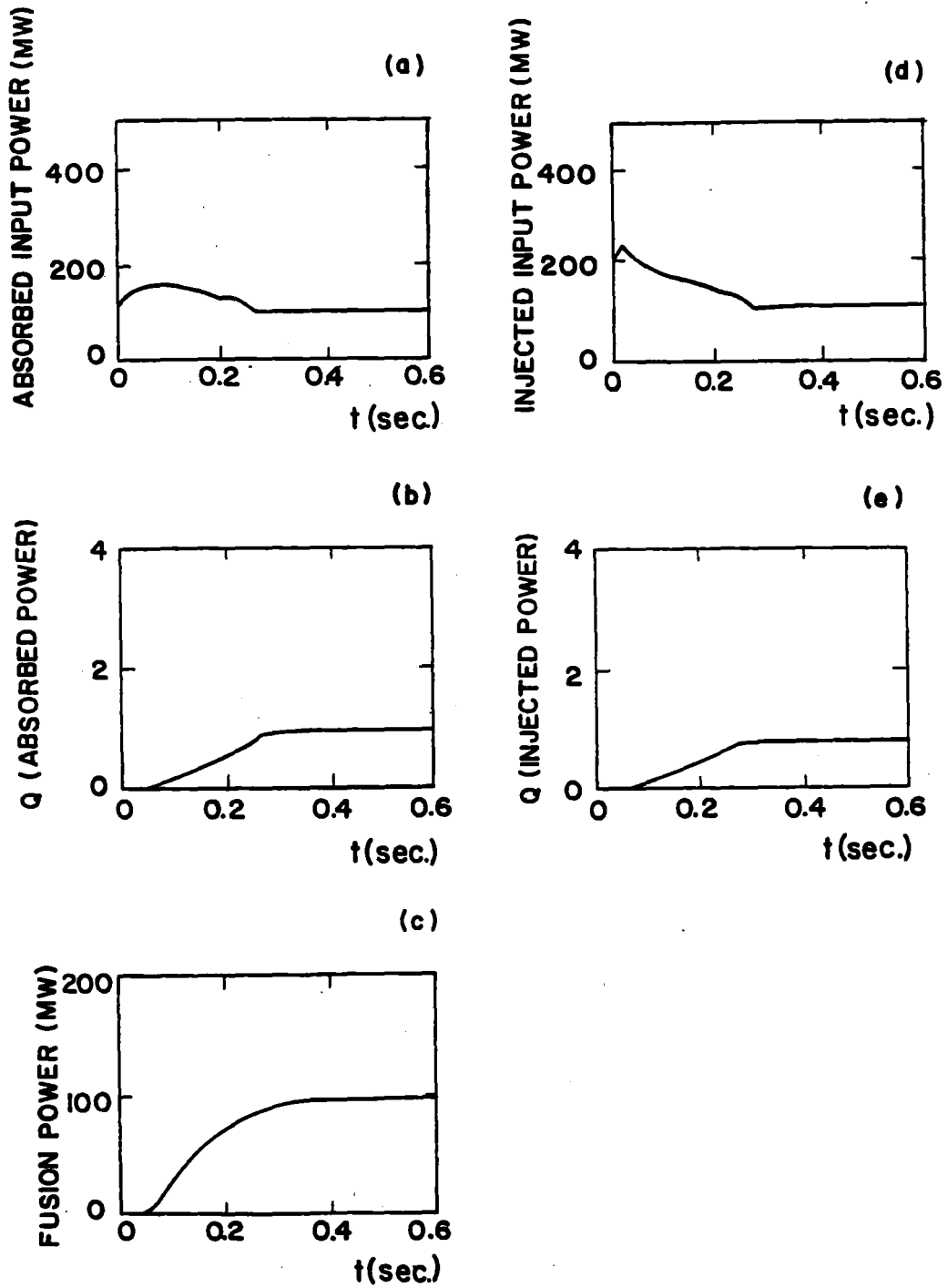
Fig. IX.1-11. Time evolution of: (a) total absorbed input power; (b) Q (absorbed power); (c) fusion power; (d) total injected power; (e) Q (injected power).

produced, total injected power in the plasma and amplification factor of the injected power. With respect to the central cell results one can see the large amount of extra heating and fueling, with respect to steady state values, that are needed to obtain the buildup of the central cell plasma. For this startup sequence the total injected power in the first stage of the buildup of the plasma, more than doubles the steady state value.

IX.1.4 Conclusions

From the results presented and from other possible startup scenarios that have been considered, there are some conclusions that can be made; their generality, however, is constrained by the validity of the physics model used.

1. In startup studies, a steady state plasma with the desired parameters can be achieved, but only with careful programming of the particle sources and injection power.

2. In steady state operation, the fueling of the central cell is provided by the passing ions produced by the ionization of the barrier pumping neutral beams. During startup the barrier neutral beams are not working at full power. Their strengths must be ramped in such a way to provide the necessary pumping power to create an increasing dip in the barrier potential. (An effective ramp of the neutral beam power can be obtained by repetitive pulsed operation with increasing duty factor.) Because of this, the central cell is underfueled and it needs an additional particle source until its buildup is completed.

3. Central cell heating in steady state operation is due to both direct ion heating by ICRF and power transferred by passing ions coming from the thermal barrier region. The latter is reduced during startup and a larger amount of ICRF power must be injected to raise the ion temperature. For a

design without any direct central cell ion heating, as was considered for the TASKA design in an earlier stage, all the central cell heating in steady state operation is provided by the barrier passing ions. This kind of design worsens the problem of lack of power to the central cell during startup since it increases substantially the extra power needed to reach the steady state central cell ion temperature and it implies the necessity of an independent heating system to be used only during startup.

4. Full RF power to the plug electrons is not needed during startup. If the nominal value of ECRH power is absorbed in a low density plasma, the rate of growth of the plug electron temperature is larger than that of any other species in the central cell and plug. This causes the plug electrons to overheat, leading to a very lossy plug plasma and eventually to the failure of the plug model.

The preceding considerations about the power required for startup apply to those powers absorbed by the plasma. The actual powers that need to be injected depend on the absorption coefficients which change dramatically with the plasma conditions. This effect influences the power injected as follows:

1. The injected power required for the barrier pumping neutral beams turns out to be approximately that of the steady state situation. This is because the power absorbed by the plasma and the absorbed fraction of the injected power increase as the barrier buildup progresses. In some sense, the barrier pumping neutral beams ramp themselves.

2. The plug neutral beam injection power needed in the first stage of startup increases by an order of magnitude. This suggests the necessity of studying other approaches. For example, initially creating a cold target

plasma of high density in the plug and using the neutral beams to heat this plasma is one possibility.

3. It has been seen that the heating characteristics of the plug region during startup are such that the absorbed ECRH power should increase gradually. Otherwise, it is known that the absorption of ECRH power improves as electron temperature increases. Therefore, it seems reasonable to expect that the ECRH system might naturally ramp itself. This will not be applicable to the RF power needed in the central cell since they're twice the steady state value of ICRF absorbed in plasma is required at startup.

It appears possible that a revision of the rate at which the central cell is built up will reduce this initial surge in the required ICRF power. Further work on various startup scenarios is required in order to be more definitive about this possibility. Further work on starting at lower initial values, i.e. more appropriate to stream gun plasma conditions, is also needed in order to model the entire startup process.

IX.2 Diagnostics, Instrumentation, and Control

IX.2.1 Introduction

The requirements for diagnostics, instrumentation, and control for TASKA can be conveniently divided into three aspects, namely General Instrumentation and Control, Neutron Diagnostics and Plasma Diagnostics. Requirements for each of these categories follow in the next three sections.

A detailed listing of each of the transducers, sensors and control instruments required by this device will not be given here; indeed such a description would be well beyond the scope of this report. However, a broad examination of the requirements will demonstrate the wide variety of diagnostic and control instrumentation necessary for a machine of this complexity, and will indicate which aspects of the instrumentation will require attention between now and the envisaged time frame for TASKA (i.e., the 1990's). In this respect, it should be noted that whereas the status of instrumentation for both general control monitoring and neutron diagnostics is in a fairly comfortable situation, the same is not true of plasma diagnostic instrumentation. This is because there are few current plasma diagnostic techniques which can be successfully integrated with the severe reactor-like environment of a fusion device such as TASKA. There appears, therefore, to be an urgent requirement for the development of fully engineered and hardened plasma instrumentation capable of sustained operation in a high power D-T environment.

IX.2.2 General Instrumentation and Control

Individual aspects of the general instrumentation and feedback control requirements for TASKA do not present the same degree of sophistication of complexity as those for the neutron and plasma diagnostics. This is due to

the fact that the majority of these requirements will be met by conventional process instrumentation which is currently available. In addition, the wealth of experience stemming from the design and application of instrumentation and control systems for fission reactors will be of direct applicability to TASKA.

In this connection, two areas of concern for the operation of conventional instrumentation in TASKA should be highlighted. Firstly, instrumentation positioned in the inner regions of the blanket or shield near the plasma will be subjected to neutron and gamma radiation fields of much higher mean energies than those encountered in fission reactors. Thus, conventional instrumentation systems in this region (e.g., temperature monitoring thermocouples, etc.) will be expected to sustain increased levels of radiation damage (see, for example, reference 1). Secondly, this instrumentation must be able to function successfully in a magnetic field environment where $\underline{B}$ will attain several teslas. Attention should, therefore, be focussed on the replacement of these susceptible hardwired signal channels and their associated transducers and preamplifiers, etc., with data transmission via light, IR or microwave techniques.

Although more or less conventional process/BOP instrumentation and control systems will be employed, TASKA will, nevertheless, be a highly instrumented device. In this connection, a total number of ~ 10,000 data channels may be assumed. A redundancy factor of the order of three will be incorporated for those data channels originating from, or directed to, inaccessible regions of the machine, thus reducing maintenance and downtime requirements. It is also envisaged that digital signal multiplexing will be employed, by which signals are digitally encoded near their source and then transmitted simultaneously to control room destinations via a few main data

highways. Such a system can be seen to result in a large reduction in wiring penetrations and installation costs.

A summary list of general instrumentation and control requirements for TASKA follows below in Table IX.2-1. As indicated above, much of the parametric data transmission will be by light/fiber-optic, IR, or microwave technology, a field which is currently undergoing rapid evolution. Microprocessor-based control, of at least one order of magnitude greater capability than present day, may be assumed.

Table IX.2-1

General Instrumentation and

Control Requirements for TASKA

1.   NEUTRAL BEAMS

NBI ion source parameters; beam diagnostics and calorimetry; injected power distribution; internal ion dump temperature and coolant conditions; vacuum conditions; getter pump cycling control; tritium injection and recycle monitoring; magnetic shielding conditions.

2.   NEUTRAL BEAM DUMPS

Residual NB diagnostics; dump temperatures; coolant conditions and flow rates; burnout detection; tritium leakage.

(Table IX.2-1 continued)

3.   ECRH

All ECRH input parameters; microwave injected power and input

distributions; gyrotron coolant conditions; gyrotron magnet cooling;

waveguide and horn temperatures and coolant conditions; SF_6 gas

parameters; vacuum conditions.

4.   ICRH

ICRH input parameters to RF oscillators; RF power to antennas; RF power

and distribution to plasma; antenna coolant conditions; coaxial line

temperature profiles; SF_6 gas conditions.

5.   MAGNET SYSTEMS

All cryogenic parameters for He, N_2, and H_2O including cryo-levels,

temperatures, flow rates, boiling detection; refrigeration plant

instrumentation; superconducting coil parameters including voltage,

currents, temperatures; coil quench detection; coil shorted turn

detection; general magnet protection feedback system; general power

supply instrumentation and quench protection; extensive field

monitoring.

(Table IX.2-1 continued)

6. VACUUM VESSEL - FIRST WALL

Vacuum conditions in each region; first wall temperatures and coolant conditions; neutron fluence levels for radiation damage assessment; structural loading.

7. BLANKET

Temperature profiles; neutron flux levels; gamma flux levels; Pb-Li coolant conditions (pressure, temperatures, flow rates); power flow; breeding ratio; tritium containment and leak detection; induced radioactivity; decay heat conditions.

8. REFLECTOR AND SHIELD

Temperature profiles, neutron/gamma leakage; tritium leak detection; induced radioactivity; decay heat conditions.

9. REGAT MODULE

General test module instrumentation; temperature profiles; neutron/gamma fluence gradients; coolant parameters; tritium leakage and contamination.

IX.2-5

(Table IX.2-1 continued)

10.   VACUUM SYSTEM

General pumps - pressures; flow rates; tritium containment; leak detection.

Cryopumps - temperature; cryo-conditions; saturation recycling monitoring; backing pump instrumentation; tritium containment and leak detection.

Getter panels - temperatures; saturation recycling monitoring; backing pump instrumentation; tritium containment and leak detection.

11.   TRITIUM FUELLING AND REPROCESSING

Tritium inventories for liquid, gas and solid phases; tritium loss and leak detection; external tritium leakage and contamination; all remote handling controls; decay heat monitoring; fuelling flow rates; impurity assay.

12.   OUTER SUPPORT STRUCTURES

Temperatures; stress profiles; operating radiation levels; induced radioactivity; tritium contamination.

IX.2-6

(Table IX.2-1 continued)

13. INNER CONTAINMENT BUILDING

Temperatures; pressures; air flow conditions; operating radiation levels; radioactivity levels; tritium leakage and contamination.

14. HEAT TRANSFER CYCLE/ELECTRICITY PRODUCTION

Pb-Li - pressure; temperatures; flow rates; tritium inventories; radiation levels; decay heat conditions.

HB-40 intermediate loop - pressure; temperatures; flow rates; tritium leakage and contamination.

Steam generators/turbines - conventional instrumentation; tritium leakage and contamination.

IX.2.3 Neutron Diagnostics

The neutron diagnostic requirements for TASKA present a degree of sophistication somewhat between those for the conventional process control and the diagnostic instrumentation for the other plasma parameters. Neutron spectrometers, by definition, are designed to operate in neutron radiation fields. However, the D-T neutron environment of TASKA presents flux levels

which are several orders of magnitude greater than those encountered in other applications of neutronics instrumentation to date (e.g., accelerator environments, neutron benchmark experiments, neutron cross section determinations, etc.).

The three main neutron diagnostic parameters of interest are the total neutron yield, the spatial variation of neutron emission intensity across the plasma and the energy distributions of neutrons originating from localized regions of the plasma.* The first of these measurements is required in the determination of the overall energy balance of the machine (i.e., system Q), while the second provides information on the spatial density variation of the plasma profile. The third neutron diagnostic parameter, i.e., high resolution spectrometry, leads to the determination of local ion temperatures from the Maxwellian-broadened modulation of output neutron line spectra.

Problems which will be encountered in TASKA and which must be surmounted for successful neutron measurements follow below; in this connection it is interesting to note that there are apparently no radiation damage problems for neutron diagnostic instrumentation:

1.   Very high radiation fields can lead to signal "pile-up" in active neutron detectors. Stringent collimation is thus required (see also point 8 below) (continued).

---

* Time dependent neutron spectrum measurements are not considered to be important here since TASKA is a steady state device; neutron detectors which give a fast time response may, however, be useful during startup.

2. Many active neutron detectors are equally sensitive to gamma radiation.[4] Some form of effective pulse-shape discrimination is, therefore, required.

3. Active detectors, especially those containing photomultipliers, must be effectively shielded from the high magnetic fields.

4. Similarly, detectors must be shielded from induced voltages resulting from dB/dt effects during startup.

5. Neutron spectrometers must be well shielded from room-returned and scattered neutrons. Again, effective collimation must be employed together with non-radiatively absorbing shield material, e.g., Li_2Co_3 (see also point 8 below).

6. Sensitivity of active detectors to mechanical vibration. This is especially important for ion chambers and ^3He proportional counters.

7. Spurious D-D and D-T neutron production from the neutral beam dumps (see Section VI.3). Such neutron production presents a serious problem from the point of view of spectral measurements. It is, however, of no consequence in a total neutron yield determination, since it represents just another output term in the determination of the overall Q of the device.

8. Access and penetrations. Neutron spectrometer systems in a DT reactor environment such as this will require shielding enclosures comprising concrete, Li_2O_3, paraffin wax, etc., with a total mass in the region of several tonnes, together with collimation paths of the order of meters. Thus, the detector systems must be situated well back from the z-axis of the machine and, for the central cell, must be located outside of the superconducting magnets. This, therefore,

results in a considerable number of line-of-sight penetrations* to the plasma, especially in the case of the profile monitor system where a typical design will require an array of approximately twenty radial penetrations in the x-y plane (see for example Jarvis, et al.[5] and Hendel and Seiler[6].

Table IX.2-2 summarizes the neutron diagnostic requirements for TASKA and indicates the appropriate instrumentation. Such instrumentation is either currently available or under development. In this respect, neutron diagnostic instrumentation is considerably further advanced than diagnostic instrumentation for other plasma parameters (see the section following).

It should be noted in connection with Table IX.2-2, that the range of neutron fluxes encountered in TASKA will span ~ 8 orders of magnitude, from low power startup to full power. Neutron yields from the end cells of the machine during normal operation will always be at least an order of magnitude below those in the central cell.

IX.2.4 Plasma Diagnostics

By contrast to both the conventional process instrumentation and the neutron diagnostic instrumentation for TASKA, the requirements for the plasma diagnostics present a much more formidable problem. During the preliminary testing stage of TASKA, a pure hydrogen fueled phase is envisaged. This phase would be able to make use of the extensive plasma diagnostic techniques

---

* Although these penetrations must be line-of-sight, they do not, of course, require evacuating and may be sealed by the vacuum vessel or by stainless steel windows of ~ 1 cm thickness.

Table IX.2-2
Neutron Diagnostic Instrumentation for TASKA

NEUTRON MEASUREMENT TYPE	SUGGESTED INSTRUMENTATION
1. Total time integrated yield (total fusion reaction rate and Q determination)	$^{235}U/^{238}U$ fission chambers; foil activation with pneumatic rabbit system; BF_3 long counters
2. Time dependent neutron flux (startup reaction rate monitor)	Fission chambers; BF_3 long counters; (time resolution~ ~ 1 ms)
3. Radial profile determination (spatial profile of reaction rate)	Collimated x-y array of either fission chambers or NE 213 scintillators.
4. High resolution* neutron spectrometry (localized ion temperature distributions)	$D(d,n)^3He$ neutron spectrum: - ^3He proportional counter (2%); NE 213 scintillator (6%); ^3He/Si-surface barrier sandwich (2%); proton recoil telescope (3%) $T(d,n)^4He$ neutron spectrum: - NE 213 scintillator (4%); proton recoil telescope (1%).

* Figures in brackets after each spectrometer here indicate the best resolution obtained with that detector type.

which are currently available and employed on present day test devices. However, the D-T phase of operation will require a considerable advance in the "hardening" aspects of diagnostic instrumentation. Many types of current plasma diagnostic instruments would not survive the reactor-like environment of TASKA while others simply would not work (e.g., soft X-ray measurements for purposes of plasma electron temperature or impurity determination would be swamped by the large low energy gamma flux present in the system).

The major aspects of the TASKA fusion environment which place severe constraints on the plasma diagnostic instrumentation can be summarized as follows:

1. Very high neutron and gamma first wall fluxes of the order of 8×10^{13} $cm^{-2}s^{-1}$ (14 MeV) and 10^{13}-10^{14} $cm^{-2}s^{-1}$ (~ 0.5 MeV), respectively, with attendant severe radiation damage and activation problems.

2. Very high X-ray fluxes of $\sim 10^{15}$-10^{16} $cm^{-2}s^{-1}$ in the region of 10-100 keV and 0.5-2.5 keV resulting from bremmstrahlung and soft X-ray processes in the plasma, respectively.

3. Charged fusion products (mainly 3.5 MeV alpha particles) and charge exchange neutral particles with intensities $\sim 3 \times 10^{10}$ cm^{-2} s^{-1} and $\sim 10^{15}$-10^{16} cm^{-2} s^{-1} respectively. (These are only a problem to direct line-of-sight plasma instrumentation with evacuated penetrations).

4. High in-situ temperatures of up to 440°C.

5. High direct heating rates from incident particle fluxes (greater problem for direct line-of-sight instrumentation).

6. Very high magnetic fields in the region of several teslas.

7. Beta-decay from tritium inventory causing serious perturbation of

charged-particle sensitive instrumentation (only a problem for instrumentation requiring a vacuum access to the plasma).

It is interesting here to note that plasma diagnostic instrumentation requirements for INTOR, a fusion device of approximately the same time frame as TASKA, have recently been reported.[2] Again, the limitations of present day instrumentation in D-T power environments were emphasized. In addition, it was expected that the rather limited list of suitable instruments which are currently available would remain basically unchanged until experimentation in current fusion devices (e.g., TFTR, ISX, JET, JT-60, etc.) begin to add to the list. The results from such experiments will also have direct applicability for improved specification of TASKA plasma instrumentation.

Diagnostic requirements for MFTF-B have also been recently outlined.[3] Even though this machine will only be D-D fueled and will not include a D-T phase of operation, proposed plasma diagnostics which will be situated near the plasma must withstand power fluxes of ~ 100 W cm^{-2}, enough to seriously damage many materials.

Table IX.2-3 summarizes the major plasma diagnostic requirements for TASKA. The various problems associated with the operation of each of the suggested diagnostic methods in the D-T environment of TASKA are documented in footnotes at the end of the table. The diagnostic instrumentation which is most at risk is seen to be those methods which require a direct line-of-sight vacuum access to the plasma (e.g., charge exchange analyzers, bolometers, UV spectrometers, ion beam probes., etc.) or which must be placed on, or across, system field lines (e.g., electrostatic end loss analyzers, etc.). Instrumentation operating via "optical" signals (e.g., laser scattering

Table IX.2-3
Plasma Diagnostic Requirements for TASKA

(Footnotes documenting the problems of operating the suggested diagnostic techniques in the D-T reactor-like environment of TASKA are included at the end of the table).

PLASMA PARAMETER	POSSIBLE DIAGNOSTIC METHODS
1. Ion temperature profile - central cell and end plugs	Charge-exchange analyzer[A,F,G,H]; reaction ion analyzer[B,F,G,H]; neutron methods (see above);
2. Plasma density profile - central cell, barriers and end plugs	Reaction ion analyzer[B,F,G,H]; neutral beam attenuation detector[A,E,H]; neutron techniques (see above);
3. Electron temperature profile - central cell, barriers and end plugs	Doppler shift of Thomson-scattered laser light[C]; continuum soft X-ray detector[D];
4. Electron density profile - central cell, barriers and end plugs	Microwave and far-IR interferometry[C]
5. Electrostatic potential profiles - barriers and end plugs relative to the central cell	Ion-beam probes[A,G,H];

(Table IX.2-3 continued)

6. Plasma beta - central cell
   and plugs

   Diamagnetic loops[H]

7. Radiated power (for Q
   determination) - central
   cell, barriers and end
   plugs

   Neutron methods (see above);
   bolometers; radiometers[A,F];

8. Plasma impurity content
   - central cell, barriers
   and end plugs

   Line X-ray detector[D]; UV
   spectrometers[A,F];

9. Spectra of ions to
   direct convertor/end
   dump

   Electrostatic end loss
   analyzer[B,F,G,H];

10. Plasma instabilities
    - central cell, barriers
    and end plugs

    Radiofrequency probes[A,H];

11. Background gas density
    - central cell, barriers
    and end plugs

    Residual gas analyzer[F,G];

A. Requires direct line-of-sight vacuum access to plasma.

(Table IX.2-3 continued)

B. Requires positioning on, or across, system field lines - high particle impact rate.

C. Direct line-of-sight not required here but associated mirrors and windows subject to high neutron, gamma and X-ray fluxes; attendant problems of high heat loads and radiation darkening.

D. Soft X-ray detector will be swamped by low energy gamma ray flux from system; additional contamination of continuum spectrum by line radiation from impurities.

E. High incident neutral beam power density - high heat loads.

F. Signal perturbation due to tritium beta decay radiation.

G. Large neutron/gamma noise background for ion spectrometers.

H. High direct particle heat fluxes; radiation damage problem.

methods, far-IR interferometers, etc.) can take advantage of stepped-port penetrations with reflection mirrors at junctions and vacuum seal entry windows. Although these latter folded-path techniques have the dual advantage of much less neutron and X-ray streaming to the detectors and no tritium beta ray contamination, there will be considerable damage and heat loads to the mirrors, windows and seals which face the plasma chamber. An additional consideration for direct-path instrumentation is that it will probably be integrated with each blanket or system module and will, therefore, require lifetimes consistent with the module changeout time. By contrast, the primary transducers in the folded-path diagnostic systems can be situated in shielded enclosures, well away from the main plasma and radiation environments. Maximum fluence or heating rate specifications for such instrumentation would, therefore, be comparable to, or less than, those for the superconducting

magnet systems, with the added advantage of ease of access and replacement.

As a summary to this section it can be seen that, at present, there are few plasma diagnostic techniques which can be successfully integrated with the reactor-like environment of TASKA. There is thus an urgent need for the development of fully-engineered and hardened plasma instrumentation in order that diagnostic requirements for the next generation of D-T fusion devices (e.g., TASKA, INTOR, FED, TMNS, NET, etc.) can be satisfied.

References for Section IX.2

1. U.S. INTOR Group "U.S. INTOR - the U.S. Contribution to the International Tokamak Reactor Phase-1 Workshop", U.S.A. INTOR/81-1, Chapter XII, 13-15 (1981).

2. Ibid, Chapter XII, 1-21.

3. See,for example, Simonen, T.C. and Leppelmeier, G.W., "Diagnostic Instrumentation for Mirror Confined Plasmas", Energy and Technology Review, UCRL-52000-80, Lawrence Livermore National Laboratory (1980).

4. See, for example, Perkins, L.J., "The Application of Pulse Shape Discrimination in NE 213 to Neutron Spectrometry", Nucl. Instr. Meth. 166, 451 (1979).

5. Jarvis, O.N., Uttley, C.A., and Swinhoe, M.T., "Neutron Diagnostics Design Report - JET Diagnostic Design Study 10.2/3(a)", AERE G1644, UK Atomic Energy Research Establishment, Harwell, UK (1980).

6. Hendel, H.W. and Seiler, S, "TFTR Diagnostic Physics Review", Neutron Diagnostics, p. 120, Princeton Plasma Physics Laboratory (16-17 November 1978).

X. Maintenance

X.1 General Aspects and Plant Layout

A successful operation of TASKA can only be achieved if the shut-down time required for maintenance operations as well as the radiation hazard for the maintenance personnel are kept to a minimum. As usual in nuclear plants, both requirements lead in most cases to opposite technical solutions and management procedures. This is due to the fact that remote handling operations of a medium or high degree of complexity are up to one order of magnitude more time consuming than contact operations.

The environmental conditions in the vicinity of TASKA after shut-down are characterized by

- low neutron induced radioactivity of the outer structures

- possible airborne tritium contamination

- possible residual magnetic fields.

It is anticipated that these conditions allow limited personal access to the major part of the components one day after shut-down if they are in place.

In addition to this, hot areas have to be anticipated in the course of time resulting from

- neutron streaming through openings (vacuum, coolant, injection, diagnostic etc.) and unavoidable mounting interstices in the shields

- radioactive deposites in the coolant and auxiliary circuits after long operation or accidental coolant contamination

- accumulated outer surfaces contamination in the facility after repeated handling of highly activated components or after unexpected activity release incidents.

Experiences from nuclear fission reactor operation show that these factors tend to yield additional restrictions for direct personal access.

Finally there are two additional important aspects which have to be taken into account for achieving a sufficiently high availability of the plant:

- The reactor hall has to be evacuated from personnel when parts of the shielding are to be removed or failed radioactive components are to be replaced.

- Personal access to the building is restricted after accidents with a high radioactivity release which cannot be removed by repeated air exchange or confined by remotely placed shielding.

In existing nuclear fission reactor and fuel cycle facilities similar problems can often be limited by subdividing the total system into groups of components and placing them into various separately sealed rooms or shielded cells. In the case of TASKA with its size and shape and its multitude of directly attached components this is hardly possible. Thus the accessibility of the whole plant suffers considerably if scheduled or unscheduled high radiation fields exist or occur in the reactor hall during maintenance or repair periods.

As a result the maintenance concept for the facility has to be based on

- maximum contact procedures
- option of remote repair or replacement.

X.1-2

The latter principle dominates as for the general layout of the plant, the design of the components and the maintenance equipment. The first one is important for the shielding thickness and some less decisive plant characteristics.

In order to meet the requirements for at least the necessary remote operations the reactor building for TASKA has to show typical features of a large hot cell (Fig. X.1-1) for indirect remote handling and viewing.

The building walls have to reduce the radiation level to such an extent as to permit continuous presence of personnel outside, both under operation as well as under high active component replacement or accident conditions. In addition they have to protect the outside environment against accidental tritium release and mechanical impacts resulting from potential accidents in the plant.

A remotely controlled overhead bridge crane is scheduled for handling the heavy items. A second crane bridge with a telescoping mast and a cantilever arm at its lower end acts as a handling and positioning system for manipulators and components. It is capable to exert the considerable horizontal forces required for extraction and insertion of plug-in devices e.g. blanket modules. Typical design parameters for both main handling machines are listed in Table X.1-1. The carriages can be driven off the bridge through a shield door into a maintenance position outside the reactor hall for maintenance during plant operation.
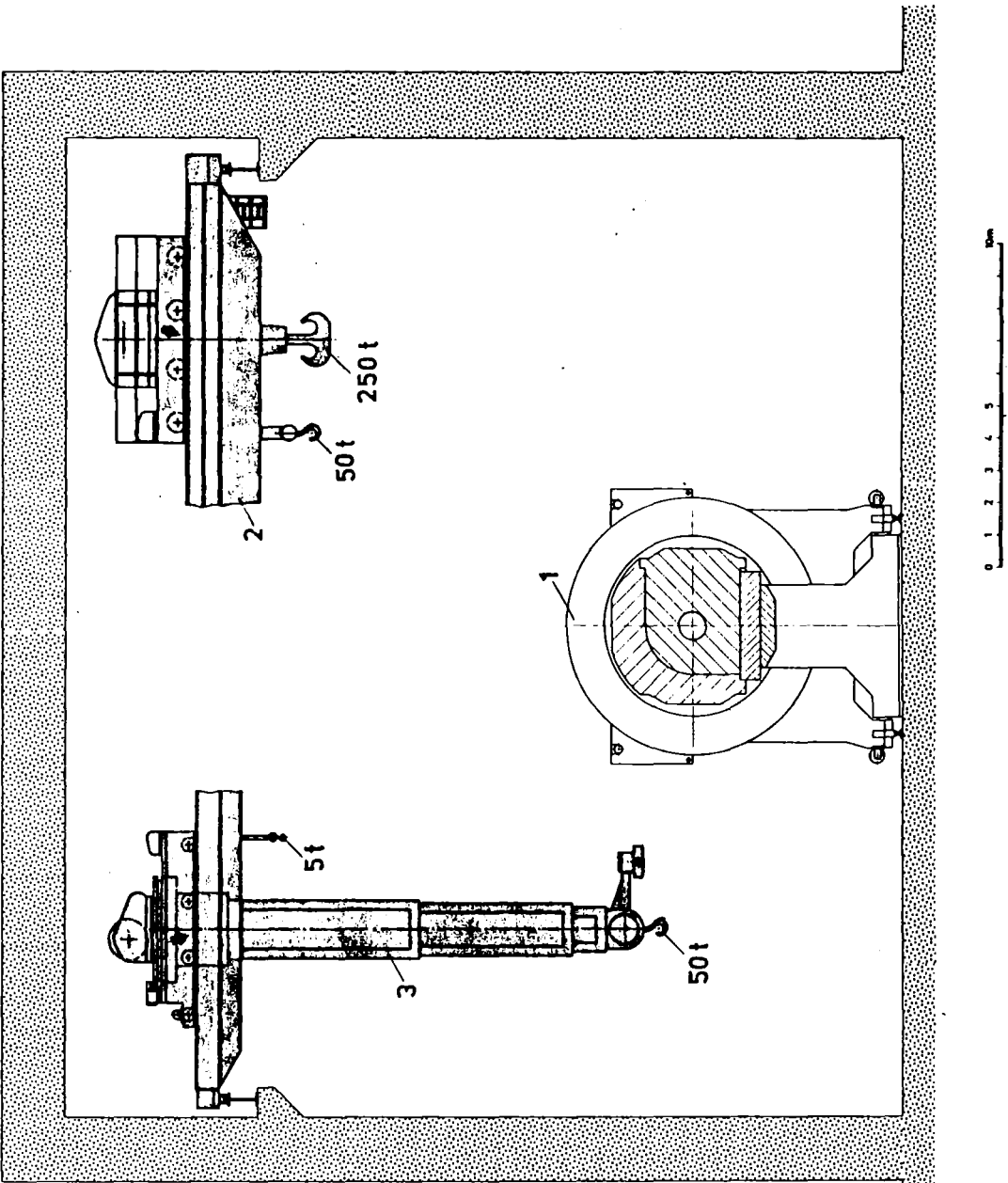
X.1-3

Fig. X.1-1 TASKA handling system

1 Test facility
2 Bridge crane
3 Component handling machine

Table X.1-1   Typical design parameters for the overhead
               bridge crane and the component handling machine

- Overhead bridge crane
  . Load carrying capacities:
    main lifting device   250 t
    auxiliary lifting device   50 t
  . Lifting / lowering heights
    main lifting device   25 m
    auxiliary lifting device   25 m

- Component handling machine
  . Load carrying capacities:
    lifting telescope   50 t
    auxiliary lifting device   5 t
  . Maximum torque at the lower
    telescope tilting head   10 tm
  . Lifting / lowering heights
    telescope   15 m
    auxiliary lifting device   25 m

The TASKA reactor and its components are arranged on the floor of the reactor hall as to permit maximum access by the handling machines from above and both sides. They have to be designed in such a way that the main handling operation can be performed as much as possible by a sequence of simple vertical and horizontal movements. The required high precision of the positioning procedures can be achieved by carefully controlling operating speeds and exerted forces.

For other remote operations such as bolting, screwing and delicate handling, powered wrenches and manipulators are available.

In order to facilitate the necessary remote connecting and disconnecting procedures non destructive techniques are to be applied as much as possible. These operations are principally well known from remotely maintained hot fission fuel processing plants, however extensive development work is still to be done to meet the high tightness and reliability requirements. Further more destructive disconnecting operations as cutting by mechanical, thermal or electric means should not present principal difficulties, whilst remote welding including edge machining and weld inspection are probably the most important maintenance and repair techniques still to be developed.

If one tries to analyse the large variety of various inspection, repair and post-repair testing operations required, it appears that only a comparatively small part of the extensive maintenance procedures ingeniously should or can be performed in-situ or inside the reactor hall. Replacement by spare components, or dismantling, repair outside the reactor hall and reintroduction will be a more suitable maintenance

management. Therefore a well equipped hot cell facility with several

compartments, mechanical master-slave manipulators and direct viewing

through shielding windows is needed for radioactive components, adjacent

to the reactor hall. In Fig. X.1-2 these cells are scheduled to be

located in the active dismantling, maintenance and testing area.

In addition to this a shielded interim storage area is required for

re-usable items. Loading and unloading for both shielded zones can be

performed via a common lock area which is connected with the reactor hall

and serves in its upper part as a semi - remote or contact maintenance

cell for the components of the reactor hall remote maintenance system.

It is estimated that the floor space needed for this active components

maintenance and storage complex is at least about one half that of the

reactor hall.

If a plant like TASKA is not situated near a component development

and testing establishment, another building complex has to be provided

which serves for developing, assembling and testing of inactive

components. It comprises the inactive mock-up area, too, which is

needed for remote procedures development work, and will be utilized

during plant operation for inactive equipment maintenance and storage.

INACTIVE ASSEMBLING, TESTING AND MOCK-UP AREA	INACTIVE STORAGE

LOADING PASSAGE

ACTIVE DISMATLING; MAINTENANCE AND TESTING AREA	LOCK AREA	ACTIVE COMPONENTS INTERIM STORAGE

POWER SUPPLY

REACTOR HALL

CONTROL BUILDING

VACUUM AND CRYOGENIC SYSTEMS	COOLING CIRCUITS AND D-T-REPROCESSING	VACUUM AND CRYOGENIC SYSTEMS
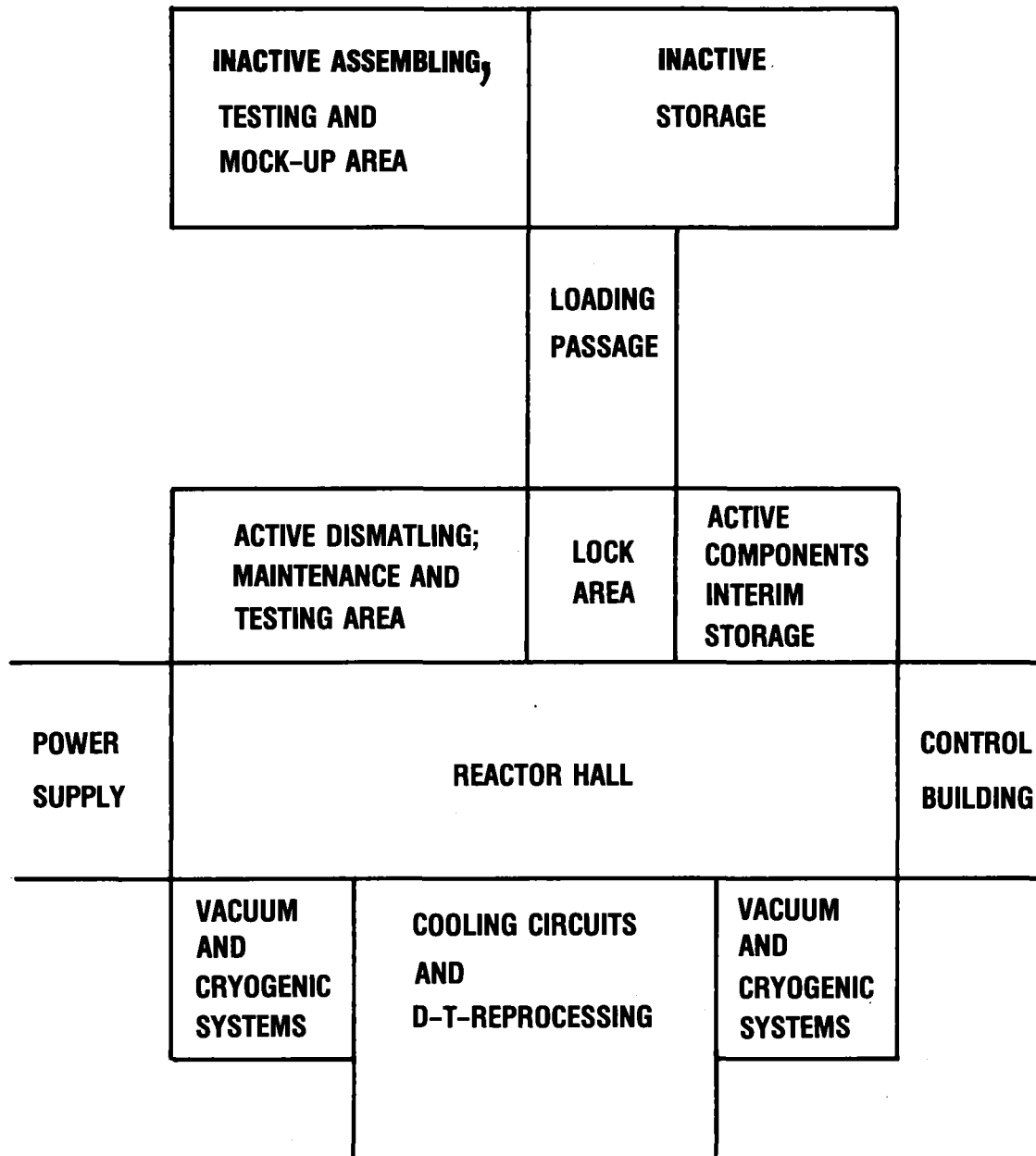
ACTIVE WASTE CONDITIONING AND TEMPORARY STORAGE

0 10 20 30 40 50   100 m
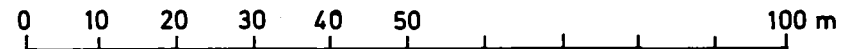
Fig. X.1-2 Reactor plant

X.2 Handling Equipment for Repair and Operation

X.2.1 Generalities

In order to perform repair work and operation in a test facility such as TASKA a great variety of handling tasks must be carried out in the reactor hall under greatly varying environmental conditions.

As long as the reactor shielding is intact provision can be made by appropriate dimensioning and design that hands on work can be done in situ by the staff. Assuming a period of e.g., ten hours per month and ten months per year of working time, the mean local dose rate according to the German Radiation Protection Ordinance must not exceed 100 μSv/h (10 mrem/h). In case the shielding must be opened at the work station, the dose rates will attain values which will require the use of remotely handled equipment.

For these reasons a handling system was conceived which comprises tools to be used under both working methods. Since many different tasks with a relatively low frequency of repetition will have to be fulfilled at widely spread places and since unexpected situations must also be anticipated, general-purpose and high-performing tools will be provided for remotely controlled work. The handling of objects varying in weight between many tons and less than 1 kg calls for several tools having highly differing capabilities. Moreover, a limited working capability in high magnetic fields should at least be aimed at in short periods of shutdown. The system (Fig. X.2-1) therefore consists of the following main components:

X.2-1

1 Test facility
2 Bridge crane
3 Component handling machine
  and manipulator carrier
4 Shielded cabin with manipulators
5 Manipulator unit
6 Raisable working-platform
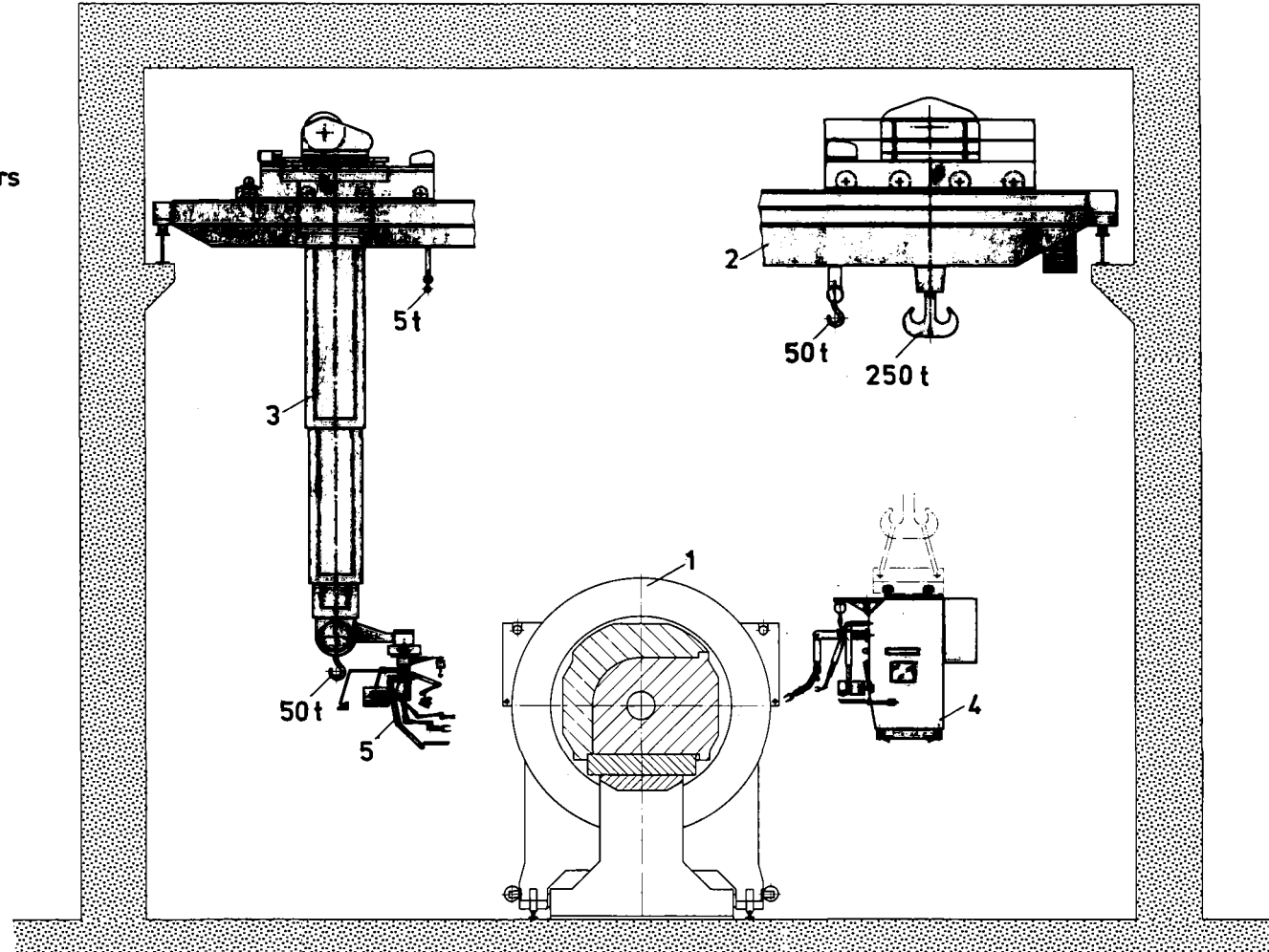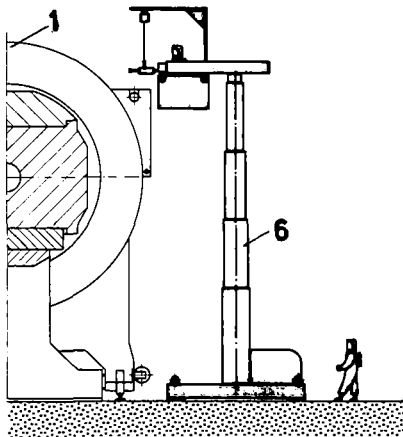
Fig. X.2-1 TASKA handling system

- for in-situ work by the staff

   . an elevated working platform from which the tools can be made

      to operate

   . temporary shieldings (not shown on the figure)

- for work by staff in situ or by remote control

   . a moveable 250 t bridge crane   ⎤ for more details
                                         ⎬ see Chapter X.1
   . a component handling machine   ⎦

- for remotely controlled work

   . a remotely controlled manipulator unit (carried by the

      component handling machine)

   . a shielded cabin with manipulators.

X.2.2 Elevated Working Platform

The elevated working platform is transferred by the bridge crane

to the respective work station and lowered there.

The platform has been designed on the following principles

(Fig. X.2-2): On a floor space a fourfold lifting telescope has been

provided; at its upper end a double telescope for forward movement and

at the front end of the double telescope a basket can be provided from

which one or two people can work. The basket can be lowered in addition

by means of chain hoists so that in the lower position of the lifting

telescope the working space can be utilized down to the floor.

Practically all types of conventional tools as well as special

purpose tools allowing to keep the distance greater with respect to

the objects can be used by the staff. To balance the weight of heavy

tools a swivelling boom with a light lifting device has been fixed at

the basket.

1 Telescopic lift tubes
2 Telescopic tubes for
  forward motion
3 Chain hoist for
  lowering
4 Basket
5 Swiveling boom
6 Crane
7 Tool
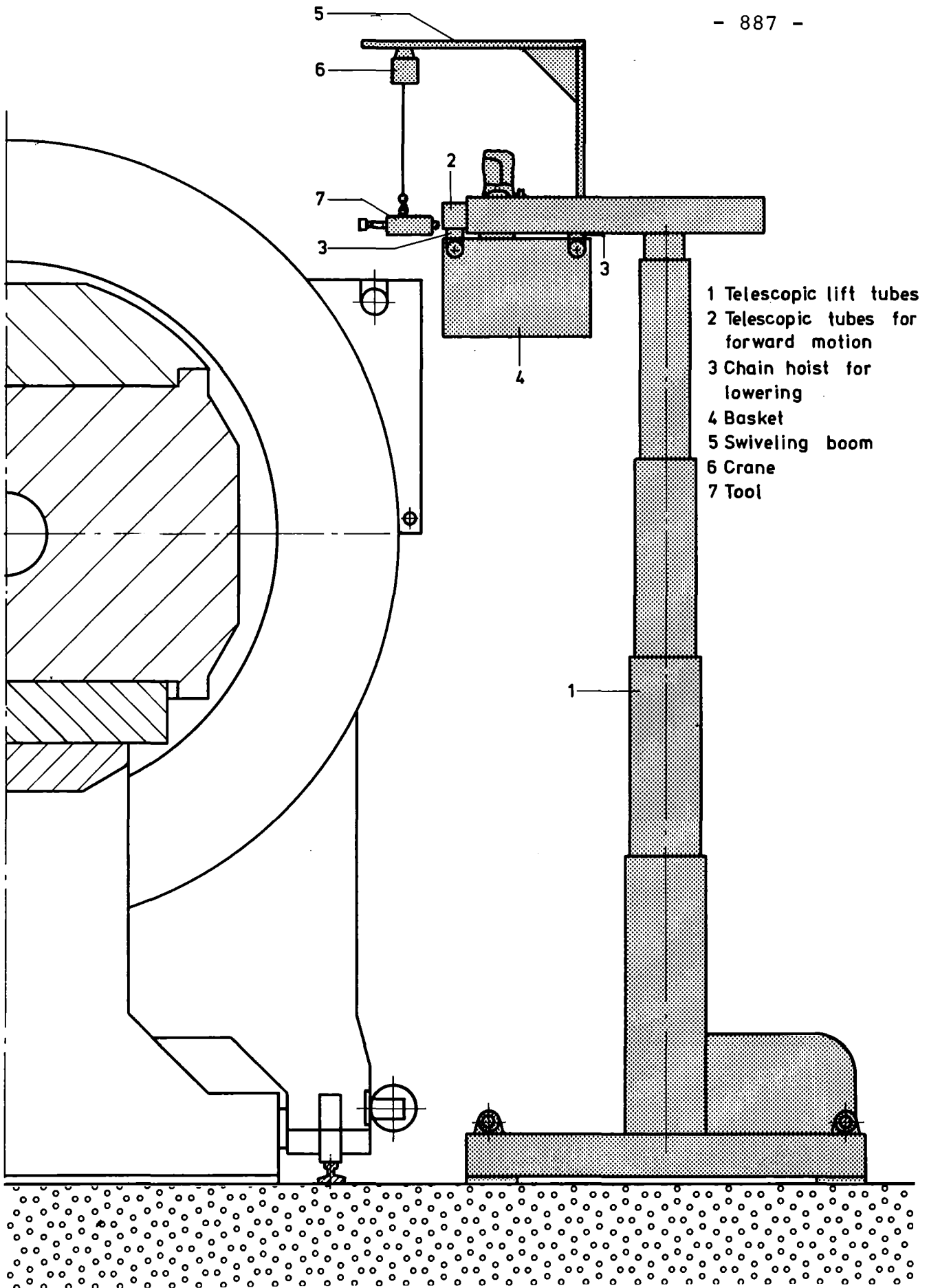
Fig. X.2-2 Raisable working platform

Hydraulic drives will be provided for the telescopes and an electric motor drive for the light lifting device.

Technical Data:

- Load carrying capacity: basket   1000 kg
                            light lifting device   50 kg

- Reaches of motion: lifting telescope   8 m
                            advance   4 m
                            basket lowering capability   2 m

Due to the potential of tritium contamination of the surroundings the staff working in the reactor hall must wear full protective suits with breathing equipment. It should be taken into account that the associated inconveniences considerably extend the required working times as compared with similar work performed under conditions usually encountered in a workshop.

X.2.3 Manipulator Unit

When maintenance work is done in a large-scale facility, the situation regarding remotely controlled work, in contrast to work performed in the classical hot cells, is characterized by the fact that instead of the objects being transferred to a work station, the manipulators and the necessary auxiliaries must be brought to the work stations. Since several small carrier systems cannot be provided in a room in which all three dimensions are large, all components must be combined into a single unit in order to become operational by one carrier system. Even simple activities in most cases require at least

two manipulators. It is reasonable to provide two arms of different
load carrying capacities so that a large scale of different work can be
coped with.

The manipulator unit (Fig. X.2-3) includes the following components
with the following design:

- a slave arm of a master-slave manipulator with electric power
  transmission, arranged on the right side

- a servo manipulator, arranged on the left side

- a driven gripping hook, placed between the manipulators so as
  to allow the transport of rather heavy components

- a lifting device fixed at a swivelling boom

- television cameras allowing observation of the work station and lights
  as well as stereoscopic microphones for noise transmission

- television cameras for viewing the scene and the respective lights

- two swivelling and extensible booms with lights for indirect lighting

- a store installed to an articulated boom to accommodate tools which
  can be used together with the manipulators

- a table attached to an articulated boom on which equipment devices
  or components can be carried and deposited.

The manipulator unit is kept ready for use in a device and can be
coupled by remote control to the plate accommodating the component handling
machine or deposited again into this device. All components of the unit
can be quickly dismounted and remounted. All drives are equipped with
electric motors. Should working in very high radiation fields become
necessary the radiation sensitive components would have to be made

X.2-6

1 Electric master-slave manipulator   6 Lighting

2 Servo manipulator   7 Microphone

3 Driven grip hook   8 Tool magazine

4 Crane   9 Table

5 TV Camera   10 Component handling machine
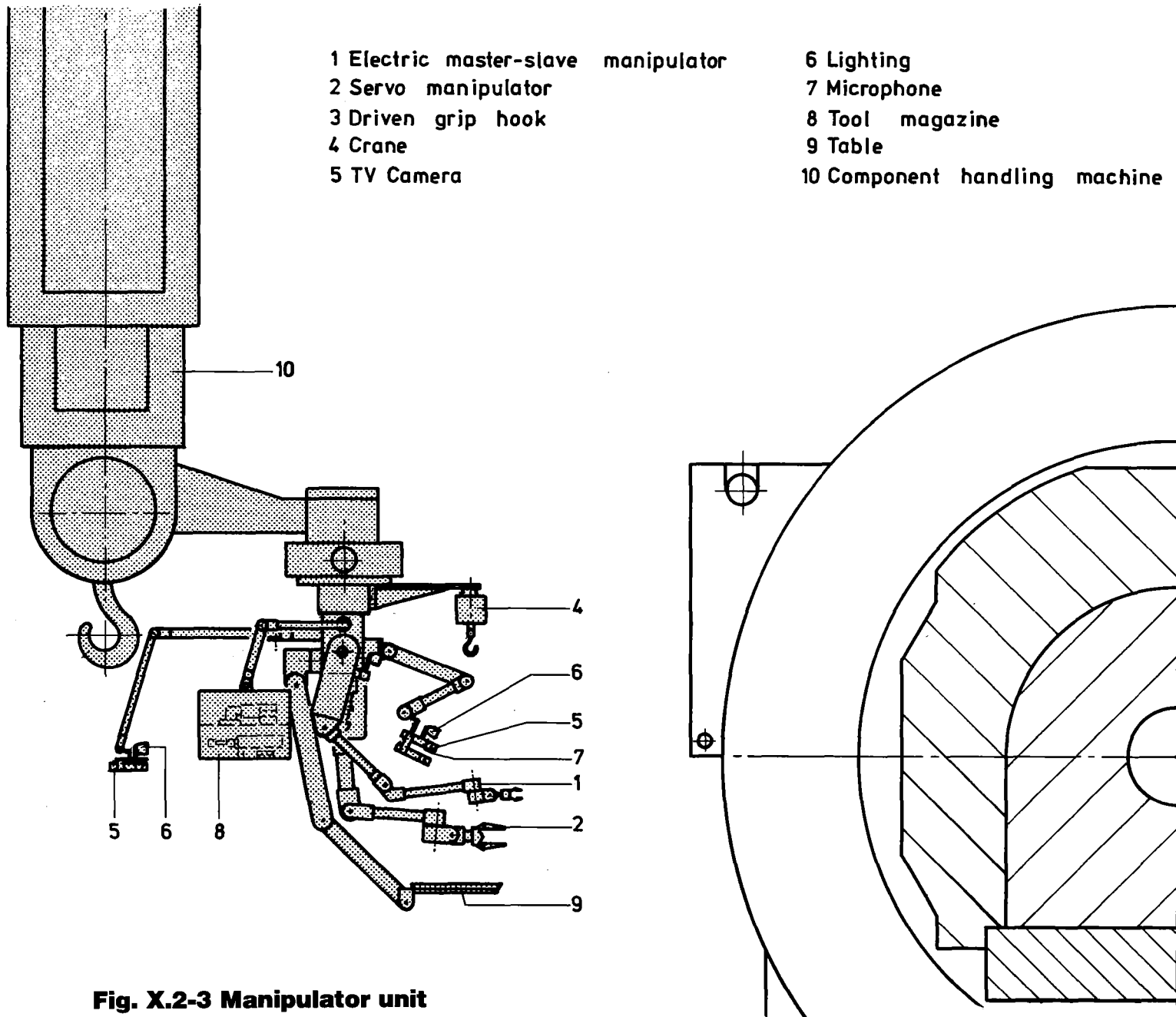
Fig. X.2-3 Manipulator unit

radiation resistant. The current is supplied from the component handling machine and the signals will be transmitted by radio. The handling and control devices are installed in a separate remote handling room.

Load Carrying Capacities of the Equipment:

- electric master-slave manipulator   45 kg

- servo manipulator   150 kg

- driven gripping hook   2000 kg

- lifting device   2000 kg

An electric master-slave manipulator (Fig. X.2-4) is particularly suited for complicated and delicate work and for the use of adapted hand held tools. The equipment possesses bilateral position control loops for all motions by which force reflection is achieved, which means that the operator gets a true feeling of pressure in his hand corresponding to the forces applied. In the upper load range the forces acting at the slave arm are amplified 10 times at the maximum as compared with the master arm. The necessary dead weight compensation is realized by electric motors. The length of the master arm is about 70% that of the slave arm. The tong and the jaws can be replaced by remote handling. Free programmability can be provided as the second mode of operation, e.g., with a view to welding operations.

The servo manipulator will be used to handle rather heavy objects and for working with heavy, adapted tools. It is an improvement of the switch controlled power manipulators with speed control, intended to increase substantially the working speed. Moreover, the arm has been

DRIVE HOUSING

INCLINE
HOUSING
±210°

SHOULDER
PIVOT
±(45°+45°)*)

UPPER ARM

X-MOTION
±(45°+155°)*)

FOREARM

AZIMUTH ROTATION
±(90°+110°)*)

WRIST ROTATION
±360°

ELBOW PIVOT
±(45°+45°)*)

GRIPPING
0÷90

TONG

WRIST ELEVATION +60°
−120°
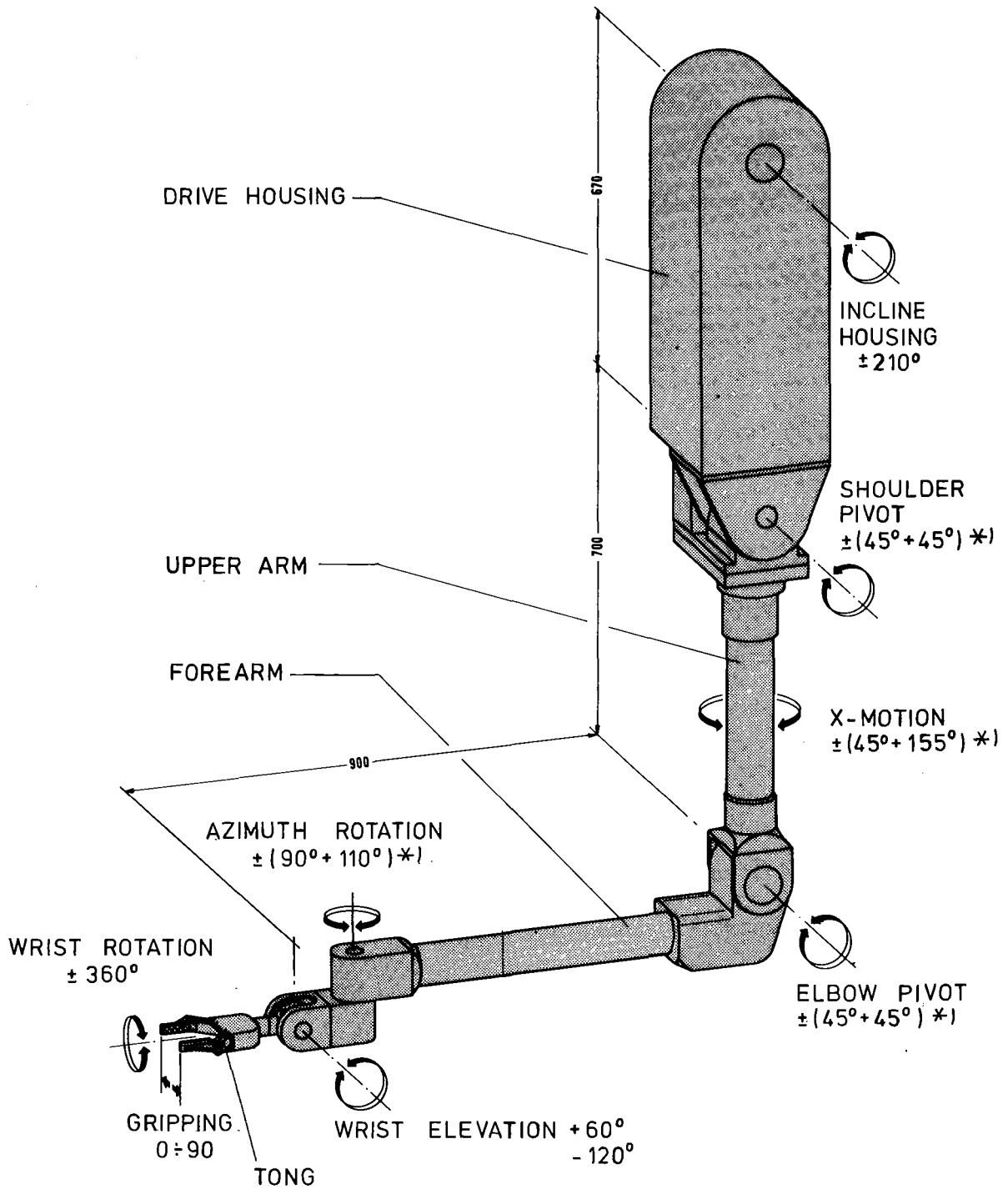
*) SLAVE AND MASTER ARMS SYNCHRONOUSLY
+ DISPLACEMENT OF SLAVE ARM RELATIVE
TO MASTER ARM

Fig. X.2-4 EMSM-WA electric master-slave manipulator,

slave arm

X.2-9

largely adapted to the electric master-slave manipulator in its basic design so that the possibility of good coordination is ensured. Position controls and a handle for operation will be provided. The tong can likewise be replaced by remote handling.

Both manipulators have seven position-controlled motions each. To extend the reach the driver housings can be inclined in addition by switch control. The electric tools are supplied with current from plugs installed near the wrists.

The effective working speed is much slower when work is done with manipulators as compared to work carried out by staff under conditions prevailing in a workshop. If master-slave manipulators are used, four times the time is required on an average and with power manipulators 50 times the time; scattering is high, independent of the degree of difficulty of the work. With the servo manipulator equipped with the control and handling device about ten times the time will presumably be needed.

The television system and the tools will be dealt with in Chapters X.2-5 and X.2-6, respectively.

X.2-4 Shielded Cabin with Manipulators

A shielded cabin will offer considerable advantage as an alternative and supplement to the remotely controlled manipulator unit because of the application of different principles for the manipulators and means of viewing a different characteristic is obtained in terms of the advantages and limits in application. Subject to the clarification of

the disturbing influences exerted by magnetic fields on the performance of electric motors, television cameras, etc. and hence of the application of the manipulator unit, the equipment of the shielded cabin can probably be so conceived that work will be possible in intense magnetic fields as well.

The cabin will be used in the reactor hall where it will be suspended from the bridge crane. In other shielded rooms it can also be moved on rails run on the ground. The effectiveness of the cabin is generally comparable with that of the manipulator unit and roughly corresponds to that available in the conventional hot cells.

The equipment of the cabin (Fig. X.2-5) consists of the following main components:

- two master-slave manipulators with mechanical power transmission
- one power manipulator
- one lifting device fixed at a swivelling boom
- four shielding windows (arranged on the front, left and right sides and in the floor) and the respective lights
- one tool store installed to an articulated boom
- one folding table which can be displaced.

Load Carrying Capacities of the Equipment:

- mechanical master-slave manipulators, tong/hook   20/50 kg
- power manipulator, tong/hook   250/400 kg
- lifting device   2000 kg

1 Shielded cabin
2 Supply unit
3 Mechanical master-slave
 manipulators
4 Power manipulator
5 Crane
6 Tool magazine

7 Table
8 Shielding window
9 Lighting
10 Carriage
11 Attachment device
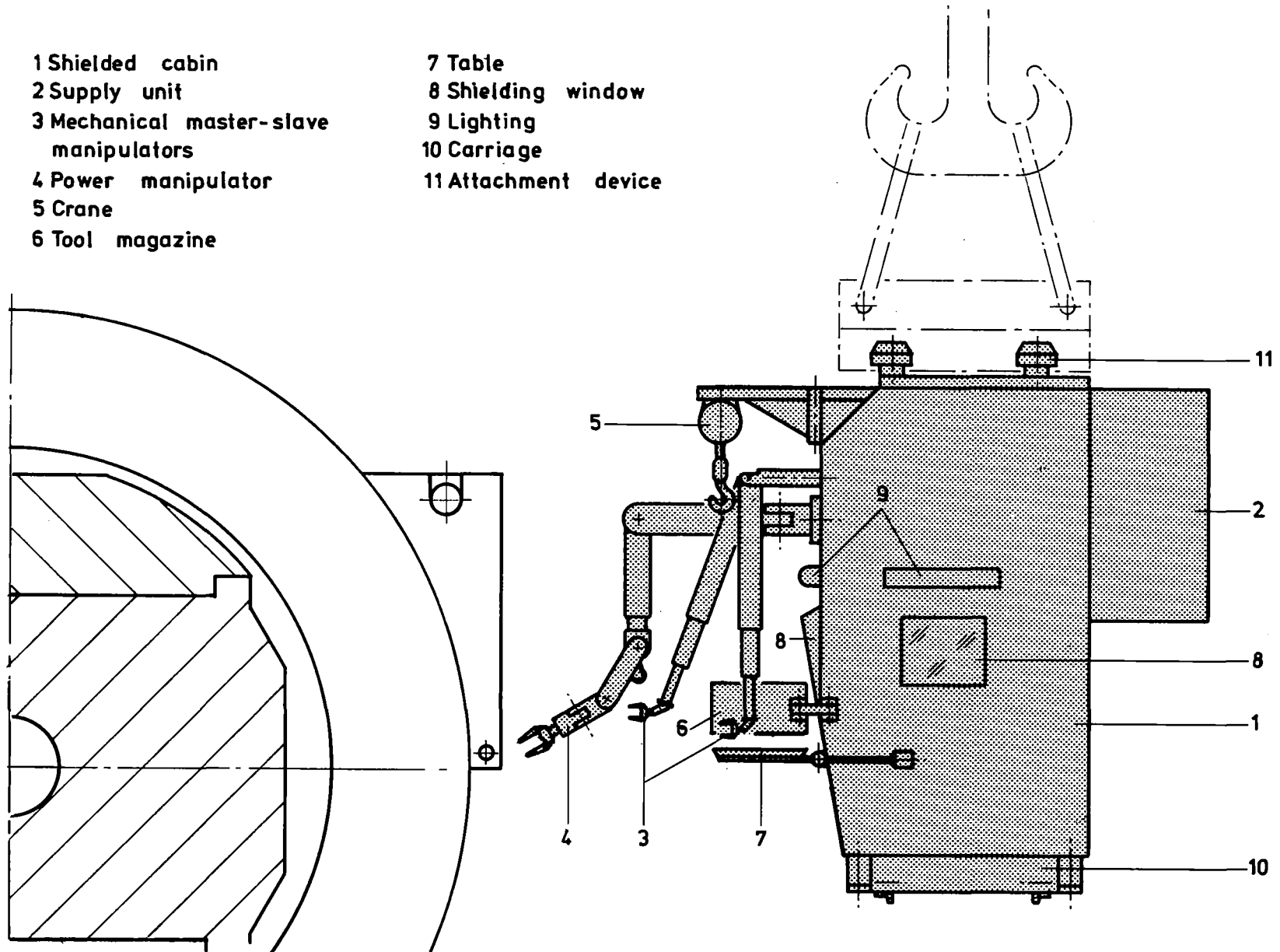
Fig. X.2-5 Shielded cabin with manipulators

Technical Data of the Cabin:

- Shielding: material   lead

                 thickness of front wall and floor   250 mm

                 thickness of lateral faces, rear
                 wall and ceiling   150 mm

                 weight   about   80 t

- Other data: crew   one or two men

                 total weight   about   95 t

Four mushroom shaped suspension heads for the crane gear have been
provided at the ceiling of the cabin. The motion drive is via an electric
motor with redundancy. Considering the mode of operation on rails, a
power supply via storage batteries is preferred. The staff enter the
cabin and leave it in the service cell. The door has been provided on
the rear side. There is an intercom from and to the control center in
the remote handling room. The ventilation system ensures a slight over-
pressure in the cabin in order to prevent contamination from entering it.
Optionally, also television cameras can be used as an additional means
of observation.

Mechanical master-slave manipulators serve the same purpose as the
manipualtors with electric power transmission. Each of the two manipulators
possesses seven motions with force reflection which allow transmission
of the motions of the operator's arms. In three of these motions the
slave arm can be adjusted in addition by electric motor control by
switches, contrary to the master arm, in order to be able to extend the
reach of work. Arms of rugged design will be provided in which the torques
will be transmitted by shafts and tooth gears. The tongs and the jaws
can be replaced remotely.

The power manipulator possesses nine motions with speed control. It is operated via master switches and the speed can be varied continuously. The gripping force of the tong and the torque of the hand rotation motion can be preselected. The tong can be replaced by remote handling.

Both manipulators will be equipped with hydraulic drives for work in intense magnetic fields.

X.2-5   Television Camera System

To be able to work speedily and safely with a remotely controlled manipulator unit the production of stereoscopic images is indispensable. The stereoscopic systems should comprise two channels in order to avoid that the vertical image resolution or the horizontal angle of viewing is cut in half. Color television systems will be provided since they allow much better visibility than black and white systems. Color systems of the German standards operate at 625 lines, 50 Hz and in the PAL-B mode.

The system for observing the work station possesses one pair of stereoscopic television cameras and two additional monoscopic cameras for enlarging the viewing field in the horizontal direction. The survey system furnishes a picture of the whole scene so that the manipulators can be moved safely over large spaces also and in case of restricted space. This system likewise comprises one pair of stereoscopic cameras. The cameras of both systems are mounted on articulated booms so that their positions relative to the manipulators can be varied in order to select the desired viewing angle and the distance of observation.

X.2-14

With a view to the dimensions, single-tube color cameras will be provided. The diameter of the camera tubes is 1" and the stereoscopic base is 130 mm. All cameras will be equipped with zoom lenses with a maximum horizontal viewing angle of 45° and a focal length ratio of 1:6.

It is proposed to use monitors with a diagonal image of at least 51 cm.

To display the stereoscopic images the polarization method was selected in the test because it produced the best image quality (Fig. X.2-6). Moreover, this method requires but little special auxiliaries. The monitors have been arranged at right angle to each other. Filters have been placed in front of the screens which act as vertical and horizontal polarizations, respectively. Between the monitors a diagonal semi-permeable mirror has been installed which lets pass the image from the monitor installed in front of the operator and reflects the image of the other monitor into the direction of view of the operator. The operator wears spectacles with appropriated polarizing filters so that the left eye sees only the picture taken by the left camera and the right eye only the picture taken by the right camera.

MONITOR FOR
RIGHT CAMERA

POLARIZATION FILTER

MONITOR FOR
LEFT CAMERA

SEMIPERMEABLE
MIRROR

SPECTACLES WITH
ANALYZER FILTER
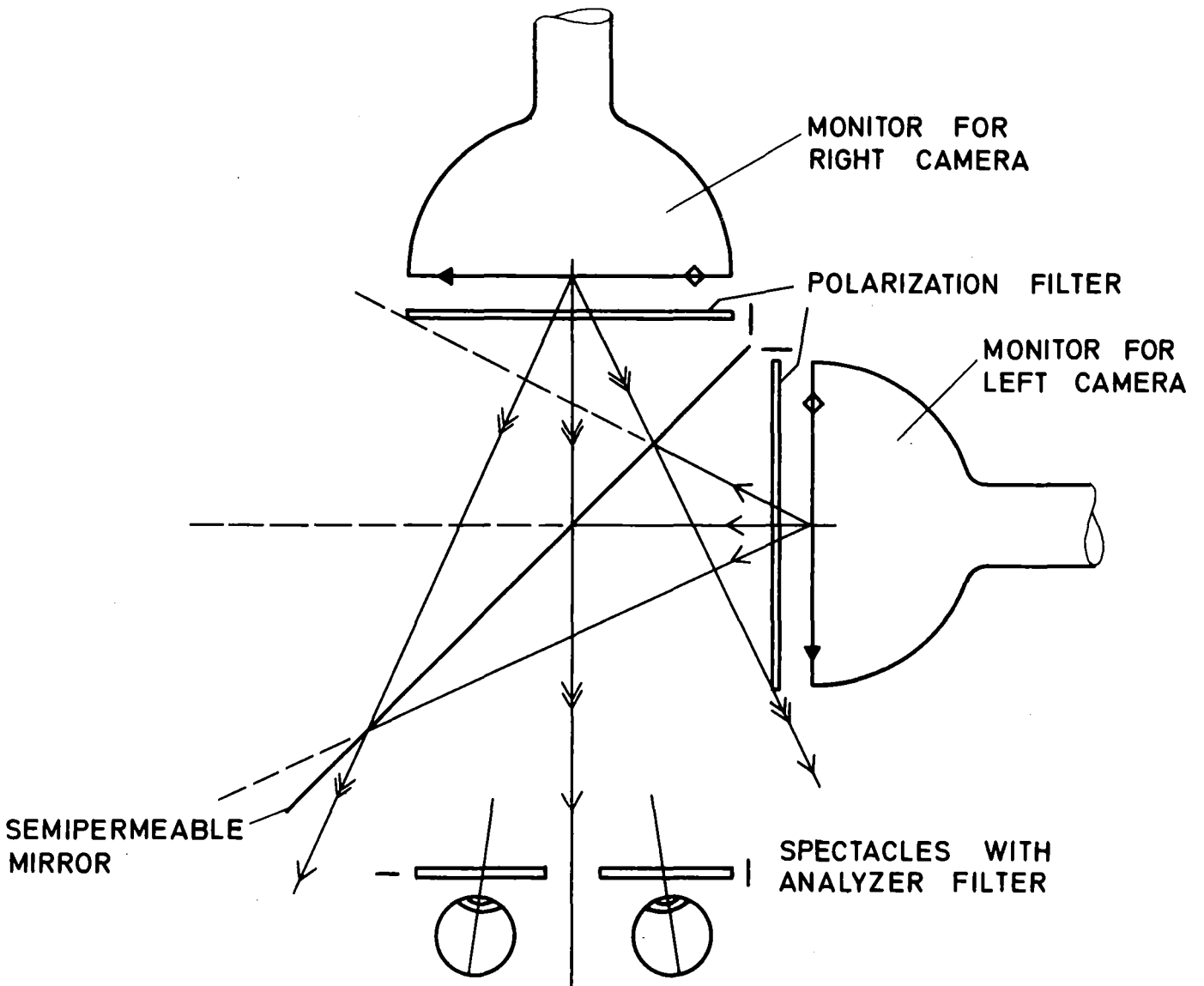
Fig. X.2-6 Viewing equipment for stereo television

X.2-16

900 -

X.2.6 Tools for Manipulators

Together with the manipulators described a great variety of adapted tools can be used which must be actuated together with a manipulator. Moreover, almost all types of driven tools can be used such as impact wrenches, drilling machines, compass saws, circular saws, angle sanders, cutting tools or hammers. Depending on whether these tools will be used together with the manipulator unit or with the manipulators of the cabin the drives are by electric motor or hydraulic.

In cases where a connection of plant components through a bolted flange is not possible, seam welding must be performed remotely. Four main working steps are required to replace a welded component:

- for disconnecting careful mechanical or thermal separation.

    and

- for connecting and preparation of the joint, welding of the seams,

    and, if applicable, inspection of the welded seam.

Of the four operations seam welding is the most difficult. To obtain satisfactory quality, the welding process must be automated. Two methods are applicable in principle. Either a device performing the welding process automatically is transferred to the work station via a manipulator and fixed there or the manipulator is freely programmable and moves the welding head along the seam.

In the first method the welding device for large components could be, for example, a small carriage approaching the component on rails. For welding pipework rotating heads and tongs with a rotating unit made in the conventional technology are currently used.

In the second method the manipulator control would have to be
backfitted accordingly for automated welding (Fig. X.2-7). Because of
the required tolerances of the component on the one hand, and the
accuracy of positioning of the welding head of about $\pm$ 1 mm, on the
other, satisfactory results can only be obtained with correction of
the track provided by sensors. For this purpose, tactile sensors,
induction sensors and television cameras have so far been used. Use of
a television camera (Fig. X.2-8) has the advantage that several sensors
are not required for the sizes to be covered and the design of the plant
component can be much less sophisticated at the work station. The
molten pool and the wire end are observed with the camera. The image
is evaluated by methods of pattern recognition in order to obtain the
correction signals. Depending on the deviations from the nominal
geometries, the welding head height and the lateral position as well
as the rate of advancement are controlled.
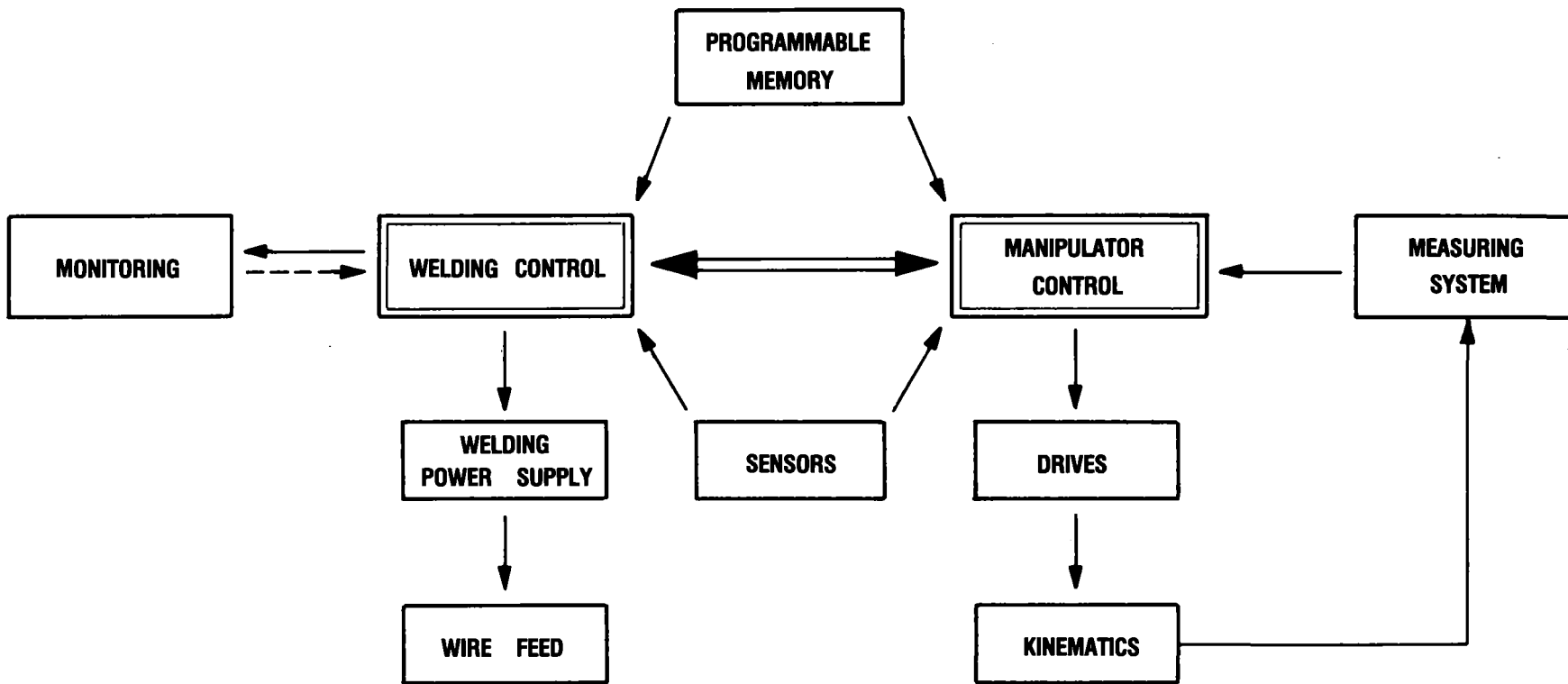
Fig. X.2-7 Components of a free progammable manipulator with equipment for arc welding

WELDING   TORCH

TV CAMERA

VIDEO SIGNAL
PROCESSING

BINARY   IMAGE   SIGNAL

ANALOG   IMAGE   SIGNAL

SERVO   MOTORS

TORCH   HEIGHT

TORCH   SIDE   DEFLECTION

FEED   SPEED

CONTROL   AMPLIFIER

FEATURES
EXTRACTION

TORCH   HEIGHT   DISPLACEMENT

TORCH   SIDE   DISPLACEMENT

PUDDLE WIDTH
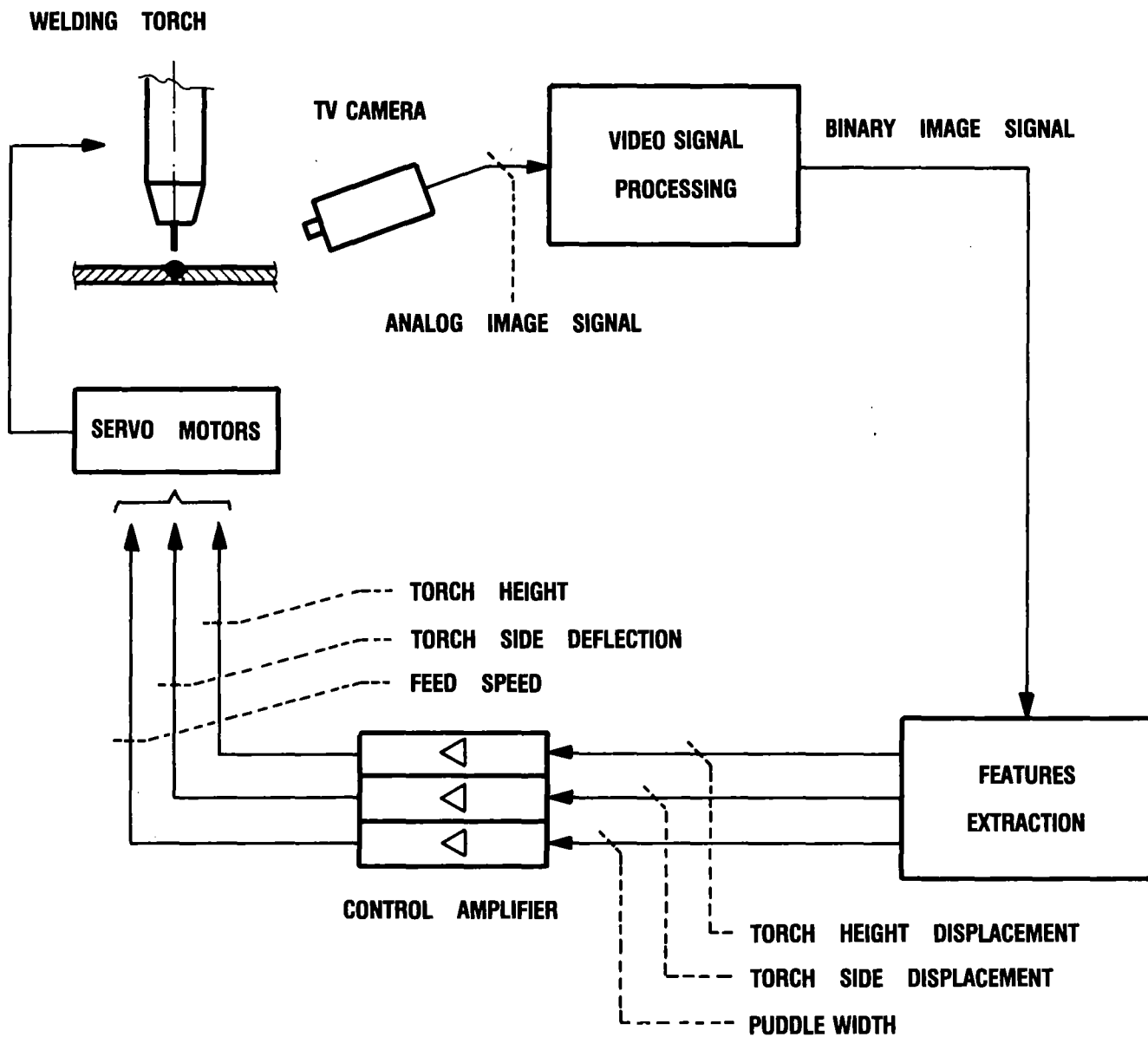
**Fig. X.2-8 Block diagram for welding control circuit
with TV camera as sensor**

X.2.7 Concluding Remarks

To realize the necessary equipment for remotely controlled work in repair and operation of a facility such as TASKA, one can rely on a broad spectrum of technologies both from the nuclear and the conventional areas. However, since the task is a new one, adaptations and improvements are required. The central topics of development work would include the kinematic systems of the manipulators with drives by electric motors, the control system for the electric master-slave manipulator, and the automated seam welding device. So far no problem can be recognized which does not seem solvable.

In case the proposed versatile remote handling system will be realized and, moreover, the components will be so designed as to meet the needs of remote operation, guarantee convenient access to the active zones and be capable of backfitting, settlement of the problems at hand will be ensured.

X.3 Maintenance Classification

To get overview of maintenance tasks as well as necessary equipment major subsystems and components are categorized into the four general classes as shown in Tables X.3-1 and X.3-2. The classes spread from operating for the design life of the system without scheduled replacement to short lifetime. Between these categories are placed two further classes with expected liftetimes of more and less three full power years (FPY). Beyond the distinction dependend on the lifetime we also distinguish between scheduled replacement because of e.g. radiation damage and unexpected replacement or repair due to random component failures. In addition to this classification, masses and sizes of main components are shown in Table X.3-3.

To demonstrate the practicability of maintenance tasks four typical cases have been selected; i.e. the exchanges of:

- blankets

- neutral beam injector components

- central cell coil and

- barrier coil especially the barrier insert coil (see Fig. X.3-1).

Reasons for this selection were the frequency of required replacement in the first two cases and difficulty and complexity of the removal in the other cases.

X.3-1

Table X.3-1   Classification of Components in

Dependence on Lifetime

- Class 1   Components (full lifetime)

  hands on or remote repair / replacement not necessary

  e.g.: building- and support structures, parts of the vacuum vessel

- Class 2   Components (lifetime $\geqslant$ 3 FPY)

  remote repair / replacement complicated but possible during

  long shutdown periods

  e.g.: magnet coils

- Class 3   Components (average lifetime)

  remote repair / replacement foreseen during regular shutdown

  periods

  e.g.: blanket and material test modules, injector components

- Class 4   Equipment (short lifetime)

  remote replacement foreseen immediately after shut down

  or during operation

  e.g.: handling- and experimental equipment

X.3-2

Table X.3-2   Categories of Maintenance in Dependece of Lifetime /1/

System	Class 1 Full Lifetime	Class 2 Lifetime $\geqslant$3 FPY	Class 3 Average Lifetime $<$3 FPY	Class 4 Short Lifetime
Building and support structure	x			
Shield	x			
Vacuum vessel	x			
Breeder test blanket			/x/	
Permanent breeder blanket	x	(x)		
Material test blanket			/x/	
Samples of material test blanket				/x/
Coils	x	(x)	(x)	
Insert coils		/x/	(x)	
Cryopumps	x	(x)		

/x/ scheduled replacement   (x) replacement in the case of failures

Table X.3-2   Categories of Maintenance in Dependence of Lifetime (continued)

System	Class 1 Full Lifetime	Class 2 Lifetime $\geq$ 3 FPY	Class 3 Average Lifetime $<$ 3 FPY	Class 4 Short Lifetime
Neutral beam injectors total		(x)		
NBI - ion source			/x/	
NBI - ion dumps		(x)	(x)	
NBI - getter panels		/x/	(x)	
ECRH		(x)	(x)	
ICRH		/x/	(x)	
Beam dumps		/x/	(x)	
Diagnostics		/x/ (x)	/x/ (x)	
Heat exchanger		(x)		
T-system		(x)		
Maintenance equipment	x	(x)	(x)	

Table X.3-3   Main Components -
             estimated sizes and weights

	size /m/	weight /t/
Vacuum chamber (section)	3.0x3.0x6.0	17
Permanent breeding module	3.0x3.0x1,5	35
Breeding test blanket	3.0x3.0x1.4	50
Central cell coil	7.2 ∅ x 1.6	127
Barrier coil	4.7 ∅ x 3.5	250
Transition coil	6.8x5.0x4.0	135
Yin/Yang coil	8.0x3.5x5.5	230
ECRH	1.5 ∅ x 6.0	47
Neutral beam injector	3.5x3.5x7.5	160

References

1. J.N. Doggett, et al.:

   University of California Lawrence Livermore National
   Laboratory, Proceedings of the 28th Conference on Remote
   Systems Technology, CRSTBJ 26 1-460 (1978)
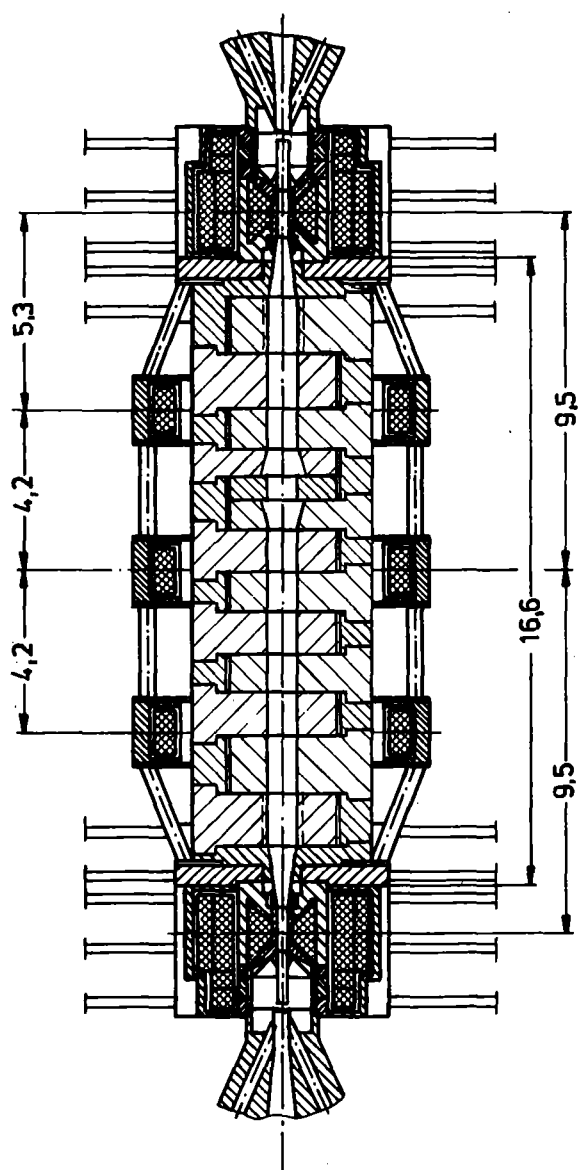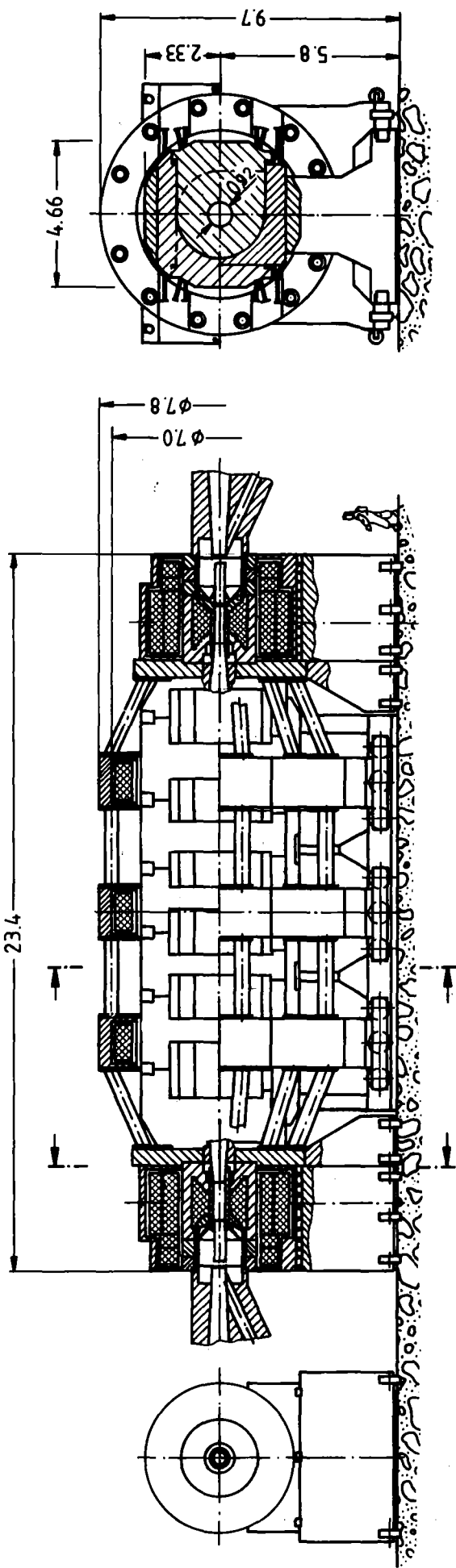
Fig. X.3-1 Central cell
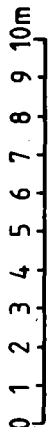
X.4 Short Lifetime Components

Besides samples inserted in material test blankets which can be exchanged comperatively easily by suitable methods during the operation phase, all the other components being in immediate connection with the facility have to be replaced during shutdown periods. This is not only due to radiation, but also due to the high magnetic fields in the coils, making access impossible and largely preventing the application of electrical machines.

The most frequently replaced components of the central cell are the test blankets, material test blankets as well as breeding test blankets and of the plug region the neutral beam injectors, especially the ion sources and the getter panels.

X.4.1 Blankets

The blankets inside the vacuum chamber surround the plasma and face the plasma directly. They are the moderator for the high energetic neutron flux and convert it to thermal heat. The first wall in particular is subjected to extreme thermal and radiation loads. Therefore it is possible, that besides the test blankets which have to be replaced more frequently according to the maintenance schedule during regular shutdown periods in order to perform checks, repairs and test material sample investigations, the permanent breeder blanket modules which are designed for the full lifetime of the machine have to be exchanged in event of failures.

The replacement of blanket modules raises two questions:

. the dose rate at the surface of the blanket one day after shutdown

   is $\sim$1000 rem/h,

. the weight of $\sim$ 50 t for each blanket module makes handling difficult.

In consequence of the first point hands on techniques are only possible as long as the shield is intact. In this case the biological dose rate one day after shutdown is less than 12 mrem/h. Additional transportable shield walls protect the personnel against scattered radiation from other regions where the immediate radiation is higher. But all subsequent operations performed after removal of the blanket flange bolts have to be performed by remote handling techniques.

To render possible the handling of blankets roller rails are installed at the bottom of the vacuum chamber and a special transportable carriage support structure can be adapted at the test facility (see Fig. X.4-1). This carriage support structure is composed of an adjustable frame with linked tilting carriage tracks lifted by hydraulic cylinders, a screw driven carriage and a separate lifting traverse also raised by hydraulic cylinders to support the blanket after withdrawal. This traverse serves simultaneously as a blanket auxiliary structure in combination with the load attachment device shown in Fig. X.4-2 to transport blankets. The device itself is equipped with three revolving rods driven by electric motors. The front parts of the rods are shaped as bayonet joints matching with a lug at the front of the blanket and the lifting traverse. By remote turning the rods attachment device and blanket resp. lifting traverse will be connected automatically.

X.4-2
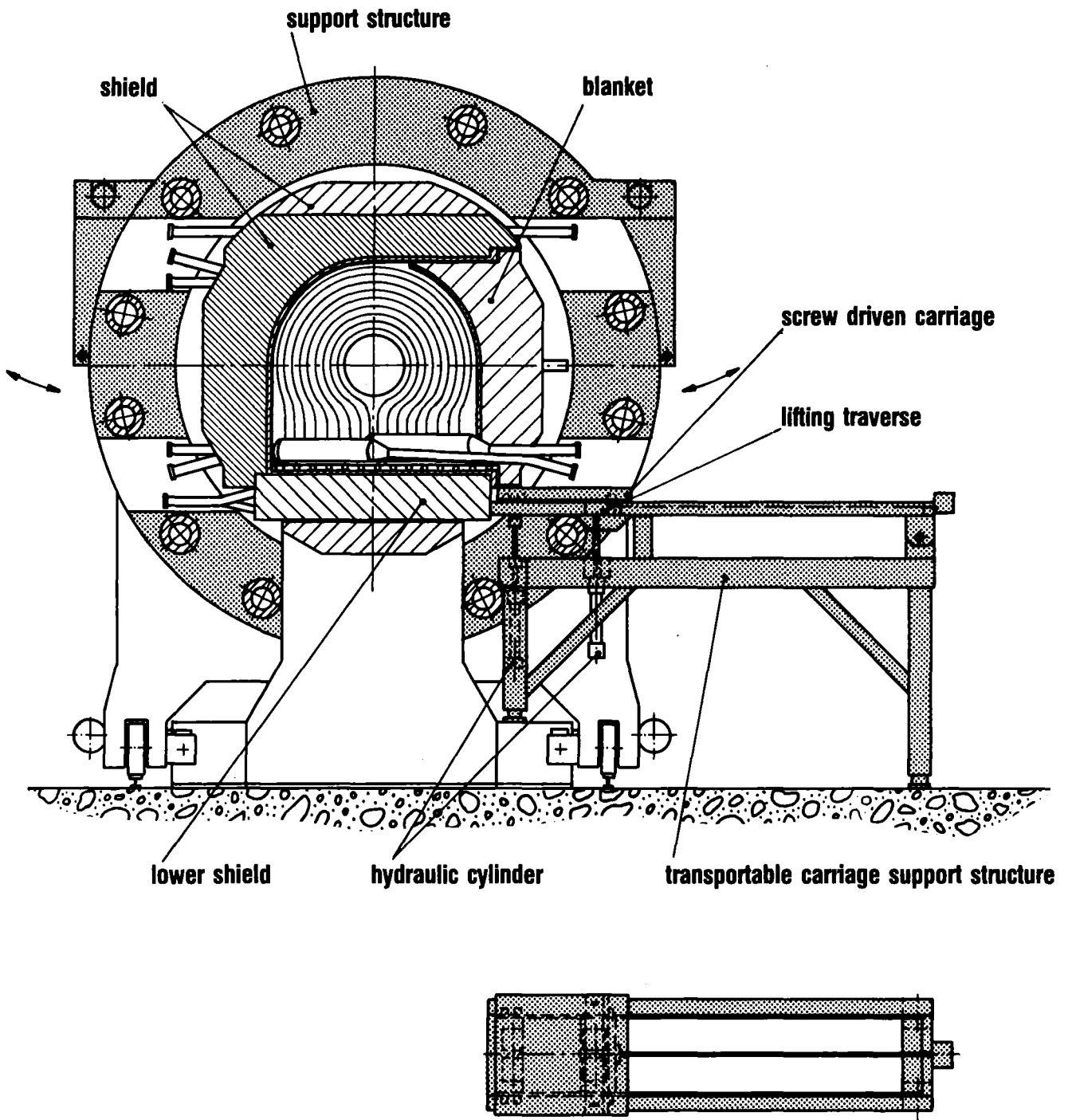
Fig. X.4-1 Blanket exchange equipment

load attachment device

1.step

2.step
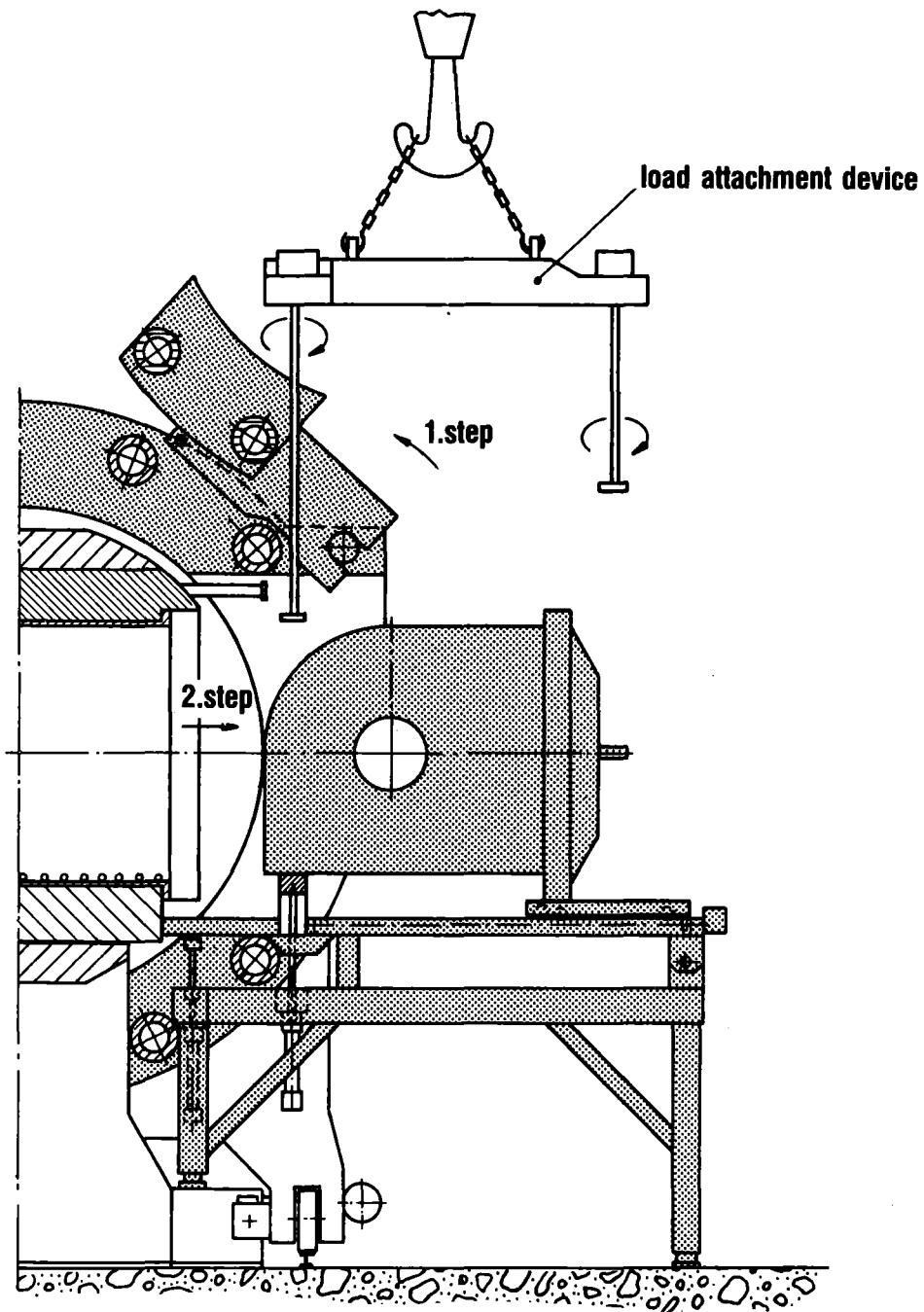
Fig. X.4-2 Blanket exchange

As mentioned in Chapter VI.1 blanket exchange is possible without dismantling the shield and reflector. At first the superconducting coils are deenergized and the tritium and lithium as well as the coolant gas have to be drained. Subsequently the supply connections will be disconnected and the support structure swung away. After unscrewing the blanket flange bolts (shown in Fig. X.4-2) the carriage support structure will be adapted and the carriage track lifted hydraulically until the front part of the blanket rests on the carriage. The blanket can then be withdrawn by means of the carriage. Before the blanket is totaly withdrawn from the vacuum chamber, the lifting traverse is raised hydraulically to support the blanket until it will be taken over by the 250 ton overhead crane with the aid of the load attachment device (see Fig. X.4-3). For further operation it can then be transported into the temporary storage or hot cell. Blanket assembly can be performed in a reverse sequence.

X.4-5

X.4-2 Neutral Beam Injectors

Altogether the plug regions will have 12 neutral beam injectors.
As can be seen from Table X.3-2, parts of the neutral beam injectors
are the most replaced components in the facility. Figure X.4-4 shows a
cross section of an injector where the main components are the ion source
assembled with the cover, ion sweep magnet, ion dump, calorimetric
target diagnostics, neutralizer, gas pumping panels and collimators.
To provide the capability for adjusting the neutral beam box relative
to the vacuum chamber a bellow will be needed between the box and the
valve. The injectors operate at high voltages. To avoid failures caused
by vacuum and water leaks and to minimize replacement time, an attempt
has been made to combine components with units which have the fewest
penetrations to be sealed. Thus, gas pumping panels, including bearing
and panels drive, as well as the neutralizer and collimators are sealed
as a unit with a single flange. Further, all supply tubes and cables
are routed and attached to the same flange.

To protect the ion source and the beams from stray magnetic fields
from adjacent coils it is necessary to shield them. Therefore, the box as
well as the covers consist of approx. 20 cm thick shielding material,
making these components heavy and difficult to handle.

3.step
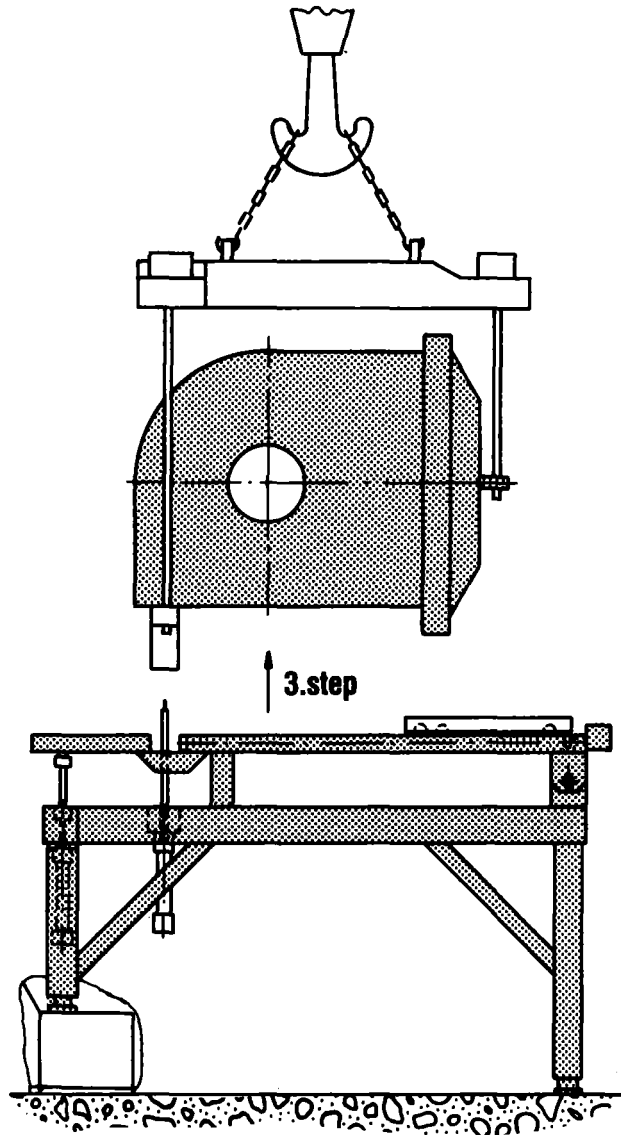
Fig. X.4-3 Blanket transport
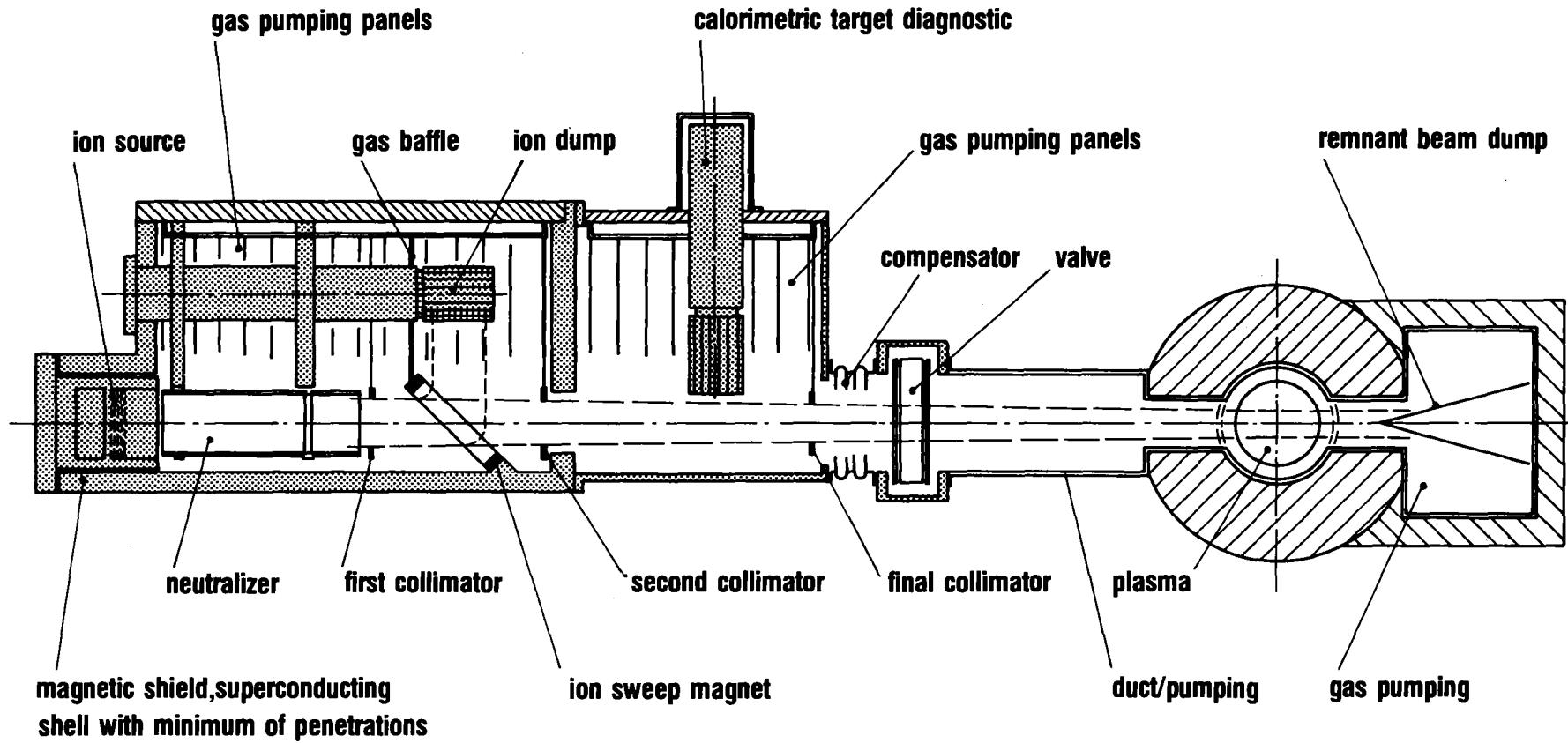
Fig. X.4-4 Neutral beam injector

X.4.2.1 Replacement of Ion Sources (Fig. X.4-5)

In order to isolate the vacuum chamber from the neutral beam box during replacement operations the valve between neutral beam box and duct will be closed. Subsequently the supply connections will be broken and after unscrewing the flange bolts and attaching the component handling machine with the ion source exchange device to the flange, it can be withdrawn along with the source. The assembly of a new one can be accomplished in the reverse manner.

X.4.2.2 Replacement of Getter Panels

Gas pumping panels foreseen to operate in a DC-mode are assembled as blocks of volume getter panels. Ever two panels are assembled in a common frame back to back. The frames themselves are arranged in a saw tooth fashion (see Fig. X.4-6) with the consequence that simultaneous pumping and regeneration can take place. The front panels face the ion stream at temperatures of $\sim 200^{\circ}C$, while the rear panels facing the box walls are heated to temperatures of $\sim 700^{\circ}C$ and the released gas will be pumped out by turbo molecular pumps. To change pumping and regeneration sides the frames with inserted panels are simultaneously reversed by cog wheels and toothed rack transmission drives mounted at the cover.

To replace the panels (see Fig. X.4-7) the cover has to be removed after the duct valve is closed, the ion dump is removed in a similar manner as the ion source, the supply tubes and cables are disconnected and the flange bolts are unscrewed. Removal of the cover will be performed by means of a crane. For neutral beam injectors arranged in
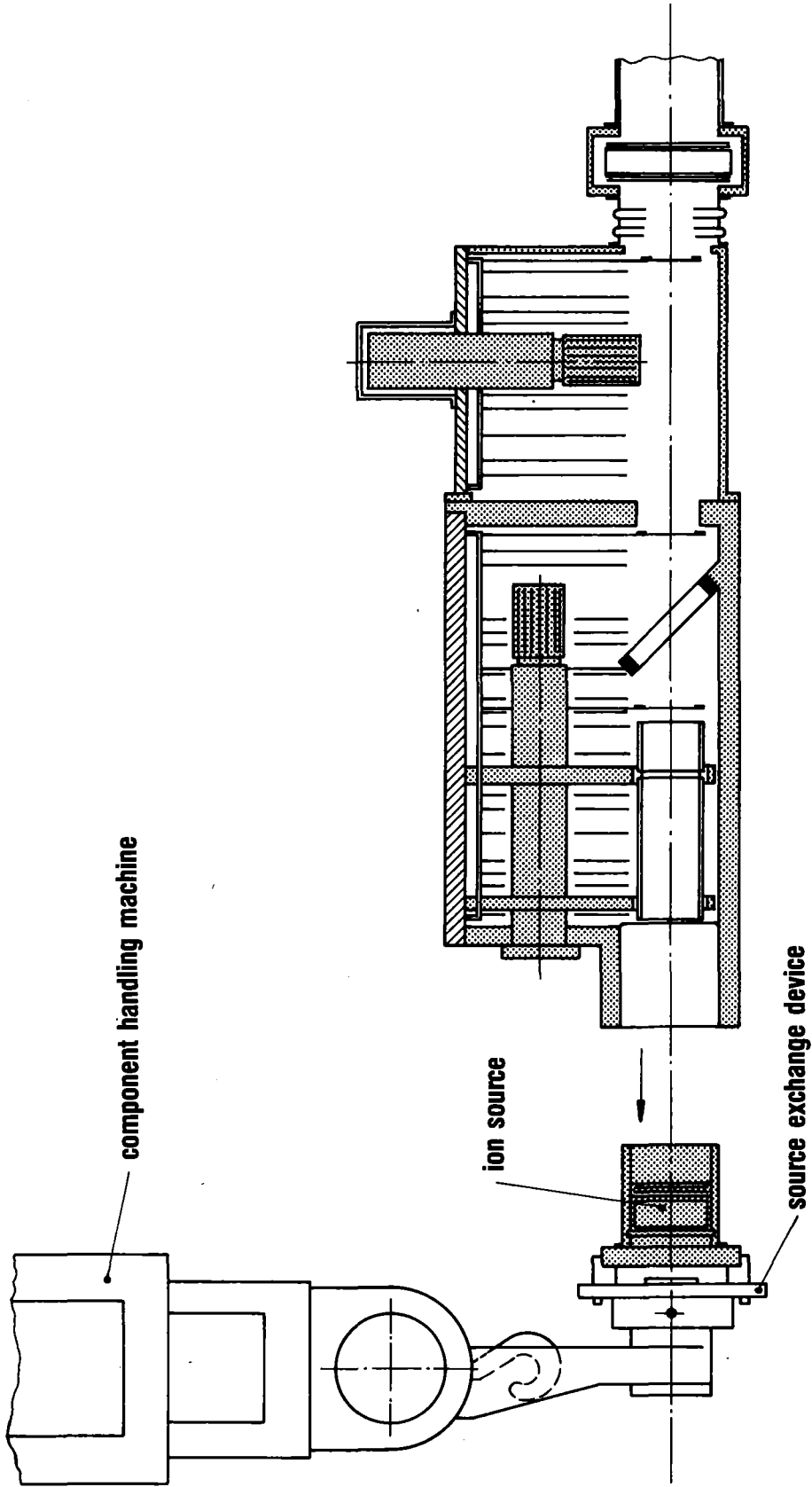
Fig. X.4-5 Neutral beam injector - exchange of the ion source

component handling machine

ion source

source exchange device

MAGNETIC SHIELDING
SUPERCONDUCTING SHELL
MINIMUM PENETRATIONS

ION SOURCE   NEUTRALIZER   FIRST COLLIMATOR   ION SWEEP MAGNET   SECOND COLLIMATOR   CALORIMETRIC TARGET DIAGNOSTIC   FINAL COLLIMATOR   BELLOW   VALVE

A

C

E

SECTION A-B

GAS PUMPING PANELS   ION DUMP   GAS PUMPING PANELS

GAS BAFFLE

B

SECTION J-K

SECTION E-H

D

SECTION C-D

Fig. X.4-6 High energy neutral beam injector

another orientation as shown in Figure X.4-7 it will be necessary after the valve is closed to disconnect the box at the compensator, displace it away from the facility and then rotate it by means of a turnover machine to a position for lifting the covers from above.

After removal the cover has to be attached to a turnover plate and rotated to a position shown on Figure X.4-8. To transmit the torque from the cog wheels to the panels a matching plug connection is provided. On the other end the panels are pivoted in a plate fixed with two screws at the frame for the getter panels. Removing the two screws allows the withdrawal of a pair of panels with relative case. The procedure is reversed for assembly of the panels.

cover assembled with:
neutralizer, gas baffle, pumping panels,
collimators

cover assembled with:
pumping panels,
calorimetric target,
collimator

2.step

2.step

ion dump

1.step

shielded casing
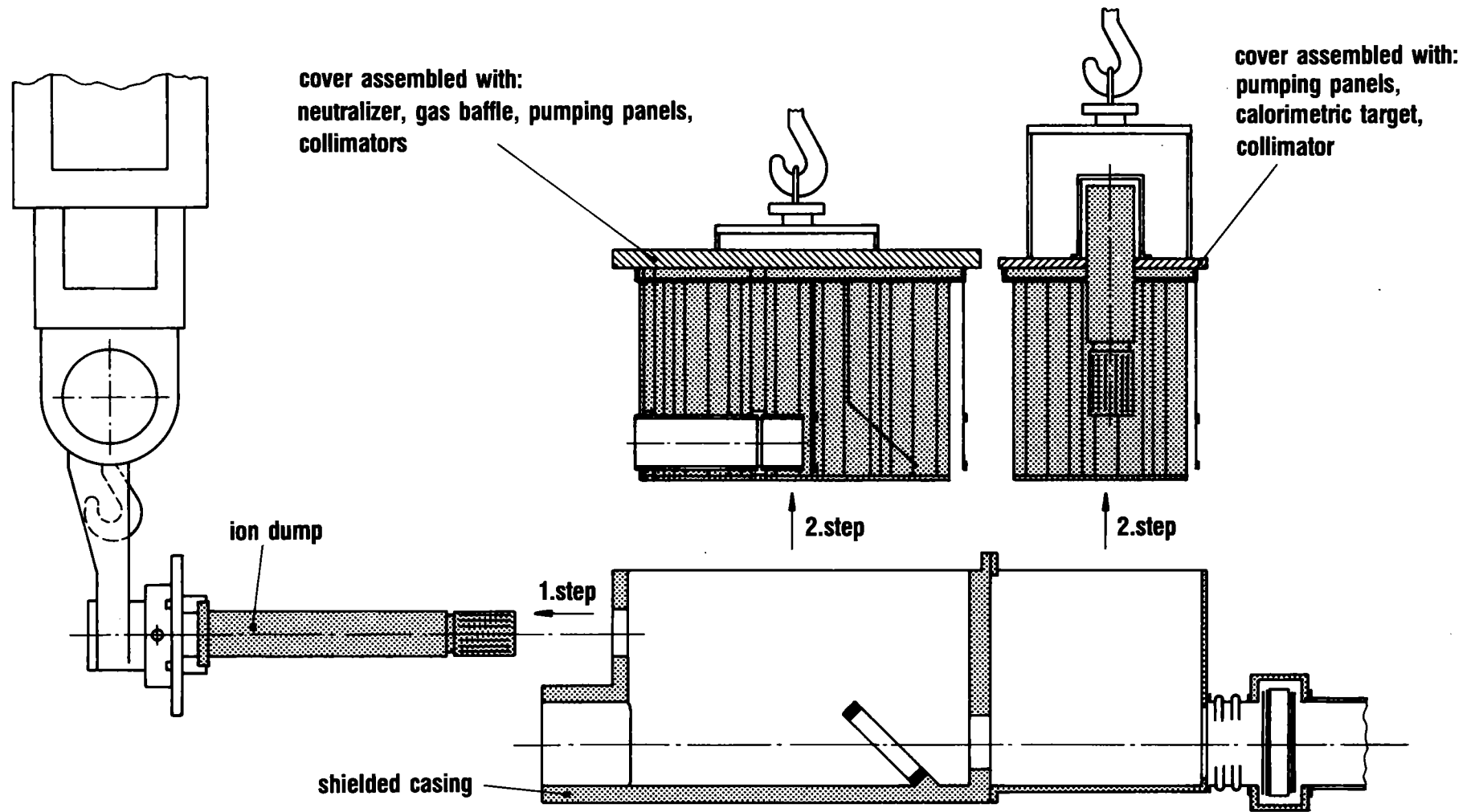
Fig. X.4-7 Neutral beam injector - exchange of the cover

exchange device suitable for
attachment to a crane or manipulator

pumping panel

cover

journal bearing

detail of
pumping panel

matching plug connection

journal bearing

cogwheel
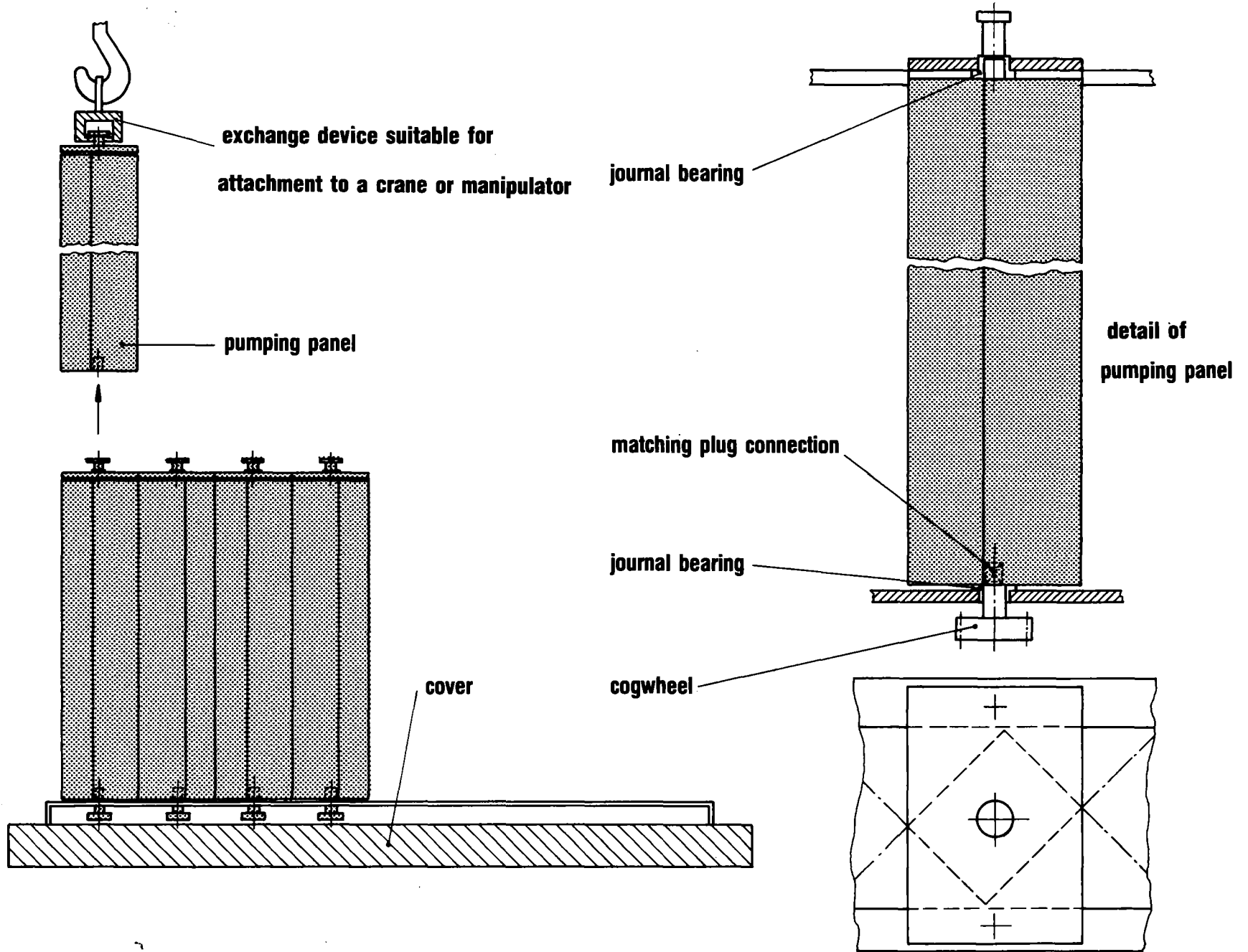
Fig. X.4-8 Neutral beam injector - exchange of pumping panels

X.5   Large Sized Components

Besides the routine operations, such as blanket exchange and neutral beam injection component replacement, there is another group of more difficult operations that must be investigated. The difficulties arise from the weight of the components, and the remote handling techniques needed. For example, it is impossible to replace the central cell coils or barrier coils without cutting into the vacuum chamber sections. Therefore, the design of the facility must take into account the separation of the vacuum chamber and integrate it into the overall system. In view of the needed vacuum chamber tightness it does not seem possible to connect the vacuum vessel sections only by mechanical gaskets and clamps. A solution seems to be a combination of tight welds and mechanical clamps (shown in Fig. X.5-1). While the clamps would transmit mechanical loads, the weld joint would provide the leak tightness. To equalize the variation in the dimensions of the sections the flanges can be made flexible to a certain degree.

X.5.1   Central Cell Coils

An exchange of coils has to be performed in the case of a possible coil failure. In this case, a longer shutdown period will be necessary and the complexity of the operation requires certain additional special equipment.

Figure X.5-2 shows a cross section of the central cell in which blanket and shield items have been removed, with the exception of the lower shield. For withdrawal this shield is equipped with roller rails such that it can be transferred to a transportable shield support structure attached to the reactor.

X.5-1

X.5-2
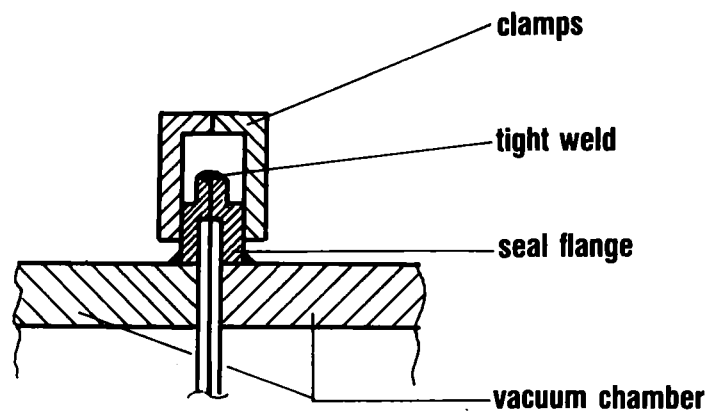
Fig. X.5-1 Vacuum chamber connection

vacuum chamber

transportable shield support structure
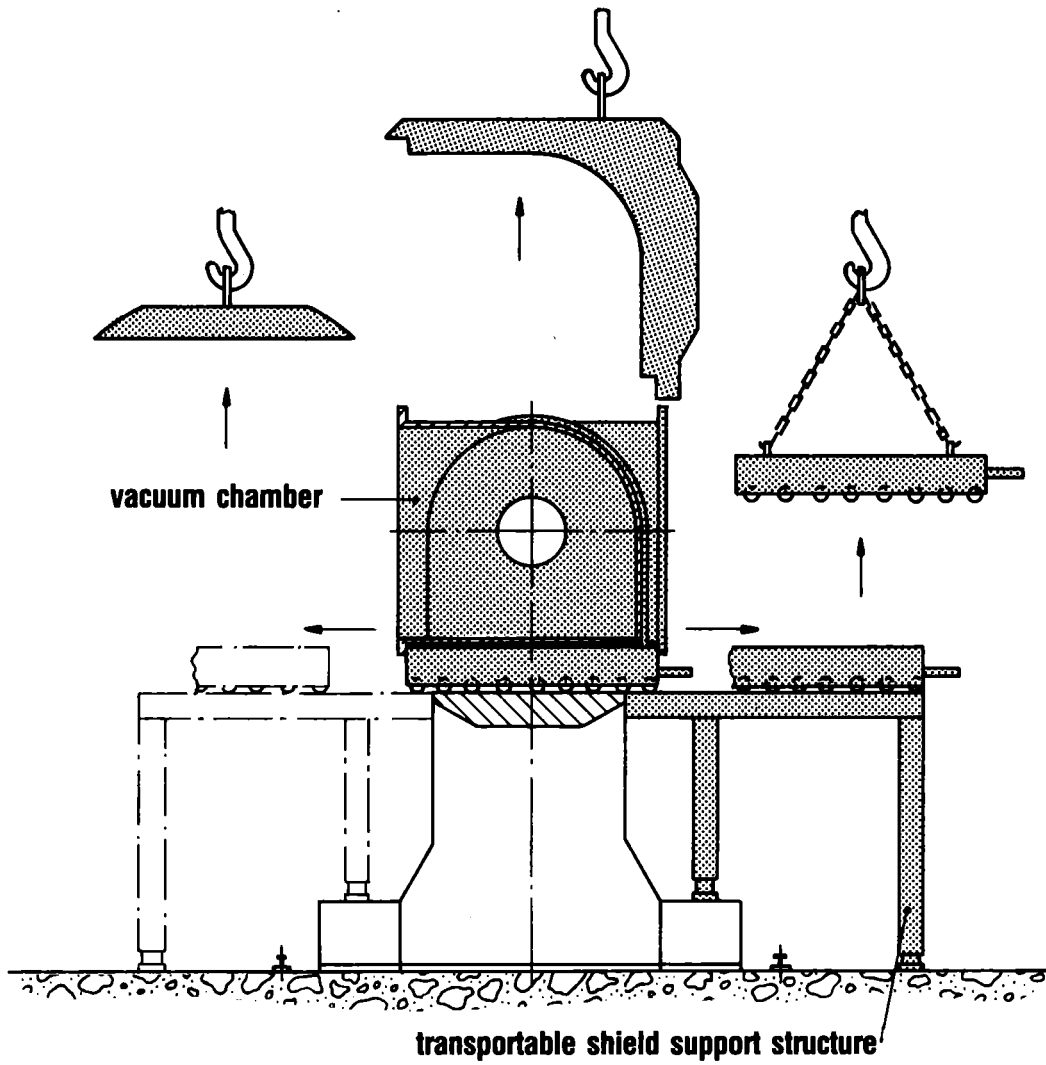
Fig. X.5-2 Exchange of central cell coils - removal of the shield

X.5-3

The most critical operation will be the rewelding of the vacuum chamber. A cutting and welding machine (see Fig. X.5-3), assembled with a cutting and welding heat guide track, serves as a basic unit where either a welding or a cutting head can be mounted. The cutting head as well as the welding head is remotely controlled and can be tilted or rotated. A guide track is mounted for welding the vacuum chamber bottom plate. The weld joints are made in a manner that would not require a refinishing operation of the flanges used to seal the blanket module closures.

To replace a central cell coil, the coils are deenergized and the blankets have to be withdrawn as shown in Chapter X.4.1. Subsequently the reflector and shield have to be drained and the supply lines disconnected. After removal of the support structure, reflector and shield units (see Fig. X.5-2) the cutting and welding machine can be attached (Fig. X.5-3). A shift of the corresponding central cell coil will be necessary. After dismantling the mechanical clamps the weld joint can be cut. A second cut on the other side of the coil makes it possible to remove the coil, chamber unit and lower support structure at the same time by means of the crane and a load attachment unit (Fig. X.5-4).

Before a new coil/chamber unit can be put into place, a check of the vessel dimensions and preparation of the weld joint must be made. After the new parts had been adjusted their position will be checked by optical measurements and the vacuum chamber welded and clamped. Additional work must follow the same operation sequence.

X.5-4

driven cutting/welding unit

transportable cutting and welding structure

vacuum chamber

auxiliary support structure

cutting resp. welding head

A

cutting and welding head guide track
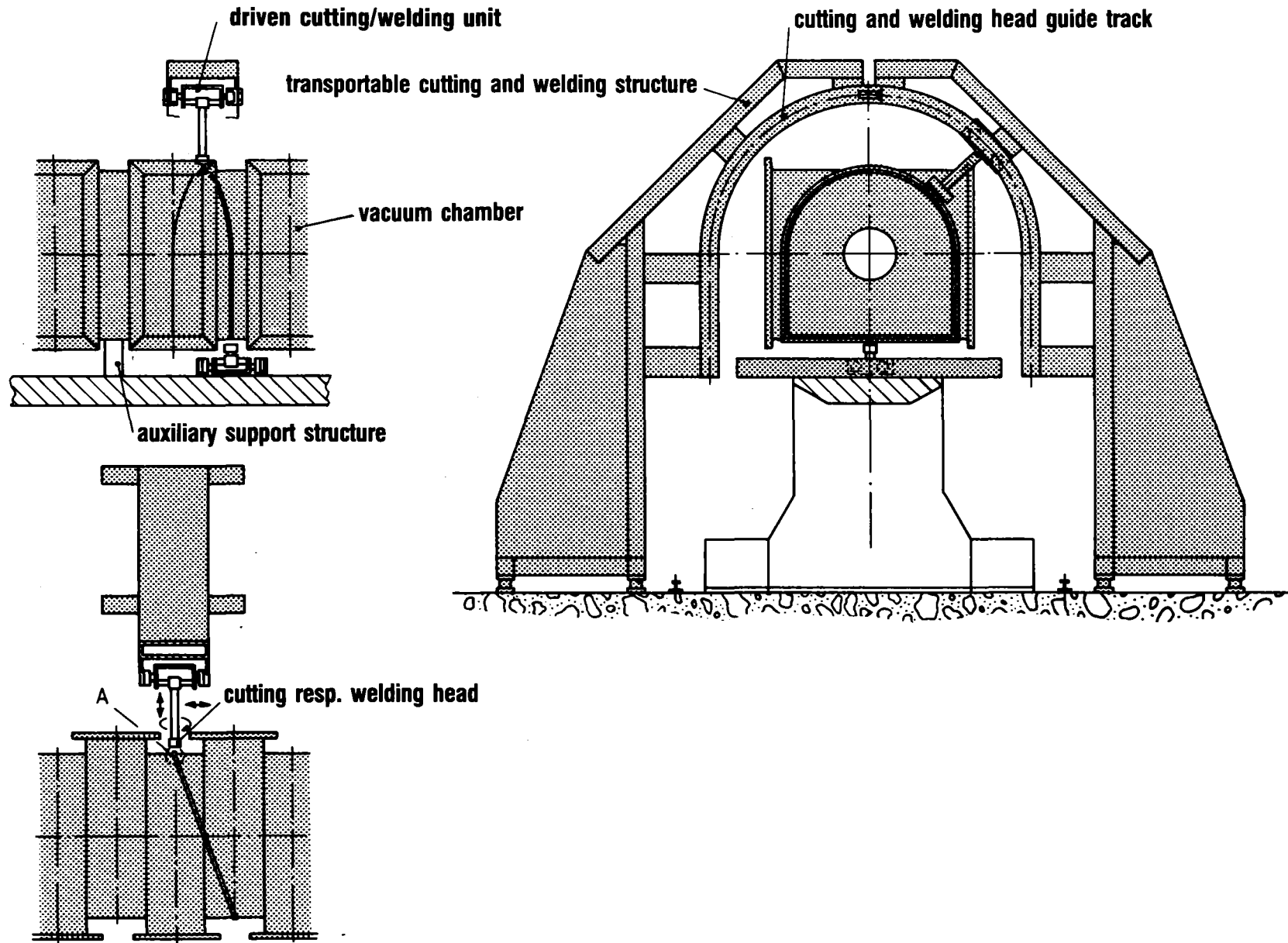
Fig. X.5-3 Exchange of central cell coil - welding of vacuum chamber

coil

load attachment unit

vacuum chamber

vacuum chamber

movable central cell coil support structure
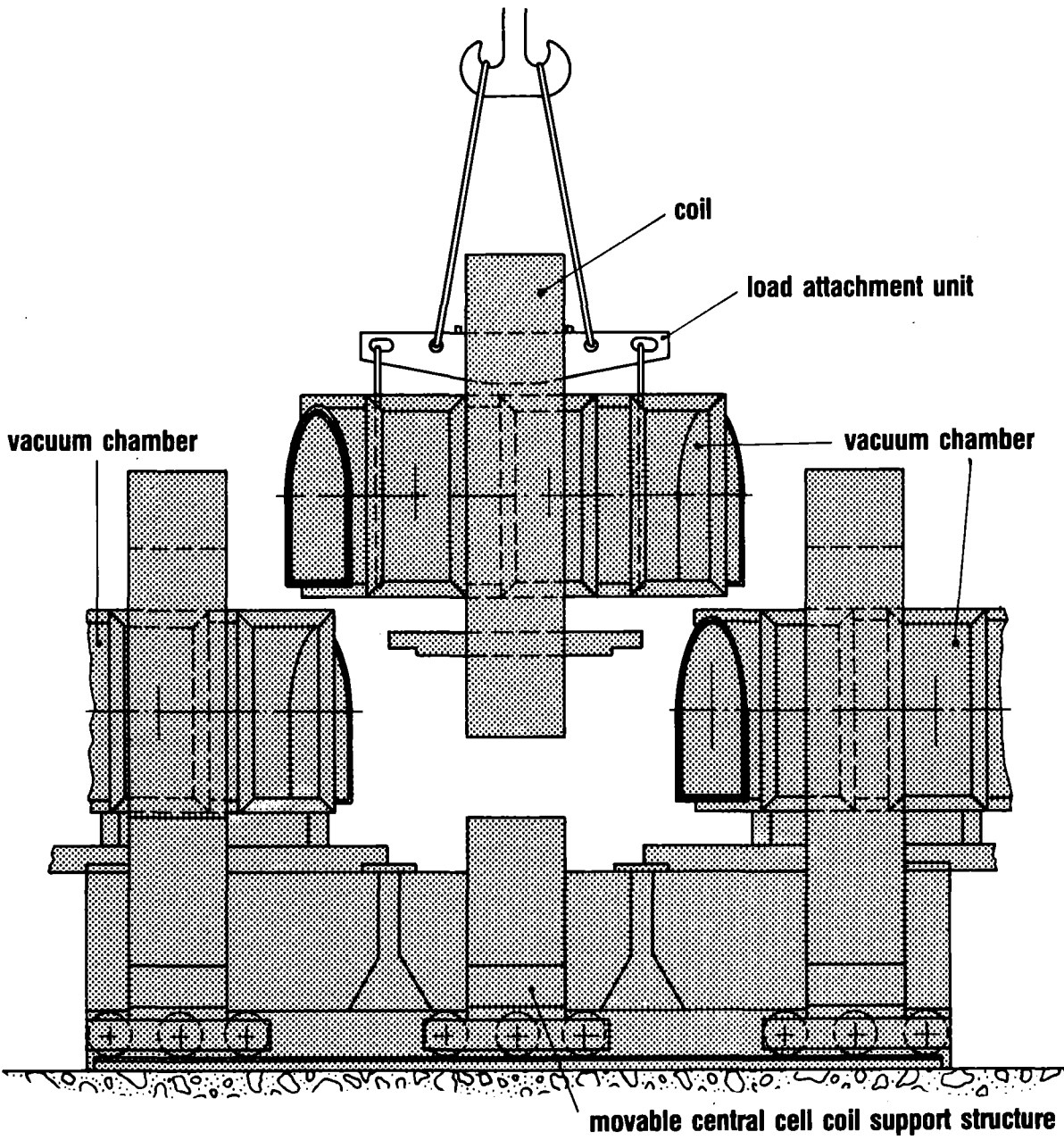
Fig. X.5-4 Exchange of central cell coil - removal of coil and vacuum chamber

X.5.2 Barrier Coil (Fig. X.5-5)

A barrier coil replacement will be necessary at least every three years due to radiation damages of the barrier insert coils and sputtering of the medium neutral beam dump.

The preliminary work of preparing a barrier coil for replacement is shown in Figure X.5-6, namely the disconnection of supply lines and the removal of support structure, the support plate which is movable on tracks and finally the shield. This gives access to the weld joint. After dismantling the clamps and mounting the cutting guide track around the vacuum chamber, the weld joint can be cut. Subsequently an auxiliary support structure will be adapted to the base structure of the barrier coil (Fig. X.5-7) and the coil equipped with roller rails can be shifted toward the central cell for cutting the weld joint on the opposite side of the barrier coil in the same manner. While the coil is being shifted, additional shield segments located inside the coil will be withdrawn. After the second cut is made the barrier coil will be shifted to its original position whereupon it can be removed together with its support structure out of the reactor (Fi.g X.5-8). Because of the weight of the barrier coil, it should be dismantled in the reactor hall before parts of it within the capability of the crane can be transported into the lock area.

Reassembly will be performed in a reverse sequence and in a similar manner as the central cell coil.

X.5-7

support structure (central cell coil)

shield

support structure (barrier coil)

barrier coil

shield

duct

beam dump

shield

insert coil

vacuum chamber

movable coil
support structure
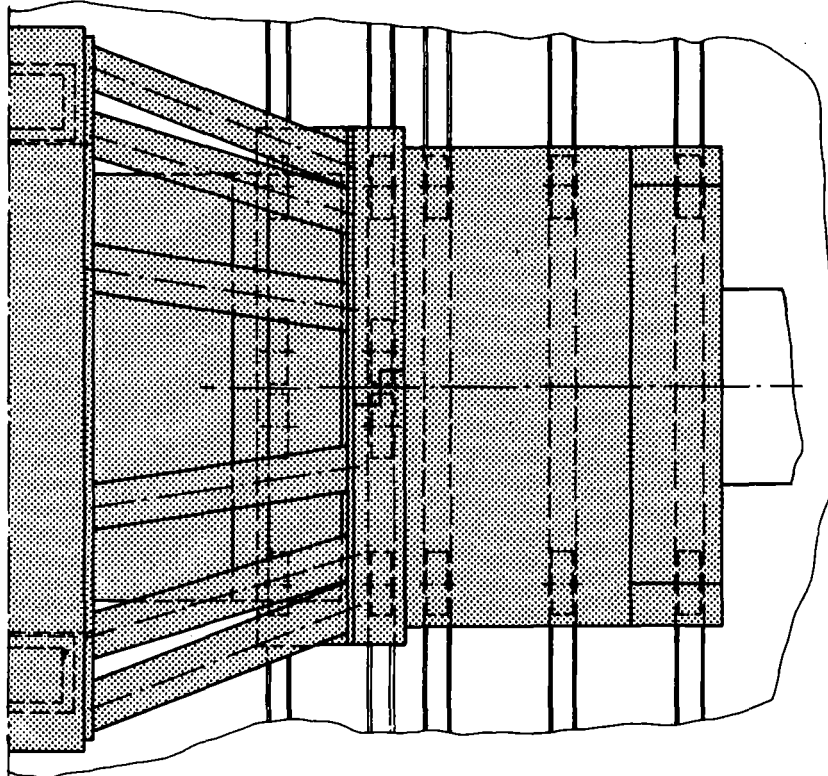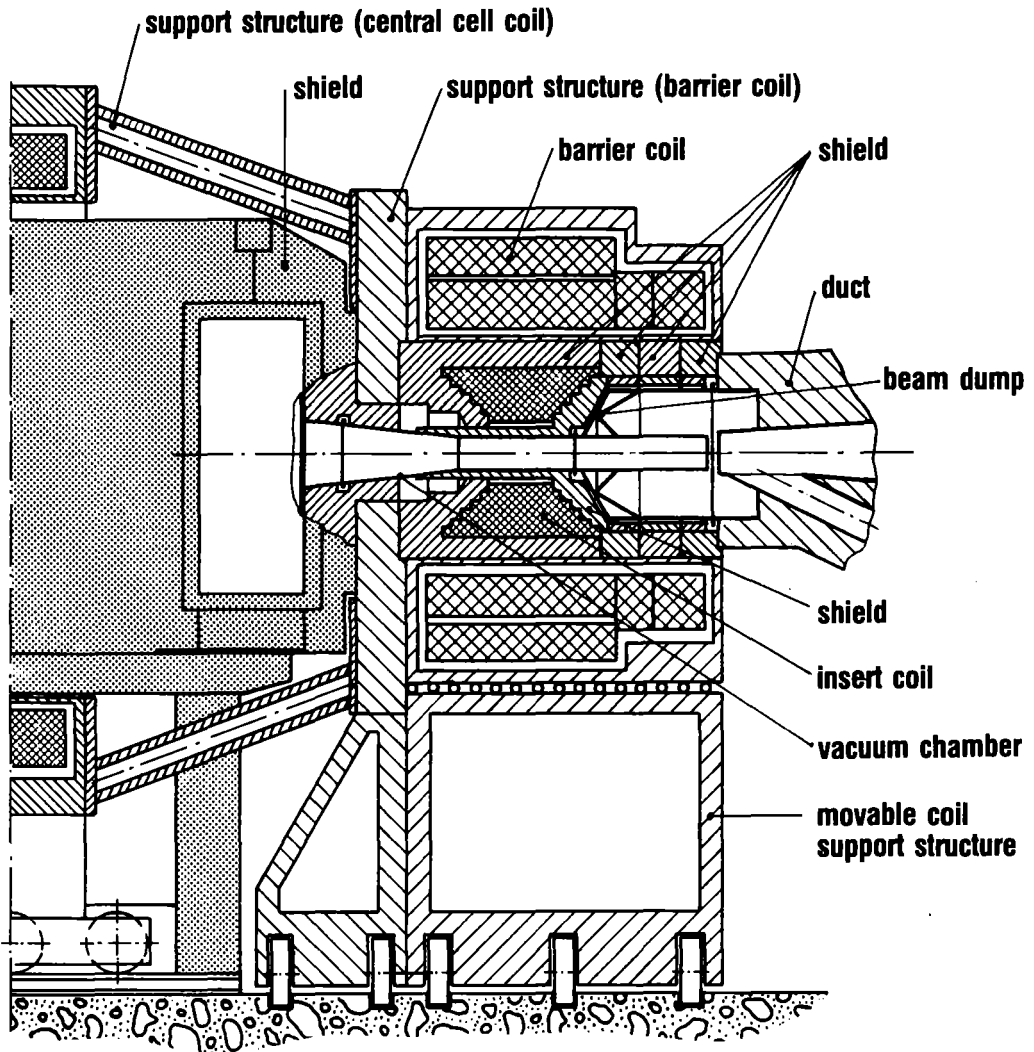
Fig. X.5-5 Barrier region

X.5-8
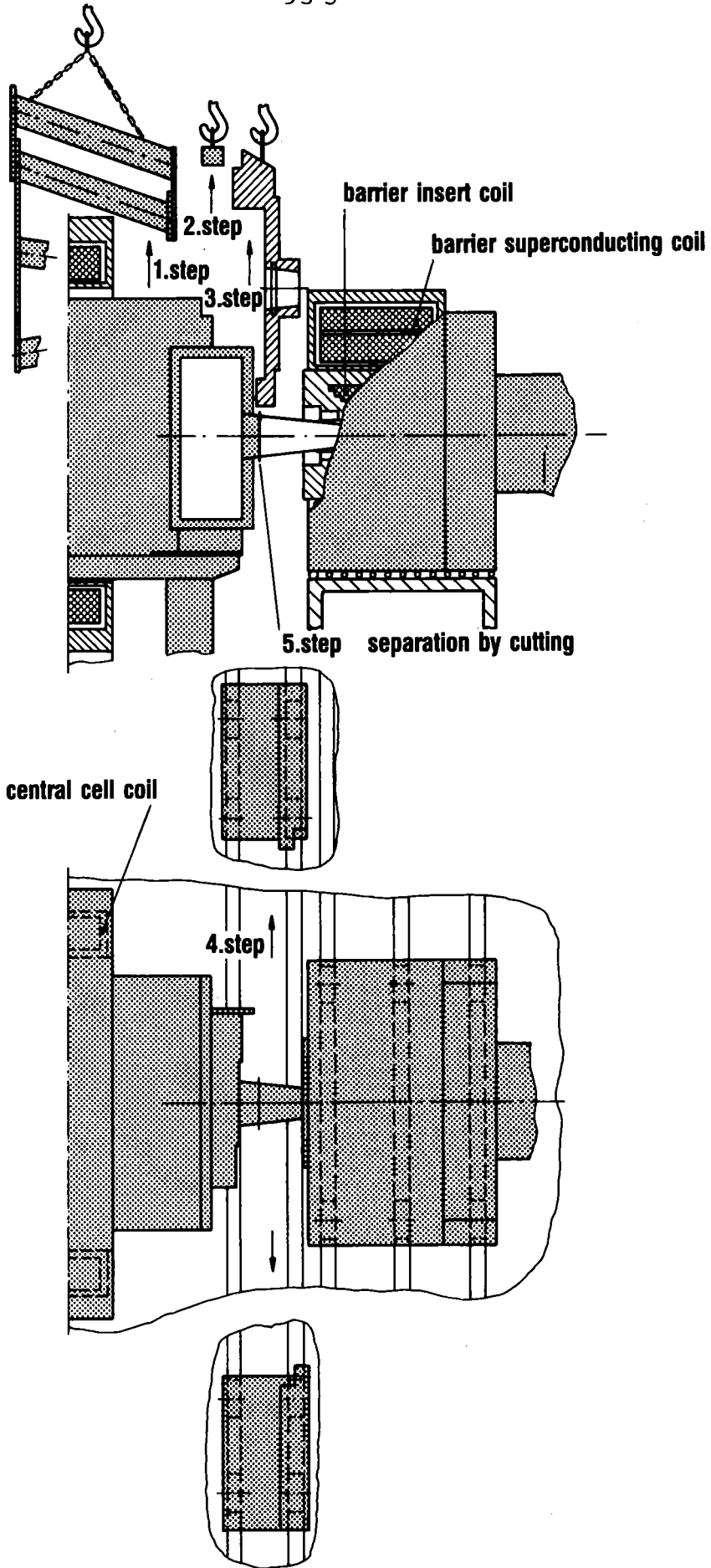
Fig. X.5-6 Components exchange at the barrier region - preliminary works

6.step

7.step

8.step seperation
by cutting

auxiliary support structure
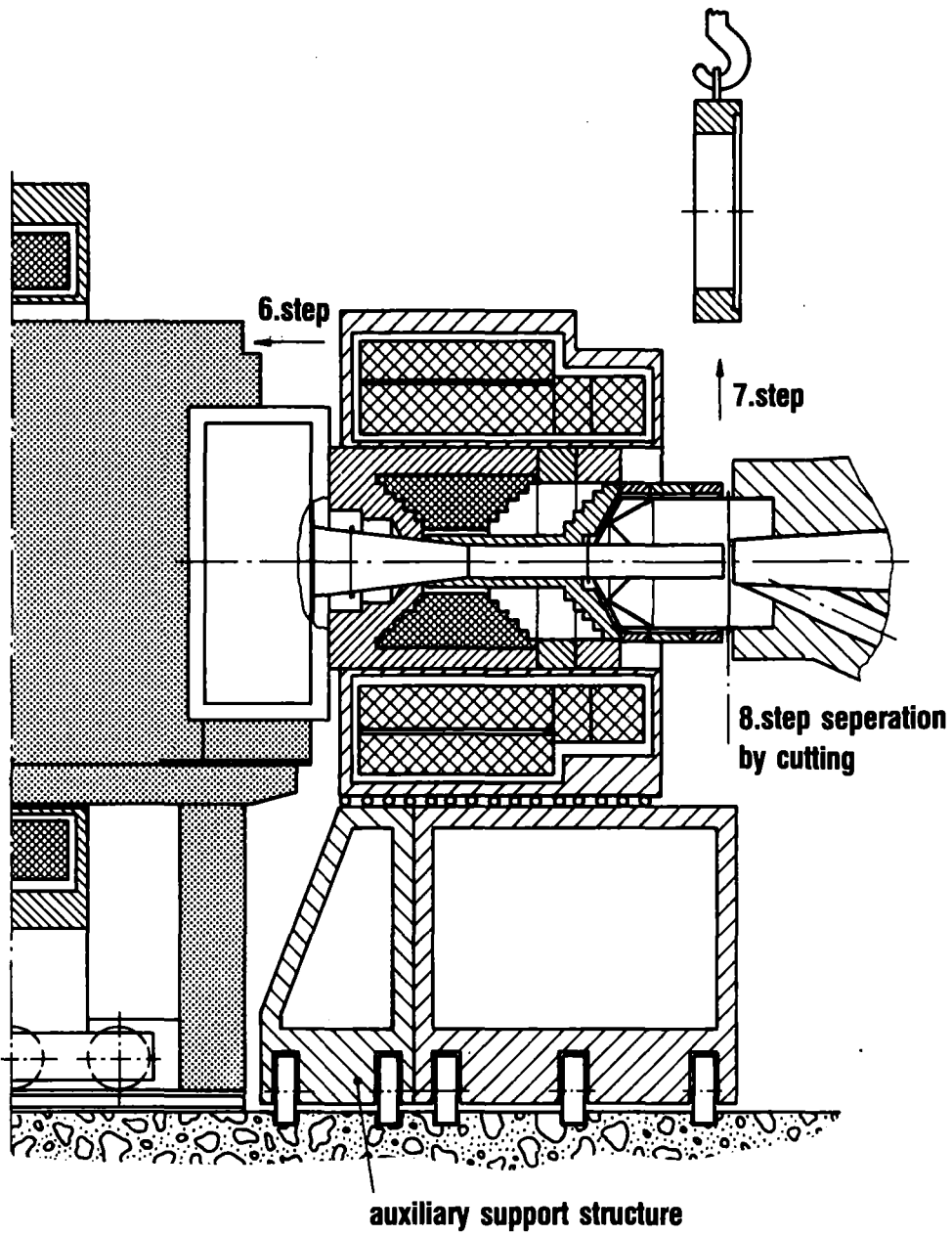
Fig. X.5-7 Components exchange at the barrier region - vacuum chamber separation

top view

separation by cutting
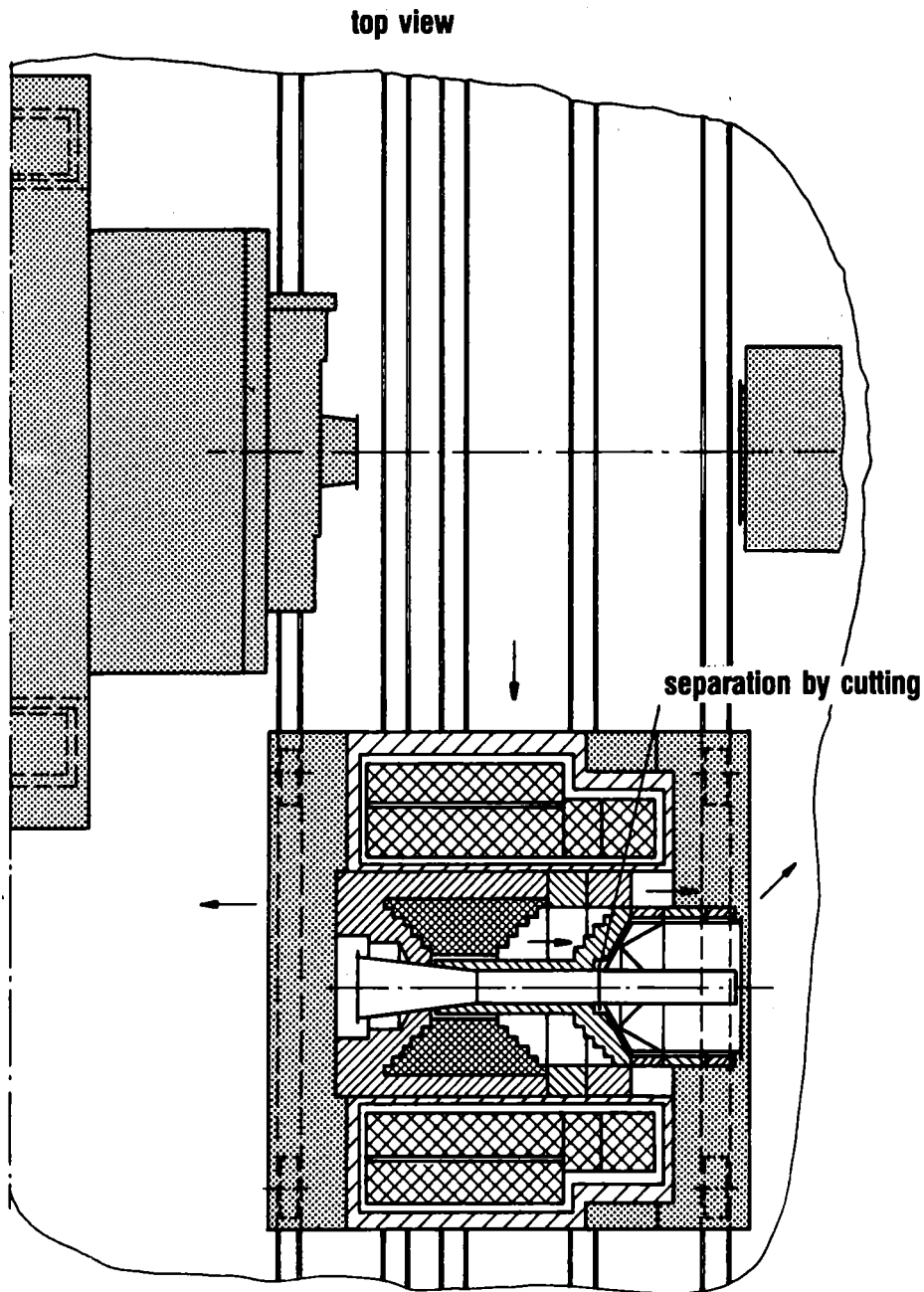
Fig. X.5-8 Components exchange at the barrier region - components dismantling

It was only possible to consider a few critical maintenance operations and the objective was to check the possibility of performance. There are numerous maintenance tasks which impact on the components design but it can also be assumed that the maintenance problems are soluble.

X.6   Barrier Coil

X.6.1   Requirement and Objective

The requirement is to replace the normal conducting insert coils and barrier pump neutral beam dumps in the barrier coil assemblies without simultaneously replacing their superconducting coils, and to do so by remote control without manual assistance.

The objective is to evolve design features and assembly/disassembly procedures to satisfy the above requirement, using criteria of cost effectiveness, operational risk, simplicity, reliability, practicality, and inspectability for quality control purposes.

X.6.2   Approach

TASKA is envisioned to produce neutron wall loadings near 1 MW/m^2 during more than 10 years of operation at machine availabilities from 15 to 50%. Hence, remote maintenance provisions approaching those of a power reactor become mandatory.

Early emphasis of remote maintenance requirements is made difficult by the fact that many individual component reliabilities and lifetimes are not well established. Due to the scope of TASKA studies, remote maintenance considerations have been restricted to the most important machine components rather than governing all configuration and design decisions from the beginning. In Sections X.1, X.2, X.3, central cell, plugs, and the exchange of test modules were discussed. In this section, replacement of a module consisting of the barrier pump neutral beam dumps (henceforth called "beam dumps") and normal conducting insert coils (henceforth called "normal coils") will be addressed. The lifetime of these coils is expected to be limited to about 5 years (at 50% availability) due to radiation damage to their ceramic

insulation. Lifetime limitation of the beam dumps, due to erosion, is expected to be comparable.

It is assumed (see Fig. X.6-1), that the central cell (station B to C) and the entire end-plug assemblies of the machine (to the left of station A, and to the right of station B) stay in place during all operations associated with replacement of the normal coils and beam dumps. The approach is to cut the vacuum vessel at two locations in the vicinity of, say, C and D, and to move the entire module between stations C and D horizontally normal to the machine axis, thus becoming accessible from its ends allowing replacement of the normal coil and the beam dumps. For reassembly, the sequence is reversed. Individual steps are explained in Section X.6.5.

To simplify the above procedure, a number of design features have been incorporated, as described conceptually in Section X.6.3.

Several alternate approaches have been considered as discussed in Section X.6.4.

X.6.3 Configuration Description

X.6.3.1 General Description

The barrier coil module consists of a superconducting coil which encircles a normal coil which, in turn, encircles a segment of the vacuum vessel. The beam dumps (and associated cooling components) are located within the vacuum vessel. Three neutral beam injection tubes intersect the vacuum vessel, each making a 25 degree angle with the plasma axis. The tubes are spaced at 120 degree intervals around the plasma axis. Units of shielding are positioned between the vacuum vessel and the coils.

BEAM DUMPS

NORMAL COIL

24,4
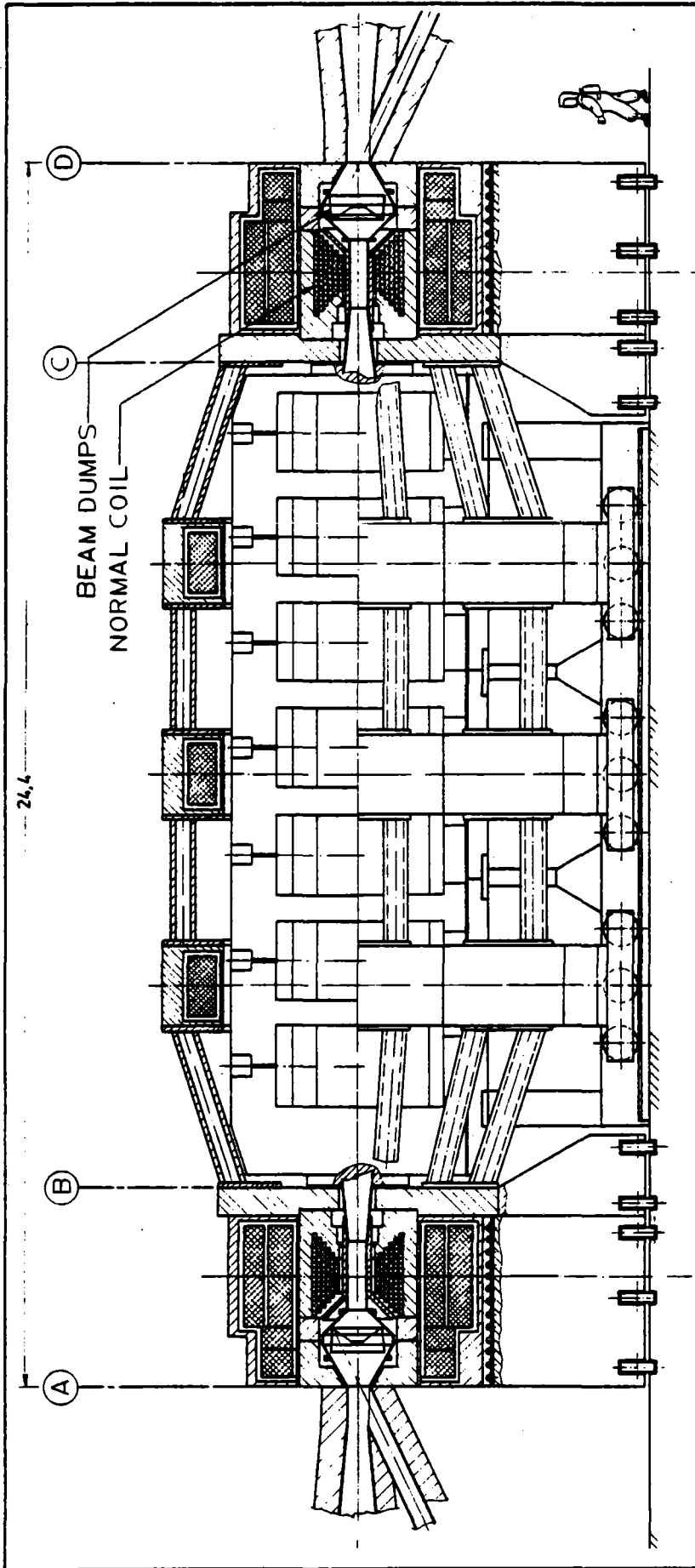
Elevation View of the Central Cell and Barrier Coils

Fig. X.6-1

X.6-3

GRUMMAN

The normal coil is encircled by a stainless steel band approximately 15 centimeters thick. The cryostat of the superconducting coil is enclosed in a structural stainless steel case varying in thickness from 5 to 20 centimeters.

A massive support plate, 50 centimeters thick, encircling the vacuum vessel, is located between the barrier coil and the central cell. Intercoil supports connect the support plate to the structural supports of the central cell solonoid coils.

Figure X.6-1 shows the relationship of the two barrier coil areas to the central cell. Figure X.6-2 presents a cross sectional view of the barrier coil module and Fig. X.6-3 illustrates its major components in an exploded view.

X.6.3.2 Remote Maintenance Configuration

To ensure that barrier coil maintenance can be accomplished within reasonable limits of time, cost and operational risk, some modification to the configuration described above has been made and is discussed below.

The structural case of the superconducting coil interfaces with and is supported by a track mounted barrier coil carriage. The carriage consists of an upper and a lower section. The upper section cradles the superconducting coil structural case. Three sets of rollers are positioned between the upper and lower carriage sections to permit at least 60 centimeters of axial translation of the barrier coil along the plasma axis for maintenance purposes.

The lower section of the barrier coil carriage is supported by floor mounted tracks in such a way that barrier coil horizontal translation normal to the plasma axis is possible. It also incorporates adjustment capability for barrier coil alignment to adjacent TASKA components. Suitable devices must also be provided to secure the carriage sections to each other (during

Fig. X.6-2

BARRIER COIL AREA, CROSS SECTION

X.6-5

Fig. X.6-3

SUPERCONDUCTING COIL

"NORMAL" INSERT COIL

VACUUM VESSEL

BEAM DUMPS

BARRIER COIL MODULE, MAJOR COMPONENTS

X.6-6
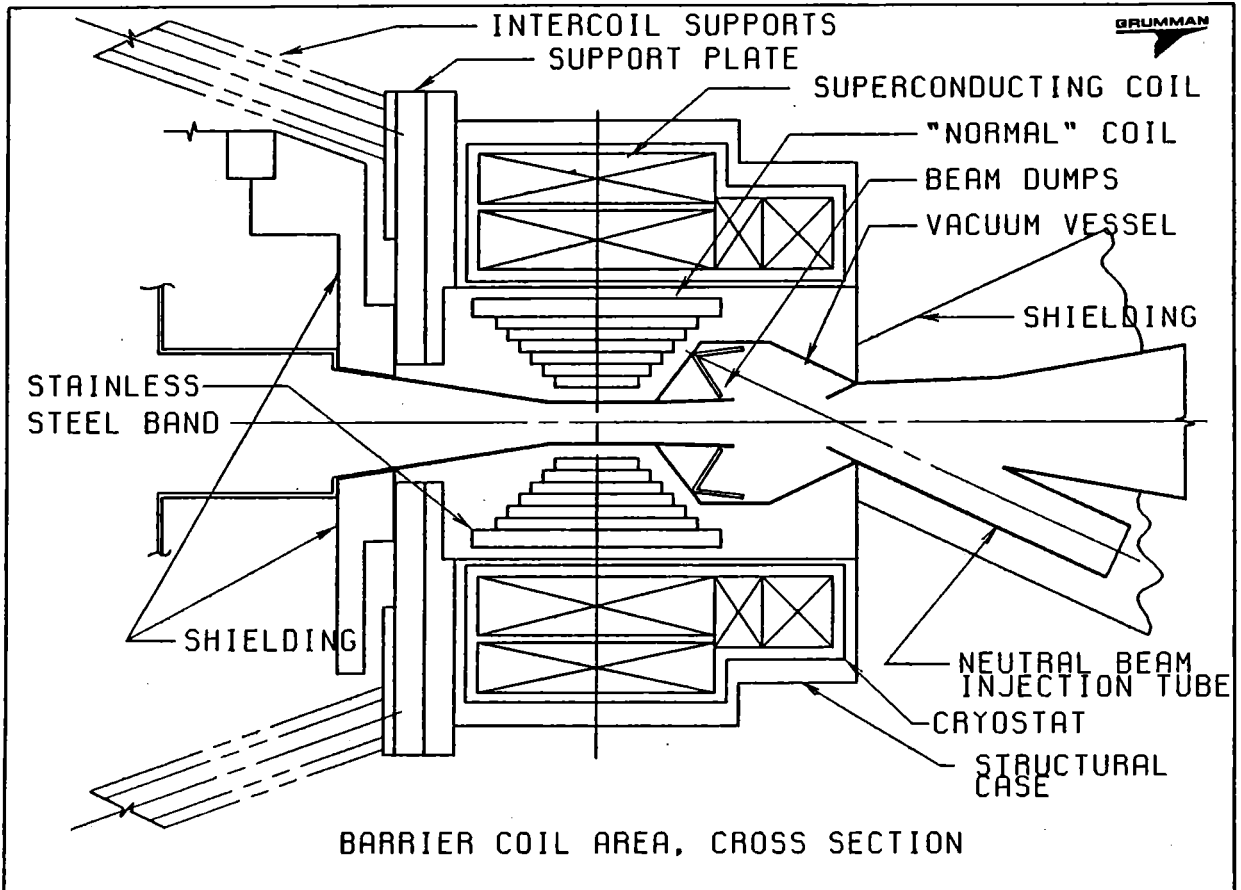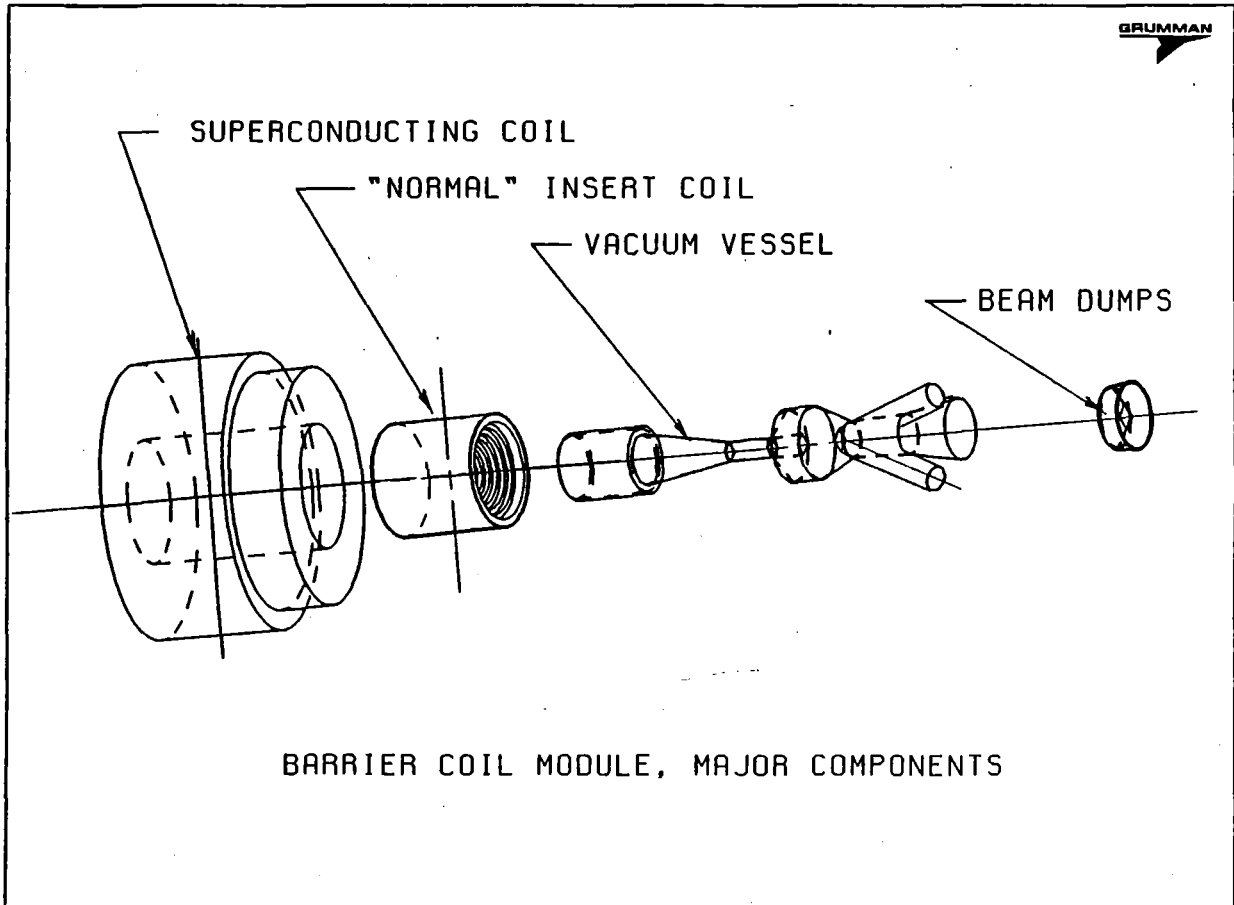
maintenance procedures) and to the facility floor during TASKA operation. Positioning devices and stops are incorporated in the barrier coil carriage and in the floor mounted tracks to simplify remote maintenance operations.

Figure X.6-4 shows the barrier coil carriage in relationship to the TASKA machine and to the facility. It is also illustrated in Fig. X.6-8 and X.6-9. Figure X.6-11 shows its axial motion (along the plasma axis) capability.

The massive support plate encircling the vacuum vessel is designed as two interlocking halves joined on the vertical centerline, enabling its removal to gain access to the vacuum vessel parting flange. Each half is supported by a carriage mounted on tracks on the floor which permit horizontal translation normal to the plasma axis. As with the barrier coil carriage, positioning devices and stops are required in the support plate carriage and its associated tracks simplify remote maintenance. The support plate carriage is illustrated in relationship to TASKA and the facility in Fig. X.6-4 and is also shown in Fig. X.6-8. Its remote maintenance usefulness is shown in Fig. X.6-9.

Although not illustrated, it is recommended that the support plate carriage incorporate provisions to stabilize and secure the support plate halves during removal procedures. These provisions may be added during maintenance procedures when the support plate halves are partially removed from their normal positions.

Two sets of parting plane flanges located to each side of the barrier coil must be incorporated into the design of the vacuum vessel so that removal of the barrier coil may be accomplished. Their recommended locations are illustrated in Fig. X.6-6. The flanges are sealed by welds at their outer circumference to provide vacuum integrity. The flanges are designed so that the seal welds may be removed by a side mill remote cutter and subsequently

Fig. X.6-4

TO STORAGE AREA

GRUMMAN

C_L
SYMMETRY

REPAIR STATION

FLOOR MOUNTED TRACKS
(6 EACH SIDE)

SERIVCE CARRIAGE (TO REMOVE
DAMAGED COMPONENTS)

BARRIER COIL
CARRIAGE

SERVICE CARRIAGE (TO INSERT
REPLACEMENT MODULE)

SUPPORT PLATE CARRIAGE

BARRIER COIL
CARRIAGE

SUPPORT PLATE STORAGE STRUCTURE

SUPPORT PLATE
STORAGE STRUCTURE

SUPPORT PLATE
CARRIAGE
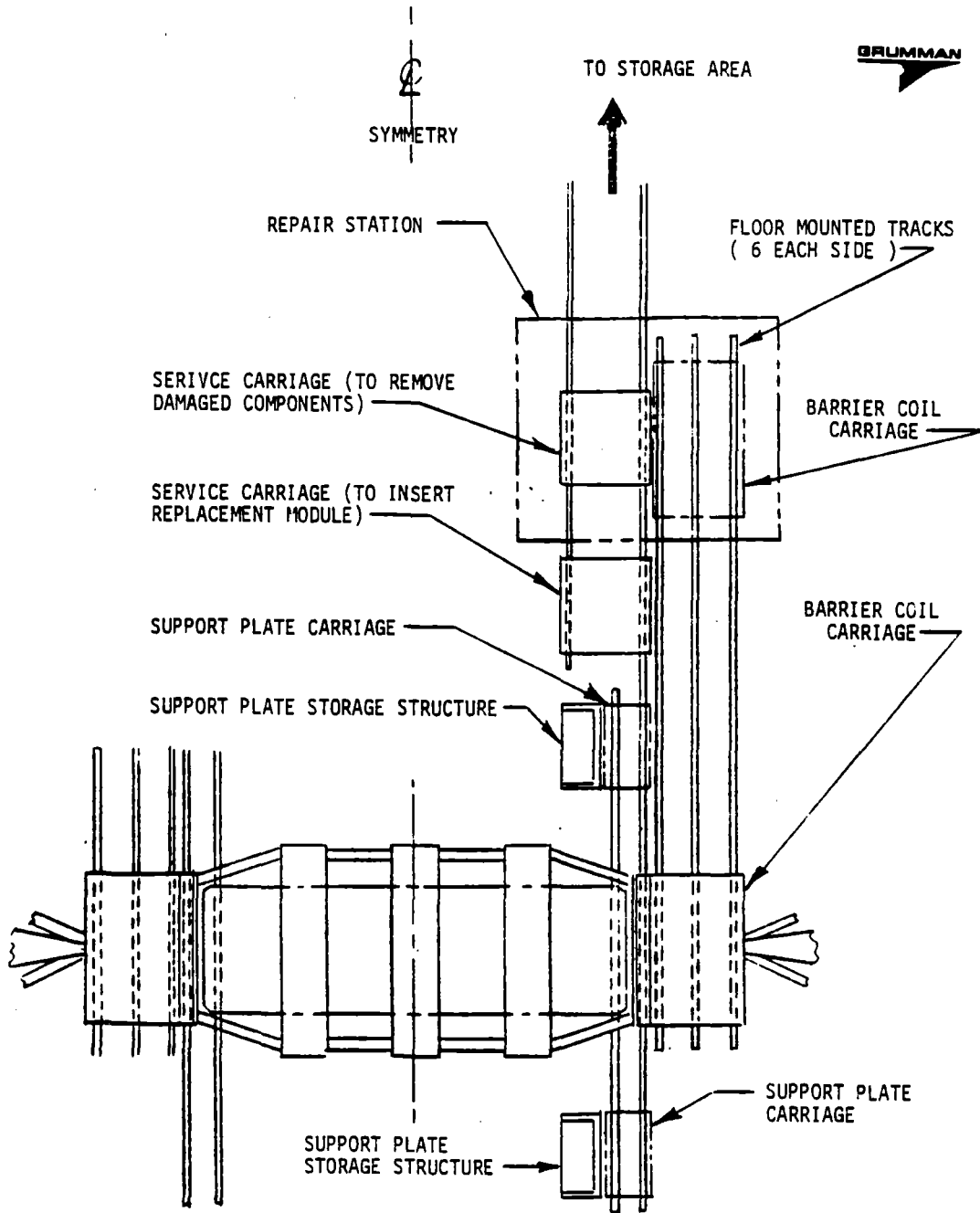
FACILITY LAYOUT, PLAN VIEW

NO SCALE

X.6-8

Fig. X.6-5

NEUTRAL BEAM INJECTION TUBES

BEAM DUMP ASSY

VACUUM VESSEL, ORIGINAL CONFIGURATION

X.6-9

Fig. X.6-6

PARTING PLANE FLANGES

BELLOWS

EXTENDED CYLINDRICAL SURFACE

VACUUM VESSEL (MODIFIED CONFIGURATION)

GRUMMAN

X.6-10

Fig. X.6-7

ACTUATOR

BEAM DUMPS

BELLOWS

CHAIN LOCATING GROOVE

GRUMMAN

DETAIL, NEUTRAL BEAM DUMP AREA

X.6-11

Fig. X.6-8

REMOVAL OF INTERCOIL SUPPORTS & SHIELDING

X.6-12

Fig. X.6-9

REMOVAL OF SUPPORT PLATES

X.6-13

Fig. X.6-10

INSTALLATION OF REMOTE CUTTER & ADAPTER

X.6-14

Fig. X.6-11

REMOTE CUTTER

ROLLERS

BARRIER COIL
CARRIAGE (UPPER
SECTION)

BARRIER COIL
CARRIAGE (LOWER
SECTION)

60.0 CM

SHIFT OF BARRIER COIL TOWARDS CENTRAL CELLS

remotely rewelded three times (three times the estimated need). Figure X.6-7 shows one of the parting plane flanges in somewhat greater scale. Refer to Section X.6.4 for a discussion of alternate parting plane and vacuum seal designs.

A construction joint in the vacuum vessel at the barrier coil throat will be required for initial TASKA assembly.

Belt chains are used to attach commercial remote pipe cutters, remote welding machines and other types of remote maintenance equipment. Therefore, locating grooves and bosses in the vacuum vessel are required to ensure the tracking accuracy of these devices and to simplify their installation and removal by remote means. Examples of these design modifications are depicted in Fig. X.6-10.

The configuration of the vacuum vessel in the beam dump area requires modification. The cylindrical vacuum vessel surface here has been lengthened and terminated by a domed end. The conical section shown in Fig. X.6-5 has been eliminated. These modifications, which are illustrated in Fig. X.6-6, provide a secure surface upon which the remote cutter and welder can travel and track circumferentially around the vacuum vessel.

As mentioned in Section X.6.2, the approach to barrier coil maintainability is to cut the vacuum vessel in the vicinity of stations A and B, C and D and to horizontally move the entire barrier coil module normal to the machine axis to an appropriate nearby repair station where the damaged barrier coil components can be removed and replaced. Milling away the seal weld from the vacuum vessel flanges while structurally decoupling the barrier coil vacuum vessel segment from its adjacent sections will leave zero clearance at the parting plane flanges. Adequate clearance must be provided to translate

the barrier coil module to its repair station and even more importantly to re-insert, align and adjust a repaired module into its position in the machine. Any system to provide clearance for module removal must be reversible to allow accurate realignment for welding. Similar requirements exist if a mechanical joint is used instead of the seal welded joint assumed here.

A bellows section, with associated actuators (to extend and contract the bellows), has been incorporated into the vacuum vessel segment to provide the neccessary clearance. At least three actuators will be required to provide smooth operation. The bellows and actuators are shown in several figures but are presented in somewhat enlarged scale in Fig. X.6-7. Alternate design approaches are discussed in Section X.6.4.

The shielding that envelopes the vacuum vessel can and must be designed in suitably sized, removable, interlocking units. "Interlocking" is used in the sense of: no straight lines of sight between shielding units will be permitted -- in order to minimize neutron streaming. No difficult design problems are envisioned in this area, however, several design features are important. The size and configuration of each shielding unit must be governed by the limitations of remote handling equipment with particular regard for weight, moment-arm and "reach" capacity. Recessed "hand holds" in each shielding unit provide gripping interfaces with remote handling equipment.

The superconducting coils are expected to satisfactorily operate through-out the TASKA lifetime. They are also extremely costly components. There-fore, a desirable maintainability goal is to retain the superconducting coils and replace only the less durable and less expensive normal coils. The life-time of the beam dumps is expected to roughly correspond to the normal coil lifetime. It does not appear to be cost or "risk" effective to attempt to re-

use the severed vacuum vessel segment. Therefore, the following is recommended: (1) provide at least one spare, preassembled replacement module consisting of a new normal coil and a new vacuum vessel segment together with its associated internal beam dump assembly, (2) withdraw the damaged components from the superconducting coil and insert the spare replacement module and (3) accomplish the above at the time of failure of either the normal coil or the beam dumps - whichever occurs first.

The weight of the normal coil is borne by the structural case of the superconducting coil (as is the weight of the vacuum vessel, once severed). The estimated twenty-five tonnes combined weight will present a high frictional resistance to withdrawal of the damaged components from the superconducting coil and/or the associated shielding. "Binding" due to possible misalignment during withdrawal (and reinsertion) must also be considered. Three built-in tracks at the interface between the superconducting coil structural case and the normal coil's stainless steel band (and the associated shielding) are proposed). The tracks may incorporate integral track rollers or accommodate remotely attachable wheels. The function of the tracks is to provide removal and insertion clearances and to position the spare replacement module until the interfacing shielding is replaced. Correspondingly, prealigned tracks will be incorporated on each of two separate service carriages: one dedicated to the withdrawal of the damaged components, the other to the insertion of the spare replacement module. The relationship of these service carriages to the repair station is shown in Fig. X.6-4. Figure X.6-12 addresses the removal of the damaged components from the superconducting coil. Section X.6.7 discusses the design and usage of the service carriage.

Fig. X.6-12

GRUMMAN

FLOOR MOUNTED
RAILS

BARRIER
COIL
TRANSPORT
CARRIAGE

BELLOWS ASSY
(CONTRACTED
6 CM)

REMAINING
VACUUM VESSEL

Z AXIS TASKA

REMOVAL OF BARRIER COIL MODULE
(PLAN VIEW)

× CLEARANCE EACH SIDE = 3 CM (SEE TEXT)

X.6-19
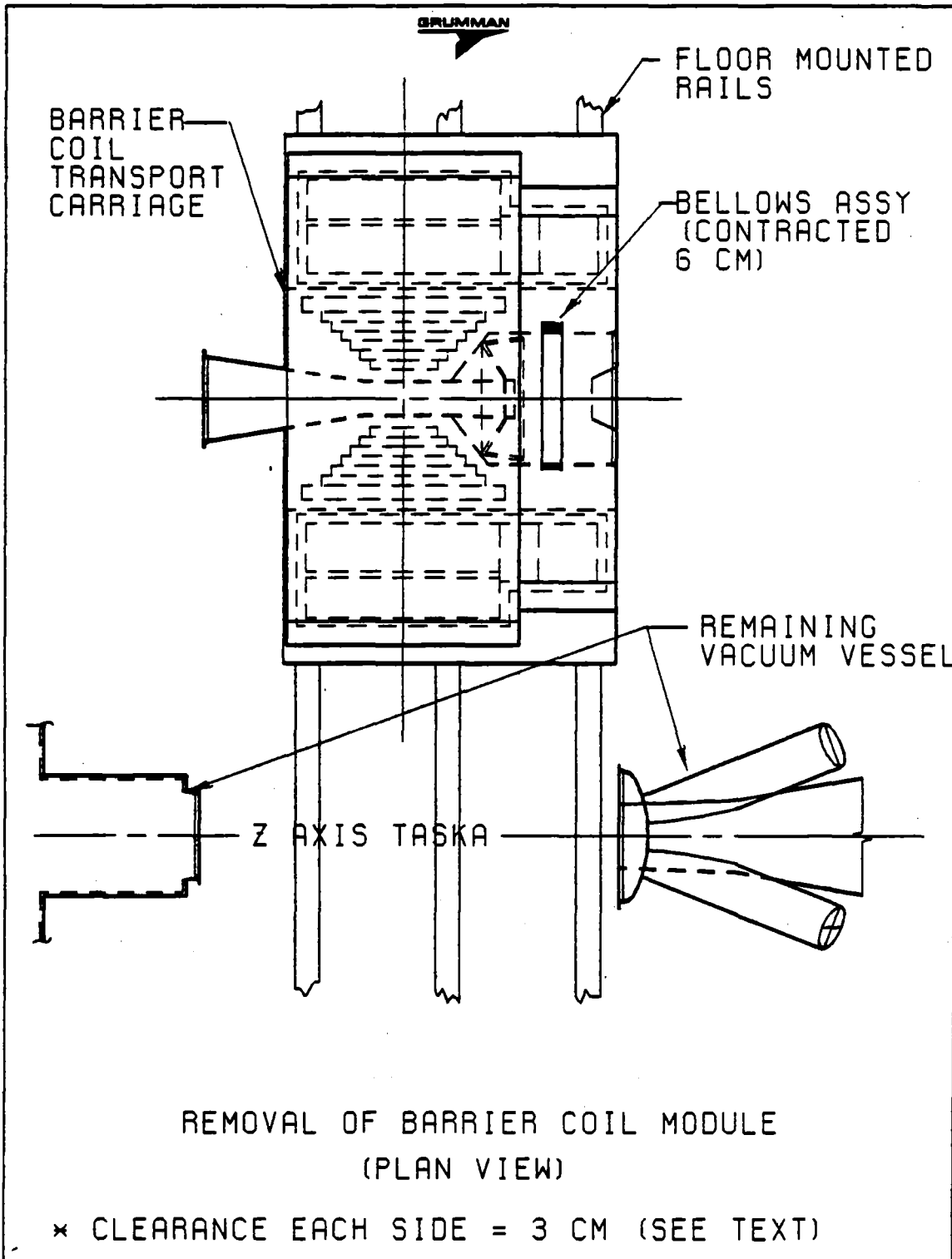
X.6.4 Alternate Designs and Procedures

X.6.4.1 History and Candidate Approaches

The desirability of following certain design directions became apparent early in the barrier coil maintenance study. It was preferable, for example, to conceive a scheme whereby the barrier coils could be removed from the TASKA machine and transported laterally to a repair station. The barrier coil module thus becomes accessible, freed from its ends, permitting replacement of the damaged components. A separate room for the repair station was at first conceived but soon abandoned because of the needless duplication of cost and equipment.

Considered from the viewpoint of economy of time, cost, operational risk, simplicity and reliability, the practicality of treating the damaged components as an entity (rather than piece by piece repair) became apparent. Given the above concepts and considering the enormous mass of the barrier coil, it was a natural and logical conclusion to conceive the barrier coil module to be permanently mounted on carriages which would serve, during TASKA operation, merely as structural supports and during maintenance procedures as movable transport devices. Mounting the carriages on tracks logically followed. Thus, the need for costly, dedicated bridge cranes or air bearing plates with their inherent inaccuracies and high operational risk was avoided.

Some major areas for study remained: how to gain access to the vacuum vessel to cut it, how to provide the required removal and reinsertion clearances and how to withdraw the damaged components from the superconducting coil with simplicity, and reliability within the limitations inherent in remote maintenance.

Solutions to these questions are discussed in the body of this text. Some alternate approaches are given below. It is interesting to note that almost identical barrier coil maintenance procedures were derived almost simultaneously by two separate groups studying independently in two different countries.

X.6.4.2 Alternate Design Candidates

X.6.4.2.1 Vacuum Vessel Parting Flange Seals

The approach selected is to seal the vacuum vessel flanges by circumferential welding. It was selected for its inherently higher reliability in comparison to mechanical seals with their susceptibility to temperature gradient induced "creep" and careful torquing and handling requirements. Nonetheless, seal welding too has its difficulties -- among them the need to acquire a remote cutter and a remote welder. It is believed that additional study should be directed to this area. It is therefore listed in Section X.6.8 "Recommendations for Further Study".

X.6.4.2.2 Vacuum Vessel Parting Flange Clearance Design

The method to achieve adequate clearance at the vacuum vessel parting flanges discussed in the text is to incorporate a bellows section in the vacuum vessel wall. Actuators are employed to contract and expand the bellows. A bellows section has the advantage of serving as a thermal expansion joint and the disadvantage of vulnerability to radiation bombardment. An alternate welded sleeve joint design with built-in clearance is illustrated in Fig. X.6-13. It has considerable merit and is therefore listed in Section X.6.8 "Recommendations for Further Study".

Fig. X.6-13

SERVICE CARRIAGE

SUPERCONDUCTING COIL

NORMAL COIL

VACUUM
VESSEL
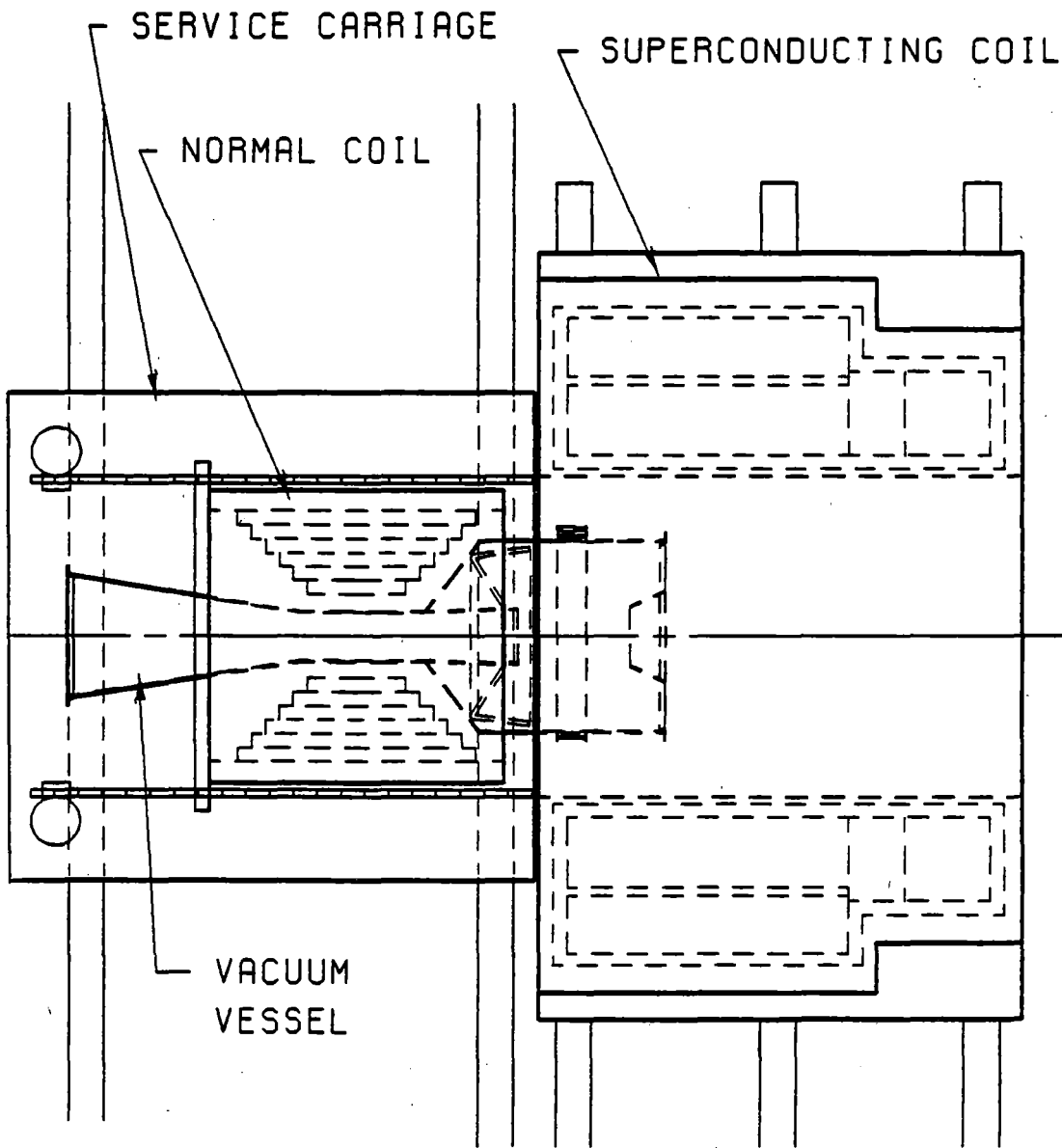
WITHDRAWAL OF DAMAGED COMPONENTS

X.6-22

- 959 -

X.6.5 Description of Selected Procedure

Replacement of the normal coil assembly may be accomplished by the following procedure.

1. Remove the high energy neutral beam (NB) injectors and store. This step is necessary only if the NB injectors are mounted in the vicinity of the barrier coil module.

2. Disconnect service lines to the barrier coil module.

3. Remove the intercoil structure using the overhead crane for lifting and transporting each section, and a general purpose manipulator unit for removal of bolts.

4. Remove the central cell shield adjacent to the barrier coil module using the overhead crane and general purpose manipulator unit as discussed above.

5. Disconnect two halves of the support plate and translate laterally.

6. Install the cutting machine adapter to the vacuum vessel segment as shown in Fig. X.6-10. The adapter is constructed of two 180° segments which clamp to the vacuum vessel. Two grooves on its outer surface are used to secure the cutting machine guide chain.

7. Install cutting machine on the adapter, connect lines to control unit and power supply.

8. Place temporary supports between the vacuum vessel segment and the coil support module. This is required to carry the vacuum vessel weight when the flange is cut. The temporary supports must allow for 60 cm axial movement between vacuum vessel and coil support.

9. Cut the vacuum vessel flange.

10. Remove the cutting machine and adapter.

X.6-23

11. Translate the barrier coil axially 60 cm toward the central cell using the axial motion mechanism provided in the coil support module. This motion provides access for cutting the remaining vacuum vessel flange.

12. Remove shielding around the vacuum vessel segment at the end plug side.

13. Install cutting machine as shown in Fig. X.6-11. Grooves for the cutting machine drive chains are machined into the vacuum vessel surface.

14. Cut the vacuum vessel flange.

15. Remove cutting machine.

16. Translate barrier coil axially 60 cm to original position.

17. Retract the bellows section of the vacuum vessel (see Fig. X.6-6).

18. Connect a tow unit to the barrier coil module and transport it to the maintenance area.

19. Position an "insert" replacement module at the maintenance area. This module contains a replacement normal coil (NC) assembly, and has provision for receiving the damaged NC assembly after removal. Also, it contains linear actuators for removal and installation of the NC assembly from ths superconducting coil (SC) assmmbly. Three rails on the insert replacement module lineup with similar rails in the SC assembly.

20. Remove the damaged NC assembly and install a replacement NC assembly.

21. Connect service lines between NC assembly and coil support module. Perform checkout tests on NC assembly.

22. Transport barrier coil module to its operational location.

23. Align vacuum vessel segment with the plasma axis using adjustments provided on the coil support module.

24. Assemble the barrier coil module to adjacent modules using a reverse order of the above procedure. Flange welding is performed by a welding

machine which mounts to the vacuum vessel similar to the cutting machine described above.

X.6.6 Facility Requirements

The following list presents the facility equipment which (in addition to the requirements of previous sections) will be specifically required to maintain the barrier coils. Figure X.6-4 presents a plan view of the suggested facility layout.

- Six floor mounted tracks extend laterally from each barrier coil. Their function is to transport the barrier coil carriage from the TASKA machine to the repair station and back again, to transport the support plate carriages to and from their appropriate temporary storage structures and lastly, to transport both service carriages from the storage area to the repair station and back again. Floor mounted tracks were selected in lieu of overhead bridge mounted cranes because of their inherent capacity to support huge weights, for easier and more accurate guidance and for their capability to incorporate stops and positioning devices.

- Two storage structures for each barrier coil for the temporary safekeeping of the support plate "halves". These structures are secured to the facility floor immediately adjacent to the floor mounted tracks which are dedicated to support plate removal. They are constructed of standard catalog structural members. It is planned that each support plate half will remain mounted on its appropriate carriage throughout the barrier coil maintenance procedures until reinstallation. The storage structures serve only as "hitching posts" to temporarily secure the heavy mass of the support plate halves.

- Storage areas for the spare barrier coil replacement modules and associated support equipment.

- "Hot" storage area for safekeeping of removed and damaged components.

- Standard leak detection equipment.

- At least two spare replacement modules (one for each barrier coil) consisting of a normal coil and a vacuum vessel segment together with its internal beam dump.

X.6.7 Special Equipment Requirements

The following items are required for the procedure described in Section X.6.5.

X.6.7.1 Remote Cutter Assembly

Existing remote pipe cutters used in the petroleum industry are suitable for the proposed procedure. A belt chain (similar to a "silent" chain) is attached circumferentially to the vessel to be cut. The cutting mechanism is pre-attached to the chain. A pneumatic self-contained motor drives the mechanism circumferentially around the vessel and powers a slide milling cutter. Various sizes and configurations of cutters are available "off-the-shelf". Various size chains are available to meet TASKA needs. The chains include a "quick release" device and tension adjustment is incorporated. A temporary attachment fixture to support the cutter on the vacuum vessel while the chain is being installed will be provided.

The commercial remote cutter assembly may need to be modified to incorporate provisions for cooling gas to be directed toward the cutter teeth to reduce heat buildup (due to cutting the vacuum vessel flanges without the benefit of lubricating fluids) and to remove cuttings from the cutter teeth. Experience with TFTR has shown that chips tend to weld themselves (albeit

somewhat loosely) to the cutter teeth and to accumulate in small masses which subsequently loosen and find their way between the teeth and material being cut. An unsatisfactory cut may result. A transparent plastic shield or hood to momentarily contain and collect cuttings must be incorporated, as well as a vacuum source to remove cuttings from the plastic hood and vacuum vessel area. Additionally the remote cutter will be modified for interface with remote handling equipment. Reliability requirements on the manufacture may require strengthening.

X.6.7.2 Remote Welder Assembly

Commercial tungsten inert gas welders and associated controls are available and are suitable for the proposed procedure without extensive modification. The only modifications envisioned will be for interface with remote handling equipment (e.g., remote manipulators).

X.6.7.3 Barrier Coil Carriage

The barrier coil carriages (one is required for each barrier coil) are the structural supports for the 2 barrier coil modules. They have the added functions of adjusting and transporting the coils in various directions for maintenance purposes. In fact, each barrier coil carriage has four functions: it supports and positions the barrier coil module in the TASKA machine - reacting the gravity loads to floor mounted tracks; it adjusts the barrier coil module to adjacent TASKA components; it translates the barrier coil module along the plasma axis and lastly, it transports the barrier coil module to the repair station where it will interface with both service carriages.

The carriage is designed in an upper and a lower section. The upper section cradles and supports the superconducting coil structural case. It interfaces with the lower section through three sets of rollers which permit

at least 60 centimeters of translation of the barrier coil module along the plasma axis for improved access to the vacuum vessel parting flanges on the end plug side of the barrier coil module. Figure X.6-11 shows the upper section translated sixty centimeters towards the central cell.

The lower section is mounted on wheels which, in turn, are set into the floor mounted tracks illustrated in Fig. X.6-4. The primary function of the lower section is to transport the upper section, together with the barrier coil module, from the TASKA machine to the repair station and, eventually, back again. It also includes provisions to drive the upper section hori- zontally along the plasma axis and to adjust and align the barrier coil module with respect to adjacent TASKA components. The lower section incorporates measures to secure each to the other and to control the relative motions between them.

Section X.6.3.2 discusses the need to provide clearance at the vacuum vessel parting flanges and proposes a device to provide six centimeters total clearance. Advantage will be taken of the barrier coil carriage's axial translation capability to "split-the-difference", thereby assuring equal clearance on each side of the severed vacuum vessel.

X.6.7.4 Service Carriages

There are two service carriages. They are similar in design but each is dedicated to a specific task. Their relationship to the facility, and to the barrier coil carriage is illustrated in Fig. X.6-4. The service carriages will be used to maintain both barrier coils.

It is preferable that prior to the removal of TASKA shielding and while "hands on" operations are possible, the first service carriage, containing a spare replacement module, be moved to the position shown in Fig. X.6-4. The

second service carriage will follow behind the first and be secured to the facility floor at a preselected position at the repair station - ready to remove the damaged barrier coil components and subsequently transport them to the "hot" storage area.

The service carriages will incorporate equipment (e.g. power screws) to withdraw the damaged components from the barrier coil module and insert replacements. An adapter plate (integral with the withdrawal equipment) will interface with and secure to the stainless steel band encircling the normal coil (previously described in Section X.6.3.1).

Tracks are incorporated on the service carriages which correspond to and will mate with the "built-in" tracks of the barrier coil module which were previously discussed at the end of Section X.6.3.2. The function of these tracks is to support and guide the coil components during the removal and insertion processes. The service carriages include provisions to adjust their tracks to those of the barrier coil module and it is planned that all neces- sary adjustments and alignments will be accomplished manually prior to the first TASKA operational cycle.

The service carriages include provisions for them to be secured to the facility floor and to the barrier coil carriage as well as devices to cor- rectly position them with respect to the barrier coil module.

Figure X.6-12 shows the role of a service carriage during the withdrawal of damaged components. An alternate design is discussed in Section X.6.5.

X.6.7.5 Support Plate Carriages

Because it is necessary to remove the support plate (to gain access to a vacuum vessel parting flange) it is designed in two vertical interlocking halves and each half is cradled and supported by a support plate carriage so

that horizontal translation normal to the plasma axis is possible. In turn, the support plate carriage interfaces, through wheels, with floor mounted tracks. Positioning devices and stops are required in the support plate carriage and its associated tracks to simplify remote maintenance. The support plate carriage is illustrated in relationship to TASKA and the facility in Fig. X.6-4 and is also shown in Fig. X.6-8. Its remote maintenance usefulness is shown in Fig. X.6-9.

X.6.7.6 Remote Cutter/Welder Mounting Adapter

The conical section of the vacuum vessel adjacent to the central cell is not suitable for mounting a remote cutter and welder. Therefore, an adapter is required to encompass the conical section and to provide a secure cylindrical surface upon which the cutter and welder can travel and track circumferentially around the vacuum vessel.

The adapter contains the necessary positioning devices to simplify remote installation of the cutter and welder. It is constructed in two interlocking halves with quick release latching devices and remote handling grips for ease of installation. It is positioned on the vacuum vessel between the parting flanges and locating bosses incorporated on the vessel wall. These bosses are designed to ease adapter installation under remote handling conditions.

X.6.7.7 Vacuum Vessel Temporary Support

Temporary supports will be required to support and position the vacuum vessel segment at the parting flanges during the cutting operations. Their purpose is to assure cutting accuracy and prevent damage to the vacuum vessel segment and to the cutting tools. At present, they are envisioned as straps attaching the vacuum vessel segment to the superconducting coil structural case.

X.6.8 Recommendations for Further Study

Further study is highly recommended with the effort directed toward revision of the present baseline design in order to simplify maintenance procedures and reduce costs.

X.6.8.1 Vacuum Vessel Parting Flange Seals

A number of good mechanical seals are currently available. Their design is within state of the art. Particular attention must be devoted to the effects of thermal gradients on structural flange design. A successful conclusion of this study would eliminate the need for a remote cutter and welder and, of course, the need to install these devices under remote handling conditions.

X.6.8.2 Vacuum Vessel Parting Flange Clearance Design

The alternate design shown in Fig. X.6-14 has considerable merit with the advantage of eliminating the bellow-actuator section of the vacuum vessel segment. Additional study is required to develop procedures to axially translate the sleeve without binding under remote conditions. A stress analysis of the loads in the welds will be required.

X.6.8.3 Relocation of Vacuum Vessel Parting Flange

When additional design definition is available, it is recommended that an indepth study be conducted to determine if the vacuum vessel parting flange can be axially relocated towards the end plug side of the barrier coil module thus eliminating the need for axial translation of the barrier coil module and reducing the complexity of the barrier coil carriage. This approach, if possible, would result in a much easier remote maintenance task.

The installation of a remote cutter circular adapter similar to that shown in Fig. X.6-10 might accomplish the same purpose.

Fig. X.6-14

GRUMMAN

SLEEVE

SERRATION
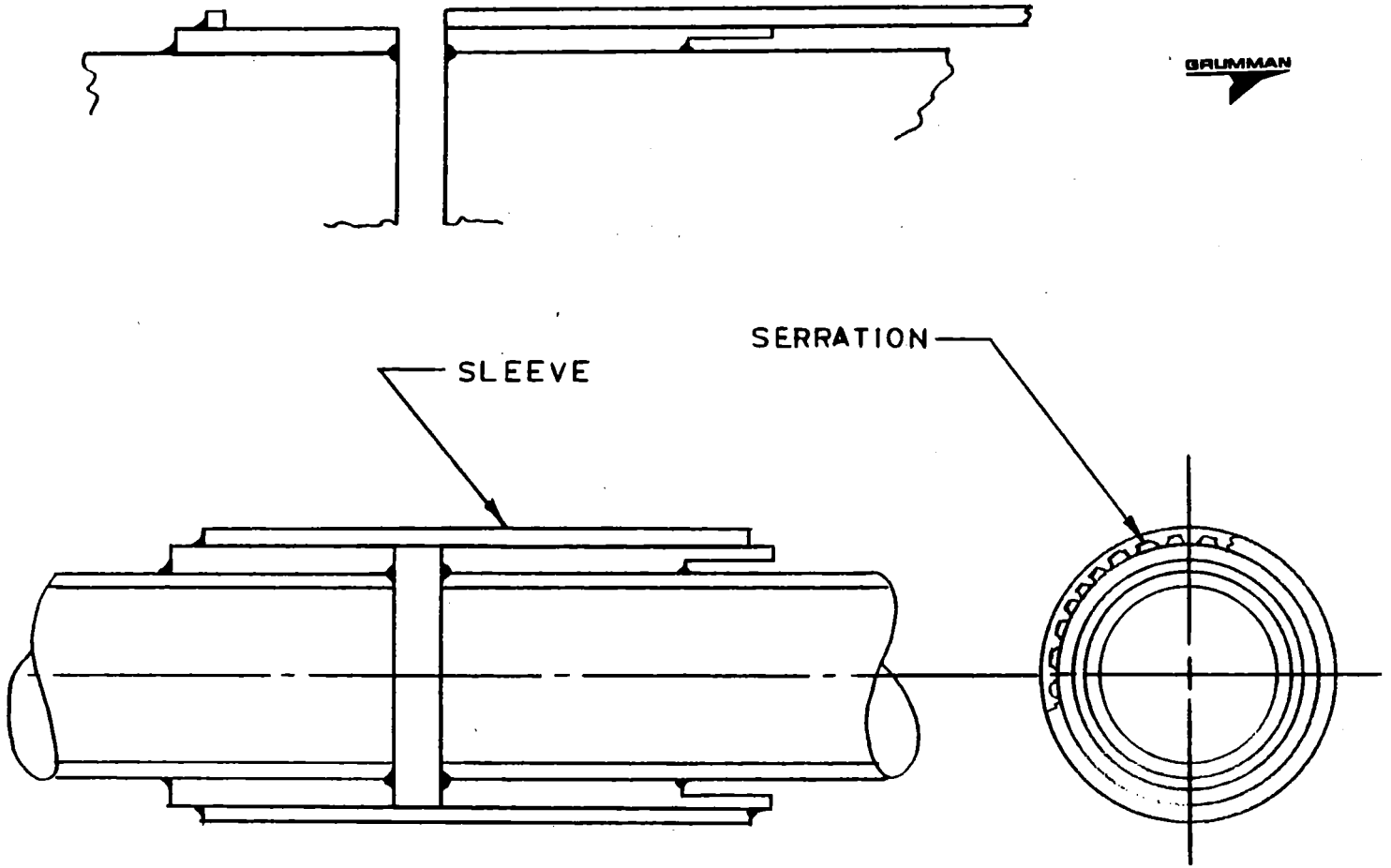
ALTERNATE DESIGN OF PARTING FLANGE

X.6-32

The baseline approach described in the body of the text, however, can be successfully employed for all configurations of the vacuum vessel and super-conducting coil considered so far during the TASKA study effort.

X.7 Availability and Maintainability

X.7.1 Introduction and Summary

TASKA steady state availability has been analyzed. The system has been broken down into several main subsystems and a logic diagram of the device has been put together. A computer code using the Monte Carlo method has been used to find the availability that can be expected.

Since the computer code is still under development, a very simplistic model resulted. Therefore, the results would probably tend to be on the optimistic side. However, both routine maintenance and unexpected random failures were taken into account. Redundancy and spares of certain subsystems and overdesign (i.e., more subsystems operating than the minimum needed for successful operation) have also been incorporated.

Due to lack of data, only subsystem levels have been treated. This means that no attempt has been made yet to assess the availability of each subsystem using the failure rate and repair rate data of constituent components. Instead, we employed the failure rate and repair rate data estimates for each subsystem. Large spreads in estimates have been observed, hence three cases have been run: one, using the pessimistic set of data, which yielded an overall steady state availability of 24-30%; secondly, the median set of data, yielding 40-48% availability; and the optimistic set of data yielding an average availability above 70%. In order to improve availability, it is suggested that either the quality of the magnets be increased and/or their number decreased. To a lesser extent, the same recommendations apply to the neutral beam and the RF heating subsystems.

X.7.2 Main Subsystems in TASKA and Their Logic Interconnection

The main subsystems in TASKA are presented in Table X.7-1. Some simplifications are evident in this table; for instance, both the permanent and the test blanket have been lumped under the term "blanket". The more frequent replacement of the test blanket is assumed to take place during the annual shutdown period.

Table X.7-1 also provides information on the total number of each kind of subsystem operating, the minimum number necessary for operation of the plant and number of redundant subsystems (meaning idle subsystems that can be switched on instantaneously to substitute for a failed subsystem of the same kind). Note that, in order to increase the availability, a certain amount of liberty was used. For example, redundancy was provided for the 250 keV neutral beam subsystem, even though the design does not specifically call for it, because sufficient space exists for installing another 250 keV injector.

The logic diagram of TASKA is given in Fig. X.7-1; only the most important interconnections have been shown.

X.7.3 The Computer Code for Analysis of Availability

The computer code we used to analyze the availability of TASKA employs the Monte Carlo method. This means that the reliability R, of the ith subsystem in a time interval Δt, $R_i = \exp(-\lambda_i \Delta t)$, is compared to a random number N_n (between 0. and 1.) generated by the computer. If $N_n < R_i$, no failure of that subsystem occurs in this time interval; if $N_n > R_i$, a failure occurs in this time interval.

λ_i is the failure rate of subsystem i. It can be constant in time (random failures, which was used here) or it can have a general dependence on time of the form:

Table X.7-1. Main Subsystems in TASKA

Subsystem	Number of Units	Redundancy	Minimum Number
Shield	1	0	1
Blanket	1	0	1
CC Coils (1 side)	3	0	2
CC-TB Coils	2	0	2
Plasma Cross Section Coils	2	0	2
Yin-Yang Coils	2	0	2
Recirc. Coils	2	0	2
TB Coils	8	0	8
Cryosystem and Vacuum	1	0	1
Neutral Beams (one side)			
250 keV	1	1	1
50 keV	1	0	1
76 keV	1	0	1
2 keV	1	0	0
ECRH (one side)	2	0	2
ICRH	16	0	13
Direct Convertor (one side)	1	0	1 either side
Instrumentation	1	0	1
Balance of Plant	1	0	1
Tritium System	1	0	1

1 1

2 2/3

3 2/3

4 2

5 2

6 2

7 2

8 2

9 2

10 2

11 2

12 8

13 8

A

14 1

15 1

16 2/3

17 2/3

18 1

19 1

20 1

21 1

B

22 2

23 2

24 16

C

25 1

26 1

27 1

D

28 1/2

29 1

30 1

E

LEGEND

AND GATE

OR GATE

16 2/3
Minimum number needed
Total number operating
Subsystem ID number

A MAGNET SYSTEM
B NEUTRAL BEAM SYSTEM
C R F HEATING SYSTEM
D HEAT TRANSFER & TRITIUM SYSTEM
E PLANT OUTPUT
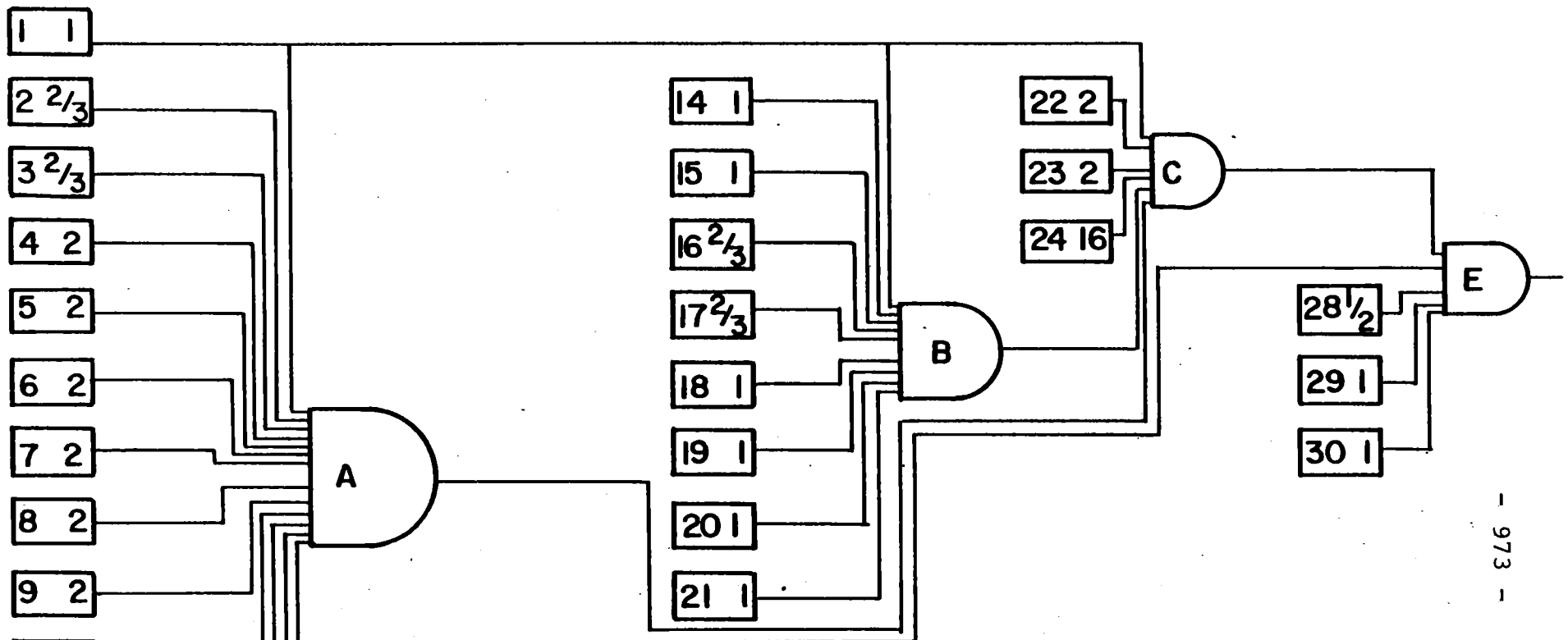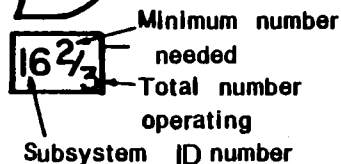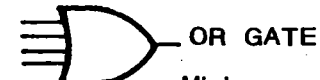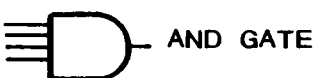
1 CRYOGENIC SYSTEM
2 CC COILS ONE SIDE
3 CC COILS other SIDE
4 & 5 CC/TB COILS
6 & 7 Plasma Cross-Section Coils
8 & 9 Yin-Yang Coils
10 & 11 Recirc. Coils
12 & 13 TB COILS
14 & 15 250 KeV NB SYSTEM
16 & 17 50 KeV NB SYSTEM
18 & 19 76 KeV NB SYSTEM
20 & 21 2 KeV SYSEEM
22 & 23 ECRH SYSTEM

24 ICRH SYSTEM
25 TRITIUM SYSTEM
26 BLANKET
27 BALANCE OF PLANT
28 DIRECT CONVERTOR
29 INSTRUMENTATION
30 SHIELD

Fig. X.7-1. **LOGIC DIAGRAM OF TASKA**

$$\lambda(t) = \lambda_c \beta t^{\beta-1}$$

where λ_c is a constant.

If this relationship is plotted with β as a parameter, Fig. X.7-2, a bathtub curve results, which is a typical time dependence of λ over the life of a component. For $\beta < 1$, we have a decreasing failure rate in time. For obvious reasons, this period is called the "burn-in" or "debugging" period. It is expected that this will last about 7 years for TASKA, or about the first half of the plant lifetime. The burn-in period is usually followed by a "random failure" period where λ is constant and $\beta \approx 1$. The last portion of the curve is the "wear out" period, where $\beta > 1$, and the failure rate is increasing in time. We have concentrated on the random failure period of each subsystem for simplicity, assuming that the worn out components will be replaced during the 28-day annual scheduled maintenance period.

The random number generator employs the recursive congruential method. This means that the random number is related to the remainder of division of the previous random number by a constant.

Basically, the computer code works as follows. The input data is read in; this includes the length of the time step, number of time steps, data for each subsystem (failure rate, mean time to repair or MTTR, number of identical units, redundancy, minimum number necessary for operation), logic interconnections (number of AND and OR gates, identification of subsystems and gates tied to the inputs of each gate).

The clock is then started and the reliability of R_i of each subsystem is computed and compared to a random number. In case of failure, the subsystem is down until the elapsed time is greater than the MTTR of that subsystem.

FAILURE
RATE
$\lambda(t)$

$\beta < 1$
Burn-in

$\beta > 1$
Wear-out

$\beta \approx 1$
Random failures
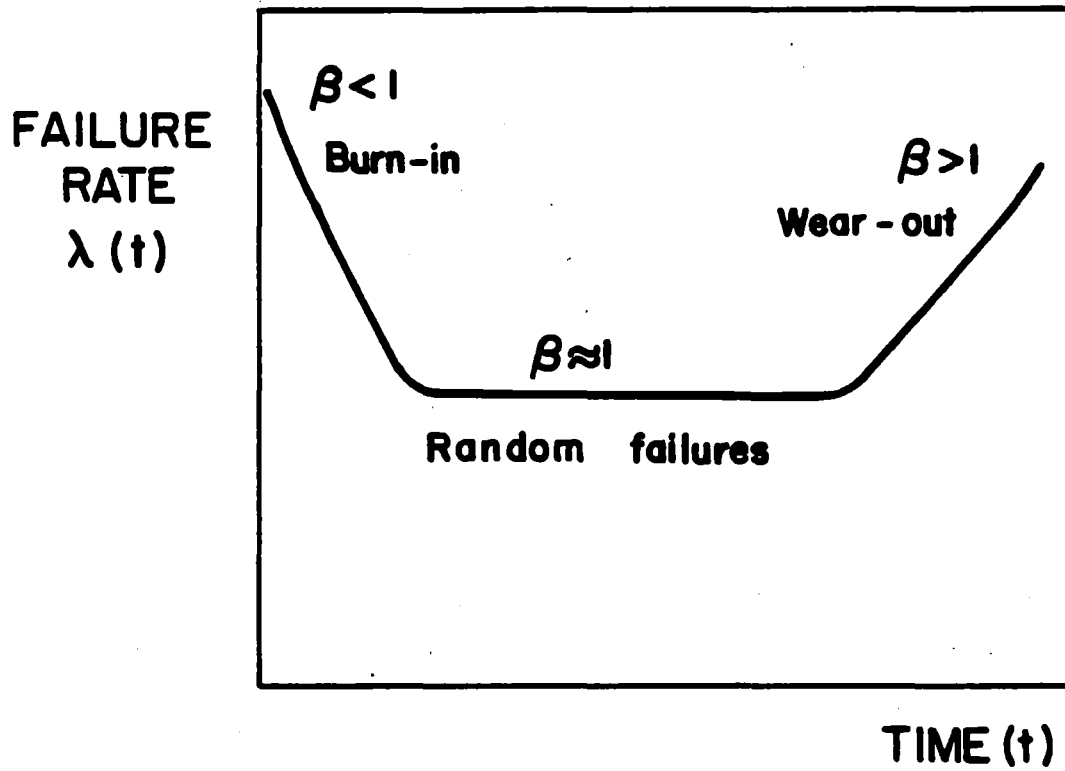
TIME (t)

Fig. X.7-2. The bath tub curve.

X.7-6

The availability of each subsystem during a mission is computed as:

$$a_i = \frac{\text{total up time during mission}}{\text{total mission time}} \quad .$$

The status of each gate is computed from the states of all its inputs as follows:

for an AND gate with inputs $i = 1, \ldots, N$:

$$A_{AND} = \prod_{i=1}^{N} a_i$$

where a_i's are either availabilities at the inputs (for time independent analysis) or the states of the inputs (0's or 1's). A_{AND} is then the average availability of the gate or its state during a particular time step (0 or 1).

For an OR gate:

$$A_{OR} = 1. - \prod_{i=1}^{N} (1. - a_i) \quad .$$

The availability of the system is then equal to the availability at the output of the last logic gate in the logic diagram of the system.

At this time, the computer code can handle spares, redundancy, overdesign (greater number of subsystems than the minimum necessary), immediate repair.

The assumptions built into the code at this time are that there is a 28-day shutdown period for each year of operation of the plant, in order to accomplish routine maintenance. In case of shutdown, no residual failures are assumed to occur. Only constant failure rates are treated at this time.

X.7-7

X.7.4 Data

For obvious reasons, only crude estimates of the data needed exist. Due to the spread in data, three types of runs were made: one, using the most pessimistic data (both for the failure rates and the MTTR's); secondly, using the most optimistic data; and thirdly, using most reasonable data which are similar to the data employed in the ETF availability estimate.[2] The data have been found in recent fusion design reports and papers which are listed in the Reference section, and also from discussions with the people in the field.

The data used are presented in Table X.7-2.

X.7.5 Results

The results for the steady state availability under the above assumptions and assuming a 28-day scheduled annual shutdown period, are as follows:

24-30% for the most pessimistic set of data;

40-48% for the most reasonable set of data;

74% for the most optimistic set of data.

Due to the simplifying assumptions employed, the true values may be lower.

The availability drivers are magnets, because there are so many of them and because their MTTR is relatively long (~ 40 days), due to the long time for warm up and cool down required for these cryogenic components. In order to improve the overall availability, the quality of magnets must be increased. The same holds true, to a smaller extent, for the neutral beam and the RF heating subsystems.

X.7.6 Maintainability

Essentially the same philosophy of maintainability will be followed as in previous fusion plant designs.[6,1]

Table X.7-2. Failure Rates and Mean Times to Repair for

Various Subsystems in TASKA

Subsystem	$\lambda(hr^{-1})$	MTTR (hr)
Shield	2.3E-5, 1.9E-5, 5.7E-6	24., 240.
Blanket	1.7E-4, 1.1E-4, 1.9E-5	120., 240.
All Coils	3.8E-5, 4.6E-6, 2.9 E-6	1056., 3600., 26298.
Cryosystem (Vacuum)	5.7E-5, 4.1E-5, 2.3E-5	24., 432., 4824.
All Neutral Beams	1.4E-3, 2.3E-4, 5.7E-5	24., 240., 864.
All ECRH	1.0E-3, 4.6E-4, 1.1E-5	240., 480.
ICRH	1.1E-4, 5.7E-5	240.
All Direct Convertors	2.3E-4, 1.1E-4, 2.3E-5	950.
Instrumentation	5.7E-5, 2.3E-5	144.
Balance of Plant	1.1E-4, 5.7E-5	240.
Tritium System	2.3E-5	60.

The mirror reactors pose fewer accessibility problems than the tokamaks. The central cell can be built out of modular sections, which can be replaced using an overhead gantry crane. An approach similar to that in the WITAMIR-I reactor can be employed here to provide maintenance of the blanket, coils and the shield sections.

References for Section X.7

1. "STARFIRE - A Commercial Tokamak Fusion Power Plant Study," Argonne National Laboratory, ANL/FPP-80-1 (1980).

2. Grumman Aerospace Corporation, unpublished report

3. E.R. Hager, private communication

4. P.T. Spampinato, private communication

5. "FRG Contributions, TASKA Review Meeting," Madison, Wisconsin, 2./3. Nov. 81

6. B. Badger et al., "WITAMIR-I, A University of Wisconsin Tandem Mirror Reactor Design," University of Wisconsin Fusion Engineering Program Report UWFDM-400, (1980).

X.8 Conclusion

To achieve successful operation of TASKA with high availability, the maintenance of the whole facility as well as its major components has been considered. A steady state availability has been analyzed, where both routine maintenance and unexpected random failures were taken into account. The results show that the availability drivers are magnets and, to a smaller extent, neutral beam and RF heating subsystems.

To demonstrate the practicability of maintenance tasks, four typical cases have been selected; i.e. the exchange of blanket modules, neutral beam injector components, central cell and barrier coils. Reasons for this selection were either the frequency of required replacement or the difficulty and complexity of the exchange. The latter necessitated a more detailed approach to the barrier coil replacement.

Due to the great variety of handling tasks to be performed under greatly vayring environmental conditions, a handling system was conceived which comprises hands-on devices and tools as well as remotely handled equipment.

The consideration of critical maintenance operations impacts on component design but it can also be assumed that the maintenance problems are soluble.

XI Costs

XI.1 Introduction

The direct costs developed for TASKA follow the format adopted for INTOR. Thus, the accounts are divided into the following categories:

  1.1 Blanket and Shield

  1.2 Magnets

  1.3 Plasma heating

  2.0 Reactor Support systems

  3.0 Buildings

The Reactor Support Systems in turn include the following:

  2.1 Electrical

  2.2 Auxiliary Cooling

  2.3 Intrumentation and Control

  2.4 Fuel Handling and Storage

  2.5 Maintenance Equipment

  2.6 Primary Heat Transport

  2.7 Secondary Heat Transport

  2.8 Reactor Vacuum System

  2.9 Radwaste Treatment

  2.10 Thermal Dumps

  2.11 Direct Convertor

  2.12 Reactor Support Structure.

Wherever possible, unit costs and cost algorithms were obtained from the "INTOR - Summary of Cost/Schedule/Manpower" FEDC-M-81-SE-062. The costs which were not available from INTOR were taken from PNL-2987 "Fusion Reactor Design

Studies: Standard Cost Estimating Rules," issued by Pacific Northwest Labs

and DOE; the "Unit Cost Documentation" WFPS-TN-057 issued by ORNL with

Westinghouse and industrial sources. The sources of the unit costs will be

identified as INTOR, PNL/DOE, WFPS and industry.

XI.2 Costs in Individual Accounts

In the following section, the accounts will be broken down into their constituents and tabulated wherever possible as to the quantities, unit cost, cost source and total cost.

1.1 Blanket/Shield

	Material	Quantity $(10^3$ kg)	Unit Cost $/kg	Source	Total $ x 10^6
Vacuum Chamber	316 SS	144.47	45	INTOR	6.50
Blanket	HT-9	39.87	45	INTOR	1.79
Breeding Material	$Pb_{83}Li_{17}$	600.	10.8	PNL/DOE	6.48
Reflector	316 SS	273.9	10	INTOR	2.74
Shield	1442 Steel	1481.2	10	INTOR	14.81
	B_4C	191.76	50	INTOR	9.59
	Pb	538.35	4	INTOR	2.15
	W	33.45	60	Industry	2.01
Neutral Beam Dumps	TZM	1.095	200	Industry	0.22
TOTAL					46.29

1.2 Magnets

Here the costs of recent big projects such as LCT and MFTF have been used as the basis for cost estimates.

On this basis the following reference values have been adopted for the TASKA-magnets.

1. Superconductor costs

      NbTi cryostable, reinforced   14.5[*] $/kA·m at 6 T

      Nb_3Sn, cryostable, reinforced   34.5 $/kA·m at 10 T

2. Winding costs

      (equipments, insulation, labor)   46 $/m of wound conductor

3. Coil case   46 $/kg of final steel case

4. Intercoil structure   13.8 $/kg of steel

5. Normal conducting coils   55.2 $/kg of winding

6. Pretesting and special cryogenic

      engineering   20% of items 1 to 3

Based on these specific values the costs for the several magnets are (values in $ x 10^6):

Magnet	CC1-CC3	C 2	Barrier S.C. Part	Barrier N.C. Part	TC-RC	Yin-Yang	FSC5+6+7+8
Conductor	2.67	1.98	20.29	{ 1.10	3.86	4.60	{ 1.37
Winding	0.83	0.6	4.46		1.06	1.24	
Case	1.29	1.2	4.74	---	1.93	2.71	---
Total per coil	5.75	4.50	35.42	1.10	8.23	10.26	1.37
Specific costs ($/kg)	50.6	46	127.9	55.2	65.3	58.4	55.2

[*](1 DM = 0.46$)

Thus the total magnet system costs are:

	$ x 10^6
Central Cell	16.01
Barrier Coils (including normal inserts)	73.05
End Plug Coils	73.97
Field Shaping coils	2.74
Intercoil/Support Structure	62.10
	227.87

1.3 Plasma Heating

NEUTRAL BEAMS	Energy (keV)	Power (MW)	Unit Cost $/W	Source	Total $ x 10^6
Low Energy Barrier	5	0.25	1.80	INTOR	0.45
Medium Energy Barrier	50	49.6	1.80	INTOR	89.28
High Energy Barrier	76	6.6	1.80	INTOR	11.88
V. High Energy Plug	250	5.4	2.50	Industry	13.50

RF-HEATING	Freq. GHz				
ECRH (Plug)	56	14.9	5	Industry	74.5
ICRH Central Cell	0.03	40	2	Industry	80.00
TOTAL					269.61

XI.2-3

2.0 Reactor Support Systems

2.1 Electrical

The magnet electrical system and the substation system were taken from INTOR as 25×10^6. A detailed estimate will be performed when all the components are identified.

2.2 Auxiliary Cooling

System	Type	Power	Basis	Source	Total $ x 10^6
Magnet and Vacuum System Cooling	Cryogenerator	7.5 MW_e	---	KfK	12.33
Ion & Electron Thermal Dump	Water	89 MW_{th}	Algorithm	INTOR	1.33
Neutral Beam Dump	Water	10.6 MW_{th}	Algorithm	INTOR	0.24
Reflector	Water	5.1 MW_{th}	Algorithm	INTOR	0.13
Shield	Water	11.3 MW_{th}	Algorithm	INTOR	0.25
ICRH Antennae	Water	11 MW_{th}	Algorithm	INTOR	0.25
Normal Inserts and Field Shaping Coils	Water	39 MW_{th}	Algorithm	INTOR	0.35
Cooling Tower for all Above	Water/Air	174 MW_{th}	Algorithm	INTOR	4.43
TOTAL					19.31

2.3 Instrumentation and Control

For the present 25×10^6 has been used. However, an attempt will be made to estimate I&C better in the future.

2.4 Fuel Handling

Item	Capacity g/day	Costing Basis	Source	Total $ x 10^6
Piping	1500	Algorithm	INTOR	1.320
Isotopic Separation	1500	Algorithm	INTOR	1.390
Glove Box	1500	Algorithm	INTOR	5.790
Miscellaneous	1500	Algorithm	INTOR	1.70
Pellet Fuel		Algorithm	INTOR	0.13
Emergency Detritiation	18,000 m^3/h	Algorithm	INTOR	6.30
T_2 Storage	5000 g	$80,000/unit	PNL/DOE	0.080
TOTAL				16.71

2.5 Maintenance Equipment

Item	Source	Total $ x 10^6
Overhead bridge crane	KfK	1.20
Component handling machine	KfK	2.00
Shielded cabin	KfK	0.90
Manipulator unit	KfK	1.00
2 work platforms	KfK	0.20
Temporary shielding	KfK	0.20
NBI turnover machine	KfK	0.50
Blanket carriage/barrier coil support structures	KfK	0.40
Cutting/welding unit	KfK	0.90
Auxiliary remote equipment	KfK	2.50
20 hot cell work stations	KfK	4.00
Active service area bridge crane	KfK	0.80
Overhead manipulator system	KfK	2.20
Supplementary tools and devices	KfK	3.50
TOTAL		20.30

2.6 Primary Heat Transport

Item	Material	Capacity Size	Unit Cost	Source	Total $ \times 10^6$
Piping	HT-9	D = 40 cm	$120,000/m	PNL/DOE	6.00
		L = 50 m			
	HT-9	D = 22 cm	$65,000/m	PNL/DOE	1.95
		L = 30 m			
	HT-9	D = 20 cm	$60,000/m	PNL/DOE	1.80
		L = 30 m			
Pump	---	10^7 kg/hr		PNL/DOE	3.30
IHX	---			B&W	3.26
Cleanup System	---	6×10^5 kg	$2/kg	PNL/DOE	1.20
Dump Tanks & Piping	Steel	6×10^5 kg			3.00
Valves	Steel	60	25,000 ea	Industry	1.50
TOTAL					22.01

2.7 Secondary Heat Transport

Item	Material	Capacity Size	Unit Cost	Source	Total $ \times 10^6$
Intermediate Coolant	HB-40	1.4×10^4 kg	$0.8/kg	*	.01
Piping	Steel	D = 36 cm	$3,500/m	PNL/DOE	0.35
		L = 100 m			
Pump	Steel	6.1×10^5 kg/hr		PNL/DOE	0.73
Preboiler	Steel			B&W	0.67
Evaporator	Steel			B&W	1.20
Superheater	Steel			B&W	0.62
Steam Drum	Steel			B&W	0.12
Misc. Piping	Steel			---	0.50
Cooling Tower	---	30 MW	Algorithm	INTOR	1.29
TOTAL					5.49

*Whiteshell Nuclear Research Establishment, Canada.

XI.2-6

2.8 Reactor Vacuum

System	Type	Capacity	Cost Basis	Source	Total $ x 10^6$
Helium Pumping	Cryosorption	1×10^6 ℓ/s	Algorithm	INTOR	0.520
DT Pumping	Cryocondens.	2.4×10^7 ℓ/s	Algorithm	INTOR	~7.2
Regeneration	Roots Blowers	10^5 ℓ/s x 10	Algorithm	INTOR	0.400
Valves	Hard Seal	D = 1.2 m N = 50	Algorithm	INTOR	6.95
Ducting	Steel	---	---	---	1.00
TOTAL					16.07

2.9 Radwaste Treatment

According to PNL/DOE the radwaste treatment equipment costs $850/MW$_{th}$. For TASKA ($\sim$ 50 MW$_{th}$) this is $42,500.

2.10 Thermal dumps

The neutral beam dumps were included in the Blanket/Shield account. The ion and electron thermal dumps must dissipate $\sim$ 90 MW of power. They are constructed of water cooled stainless tubes and are estimated to require $\sim$ 7.35 x 10^3 kg including the manifolding. Using a unit cost of $45/kg we get $0.33 x 10^6.

2.11 Direct Convertor Module

The direct convertor module intercepts 1.2% of the ion thermal dump current or $\sim$ 0.65 m^2 in area. We assume the extended area PDC is $\sim$ 1.0 m^2. According to UCRL-86026, such a single stage PDC costs $7,500/m^2. The cryosurfaces were included in the auxiliary cooling system.

2.12 Reactor Support Structure

The intercoil and support structure for the magnets was included in the magnet account. For the remainder of the system we estimate ~ 900 MT at ~ \$15/kg, and get \$13.5 x 10^6.

3.0 Buildings

Building	Volume/Area	Unit Cost	Source	Total \$ x 10^6
Reactor Hall	78,000 m^3	Algorithm	INTOR	47.04
Lock Area & Active Comp. Inter. Storage	15,000 m^3	\$270/m^3	INTOR	4.05
Active Dismant. Maint. & Testing	15,000 m^3	\$270/m^3	INTOR	4.05
Active Waste Cond. & Temp. Storage	15,000 m^3	\$270/m^3	INTOR	4.05
Inactive Assem. Testing	15,000 m^3	\$270/m^3	INTOR	4.05
Inactive Storage	15,000 m^3	\$270/m^3	INTOR	4.05
Vac. & Cryo. Systems	13,000 m^3	\$270/m^3	INTOR	3.51
Cooling & DT Reprocess.	25,000 m^3	\$270/m^3	INTOR	6.75
Control	4,500 m^3	\$270/m^3	INTOR	1.21
Administr.	15,000 m^3	\$80/m^3	INTOR	1.20
Diesel Gen. Bldg.	5,000 m^3	\$80/m^3	INTOR	0.40
TOTAL				80.36

XI.3 Summary of Accounts

		$ x 10^6
1.1	Blanket/Shield	46.29
1.2	Magnets	227.87
1.3	Plasma Heating	269.61

Support Systems

2.1	Electrical	25.00
2.2	Auxiliary Cooling	19.31
2.3	Instrumentation and Control	25.00
2.4	Fuel Handling	16.71
2.5	Maintenance Equipment	20.30
2.6	Primary Heat Transport	22.01
2.7	Secondary Heat Transport	5.49
2.8	Reactor Vacuum	16.07
2.9	Radwaste Treatment	0.04
2.10	Thermal Dumps	0.33
2.11	Direct Convertor Module	0.01
2.12	Reactor Support Structure	13.50
3.0	Buildings	80.36
	Total Direct Costs	787.90

In addition to the direct costs, certain percentages for indirect costs such as engineering, assembly and contingency have to be accounted for. As an example, in INTOR these consisted of 45% and 15% of the direct costs for engineering and assembly respectively, and 30% of the direct and indirect costs for contingency.

XI.3-1

XI.4 Annual Operating Costs

The operating expenses for TASKA consist of the operation and maintenance costs and the power costs. O & M costs were taken as 3% of the direct costs or $24 x 10^6$/year. Annual power costs depend on the availability which is taken to be the same as INTOR, namely 10% the first year, 15% the second and third year, 25% for the fourth-seventh years and 50% for the eigth-fifteenth years. Power consumption for TASKA is 8.7 MW_e continuously and an additional 189 MW_e during operation. We have taken 45 mills/kW_h as the cost of electricity. Table XI.4-1 summarizes the operating costs.

The levelized annual operating cost is $54 x 10^6$. It is interesting to note that if the normal coils (barrier inserts and field shaping coils) cannot be deenergized during the downtime, the levelized annual operating cost rises to $64 x 10^6$.

Table XI.4-1. Summary of Operating Costs

Year	Avail. (%)	O & M ($ x 10^6$)	Annual Power ($ x 10^6$)	Annual Cost ($ x 10^6$)
1	10	24.0	10.9	34.9
2-3	15	24.0	14.6	38.6
4-7	25	24.0	22.1	46.1
8-15	50	24.0	40.8	64.8

TASKA PARAMETER LIST

1. PHYSICS PARAMETERS

1.1 General Power Parameters

Fusion Power, MW	86
Q	0.74
Neutron wall loading, MW/m^2	
Central cell	1.52
Barrier	0.566
Plug (max)	0.056
Surface heat load, W/cm^2	
Central cell (max)	5
Barrier (max)	38
Plug (max)	44
Central cell plasma power density, MW/m^3	17

1.2 Dimensions

Central cell	
Plasma radius, m	0.32
Minimum wall radius, m	0.46
Physics length, m	19.2
(B field peak to peak -- see diagram)	
Barrier	
Minimum plasma radius, m	0.099
Average plasma radius, m	0.20
Maximum plasma radius, m	0.50
Physics length, m	15.6
(barrier B peak to first plug B peak -- see diagram)	
Effective length,* m	9
Plug	
Midplane radius, m	0.28
Physics length, m	5.0
(B field peak to peak -- see diagram)	

---

*Region over which barrier potential is less than central cell potential; for purposes of effective volume computation.
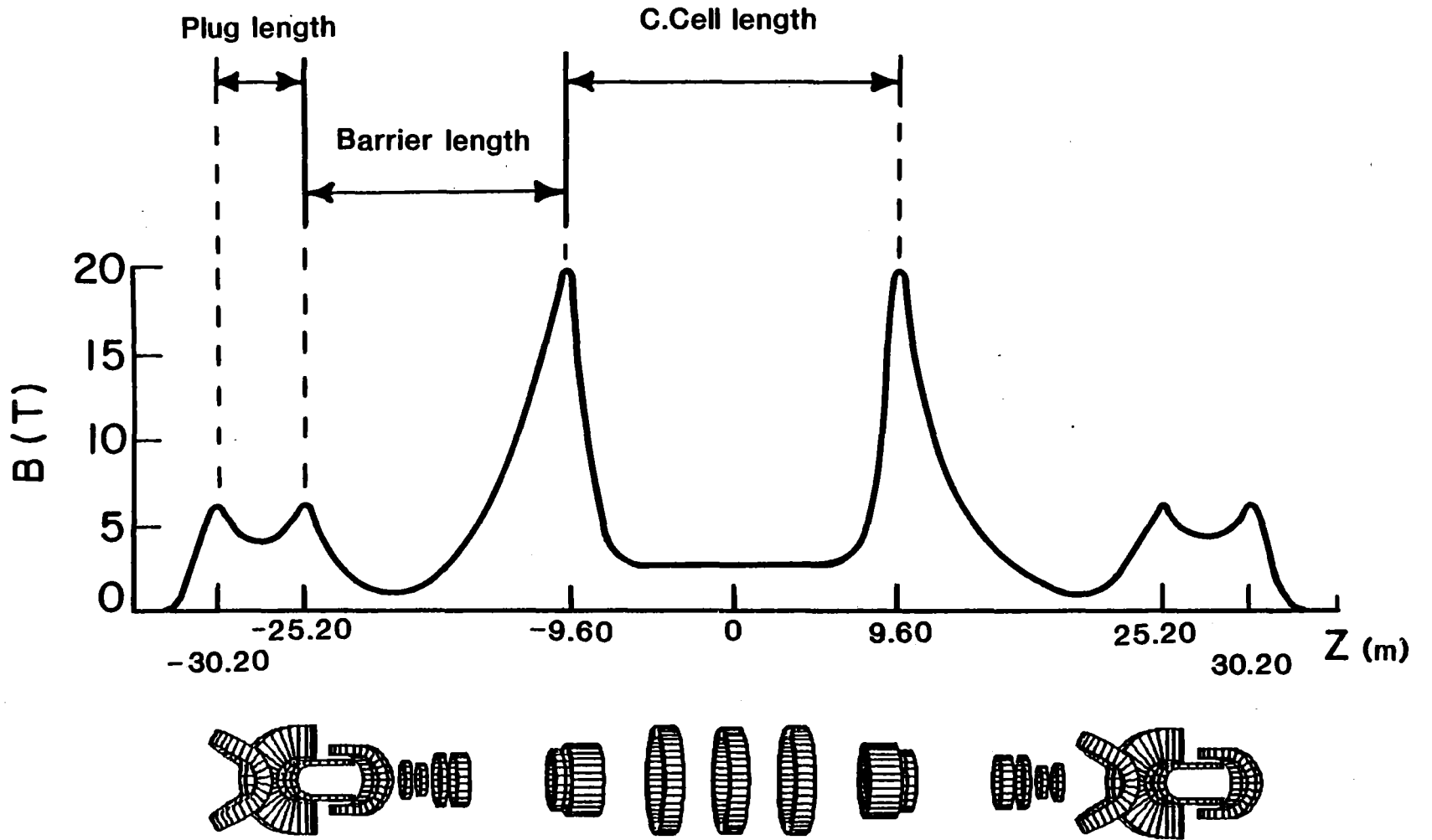
Length definitions for plasma physics purposes

Figure A-1

1.3 Magnetic Fields on Axis

Central cell average, T	2.7
Barrier maximum, T	20
Barrier minimum, T	0.8
Plug maximum, T	6.25
Plug minimum, T	4

1.4 Heating

Plug neutral beam

Neutral beam power, MW	5.4
Neutral species	H°
At energy, keV	250
At angle	60°
At trapping fraction	0.21

Barrier ME neutral beam

ME neutral beam power, MW	49.7
Neutral species	T°(56%), D°(44%)
At energy, keV	50
At angle	25°
At trapping fraction	0.95

Barrier HE neutral beam

HE neutral beam power, MW	6.6
Neutral species	D°
At energy, keV	76
At angle	20°
At trapping fraction	0.42

Barrier LE neutral beam

LE neutral beam power, MW	0.2
Neutral species	D°
At energy, keV	2-5
At angle	45°
At trapping fraction	0.99

RF Heating

Plug ECRF power, MW	14.9
At frequency, GHz	56
CC ICRF power, MW	40

At frequency, MHz   30

1.5 Heating Power Balance

Plug neutral beams
    Total (wall plug), MW   6.75
    Injected, MW   5.40
    Absorbed, MW   1.13

Barrier HE neutral beams
    Total (wall plug), MW   8.25
    Injected, MW   6.60
    Absorbed, MW   2.77

Barrier ME neutral beams
    Total (wall plug), MW   62.13
    Injected, MW   49.70
    Absorbed, MW   47.22

Barrier LE neutral beams
    Total (wall plug), MW   0.25
    Injected, MW   0.20
    Absorbed, MW   ~ 0.20

ECRH
    Total (wall plug), MW   27.60
    Injected, MW   14.90
    Absorbed, MW   14.90

ICRH
    Total (wall plug), MW   44.40
    Injected, MW   40.0
    Absorbed, MW   32.0

Total
    Total (wall plug), MW   149.38
    Injected, MW   116.8
    Absorbed, MW   98.22

1.6 Particle Balance

Axial loss rate, sec^{-1}
    Deuterium 1.8×10^{21}
    Tritium 1.8×10^{21}
    Alphas 3.1×10^{19}

Protons	2.6×10^{19}
Fueling, sec^{-1}	
By high energy NB (100% D)	3.2×10^{21}
By medium energy NB (56% T, 44% D)	1.6×10^{20}
By low energy NB (100% D)	2.0×10^{20}
By pellets	0
By gas puffing	0
Injected burn fraction,* %	.87
Barrier trapping current, A	437

1.7 Plasma Parameters

Central cell	
Density, cm^{-3}	1.9×10^{14}
Ion temperature, keV	30
Electron temperature, keV	11.5
Beta	0.5
$(n\tau)_{ic}$, cm^{-3} sec	5.4×10^{13}
$(n\tau)_{ec}$, cm^{-3} sec	5.3×10^{13}
Potential, ϕ_c, keV	43
Barrier	
Minimum density, cm^{-3}	6.8×10^{12}
Passing electron fraction	1
Beta	0.054
Potential, ϕ_b, keV	38
Pumping parameter, g_b	2
Plug	
Density, cm^{-3}	6.3×10^{13}
Species	p
Mean ion energy, keV	388
Electron temperature, keV	59
Beta	0.64

---

*Number of T atoms burnt s^{-1} in the plasma divided by the number of T atoms injected s^{-1} into the reactor vessel.

$(n\tau)_{ip}$, cm^{-3} sec	2.9×10^{13}
$(n\tau)_{ep}$, cm^{-3} sec	7.5×10^{11}
Potential, $\phi_c + \phi_e$, keV	109

2. PLASMA HEATING - EM WAVES

2.1 Electron Cyclotron Resonance Heating (ECRH)

Location	Plug
Total (wall plug) power, MW	27.6
Injected power, MW	14.9
Absorbed power, MW	14.9
Frequency, GHz	56
Resonance B-field, T	2
Propagation mode	Ordinary
Injection angle, deg	40-50
Overall efficiency, %	54
Cyclotron efficiency, %	60
Launching structure losses, %	10
Absorption efficiency, %	100
Gyrotron output power per tube, MW	0.35

2.2 Ion Cyclotron Range of Frequencies (ICRF)

Location	Central cell
Number of antennas (both ends)	8
Antenna radius (average), cm	46
Antenna material	Cu-plated HT-9
Faraday shield material	Mo
Total (wall plug) power, MW	44.44
Injected power, MW	40
Absorbed power, MW	32.0
Frequency, MHz	30
Overall efficiency, %	72
Antenna efficiency, %	80

3. NEUTRAL BEAMS AND BEAM POWER DUMPS
(for neutral beam injector power requirements see 1.4 Heating)

3.1 Plug Region

Neutral species	H°
Beam energy, keV	250
Number of beam lines	2
Ion sources/NBI	1
Ion source type	Ehlers
Extraction area, cm^2	~ 20 x 50
Ion current/NBI, A	23
Neutral current/NBI, A	10.8
Neutral beam power/NBI, MW	2.7
Pulse duration	DC
Gas input, Torr ℓ/s	~ 20
Gas efficiency,* %	~ 5

3.2 Barrier Region - Medium Energy Beams

Neutral species	T°(56%),D°(44%)
Beam energy, keV	50
Number of beam lines	6
Ion sources/NBI	3
Ion source type	Bucket
Extraction area, cm^2	~ 2700
Ion current/NBI, A	121
Neutral current/NBI, A	55
Neutral beam power/NBI, MW	8.27
Pulse duration	DC
Gas input, Torr ℓ/s	49.5
Gas efficiency,* %	30

---

*Fraction of gas molecules handled which
are injected as neutral particles

3.3 Barrier Region - High Energy Beams

Neutral species	D°
Beam energy, keV	76
Number of beam lines	2
Ion sources/NBI	1
Ion source type	Bucket
Extraction area/NBI, cm^2	~ 20 x 45
Ion current/NBI, A	108.8
Neutral current/NBI, A	43.4
Neutral beam power/NBI, MW	3.3
Pulse duration	DC
Gas input Torr ℓ/s	15.1
Gas efficiency,* %	26

3.4 Barrier Region - Low Energy Beam

Neutral species	D°
Beam energy, keV	2 to 5
Number of beam lines	2
Ion sources/NBI	1
Ion source type	Bucket
Extraction area/NBI, cm^2	~ 20 x 45
Ion current/NBI, A	97.5
Neutral current/NBI, A	50.0
Neutral beam power/NBI, MW	0.1-0.25
Pulse duration	DC
Gas input, Torr ℓ/s	13.0
Gas efficiency,* %	33%

3.5 Beam Dumps

Plug region

Dump power density (normal operation), kW cm^{-2}	1.0
Dump power density (no plasma condition), kW cm^{-2}	1.27
Configuration	Rectangular-V
Material	Mo
Inclination angle	76.7°
Surface temperature, °C	510

Coolant H_2O

Barrier region - high energy beams

    Dump power density (normal operation), kW cm^{-2} 0.58

    Dump power density (no plasma condition), kW cm^{-2} 1.0

    Configuration   Rectangular-V

    Material   Mo

    Inclination angle   61.9°

    Surface temperature, °C   495

    Coolant H_2O

Barrier region - medium energy beams

    Dump power density (normal operation), kW cm^{-2} 0.20

    Dump power density (no plasma condition), kW cm^{-2} 4.0

    Configuration   Circular-V

    Material   Mo

    Inclination angle   58.1°

    Surface temperature, °C   277

    Coolant H_2O

    Beam-generated DT neutron yield, s^{-1} 4×10^{10}

    Implanted tritium inventory, g   0.50

Barrier region - low energy beams

    No dump required

    (Opposing first-wall power density, kW cm^{-2} 4×10^{-4})

4. MAGNETS

4.1 Central Cell

Coil type	Solenoid
Number of coils	3
Function	Central cell
Minor radius, m	2.8
Major radius, m	3.38/3.3[*]
Bundle cross section, m x m	1.2x0.58/1.2x0.5[*]
Mean turn length, m	19.17/19.42[*]
Volume of winding per coil, m^3	13.5/11.5[*]
Weight of winding per coil, tonnes	86/72.5[*]
Overall current density, A/cm^2	1350/1160[*]
Ampere-turns, 10^6 A-turns	9.4/6.96[*]
Self-inductance per N^2, 10^{-6} H/N^2	8.32/8.34[*]
Stored self-energy, GJ	0.37/0.2[*]
Operating temperature, K	4.2
Magnetic field on axis, T	2.7
Maximum magnetic field on conductor, T	< 6
Maximum ripple, %	< 5
Superconductor	NbTi
Stabilizing material	Al
Structure material	SS
Maximum working strain, %	0.24
Maximum working stress, MPa	500
Coil separation (wind/wind), m	3.0
Coil separation (mid/mid), m	4.2

4.2 Barrier Coil

Coil type	Hybrid, nested solenoids
Number of coils	2
Function	Mirror

[*] Outer solenoids / center solenoid

Dimensions	See Tables V.3-1 and V.3-2
Weight of winding per superconducting solenoid, tonnes	200
Ampere-turns, 10^6 A-turns	57
Stored self-energy, GJ	2.67
Operating temperature, K	4.2
Magnetic field on axis, T	14 + 6
Maximum magnetic field on conductor, T	15/20.7
Superconductor	Nb_3Sn/NbTi
Stabilizing material	Cu/Al
Structure material	SS
Maximum working strain, %	0.24
Maximum working stress, MPa	500
Coil separation (wind/wind), m	18
Coil separation (mid/mid), m	19

4.3 Transition Coil

Coil type	Reversed-C
Number of coils	4
Function	Change of flux bundle cross section
"Minor radius", m	1.6
"Major radius", m	1.4
Sweep angle, degree	60
Bundle cross section, m x m	1.0 x 0.6
Mean turn length, m	19.9
Volume of winding per coil, m^3	11.94
Weight of winding per coil, tonnes	84
Overall current density, A/cm^2	1900
Ampere-turns, 10^6 A-turns	11.4
Self-inductance per N^2, 10^{-6} H/N^2	7.5
Stored self-energy, MJ	487
Operating temperature, K	4.2
Maximum magnetic field on conductor, T	< 8

A-12

Superconductor	NbTi·
Stabilizing material	3/4 hard Cu
Structure material	3/4 hard Cu
Maximum working strain, %	0.24
Maximum working stress, MPa	500

4.4 Plug Yin-Yang

Coil type	Yin-Yang
Number of coils	2 + 2
Function	Mirror, magnetic well
Minor radius, m	0.9
Major radius, m	1.4
Sweep angle, degree	90°
Bundle cross section, m x m	2.0 x 0.38
Mean turn length, m	21.93
Volume of winding per coil, m^3	16.67
Weight of winding per coil, tonnes	117
Overall current density, A/cm^2	1630
Ampere-turns, 10^6 A-turns	12.4
Self-inductance per N^2, 10^{-6} H/N^2	5.35
Stored self-energy, MJ	411
Operating temperature, K	4.2
Magnetic field on axis, T	6.25 to 4
Maximum magnetic field on conductor, T	< 8
Superconductor	NbTi
Stabilizing material	3/4 hard Cu
Structure material	3/4 hard Cu
Maximum working strain, %	0.24
Maximum working stress, MPa	500

5. CENTRAL CELL PARAMETERS

5.1 Composition

Blanket structural material	HT-9
Blanket coolant	$Li_{17}Pb_{83}$
Breeding material	$Li_{17}Pb_{83}$ (90% Li^6)
Blanket composition, v/o	
Structure	7
Coolant/breeder	73
Void	20
Reflector composition, v/o	
Structure	90 (316 SS)
Coolant	10 (H_2O)
Void	0
Shield material	
Material 1	Fe-1422
Composition, v/o	56
Material 2	B_4C (87 v/o)
Composition, v/o	26
Material 3	Pb
Composition, v/o	14
Coolant	H_2O
Composition, v/o	4

5.2 Dimensions

Central cell I.D., m	0.92
Non-testing first wall area m^2	25.5
Testing zone area, m^2	7.8
First wall thickness,[+] mm	3

[+] Thickness of first wall tubing

Blanket thickness, m   1

Reflector thickness, m   .28

Shield thickness, m   .25

5.3 Neutronic Summary

(3-D results except where indicated by an asterisk)

Fusion power, MW	86
14 MeV neutron wall loading, MW/m^2	1.52
Blanket multiplication[+]	0.616
Overall tritium breeding ratio	1.04
Local tritium breeding ratio	1.65
Power in first wall, MW	1.052
Power in breeding blanket, MW	42.42
Power in reflector, MW	5.08
Power in shield, MW	11.304
Max. first wall power density,[*] W/cm^3	10.4
Max. blanket power density,[*] W/cm^3	11.24
Max. reflector power density,[*] W/cm^3	0.1064
Peak dose outside biological shield,[*] during operation, mrem/hr	1.23

5.4 Thermal Hydraulics

Blanket temperature, °C	
Coolant inlet	300
Coolant outlet	400
Maximum structure temperature	420
Minimum structure temperature	300
Reflector temperature, °C	
Coolant inlet	80
Coolant outlet	140
Maximum structure temp.	150

[+] Multiplication for breeding blanket only, defined by (power deposition in blanket)/(total fusion neutron power)

[*] 1-D results.

Minimum structure temp.	80
Shield temperature, °C	
Coolant inlet	80
Coolant outlet	140
Maximum structure temp.	165
Minimum structure temp.	80
Blanket coolant conditions	
Maximum velocity, cm/s	9.7
Maximum pressure drop,[*] MN/m^2	1.08
Maximum pressure, MN/m^2	1.02
Total coolant flow, kg/hr	1.05×10^7
Pumping power, kW	500
Reflector coolant conditions	
Maximum velocity, cm/s	100
Maximum pressure drop, MN/m^2	.01
Maximum pressure, MN/m^2	.3
Total coolant flow, kg/hr	7.2×10^4
Pumping power, kW	1
Shield coolant conditions	
Maximum velocity, cm/s	100
Maximum pressure drop, MN/m^2	.01
Maximum pressure, MN/m^2	.3
Total coolant flow, kg/hr	1.6×10^5
Pumping power, kW	2

---

[*]Including head pressure.

A-16

6. MATERIALS TEST MODULE

6.1 Gas Cooled REGAT Module

Width (m)	0.7
Thickness (m)	0.2
Area (m^2)	2.02
Module volume (liters)	493
Capsule volume -- 40% of module volume (liters)	197
Module structure and v/o	Ti-6Al-4V 20 v/o
Coolant and v/o	Helium 40 v/o
Specimen and capsule structure and v/o	316 SS 20 v/o
Thermal contact material and v/o	NaK 20 v/o
Average dpa per MW-yr/m^2	7.3
Cumulative dpa·ℓ (5.3 FPY operation)	11416
Average He appm per MW-yr/m^2	49.03
Cumulative He appm·ℓ (5.3 FPY operation)	76861
Average power density (W/cm^3)	3.27

6.2 Water Cooled REGAT Module

Width (m)	0.5
Thickness (m)	0.2
Area (m^2)	1.45
Module volume (liters)	352
Capsule volume (liters)	141
Module structure and v/o	316 SS 20 v/o
Coolant and v/o	H_2O 15 v/o
Module void v/o	25 v/o
Specimen and capsule structure and v/o	316 SS 20 v/o
Thermal contact material and v/o	NaK 20 v/o
Average dpa per MW-yr/m^2	5.14
Cumulative dpa·ℓ (5.3 FPY operation)	5764
Average He appm per MW-yr/m^2	44.0
Cumulative He appm·ℓ (5.3 FPY operation)	49322
Average power density (W/cm^3)	7.36

7. NEUTRONICS
(Based on 1 MW/m^2 Wall Load)

7.1 General

Overall Breeding ratio	
^{6}Li	0.976
^{7}Li	0.064
Total	1.04
Energy deposition per 14.1 MeV neutron, MeV/fusion	
Neutron	8.25
Gamma	6.72
Total	14.97
Overall energy multiplication	1.06

7.2 First Wall

Radius, cm	46
Volume, m^3	0.1
Thickness,[+] cm	0.3
Av. power density, W/cm^3	
Neutron	3.03
Gamma	3.8
Total	6.83
Peak DPA per FPY[*]	14.8
Peak H production[*], appm/FPY	347.6
Peak He production[*], appm/FPY	107.1
Energy deposition per 14.1 MeV neutron, MeV/fusion	
Neutron	0.095
Gamma	0.12
Total	0.215

---

[*] 1-D results

[+] Thickness of first wall tubing

7.3 Breeding Blanket

Radius, cm	46.3
Volume, m^3	51.7
Thickness, cm	100
Av. power density, W/cm^3	
Neutron	0.306
Gamma	0.234
Total	0.54
Energy deposition per 14.1 MeV neutron, MeV/fusion	
Neutron	4.91
Gamma	3.77
Total	8.68

7.4 Reflector

Radius, cm	155
Volume, m^3	39.5
Thickness, cm	28
Av. power density, W/cm^3	
Neutron	0.0084
Gamma	0.057
Total	0.065

7.5 Shield (Central Cell)

Radius, cm	183
Volume, m^3	96.78
Thickness, cm	25
Av. power density, W/cm^3	
Neutron	0.042
Gamma	0.035
Total	0.077
Energy deposition per 14.1 MeV neutron, MeV/fusion	
Neutron	1.26
Gamma	1.05
Total	2.31
Percent of total energy in shield	15%

7.6 Barrier Insert Coil Shield

First wall radius, cm   17

Shield thickness, cm   12

Shield composition   80 v/o W (90%)

                                             10 v/o 316 SS

                                             10 v/o H_2O

7.7 Barrier Zone Shield

Shield thickness, cm   20/30

Shield composition   56 v/o Fe 1422

                                             26 v/o B_4C (87%)

                                             14 v/o Pb

                                             4 v/o H_2O

7.8 Plug Zone Shield

Shield thickness, cm   60

Shield composition   56 v/o Fe 1422

                                             26 v/o B_4C (87%)

                                             14 v/o Pb

                                             4 v/o H_2O

7.9 Direct Convertor Zone Shield

Shield thickness, cm   20

Shield composition   56 v/o Fe 1422

                                             26 v/o B_4C (87%)

                                             14 v/o Pb

                                             4 v/o H_2O

7.10 Magnets[+]

7.10.1 Central Cell Coils

Coil radius, cm	280
Peak dose in mylar, rad/FPY	1.85 E7
Peak dose in epoxy, rad/FPY	1.61 E7
Peak DPA in Al per FPY	1.05 E-5
Peak power density, W/cm^3	
Neutron	5.31 E-6
Gamma	7.77 E-6
Total	1.308 E-5

7.10.2 Barrier Coils

Wall loading, MW/m^2	0.566
Normal conducting insert coils	
Coil radius, cm	30
Peak dose in MgO, rad/FPY	4.354 E11
Peak power density, W/cm^3	
Neutron	0.178
Gamma	0.698
Total	0.876
Superconducting coils	
Coil radius, cm	130
Peak dose in mylar, rad/FPY	1.307 E6
Peak dose in epoxy, rad/FPY	1.047 E6
Peak DPA in Al, dpa/FPY	8.624 E-7
Peak DPA in Cu, dpa/FPY	2.935 E-9
Peak power density in LI[*] coil	
Neutron, W/cm^3	1.59 E-7
Gamma, W/cm^3	2.14 E-7
Total, W/cm^3	3.73 E-7
Peak power density in LO[*] coil	
Neutron, W/cm^3	6.27 E-10

[+] 1-D results

[*] For diagram of superconducting coil modules see Chapter V.

Gamma, W/cm^3 2.359 E-9

Total, W/cm^3 2.986 E-9

7.10.3 Field Shaping Coils

Max. wall loading, MW/m^2	7.28 E-4
Smallest coil radius, cm	100
Peak dose in MgO, rad/FPY	3.87 E8
Peak power density, W/cm^3	
Neutron	2.03 E-4
Gamma	4.4 E-4
Total	6.43 E-4

7.10.4 Transition and Yin-Yang Coils

Max. wall loading, MW/m^2	0.056
Smallest coil radius,cm	90.0
Peak dose in mylar, rad/FPY	2.03 E8
Peak dose in epoxy, rad/FPY	1.92 E8
Peak DPA in Cu, dpa/FPY	8.47 E-5
Peak power density, W/cm^3	
Neutron	3.69 E-5
Gamma	4.13 E-5
Total	7.82 E-5

8. RADIOACTIVITY

Operating period for radioactivity calculations, FPY   2

8.1 Activity at Shutdown (Ci/W$_{th}$)

Central cell (total)	1.077
Blanket	1.005
Vacuum boundary	1.25×10^{-2}
Reflector	5.84×10^{-2}
Shield	4.41×10^{-4}

8.2 Percent Afterheat at Shutdown (%)

Central cell (total)	7.07×10^{-1}
Blanket	6.36×10^{-1}
Vacuum boundary	1.28×10^{-4}
Reflector	0.575×10^{-4}
Shield	6.57×10^{-6}

8.3 BHP at Shutdown (Air) km^3(air)/kW$_{th}$

Central cell (total)	9.14×10^{1}
Blanket	87.9×10^{1}
Vacuum boundary	7.11×10^{-1}
Reflector	2.79
Shield	2.27×10^{-2}

8.4 Dose Outside Shield 1 Day After Shutdown (mrem/hr)

Central cell	1.004
Barrier	< 1.0
Plugs	< 1.0

9. TRITIUM SYSTEMS

9.1 Fueling

Central cell isotope injection rates*

Barrier neutral beams

D (atoms/s)	3.87×10^{21}
T (atoms/s)	3.50×10^{21}

Fraction of tritium gas handled
in beam lines but not injected — 0.70

Plug neutral beams*

H (atoms/s)	1.3×10^{20}

9.2 Plasma

Injected fractional burnup of T [+]	.0087
T burned (atoms/s)	3.0×10^{19}
D burned (atoms/s)	3.0×10^{19}

9.3 Exhaust

Particles pumped from reactor

T (atoms/s)	3.5×10^{21}
D (atoms/s)	3.84×10^{21}
H (atoms/s)	1.3×10^{20}
He (atoms/s)	3.0×10^{19}

Thermal dump

T inventory due to implantation (g)	0.02
Coolant type	$H_2O(\ell)$
T loss to coolant (Ci/d) (T barrier factor X-100)	0.07
Plate material	Stainless steel

---

*Including atoms not trapped in plasma

[+] Tritium burn-rate / tritium injection-rate

ME beam dump (D/T beam)

    T inventory due to implantation (g)   0.50

    Coolant type $H_2O(\ell)$

    T loss to coolant (Ci/d)   0.16

    (T barrier factor x 100)

    Plate material   Mo

9.4 Blanket

Breeder

Material	$Li_{17}Pb_{83}$
Temperature (°C)	
High	400
Low	300
Average	350
Breeder inventory (kg)	5.7×10^5
Tritium	
Overall breeding ratio	1.0
Breeding rate (atoms/s)	3.0×10^{19}
Concentration (wppm)	0.032
Pressure at average temperature (torr)	0.39
Inventory (g)	18.2
Extraction scheme	In-situ diffusion

Blanket coolant

Material	$Li_{17}Pb_{83}$
Flow rate (kg/s)	2900
Temperature (°C)	
Coolant in	300
Coolant out	400
Coolant inventory (kg)	5.7×10^5
Tube area (m^2)	1234
Tube thickness (mm)	2.27
Pressure (torr)	0.39
Tritium concentration (wppm)	0.032

9.5 Heat Exchanger Tubes in Intermediate Loop

Composition	HT-9
Thickness (mm)	2.27
Surface area (m^2)	895
Temperatures (°C)	
Coolant in	371
Coolant out	271
T permeation to intermediate loop (Ci/d)	370
(T barrier factor x 150)	

9.6 Tritium Inventory (g)

Fueling and exhaust	
Neutral beam pumps (Zr/Al getters)	259
Thermal and beam dump	0.52
End cell and beam dump cryopumps	125
(Time cryopumps on-line) (hr.)	2
Cryogenic distillation columns	28
Fuel cleanup	47
Blanket	
Breeding material	18.2
Breeder processing	0
Structural material and piping	0.12
Heat exchange cycle	
Inventory intermediate loop (g)	15.0
Total active tritium inventory, g	493
Total active tritium inventory, Ci	4.9×10^6
Storage (number of days/g)	5000

10. MATERIALS

10.1 Central Cell

10.1.1 "Fixed" Blanket Structure

Material	HT-9
Neutron wall load, MW/m^2	1.52
dpa/s (Max)	7.13×10^{-7}
dpa/FPY (Max)	22.5
Peak H production, appm/FPY	528.4
Peak He production, appm/FPY	162.8
Operating temp. range, °C	300-420
Number of cycles/y	~ 100

10.1.2 Coolant

Material	$Pb_{83}Li_{17}$
Temp. range, °C	300-400
Velocity, m/s	.097
Pressure, MPa	1.02

10.1.3 Breeder

Material	$Pb_{83}Li_{17}$
Temp. range, °C	300-400
Velocity, m/s	.097
Pressure, MPa	1.02

10.1.4 Reflector

Material	HT-9
Max. dpa/FPY	0.065
Peak H production, appm/FPY	0.014
Peak He production, appm/FPY	0.003
Coolant	H_2O
Operating temp., °C	80-140

10.1.5 Shield

Materials	SS-B$_4$C-Pb
Coolant	H_2O

A-27

Operating temp., °C	80-140
Max. dpa/FPY	4.92E-03
Max. He/FPY	8.64 E-4
Peak H production, appm/FPY	1.5 E-4
Peak He production, appm/FPY	3.8 E-5

10.1.6 Magnets

Materials

Superconductor	NbTi
Stabilizer	Al
Electrical insulation	G-10
Thermal insulation	Mylar
Structure	SS
Dewar	SS
Max. dpa/FPY in stabilizer	1.6×10^{-5}
Peak dose in mylar, rads/FPY	2.81×10^{7}
Peak dose in epoxy, rads/FPY	2.45×10^{7}

10.2 End Plug Region
10.2.1 Barrier Coil

Shield

Insert shield	W-SS
Zone shield	$Fe-B_4C-Pb$
Heat flux, W/cm^2	38 (max)
Coolant	H_2O
Temperature, °C	80-140

Magnet

Superconducting solenoid

Superconductor	$Nb_3Sn/NbTi$
Stabilizer	Al/Cu
Electrical insulator	G-10
Thermal insulator	Mylar
Structure	SS
Dewar	SS
Peak DPA in Al, dpa/FPY	8.62×10^{-7}
Peak DPA in Cu, dpa/FPY	2.94×10^{-9}

Peak dose in mylar, rad/FPY	1.31×10^6
Peak dose in epoxy, rad/FPY	1.05×10^6

Normal conducting insert

Conductor	OFHC (Cu)
Insulator	MgO (compacted)
Coolant	H_2O
Peak dose in MgO, rad/FPY	3.87×10^8

10.2.2 Field Shaping Coils

Conductor	OFHC (Cu)
Insulator	MgO (compacted)
Coolant	H_2O
Peak dose in MgO, rad/FPY	3.87×10^8

10.2.3 Transition, Recirculating and Yin-Yang Coils

Shield

Material	$Fe-B_4C-Pb$
Heat flux, W/cm^2	44 (max)
Coolant	H_2O
Temperature, °C	80-140

Magnet

Superconductor	NbTi
Stabilizer	Cu
Electric insulator	G-10
Thermal insulator	Mylar
Structure	Cu/SS
Dewar	SS
Max. DPA in Cu, dpa/FPY	8.47×10^{-5}
Peak dose in mylar, rad/FPY	2.03×10^8
Peak dose in epoxy, rad/FPY	1.92×10^8

11. DIRECT CONVERTOR AND POWER DUMP

11.1 Direct Convertor - Grids

Material	316 SS
Particle flux, cm^{-2}, s^{-1}	
D	3.2×10^{15}
T	3.2×10^{15}
p	2.4×10^{13}
He (low energy)	3.6×10^{13}
He (medium energy)	8.9×10^{12}
He (high energy)	1.4×10^{12}
Average particle energy, keV	
D	139
T	139
p	307
He (low energy)	248
He (medium energy)	808
He (high energy)	3,630
Heat flux, W/cm^2	150
Max temperature, °C	546
Coolant	H_2O
Coolant velocity, m/s	2.5
Coolant pressure, MPa	1.0
Coolant temp., °C	60-110

11.2 Direct Convertor - Collector Plate

Material	316 SS
Particle flux, cm^{-2} s^{-1}	
D	3.2×10^{15}
T	3.2×10^{15}
p	2.4×10^{13}
He (low energy)	3.6×10^{13}
He (medium energy)	8.9×10^{12}
He (high energy)	1.4×10^{12}
Average particle energy, keV	
D	39

T	39
p	207
He (low energy)	48
He (medium energy)	608
He (high energy)	3,430
Heat flux, W/cm^2	34
Maximum temperature	270
Coolant	H_2O
Coolant velocity, m/s	1.5
Coolant pressure, MPa	1.0
Coolant temperature, °C	60-100

11.3 Electron Power Dump

Material	316 SS
Particle flux, cm^{-2} s^{-1}	
p	2.2×10^{14}
He (medium energy)	8×10^{13}
He (high energy)	1.2×10^{13}
e^-	5.8×10^{16}
Average particle energy, keV	
p	307
He (medium energy)	808
He (high energy)	3,630
e^-	11.5
Electron heat flux, W/cm^2	121
Non-electron heat flux, W/cm^2	29
Coolant	H_2O
Coolant temp., °C	60-110°C
Coolant pressure, MPa	1.0
Coolant velocity, m/s	1.5

12. REMOTE REPLACEMENT CHARACTERISTICS
("Average lifetime" is near time between failures)

12.1 Vacuum Vessel (central cell)

Max. dimension, m	5ϕx3
Max. weight, tonne	30
Ave. lifetime, y	15
Lifetime, min-max, y	5-20
Max. activity 1d after shutdown, Ci/cc	4.99x10^{-2}

12.2 Test Blanket + Breeding Blanket

Max. dimension, m	1.7x3.2x1
Max. weight, tonne	30
Ave. lifetime, y	2
Lifetime, min-max, y	0.67-6
Max. activity 1d after shutdown, Ci/cc	0.239

12.3 Shield (central cell)

Max. dimension, m	3x1.5x0.84
Max. weight, tonne	30
Ave. lifetime, y	15
Lifetime, min-max, y	5-20
Max. dose 1d after shutdown, mrem/hr contact	0.106

12.4 Central Cell Coils

Max. dimension, m	7.0x1.2
Max. weight, tonne	150
Ave. lifetime, y	3
Lifetime, min-max, y	2-40
Max. activity 1d after shutdown, Ci/cc	< 10^{-5}

12.5 Barrier Coil

Max. dimension, m	3.5
Max. weight, tonne	350
Ave. lifetime, y	3
Lifetime, min-max, y	2-40

Max. activity 1d after shutdown, Ci/cc $< 10^{-5}$

12.8 Transition Coil

Max. dimension, m	7x5
Max. weight, tonne	200
Ave. lifetime, y	3
Lifetime, min-max, y	2-40
Max. activity 1d after shutdown, Ci/cc contact	$< 10^{-5}$

12.9 Yin-Yang Coil

Max. dimension, m	7.5x3
Max. weight, tonne	200
Ave. lifetime, y	3
Lifetime, min-max, y	2-40
Max. activity 1/10 d after shutdown, Ci/cc	$< 10^{-5}$

12.10 Neutral Beam Injector

Ave. lifetime, y	0.5
Lifetime, min-max, y	0.08-2

12.11 ECRH Units

Ave. lifetime, y	0.5
Lifetime, min-max, y	0.11-5

12.12 Direct Convertor

Ave. lifetime, y	0.5
Lifetime, min-max, y	0.5-5

12.13 Vacuum Equipment

Ave. lifetime, y	2
Lifetime, min-max, y	2-5

12.14 Vacuum First Wall - End Cell

Ave. lifetime, y	15

12.15 Auxiliary Equipment

Instrumentation - ave. lifetime, y   5

Heat exchangers - ave. lifetime, y   2

13. POWER CONVERSION

Blanket thermal power, MW(th)	42.42
Generation cycle efficiency, %	31.0
Net electrical output, MW(e)	13.15
IHX surface area, m^2	639
Intermediate coolant	HB-40
Coolant temperature, °C	271/37
Coolant flow rate, kg/sec	170
Steam generator surface area, m^2	537
Steam temperature, °C	343
Steam pressure, MPa	6.6
Water flow rate, kg/sec	7.2